Porous materials : constitutive modeling and computational issues

Sokratis Xenos

INSTITUT POLYTECHNIQUE DE PARIS

UNIVERSITY OF THESSALY

ÉCOLE POLYTECHNIQUE

IP PARIS

NNT : 2024IPPAX040

Thèse de doctorat

Modélisation théorique et numérique des matériaux poreux

Thèse de doctorat de l'Institut Polytechnique de Paris
préparée à l'École polytechnique

École doctorale n°626 École doctorale de l'Institut Polytechnique de Paris (EDIPP)
Spécialité de doctorat : Mécanique des fluides et des solides, acoustique

Thèse présentée et soutenue à Palaiseau, le 28 Juin 2024, par

SOKRATIS XENOS

Composition du Jury :

M. Samuel FOREST Professeur, Centre des Matériaux MINES, ParisTech	Président
Mme Carole NADOT-MARTIN Professeur, ISAE-ENSMA, Institut Pprime	Rapporteur
M. Léo MORIN Maître de Conférences, Institut de Mécanique et d'Ingénierie, Université de Bordeaux	Rapporteur
M. Robert MCMEEKING Professeur, Department of Mechanical Engineering, University of California, Santa Barbara	Examinateur
M. Martin GENET Professeur, LMS, C.N.R.S., École polytechnique	Examinateur
M. Michalis AGORAS Professeur Assistant, Department of Mechanical Engineering, University of Thessaly	Examinateur
M. Konstantinos DANAS Directeur de recherche, LMS, C.N.R.S., École polytechnique	Directeur de thèse
M. Nikolaos ARAVAS Professeur, Department of Mechanical Engineering, University of Thessaly	Co-directeur de thèse

Porous materials: constitutive modeling and computational issues

Ph.D. Thesis
Submitted by

Sokratis XENOS

Thesis advisors:
Konstantinos DANAS
Nikolaos ARAVAS

Laboratoire de Mécanique des Solides (LMS)
École Polytechnique
Institut Polytechnique de Paris

To my family

Η κάθε γλώσσα να μιλεί την καλοσύνη της ημέρας.
Ήμερα να χτυπάει στις φλέβες ο παλμός της γης.
– Οδυσσέας Ελύτης, *Ήλιος ο Πρώτος, 1943*

Acknowledgements

This research was conducted at the Laboratoire de Mécanique des Solides (LMS) and the Laboratory of Mechanics & Strength of Materials under a cotutelle doctoral program between École Polytechnique (l'X) and University of Thessaly (UTH). The thesis work was partially funded by LMS, fellowships from the Department of Mechanical Engineering via the Research Committee of University of Thessaly, and from the European Project RFCS-02-2022-RPJ.

First and foremost, I would like to express my sincere gratitude to my supervisors, Professors Kostas Danas and Nikolaos Aravas for their continuous guidance, support and faith in my abilities. I was really privileged to have both of them as mentors and teachers who have instilled me with their knowledge and have elevated my way of thinking. Their passion for excellence in the field of mechanics and generally in life will always serve as an inspiration for me.

I would also like to thank Professor Léo Morin and Professor Carole Nadot-Martin for accepting to spend their valuable time to review and comment on my manuscript. I am also extremely grateful to Professor Samuel Forest for accepting to be president of the committee as well as to Professors Robert McMeeking, Michalis Agoras, and Martin Genet for accepting my invitation to participate in the thesis committee.

A big word of thanks goes to all people in the administrative, HR and IT departments of both institutions for their invaluable assistance and will to help with anything that came up along the way. In particular, I would like to thank Anna Johnsson, Alexandra Joly, and Valérie Jamet for helping me with my trips and stay in Paris as well as Arxontoula Gialmanidi, Ntora Pappa and Eleana Pappa in Greece. I am also indebted to Nikos Cholevas for introducing me to Linux OS and helping me with various technical issues as well as Abtelfattah Halim for the IT support during my stay at LMS.

I could not, of course, forget to express my gratitude to all the friends, officemates and colleagues with which I have shared valuable moments and experiences throughout the past four and a half years. First, I would like to thank my long lasting undergrad friend Giorgos Aretis for his support and especially for taking his first trip out of Greece with me, during my initial visit to Paris. I want to deeply thank my dear friend Marios Sotiriou for his continuous support and amazing moments that we have had together before and after he left to pursue his own dreams in the US. Also, I would like to thank my friend Kostas Bouchoris for our fruitful discussions during our parallel journey as doctorate students at UTH. Special thanks go to Hsu-Cheng Cheng, Arnaud Coq, and Vignesh Selvam for the moments we shared together when in Paris, Zahra Hooshmand Ahoor and Haoming Luo for their overall support as well as Aris Stamou, Ilias Gavriilidis, Sotiria Houliara, and Professors Alexis Kermanidis and Emmanouil Bouzakis in Greece for our enriching interaction during the days at office.

Above all else, I want to express my deepest gratitude to my family, especially my parents, Dionisis and Vivi for their limitless support, unconditional love, and sacrifices that they have made for us during all of these years. I also owe a debt of gratitude to my older brother, Haralabos, who has been a constant source of inspiration for me since our childhood. Without them I would have neither made it this far nor been the person I am today.

Finally, I want to thank with all of my heart my dear companion, Dimitra, for her love, support and patience she has shown all of these years that we've been together. Our little, everyday moments helped me push through the difficulties and made me realize that happiness and beauty of life lie in simple things.

Contents

List of Figures

List of Tables

Abstract

This work is concerned with the development, calibration, and numerical implementation of a novel fully explicit isotropic, rate-independent, elasto-plastic model for porous metallic materials. The microstructure is assumed to consist of a random, with uniform probability, distribution of randomly oriented spheroidal voids of the same shape. The proposed model is based on earlier homogenization estimates that use a Linear Comparison Composite (LCC) theory. The resulting expressions exhibit the simplicity of the well known Gurson model and, thus, their numerical implementation in a finite element code is straightforward. To assess the accuracy of the analytical model, we carry out detailed finite-strain, three-dimensional finite element (FE) simulations of representative volume elements (RVEs) with the corresponding microstructures. Proper parameter calibration of the model leads to fairly accurate agreement of the analytical predictions with the corresponding FE average stresses and porosity evolution. We show, both analytically and numerically, that the initial aspect ratio of the voids has a significant effect on the homogenized effective response of the porous material leading to extremely soft responses for flat oblate voids (e.g., aspect ratio less than 0.5) especially at high stress triaxialities.

Next, we examine the computational issues related to the numerical implementation of rate-independent constitutive models that lead to softening behavior. It is shown analytically that elastic-plastic models based on "local" continuum formulations that do not incorporate a characteristic length scale may lead to loss of ellipticity of the governing partial differential equations (PDEs) and mesh-dependent numerical solutions. To remedy the associated numerical problems, we propose an implicit non-local version of the porous model developed in this work which is based on the introduction of a non-local porosity variable determined from the solution of an additional PDE. We show both analytically and numerically that the regularized version of the model allows for preservation of the elliptic properties of the governing equations yielding mesh-independent, converged solutions in the post-bifurcation regime. The bifurcation point (i.e., strain-to-localization) is found to be highly dependent on the micro-void's shape, with very flat voids (e.g., aspect ratio less than 0.3) leading to lower localization strains. The material length introduced by the non-local formulation is found to have minimal effect on the predicted bifurcation point, only affecting the post-bifurcation gradient of the macroscopic stress-strain curve and the size of the highly strained zone in the structure.

In the last part of this study, both the local and the non-local versions of the model are efficiently implemented in a commercial finite element code (ABAQUS). The models are used for the numerical solution of boundary value problems (BVPs) related to forming and ductile fracture processes under both quasi-static and dynamic conditions. In particular, the industrially relevant problems of Hole expansion (HET) and Charpy impact (CVN) test, the cup-and-cone fracture phenomenon as well as ductile fracture of a specimen with complex geometry and comparison with corresponding experimental results are analyzed in detail. Numerical predictions in all cases indicate that ductility is an increasing function of the void shape parameter and materials comprising flat oblate voids of low aspect ratio exhibit early macroscopic crack initiation and propagation compared to materials with spherical/almost spherical voids. Finally, the model's capability to reproduce experimental results with sufficient accuracy suggests that it can be utilized to provide predictions with only a small amount of parameters that may be calibrated from either micromechanics calculations or experimental data.

Key words: Porous metals, Homogenization, Non-local theories, Forming simulations, Ductile fracture simulations

Résumé

Ce travail porte sur le développement, la calibration et l'implémentation numérique d'un nouveau modèle élastoplastique entièrement explicite, isotrope et indépendant du taux de déformation pour les matériaux métalliques poreux. La microstructure est supposée être constituée d'une distribution aléatoire de vides sphéroïdaux de même forme, orientés de manière aléatoire et avec une probabilité uniforme. Le modèle proposé est basé sur des estimations d'homogénéisation antérieures qui utilisent une théorie de comparaison composite linéaire (LCC). Pour évaluer l'exactitude du modèle analytique, nous réalisons des simulations éléments finis tridimensionnelles à grandes déformations d'éléments de volume représentatifs (RVE) avec les microstructures correspondantes. Une calibration appropriée des paramètres du modèle conduit à un accord assez précis des prédictions analytiques avec les contraintes moyennes éléments finis et l'évolution de la porosité. Nous montrons, à la fois analytiquement et numériquement, que le rapport d'aspect initial des vides a un effet significatif sur la réponse effective homogénéisée du matériau poreux, entraînant des réponses extrêmement souples pour les vides très oblates, surtout à des triaxialités de contraintes élevées.

Ensuite, nous examinons les problèmes computationnels liés à l'implémentation numérique de modèles constitutifs indépendants du taux de déformation qui conduisent à un comportement d'adoucissement. Il est démontré analytiquement que les modèles élastoplastiques basés sur des formulations continues "locales" peuvent entraîner une perte d'ellipticité des équations aux dérivées partielles (EDP) et des solutions numériques dépendantes du maillage. Pour remédier les problèmes numériques associés, nous proposons une version implicite non locale du nouveau modèle poreux, basée sur l'introduction d'une variable de porosité non locale déterminée à partir de la solution d'une EDP supplémentaire. Nous montrons à la fois analytiquement et numériquement que la version régularisée du modèle permet de préserver les propriétés elliptiques des équations du problème, produisant des solutions convergentes indépendantes du maillage dans le régime post-bifurcation. Le point de bifurcation s'avère être fortement dépendant de la forme des micro-vides, avec des vides très plats (par exemple, un rapport d'aspect inférieur à 0,3) entraînant des déformations à la localisation plus faibles. Il est constaté que la longueur matérielle introduite par la formulation non locale a un effet minimal sur le point de bifurcation prédit, affectant uniquement le gradient post-bifurcation de la courbe contrainte-déformation macroscopique et la taille de la zone fortement déformée dans la structure.

Dans la dernière partie de cette étude, les versions locale et non locale du modèle sont efficacement implémentées dans un code commercial d'éléments finis (ABAQUS) et utilisés pour la solution numérique de problèmes de valeurs limites liés aux processus de formage et de rupture ductile. En particulier, les problèmes de test d'expansion de trou (TET) et de test d'impact Charpy (essai Charpy), le phénomène de rupture "cup-and-cone" ainsi que la rupture ductile d'un spécimen à géométrie complexe et la comparaison avec les résultats expérimentaux correspondants sont analysés en détail. Les prédictions numériques indiquent que la ductilité est une fonction croissante du paramètre de forme des vides, et les matériaux composés de vides oblates de faible rapport d'aspect présentent une initiation et une propagation macroscopiques de fissures prématurées par rapport aux matériaux avec des vides sphériques ou presque sphériques. Enfin, la capacité du modèle à reproduire les résultats expérimentaux avec une précision suffisante suggère qu'il peut être utilisé pour fournir des prédictions avec seulement un petit nombre de paramètres qui peuvent être calibrés à partir de calculs micromécaniques ou de données expérimentales.

Mots clés: Métaux poreux, Homogénéisation, Théories non-locales, Simulations de formage, Simulations de rupture ductile

CHAPTER 1

Introduction

1.1 Modeling of porous elasto-plasticity

The problem of ductile fracture of metallic materials is closely related to the distribution and evolution of voids in the underlying microstructure. The presence of these voids can be attributed either to manufacturing induced defects, interface decohesion between the matrix and dispersed secondary particles or particle breakage during deformation. The mechanisms driving the process may vary significantly depending on the loading conditions and the local stress states developed (Noell et al., 2018), however the most prominent ones involve the growth, nucleation, and coalescence of voids (Pardoen and Hutchinson, 2000; Benzerga and Leblond, 2010; Benzerga et al., 2016).

The action of the mechanism of void nucleation, growth, and coalescence during ductile fracture is rather complex taking place prior, after or simultaneously with the localization of deformation into "shear bands" (Tekoğlu et al., 2015). From a physical perspective, shear bands can emerge in clean single crystals, polycrystalline materials, non-porous materials, or porous metals due to excessive localization of deformation in narrow zones as a result of different mechanisms acting at various length scales. In porous metallic materials shear bands may appear either due to growth of voids which leads to softening of the material and localization of deformation or the emergence of shear bands and growth and coalescence of voids may happen simultaneously. One possibility is that microvoids that exist in a number of polycrystalline metals act as nucleation sites for new voids driven by the deformation of the material. This procedure gives rise to local softening due to the growth and coalescence mechanism which in turn leads to localization of deformation into shear bands that engulf the aforementioned voids. Alternatively, especially in the cases where voids exist at multiple scales in the material, microvoids nucleate, grow and coalesce usually in the ligaments between larger voids while, at the same time, this procedure also marks the initiation of localization of deformation in the ligament area.

Perhaps, the most well-known constitutive model for the description of the macroscopic behavior of porous ductile materials is that of Gurson (Gurson, 1977), which was derived using a combination of limit analysis and homogenization by considering a spherical void embedded into a rigid-plastic von Mises matrix while assuming that the void may change its size but not its shape during plastic deformation. Despite the model's inability to yield accurate predictions for shear dominated stress states due to its restrictive assumptions,

the simplicity of the model's formulation and the versatility regarding its computational implementation have made it very attractive and several extensions have been proposed over the years. Phenomenological modifications to account for void nucleation and criteria for void coalescence were proposed soon after (Chu and Needleman, 1980; Tvergaard and Needleman, 1984), while modifications to include dependence on the third invariant J_3 of the stress deviator in order to account for shear failure effects were later proposed by several authors (Nahshon and Hutchinson, 2008; Zhou et al., 2014a; Dæhli et al., 2018; He et al., 2021; Rousselier, 2022; Khan et al., 2023). Concerning the latter, such dependencies on physical grounds stem from the fact that in real materials, voids are not spherical but they may rather have irregular shapes, and this void shape effect can play a detrimental role in the predictions of ductile fracture. For example, finite element calculations conducted by Tvergaard (2009), Nielsen and Tvergaard (2011), and Nielsen et al. (2012) indicate that void shape changes or void rotations can reduce the load-carrying capacity of the material in shear-dominated loadings without increase in porosity due the interaction of flattened, crack-like neighboring voids (Anderson et al. (1990)).

In this regard, various models have been proposed in the literature that assume more general void shapes and/or void rotation. Among others, notable references are the models proposed by Leblond and co-workers (Gologanu et al., 1993, 1994, 1997) for spheroidal voids and Madou and Leblond (Madou and Leblond, 2012a,b) for general ellipsoidal voids. These models, which were also derived through a limit analysis approach on appropriately selected representative cells by using kinematically admissible velocity fields, serve as extensions to the Gurson model that incorporate void shape effects. However, even though these models take into account more general void shapes and their evolution, they do not assess void rotation in a seamless manner. Another more rigorous class of homogenization models for porous materials was proposed by Kailasam et al. (1997) and Kailasam and Ponte Castañeda (1998) in the general context of viscoplasticity. These were developed based on the variational principles initially presented in the works of Ponte Castañeda (1991) and Willis (1991) on homogenization of nonlinear composites providing an upper bound for the effective yield function of the porous material using a linear comparison composite (LCC) methodology. Even though in these models void rotation due to plastic deformation is accounted for, bounds derived with this methodology were found to be very stiff in the case of materials with an isotropic matrix and spherical voids subjected to large hydrostatic loadings (Michel and Suquet, 1992). Modifications to existing models (e.g., Danas and Aravas (2012)) and improved (but more complex) models derived using similar principles (Danas et al., 2008b; Danas and Ponte Castañeda, 2009a,b; Agoras and Ponte Castañeda, 2013) were later proposed in an effort to amend these issues. Moreover, expressions from those homogenization models were directly borrowed in the limit analysis based models mentioned previously to include void orientation changes (Madou et al., 2013; Morin et al., 2017).

The aforementioned models share some common characteristics: i) they assume a first order effect of void shape and/or void orientation evolution (put in other words: on anisotropy induced due to void shape changes) on the related mechanisms that lead to ductile fracture and ii) they consider microstructures comprising uniform or via composite sphere/ellipsoidal assemblage type distributions of ellipsoidal voids that all have the *same orientation* (unidirectional microstructures). More often than not, the initial microstructure is assumed to comprise *spherical* voids to start off with an initially isotropic response. Nevertheless, metallic materials usually contain an initial distribution of non-spherical, irregularly shaped pores (Noell et al., 2020; Wang et al., 2021; Limodin et al., 2023). In some cases pores may

have rather flat shapes that can be even considered microcracks and are randomly oriented in space (Meynard et al., 2022). Yet, the response of these materials remains fairly isotropic in the early stages of deformation implying that those shapes are distributed with a rather random orientation. Examples from microstructures of metallic materials with distributions of irregularly shaped nano- and microvoids can be seen in Fig. 1.1.

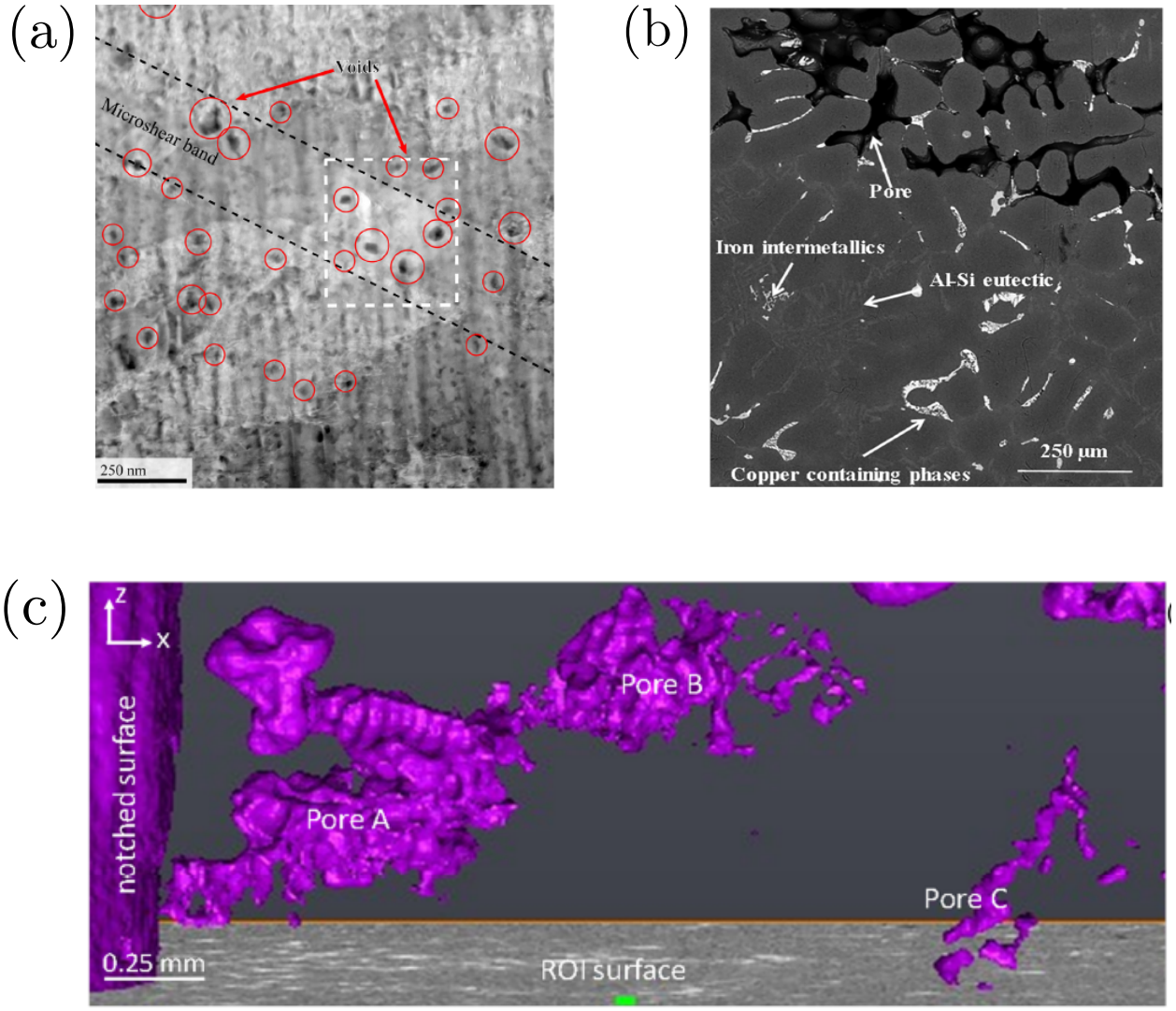

Figure 1.1 – Microstructures of metallic materials containing voids with irregular shapes: (a) High-angle annular dark-field scanning transmission electron microscopy image highlighting nanovoid distribution in Cu material (Noell et al., 2020) (b) Void distribution from two-dimensional characterization of LFC A319 Al-Si alloy (Wang et al., 2021), (c) 3D rendering of pores cluster in the LFC A319 Al-Si alloy (Wang et al., 2021).

In this view, earlier numerical and theoretical homogenization studies in elasticity (Gatt et al., 2005; Anoukou et al., 2018; Zerhouni et al., 2021) as well as limit analysis approaches for rigid-perfectly plastic materials (Vincent and Monerie, 2008; Shen et al., 2011) suggest that, the macroscopic properties of porous materials can be quite different, at the same porosity levels, for microstructures that consist of randomly orientated voids with different initial shapes. Such observations imply that initial void shape alone could potentially have important effects on the effective behavior and porosity evolution of the porous material

and consequently on its overall ductility. A more realistic modeling approach would need to consider voids which are not necessarily all aligned in the same direction but are randomly oriented in the matrix. One way to investigate this effect would be a potential extension of the model proposed in Kailasam et al. (1997), Danas and Ponte Castañeda (2009a) or Danas and Aravas (2012) for the inclusion of multiple (but finite) void families with the same shape but different orientations; in that case the general theory presented by Kailasam (Kailasam and Ponte Castañeda, 1998) in the context of nonlinear homogenization for multiple-phase composites with "particulate" microstructures could be used. Application of such an approach is computationally inefficient in practice, since it would lead to a considerable increase of the underlying microstructural variables (porosity, void shape, and orientation evolution) that would need to be kept track of. The aim of this work is to showcase a computationally feasible way of addressing such randomly oriented void distributions accepting a certain level of calibration in the final model.

1.2 Computational issues and regularization schemes

A well-known problem in the computational implementation of rate-independent plasticity models that can lead to softening material response (such as porous plasticity or continuum damage models) is that finite element (FE) solutions depend on the mesh size and thus they are unreliable. The mathematical reason for this behavior is the loss of ellipticity of the governing partial differential equations (PDEs), which allows for the development of non-smooth solutions, such as shear bands of zero thickness. Since spatially discontinuous velocity gradients can develop only across characteristic surfaces (or curves in 2D) and elliptic problems have no real characteristics, all solutions of elliptic problems are smooth functions (e.g., see Zauderer (2006), p. 135); even when non-smooth boundary conditions are used, the elliptic operators smooth out the solution in the interior of the problem domain. In *elliptic* problems, "shear bands" can still initiate at imperfections, appear as highly strained regions of *finite width* in a *smooth* solution, and can be accurately represented by finite element solutions, which converge as the mesh is refined.

When ellipticity is lost, spatially discontinuous velocity gradients (i.e., shear bands of zero thickness) may appear in the solution. In such cases, the predicted thickness of the shear band in finite element solutions reduces as the mesh is refined, but is limited by the element size; as the mesh is refined, the finite element solution does its best in trying to reduce the predicted thickness of the shear band, but it can never reproduce a discontinuous velocity gradient and capture a zero-thickness shear band, unless special elements are designed or the element boundaries are perfectly aligned with the direction of the shear band (Jirásek, 2000). As a consequence, the finite element solutions become mesh-size dependent. This difficulty of capturing non-smooth solutions is not limited to the finite element method and it would appear in any numerical method used to discretize the problem. To overcome the numerical difficulties associated with loss of ellipticity, the problem must be "regularized".

In Fluid Mechanics, regularization is often used to modify the formulation of ill-posed problems by introducing neglected physical effects like surface tension, viscosity, compressibility, strain gradients, etc., which have usually a small effect in the solution, but can become important under certain circumstances. Joseph and Saut (1990) presented several examples of ill-posed problems that are "Hadamard unstable"[1] and arise in problems involving inter-

[1] Joseph and Saut (1990) characterize a problem as "Hadamard unstable to short waves", when the growth

faces, oil recovery, granular media, and viscoelastic fluids, which are regularized in different ways.

In Solid Mechanics, several "non-local" plasticity theories either of the integral or gradient type have been introduced to regularize problems involving rate-independent softening materials (Bažant et al., 1984; Bažant and Pijaudier-Cabot, 1988; Aifantis, 1984, 1987). For instance, in the context of continnum damage mechanics, Pijaudier-Cabot and Bažant (1987) proposed to replace the local variable used to describe damage at any point in the continuum with a non-local one defined as the corresponding spatial average over a representative volume centered at the material point. In the context of porous plasticity modeling, an integral non-local version of the Gurson's model has been proposed to be used to achieve "damage delocalization" and alleviate the mesh dependence of the FE solutions (Leblond et al., 1994b; Needleman and Tvergaard, 1998; Enakoutsa et al., 2007; Enakoutsa, 2014). In this case, the authors suggest the introduction of a non-local porosity variable whose evolution is calculated directly from a convolution integral of its local counterpart with an associated weight function. However, as pointed out by several authors (Peerlings et al., 1996, 2001, 2002; Enakoutsa et al., 2007), direct use of integral non-local formulations can lead to questionable spatial interactions between material points in the vicinity highly concave geometries (such as notches or cracks).

Coleman and Hodgdon (1985) and Aifantis (1987, 1999) used a gradient version of the von Mises yield criterion in which the flow stress of the material is a function of the equivalent plastic strain $\bar{\varepsilon}^p$ and its Laplacian $\nabla^2\bar{\varepsilon}^p$. According to Aifantis (1992), the gradient terms account for underlying dislocation mechanisms at the microscale and provide a means of communication between the various scales in the macroscopic constitutive equations. These models are referred to as "explicit", since they directly modify the yield condition; the yield function becomes a *partial differential equation* (PDE) and the corresponding plastic loading/unloading criteria become more involved. Also, additional boundary conditions for $\bar{\varepsilon}^p$ are required on the boundary of the plastic zone. All these complicate the numerical implementation of such models. In finite element solutions, the yield criterion (a PDE) is enforced in a weak sense over the plastic zone and the numerical implementation of the corresponding plastic loading/unloading criteria is not straightforward (Mühlhaus and Alfantis, 1991; de Borst et al., 1995; Ramaswamy and Aravas, 1998a,b). The implications associated with the boundary conditions on the moving elastic-plastic boundary in this class of models have been discussed by Peerlings (2007). The governing equations of explicit gradient plasticity model are elliptic, unless the stresses become of the same order as the elastic modulus, which is not possible in metallic materials (Benallal and Tvergaard, 1995).

Another class of gradient plasticity models has been put forth by Peerlings et al. (1995, 1996), Geers et al. (2001), and Engelen et al. (2003), who used the von Mises yield criterion in which the flow stress depends on a non-local equivalent plastic strain e^p, which is defined in terms of the usual local equivalent plastic strain $\bar{\varepsilon}^p$ from the solution of a modified Helmholtz type PDE and appropriate boundary conditions. In this class of models, the yield function remains an *algebraic equation* and depends on both the local ($\bar{\varepsilon}^p$) and non-local (e^p) equivalent plastic strains. Such models are known as "implicit", since the algebraic yield function is enhanced by the non-local quantity e^p, which is defined implicitly in terms of $\bar{\varepsilon}^p$ from the solution of the modified Helmholtz equation. The modified Helmholtz equation is solved over *the entire domain* Ω of the problem (as opposed to the plastic zone

rate of a harmonic perturbation tends to infinity as the wavelength tends to zero (or the wavenumber tends to infinity) at any fixed time.

Ω^p only) and the required additional boundary conditions are now defined on the external boundary $\partial\Omega$ of the elastoplastic body; this avoids the aforementioned difficulties associated with the moving boundary of the plastic zone. A major advantage of the implicit non-local models is that they can be easily implemented in traditional finite element codes (such as ABAQUS) by taking advantage of the similarity between the modified Helmholtz and the heat transfer equations (Azinpour et al., 2018; Seupel et al., 2018; Papadioti et al., 2019; Aravas and Papadioti, 2021).

Non-local models based on energetic and thermodynamic considerations have also been proposed in the literature. For instance, another general class of gradient plasticity models has been also introduced by Fleck and Hutchinson (1993, 1997, 2001) and Gurtin and co-workers (Gurtin, 2003; Gurtin and Anand, 2005; Gurtin et al., 2010). These models are based on the principle of virtual power, include plastic strain gradients and higher-order stresses in the expression for the internal power, and fit within the framework laid down by Mindlin (Mindlin, 1964; Mindlin and Eshel, 1968). However, the finite element implementation of this class of models is more involved. Forest (2009) used a systematic formal procedure known as "micromorphic approach" and presented a thorough thermodynamically consistent unifying framework that covers several classes of gradient elastoviscoplasticity and damage models and is based on the introduction of additional "micromorphic" internal degrees of freedom associated with selected internal variables in the standard constitutive model. The commonly used explicit and implicit non-local plasticity and damage models can be retrieved as special cases of the micromorphic formulation. More recently, Abatour and Forest (2023) presented an interesting extension of micromorphic strain gradient plasticity models, which incorporates the effects of the gradient of *saturating* variables instead of the gradient of $\bar{\varepsilon}^p$, which is increasing monotonically during plastic flow.

In all non-local plasticity theories (integral or gradient based), dimensional consistency requires the introduction of one or more "characteristic lengths" ℓ_i. The ℓ_i's are related to the material microstructure (grain size in a polycrystal, void size or spacing in a porous medium etc.) and are small compared to the size of the problem domain. Since the ℓ_i's are small, the non-local terms have a negligible influence on solutions with moderate spatial gradients; however, the additional non-local terms can affect the solution substantially in regions of large spatial gradients, such as shear bands and strong geometrical imperfections or features (such as holes, corners, material interfaces etc.). The presence of higher-order spatial gradients in the non-local terms of the constitutive model require additional boundary conditions and always affect the mathematical character of the problem (even when they have a small influence on solutions with slow spatial variations); for example, the additional gradient terms may retain ellipticity and eliminate discontinuous solutions. The additional terms that involve the higher-order derivatives and the small ℓ_i's in the non-local models can be thought of as perturbations to the corresponding local models. Since the ℓ_i's multiply the terms with the highest spatial derivatives, the limit $\ell_i \to 0$ leads to differential equations of lower order than the original; this is commonly referred to as a singular perturbation problem and involves boundary layers, i.e., regions in which rapid changes occur in the value of a variable in the problem (e.g., see Van Dyke (1975) or Bush (1992)).

1.3 Scope of the study

The present study is concerned with the formulation and numerical application of a new fully explicit elastic-plastic model for porous materials with random microstructures. The

ultimate goal is to develop fully explicit and easy to implement models that (a) can be used both for the investigation of void shape effects on the macroscopic behavior of porous metallic materials and for the simulation of forming and ductile fracture problems in structures and (b) are free from the computational issues related to softening material behavior. The research framework adopted in the work follows a three-step approach graphically depicted in Fig. 1.2 which consists of:

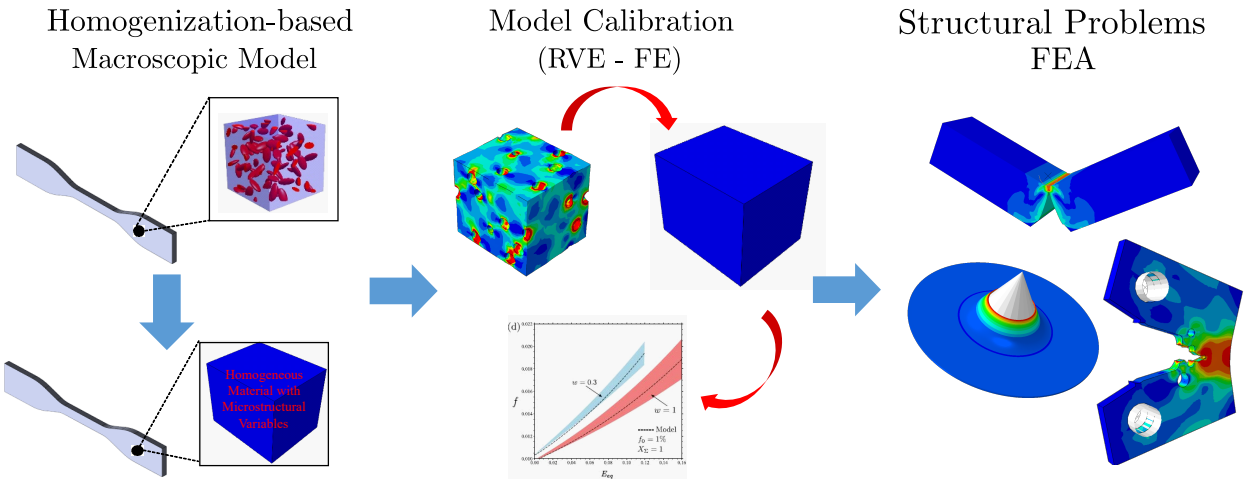

Figure 1.2 – Graphical representation summarizing the research framework of the present dissertation.

- Formulation of the constitutive equations for the analytical homogenization-based model that incorporates void shape effects in an efficient manner.
- Calibration of the analytical model through comparison with Numerical Representative Volume Element (RVE) calculations and the use of a small set of parameters.
- Numerical implementation into commercial finite-element (FE) codes, solution of industrially relevant structural problems, and comparison with available experimental results.

In this thesis, we propose a new rate-independent, elastic-plastic model for porous metals with *initially random void shape orientations* distributed randomly and isotropically in space. The model can be used to describe the effective response of metallic materials with a von Mises matrix; possible extensions to include dependence on the third invariant J_3 of the deviatoric stress can be easily incorporated in a heuristic manner for example along the lines described in Benzerga and Leblond (2010). The model takes an explicit form similar to that of Gurson, but it incorporates spheroidal voids, albeit randomly oriented, seamlessly through homogenization. This is achieved by the equivalence between projection into the space of isotropic fourth-order tensors and integral orientation averaging (Gatt et al. (2005); Moakher and Norris (2006)), leading to an overall isotropic elastic-plastic behavior. To keep the model simple with a minimum set of microstructural variables, all families of voids are assumed to have the same shape described by a single aspect ratio, which does not evolve with deformation but rather remains constant and acts as a parameter for the model. The idea for assuming a distribution of spheroids instead of general ellipsoids is twofold. Firstly, the spheroidal voids cover the interesting special case of flat random oblate voids (spheroids

with aspect ratio $w \to 0$), which in the limit of vanishing porosity correspond to random cracks (Willis, 1977; Vincent, 2006), and can have a detrimental impact on the load-carrying capacity of the material. Secondly, in the calculation of the so-called "microstructural" tensors for general ellipsoids that appear in the constitutive equations (see for example Aravas and Ponte Castañeda (2004)), elliptic integrals of the first and second kind need to be evaluated numerically, whereas, in the case of spheroidal voids, explicit analytical expressions can be obtained. This allows for a straightforward implementation of the model in finite element codes by using a methodology similar to that of the original Gurson model.

Next, we carry out detailed numerical RVE homogenization FE calculations on unit cells containing randomly oriented and distributed spheroidal voids which are used to calibrate the analytical homogenization model proposed. In order to assess the validity of the analytical model with respect to local micromechanics calculations we compare a broad range of possible microstructural configurations by considering voids of various shapes and initial volume fractions loaded under different macroscopic stress states. Based on the findings of previous studies (Cao et al., 2015; Mbiakop et al., 2015a), we propose a simple interpolation between quadratic and exponential dependence of porosity evolution on the hydrostatic stress to be used in the analytical model. This allows for very good agreement with average RVE response to be achieved using only a few parameters. Also, in order to overcome the known numerical issues related to loss of ellipticity in problems where localization is present, we propose and implement an implicit gradient version of the porous model. An implicit formulation is preferred due to the aforementioned advantages of this class of regularization models concerning their numerical implementation in existing commercial FE codes (Azinpour et al., 2018; Seupel et al., 2018; Papadioti et al., 2019; Aravas and Papadioti, 2021). We show, both analytically and numerically, that the implicit non-local porous plasticity model retains the ellipticity of the governing equations allowing for converged solutions to be possible in the post bifurcation regime, provided that a fine enough spatial discretization is used.

In the last part of this work, we use the porous models to solve boundary value (structural) problems of industrial relevance such as the Hole Expansion Test (HET), the Charpy V-notch test, cup-and-cone fracture and ductile fracture of complex specimen used in the first Sandia Fracture Challenge (SFC). The main purpose is to identify the effect of each parameter on the macroscopic response as well as to address the accuracy of the new model in predicting forming and ductile fracture processes observed experimentally. Calculations show that ductility is an increasing function of the void shape parameter w, with microstructures of flat oblate voids with low aspect ratio exhibiting early macroscopic crack initiation and loss of stress-carrying capacity. Also, good qualitative and quantitative agreement between simulations and experimental results indicates that the model can be used to make numerical predictions with reasonable computational cost and using only a few parameters that need to be calibrated.

1.4 Structure of the thesis

Following this introduction, the outline of the thesis organization is discussed next:

In Chapter 2 we present the main assumptions regarding material microstructure and the formulation of the new porous elastic-plastic model. In particular, we first review the necessary homogenization background and give explicit estimates for the linear and nonlinear behavior of two-phase porous composites with aligned microstructures. Then, we prove analytically the equivalence between integral orientation averaging and projection into the space

of isotropic fourth-order tensors and also discuss useful properties of projection tensors. This equivalence is then used to derive estimates for isotropic porous materials, with randomly oriented voids, by using the results from the homogenized response of composites comprising a single family of unidirectional voids. The elastic and plastic constitutive behaviors are treated separately and are later combined in order to yield the total elastic-plastic response. Yield surfaces as predicted by the analytical model are shown for various microstructural configurations indicating a strong dependence of plasticity on the void shape.

We present next in Chapter 3 the results of the numerical RVE homogenization framework that was used in order to assess the new analytical model. First, we discuss a general methodology for the application of periodic boundary conditions and constant macroscopic stress ratio loading for multi-axial stress states; principal loading with constant stress triaxiality and Lode angle is given as a special case. Then, we showcase the results from FE calculations regarding the average response of 3D unit cells containing randomly distributed and oriented spheroidal voids of various shapes and initial volume fractions in a von Mises matrix. These results are subsequently used to calibrate the analytical model by introducing a small number of parameters. Using the calibrated model we examine the effect of the void shape parameter on the evolution of microstructure for different average loading conditions and microstructural configurations.

In Chapter 4 we discuss in detail the computational issues related to the FE implementation of rate-independent constitutive models with softening and propose a regularized version of the model developed in Chapter 2. Specifically, we make a review of the non-local regularization methods proposed in the literature and give the general definition of non-local fields as the weighted averages of their corresponding local counterparts. We then derive the modified Helmholtz PDE that defines the non-local porosity and re-write the constitutive equations of the porous model in the context of an implicit gradient plasticity approach. We analyze in detail the mathematical character of both the local and non-local problems and show analytically that use of the non-local formulation preserves ellipticity. The analytical predictions are also verified numerically using Rice's localization analysis under plane strain conditions where we find that the use of the non-local model leads to converged solutions in the post bifurcation regime. In the context of this analysis, the effect of void aspect ratio on localization is also investigated.

Finally, in Chapter 5, we use the models developed in this work in order to numerically solve a series of BVPs under both quasi-static and dynamic conditions using the ABAQUS FE software. First, we discuss the details of the numerical implementation concerning the non-local model. We present the strong and weak forms of the implicit non-local elastic-plastic model which serve as the basis for numerical implementation using the FE method. We then introduce the necessary interpolations for the displacement and non-local porosity fields (which is now an additional degree of freedom in the model) and derive the corresponding residuals. A simple algorithm for the numerical integration of the non-local constitutive equations is proposed and an efficient implementation procedure for the non-local model using ABAQUS FE software is described. We use the local porous plasticity model to simulate the HET, which is used for steel formability characterization, especially in steel industry. Then we use the non-local model to simulate problems where strain localization conditions develop such as the cup-and-cone fracture of cylindrical specimens under tensile loading, the Charpy V-notch test and the ductile fracture of the geometrically non-conventional fracture specimen used in the first SFC.

Standard notation is used throughout. Boldface symbols denote tensors the orders of

which are indicated by the context. All tensor components are written with respect to a fixed Cartesian coordinate system with base vectors $\mathbf{e}_i$ $(i = 1, 2, 3)$, and the summation convention is used for repeated Latin indices, unless otherwise indicated. Let $\mathbf{a}$, $\mathbf{b}$ be vectors, $\mathbf{A}$, $\mathbf{B}$ second-order tensors, $\boldsymbol{\mathcal{C}}$, $\boldsymbol{\mathcal{D}}$ fourth-order tensors and $\mathbb{E}$, $\mathbb{F}$ eighth-order tensors. The following products are used in the text: $(\mathbf{a}\,\mathbf{b})_{ij} = a_i\, b_j$, $\mathbf{A} : \mathbf{B} = A_{ij}\, B_{ij}$, $(\mathbf{A}\cdot\mathbf{B})_{ij} = A_{ik}\, B_{kj}$, $(\mathbf{A}\,\mathbf{B})_{ijkl} = A_{ij}\, B_{kl}$, $(\boldsymbol{\mathcal{C}} : \mathbf{A})_{ij} = \mathcal{C}_{ijkl}\, A_{kl}$, $(\mathbf{A} : \boldsymbol{\mathcal{C}})_{ij} = A_{kl}\, \mathcal{C}_{klij}$, $(\boldsymbol{\mathcal{C}} : \boldsymbol{\mathcal{D}})_{ijkl} = \mathcal{C}_{ijpq}\, \mathcal{D}_{pqkl}$, $\boldsymbol{\mathcal{C}} :: \boldsymbol{\mathcal{D}} = \mathcal{C}_{ijkl}\, \mathcal{D}_{ijkl}$, $(\boldsymbol{\mathcal{C}}\,\boldsymbol{\mathcal{D}})_{ijklpqrs} = \mathcal{C}_{ijkl}\, \mathcal{D}_{pqrs}$ $(\mathbb{E} :: \boldsymbol{\mathcal{C}})_{ijkl} = \mathbb{E}_{ijklpqrs}\, \mathcal{C}_{pqrs}$, $(\boldsymbol{\mathcal{C}} :: \mathbb{E})_{ijkl} = \mathcal{C}_{pqrs}\, \mathbb{E}_{pqrsijkl}$, and $(\mathbb{E} :: \mathbb{F})_{ijklpqrs} = \mathbb{E}_{ijklmnyz}\, \mathbb{E}_{mnyzpqrs}$. The inverse $\boldsymbol{\mathcal{C}}^{-1}$ of a fourth-order tensor $\boldsymbol{\mathcal{C}}$ that has the "minor" symmetries $\mathcal{C}_{ijkl} = \mathcal{C}_{jikl} = \mathcal{C}_{ijlk}$ is defined so that $\boldsymbol{\mathcal{C}} : \boldsymbol{\mathcal{C}}^{-1} = \boldsymbol{\mathcal{C}}^{-1} : \boldsymbol{\mathcal{C}} = \boldsymbol{\mathcal{I}}$, where $\boldsymbol{\mathcal{I}}$ is the symmetric fourth-order identity tensor with Cartesian components $\mathcal{I}_{ijkl} = (\delta_{ik}\, \delta_{jl} + \delta_{il}\, \delta_{jk})/2$, δ_{ij} being the Kronecker delta.

List of publications resulting from this thesis

1. Aravas, N., **Xenos, S.**, 2023. "Implicit" vs "Explicit" gradient plasticity models: Do they always remove mesh dependence in softening materials? International Journal of Solids and Structures 281, 112415.
   URL: https://www.sciencedirect.com/science/article/pii/S0020768323003128,
   DOI: https://doi.org/10.1016/j.ijsolstr.2023.112415.

2. **Xenos, S.**, Aravas, N., Danas, K. 2024. A homogenization-based model of the Gurson type for porous metals comprising randomly oriented spheroidal voids. European Journal of Mechanics - A/Solids 105, 105238.
   URL:https://www.sciencedirect.com/science/article/pii/S0997753824000184,
   DOI: https://doi.org/10.1016/j.euromechsol.2024.105238.

CHAPTER 2

Description of the Homogenization-Based Model

Chapter summary: In this chapter, the constitutive formulation of the new rate-independent, isotropic elastic-plastic model for porous materials with random microstructures is described. First, a review of the homogenization estimates for linear and nonlinear porous composites with aligned microstructures which serve as a basis for the new model is presented. Then, the equivalence between orientation averaging and projection of fourth-order tensors into isotropic space is discussed in detail. Elasticity and plasticity are treated separately following a decoupled homogenization approach and are then combined in order to yield the total effective, elastic-plastic response. Instantaneous yield surfaces as predicted by the fully analytical model for various microstructures are presented and the implications of the void shape parameter on the macroscopic plastic response of the porous material are discussed.

Contents

2.1 Homgenization: General results for aligned porous microstructures

In this section we describe briefly the main features of the homogenization framework upon which the newly proposed model is based on. In particular, we give a summary of estimates for the linear-elastic and nonlinear porous materials comprising a random, with uniform probability, distribution of *aligned* voids which are all characterized by the same shape and orientation descriptors. The results given in the following are due to the energetic variational approaches proposed by several authors (e.g., Hashin and Shtrikman (1962b), Willis (1977), Ponte Castañeda (1991), Ponte Castañeda and Willis (1995)) in order to derive estimates and/or bounds for the effective behavior of multiple-phase composite materials.

2.1.1 Effective constitutive equations

Consider the general case of a representative volume element occupying volume $\mathcal{V}$ with boundary $\partial\mathcal{V}$ characterizing a two-phase composite material which comprises a matrix (phase 1) with a single family of randomly distributed inclusions (phase 2). The matrix occupies the region $\mathcal{V}^{(1)}$ while the inclusions occupy $\mathcal{V}^{(2)}$ so that $\mathcal{V} \equiv \mathcal{V}^{(1)} \cup \mathcal{V}^{(2)}$. The random microstructure is described by the binary indicator functions $\chi^{(r)}(\mathbf{x})$ $(r = 1, 2)$ which take the value 1 if $\mathbf{x} \in \mathcal{V}^{(r)}$ and 0 otherwise. For the remainder of this section, the notation $\langle\square\rangle, \langle\square\rangle^{(r)}$ is used to denote volume averages of a field over $\mathcal{V}$ and $\mathcal{V}^{(r)}$ respectively. Further assuming that the behavior of the constituents is characterized by the convex stress potentials $u^{*(r)}(\boldsymbol{\sigma}^*)$ $(r = 1, 2)$, the *local* constitutive relation (i.e., the constitutive relation at the scale of the material heterogeneities) reads

$$\mathbf{D}^* = \frac{\partial u^*}{\partial \boldsymbol{\sigma}^*}(\mathbf{x}, \boldsymbol{\sigma}^*), \qquad u^*(\mathbf{x}, \boldsymbol{\sigma}^*) = \sum_{r=0}^{2} \chi^{(r)}(\mathbf{x}) u^{*(r)}(\boldsymbol{\sigma}^*) \tag{2.1}$$

where a superscript "*" is used to refer to quantities defined at the microscale. Under the hypothesis of *seperation of length scales* and using Hill-Mandel's lemma (Hill, 1963; Mandel, 1966) the effective behavior of the composite material can be defined in a "variational setting", using the principle of minimum complementary potential energy, as:

$$\mathbf{D} = \frac{\partial u^{hom}}{\partial \boldsymbol{\sigma}}(\boldsymbol{\sigma}), \qquad u^{hom}(\boldsymbol{\sigma}) = \inf_{\boldsymbol{\sigma}^* \in \mathcal{S}(\boldsymbol{\sigma})} \langle u^*(\mathbf{x}, \boldsymbol{\sigma}^*)\rangle = \inf_{\boldsymbol{\sigma}^* \in \mathcal{S}(\boldsymbol{\sigma})} \sum_{r=0}^{2} c^{(r)} \langle u^{*(r)}(\boldsymbol{\sigma}^*)\rangle^{(r)} \tag{2.2}$$

$$\mathcal{S}(\boldsymbol{\sigma}) = \{\boldsymbol{\sigma}^* : \ \nabla \cdot \boldsymbol{\sigma}^* = \mathbf{0} \text{ in } \mathcal{V}, \ \langle \boldsymbol{\sigma}^* \rangle = \boldsymbol{\sigma}\} \tag{2.3}$$

where $u^{hom}, \mathbf{D}$, and $\boldsymbol{\sigma}$ are the *effective* stress potential, rate-of-deformation tensor and stress tensor of the composite material respectively, $\mathcal{S}(\boldsymbol{\sigma})$ is the set of statically admissible stresses that are compatible with the average stress field, and $c^{(r)} \equiv \langle \chi^{(r)}(\mathbf{x}) \rangle$ are the volume fractions of the constituents.

In the following, attention is limited to porous materials with *"ellipsoidal microstructures"* in the sense of Willis (1977). For this class of microstructures, the ellipsoidal inclusions (voids) occupy regions which are defined by all points $\mathbf{x}$ which are solution to the following quadratic equation:

$$\mathcal{V}_{\mathbf{Z}} \ : \ |\mathbf{Z}^{-T} \cdot \mathbf{x}| - 1 \leq 0, \qquad \mathbf{Z} = w_1 \mathbf{n}^{(1)}\mathbf{n}^{(1)} + w_2 \mathbf{n}^{(2)}\mathbf{n}^{(2)} + \mathbf{n}^{(3)}\mathbf{n}^{(3)} \tag{2.4}$$

where $\mathbf{Z}$ is a second-order tensor which characterizes the shape and orientation of the voids and their spatial distribution through the aspect ratios w_α ($\alpha = 1, 2$) and orientation vectors $\mathbf{n}^{(i)}$ ($i = 1, 2, 3$). Also, by assuming in this case that *statistical homogeneity*, and *no long-range order* (e.g., see Willis (1977)) hold, the two-point correlation functions of the voids' centers spatial distribution depend only on the relative distance between phases and are of the form

$$p^{(rs)}(\mathbf{x} - \mathbf{x}') = p^{(rs)}(|\mathbf{Z}^{-T} \cdot (\mathbf{x} - \mathbf{x}')|) \tag{2.5}$$

with $p^{(rs)}$ expressing the probability of finding phase r at $\mathbf{x}$ and simultaneously phase s at $\mathbf{x}'$. A generalization of this concept was later proposed by Ponte Castañeda (Ponte Castañeda and Willis, 1995) who postulated that the shape and orientation of the inclusions can be selected independently of the "shapes" and "orientations" of the spatial correlations of their centers. For porous materials, the stress potential for the vacuous phase is $u^{*(2)} = 0$ so that the variational formulation (2.2)–(2.3) reduces to:

$$\mathbf{D} = \frac{\partial u^{hom}}{\partial \boldsymbol{\sigma}}(\boldsymbol{\sigma}), \qquad u^{hom}(\boldsymbol{\sigma}) = (1 - f) \inf_{\boldsymbol{\sigma}^* \in \mathcal{S}(\boldsymbol{\sigma})} \langle u^*(\boldsymbol{\sigma}^*) \rangle^{(1)} \tag{2.6}$$

$$\mathcal{S}(\boldsymbol{\sigma}) = \{\boldsymbol{\sigma}^* : \ \nabla \cdot \boldsymbol{\sigma}^* = \mathbf{0} \text{ in } \mathcal{V}, \ \boldsymbol{\sigma}^* \cdot \mathbf{n} = \mathbf{0} \text{ on } \partial\mathcal{V}^{(2)}, \ \langle \boldsymbol{\sigma}^* \rangle = \boldsymbol{\sigma}\} \tag{2.7}$$

where $f = c^{(2)}$ and $1 - f = c^{(1)}$ are the volume fractions of the voids (porosity) and matrix material respectively while for simplicity $u^{*(1)} \equiv u^*$ denotes the stress potential of the matrix material.

It should be noted that, the problem of estimating the effective behavior of two-phase (linear or nonlinear) composites is equivalent to that of estimating the function u^{hom} given by $(2.2)_2$ (or $(2.6)_2$ for porous materials). Computation of this function exactly is not a trivial task, and would require, in general, intensive full-field numerical calculations assuming that the exact location of the phases in the RVE is known. In most of the cases however, the microstructure is not fully deterministic, and thus, the exact location of the phases in the RVE is not known. In what follows, we give a concise review of approximate results for the estimation of effective linear-elastic and nonlinear behavior of porous materials which serve as the homogenization background for the new porous elastic-plastic constitutive model developed in this work.

2.1.2 Linear-elastic estimates of the Hashin-Shtrikman type

In this subsection, we consider the special case of a porous material with an isotropic matrix which is characterized by a quadratic stress potential:

$$u^*(\boldsymbol{\sigma}^*) = \frac{1}{2}\boldsymbol{\sigma}^* : \boldsymbol{\mathcal{M}}^{\mathtt{m}} : \boldsymbol{\sigma}^*, \qquad \boldsymbol{\mathcal{M}}^{\mathtt{m}} = \frac{1}{2\,\mu_{\mathtt{m}}}\boldsymbol{\mathcal{K}} + \frac{1}{3\,\kappa_{\mathtt{m}}}\boldsymbol{\mathcal{J}}, \qquad \boldsymbol{\mathcal{J}} = \frac{1}{3}\boldsymbol{\delta}\,\boldsymbol{\delta}, \qquad \boldsymbol{\mathcal{K}} = \boldsymbol{\mathcal{I}} - \boldsymbol{\mathcal{J}} \tag{2.8}$$

where $\boldsymbol{\mathcal{M}}^{\mathtt{m}}$ is the fourth-order compliance tensor of the matrix material, $(\mu_{\mathtt{m}}, \kappa_{\mathtt{m}})$ are the corresponding shear and bulk modulus, $\boldsymbol{\mathcal{I}}$ is the symmetric fourth-order identity tensor defined in the Introduction, $(\boldsymbol{\mathcal{K}}, \boldsymbol{\mathcal{J}})$ are the deviatoric and hydrostatic fourth-order identity tensors, and $\boldsymbol{\delta}$ is the second-order identity tensor (Kronecker delta). In view of equation $(2.8)_1$, the constitutive relation $(2.1)_1$ implies that the local behavior of such material is linear. From the linearity of the problem it follows then that, the effective behavior of the porous material will also be linear so that it can be characterized from a macroscopic stress potential of the form:

$$u^{hom}(\boldsymbol{\sigma}; \mathbf{q}) = \frac{1}{2}\boldsymbol{\sigma} : \boldsymbol{\mathcal{M}}^{\mathtt{w}}(\mathbf{q}) : \boldsymbol{\sigma} \tag{2.9}$$

where $\boldsymbol{\mathcal{M}}^{\mathtt{w}}$ is the fourth-order *effective* compliance tensor of the porous material and $\mathbf{q}$ is a vector of internal variables who now incorporate microstructural information (in some average sense) in the macroscopic behavior. A *lower bound* for u^{hom} in the context of linear elasticity has been derived by Willis in Willis (1982). In that work, a generalization (see Willis (1977)) of the classical Hashin-Shtrikman variational principles (Hashin and Shtrikman (1962b)) was used to derive bounds and estimates for "particulate" composites, i.e., for composites containing N different types (families) of inclusions distributed randomly and with ellipsoidal symmetry in a well defined matrix. In the special case of a porous material, this expression simplifies to (Aravas and Ponte Castañeda, 2004; Danas, 2008)[1]:

$$\boldsymbol{\mathcal{M}}^{\mathtt{w}}(\mu_{\mathtt{m}},\kappa_{\mathtt{m}},\nu_{\mathtt{m}},f,w_{\alpha},\mathbf{n}^{(i)})=\boldsymbol{\mathcal{M}}^{\mathtt{m}}(\mu_{\mathtt{m}},\kappa_{\mathtt{m}})+\frac{f}{(1-f)\mu_{\mathtt{m}}}\boldsymbol{\mathcal{Q}}^{-1}(\nu_{\mathtt{m}},w_{a},\mathbf{n}^{(i)}), \tag{2.10}$$

with $\nu_{\mathtt{m}}=(3\,\kappa_{\mathtt{m}}-2\,\mu_{\mathtt{m}})/(6\,\kappa_{\mathtt{m}}+2\,\mu_{\mathtt{m}})$ being the matrix Poisson's ratio. In (2.10), $\boldsymbol{\mathcal{Q}}$ is a fourth-order "microstructural" tensor related directly to the well-known Eshelby–Hill tensor (Eshelby, 1957; Hill, 1963) and has both the major ($\mathcal{Q}_{ijkl}=\mathcal{Q}_{klij}$) and minor symmetries ($\mathcal{Q}_{ijkl}=\mathcal{Q}_{jikl}=\mathcal{Q}_{ijlk}=\mathcal{Q}_{jilk}$). It then follows that $\boldsymbol{\mathcal{M}}^{\mathtt{w}}$ is also symmetric, possessing both the minor and the major symmetries (i.e., $\mathcal{M}^{\mathtt{w}}_{ijkl}=\mathcal{M}^{\mathtt{w}}_{jikl}=\mathcal{M}^{\mathtt{w}}_{ijlk}$ and $\mathcal{M}^{\mathtt{w}}_{ijkl}=\mathcal{M}^{\mathtt{w}}_{klij}$ respectively). The microstructural tensor $\boldsymbol{\mathcal{Q}}$ depends both on the aspect ratios $w_{\alpha}\,(\alpha=1,2)$ and orientation vectors $\mathbf{n}^{(i)}$ $(i=1,2,3)$ of the voids and is defined as (see p. 26 in Danas (2008))

$$\boldsymbol{\mathcal{Q}}(\nu_{\mathtt{m}},w_{a},\mathbf{n}^{(i)})=\frac{1}{4\pi\det(\mathbf{Z})}\int\limits_{|\boldsymbol{\xi}|=1}\frac{\boldsymbol{\mathcal{L}}^{\mathtt{m}}-\boldsymbol{\mathcal{L}}^{\mathtt{m}}:\boldsymbol{\mathcal{H}}(\boldsymbol{\xi}):\boldsymbol{\mathcal{L}}^{\mathtt{m}}}{|\mathbf{Z}^{-1}\cdot\boldsymbol{\xi}|^{3}}d\boldsymbol{\xi},\quad \mathcal{H}_{ijkl}(\boldsymbol{\xi})=\left[\left(\mathcal{L}^{\mathtt{m}}_{ipkq}\xi_{p}\xi_{q}\right)^{-1}\xi_{j}\xi_{l}\right]_{(ij)(kl)} \tag{2.11}$$

where $\boldsymbol{\mathcal{L}}^{\mathtt{m}}=(\boldsymbol{\mathcal{M}}^{\mathtt{m}})^{-1}$ is the fourth-order elasticity tensor of the matrix material and the parentheses in $(2.11)_2$ denote the symmetric part over the appropriate indices. Notice that integration in $(2.11)_1$ is carried out on the surface of unit sphere defined by equation $\xi_1^2+\xi_2^2+\xi_3^2=1$. In the general case of ellipsoidal voids (i.e., for $w_1\neq w_2$), calculation of the components of $\boldsymbol{\mathcal{Q}}$ tensor can only be done in a semi-analytical manner since it involves the numerical evaluation of elliptic integrals of the first and second kind. In the case of *spheroidal* voids (i.e., for $w_1=w_2=w$), which is the focus of the present work, these expressions simplify considerably becoming fully analytical and explicit. Analytical expressions for the components of $\boldsymbol{\mathcal{Q}}$ tensor for both general ellipsoids and spheroidal voids are summarized for the reader's convenience in Appendix A.

2.1.3 Estimation of the effective non-linear behavior

Consider now the case of a porous material whose matrix is characterized by a *nonlinear* stress potential of the form:

$$u^{*}(\boldsymbol{\sigma}^{*})=\psi(\sigma_{e}^{*})\qquad \sigma_{e}^{*}=\sqrt{\frac{3}{2}\mathbf{s}^{*}:\mathbf{s}^{*}} \tag{2.12}$$

where σ_e^* is the equivalent von Mises stress and $\mathbf{s}^*=\boldsymbol{\sigma}^*-(\mathrm{tr}\boldsymbol{\sigma}^*/3)\boldsymbol{\delta}$ is the deviatoric stress tensor. In principle, various expressions can be selected for the explicit definition of ψ. In

[1] A general expression for the effective compliance tensor of an N-phase composite is given by Willis (see Willis (1982), p. 671).

the context of *metallic materials*, an incompressible, convex power law potential is usually employed to describe the local constitutive behavior of the matrix which, for the general case of viscoplasticity, reads:

$$\psi(\sigma_e^*) = \frac{\dot{\varepsilon}_0 \sigma_y}{N+1} \left(\frac{\sigma_e^*}{\sigma_y} \right)^{N+1} \tag{2.13}$$

where $\dot{\varepsilon}_0$, σ_y are a reference strain rate and the matrix flow stress respectively and N is the non-linearity exponent (which is the inverse of the strain-rate sensitivity parameter $M = 1/N$). Expression (2.13) describes a wide variety of behaviors with the limiting cases being linearly-viscous behavior (for $N = 1$) and rate-independent plasticity (as $N \to \infty$), which is the case in this work. In view of last equation, the stress potential characterizing the matrix behavior is a homogeneous function of degree $N+1$ in $\boldsymbol{\sigma}^*$. By making use of the latter property, it can be shown (e.g., Danas (2008)) that the homogenized stress potential characterizing the porous material will be of the form

$$u^{hom}(\boldsymbol{\sigma}; \mathbf{q}) = \frac{\dot{\varepsilon}_0 \sigma_y}{N+1} \left(\frac{\Sigma^{hom}(\boldsymbol{\sigma}; \mathbf{q})}{\sigma_y} \right)^{N+1} \tag{2.14}$$

where Σ^{hom} is an *effective* equivalent stress and $\mathbf{q}$ is a vector of internal variables who again incorporate microstructural information (in some average sense) in the macroscopic behavior. It should be noted at this point that in the original works of Ponte Castañeda (1991) and Kailasam et al. (1997) the assumption was made that in the limit of $N \to \infty$ the material behaves as perfectly plastic. In expressions (2.13) and (2.14), the initial yield stress of the matrix σ_0 is heuristically replaced with a non-constant flow stress σ_y in order to take into account possible strain hardening of the matrix material. This is done approximately here since the homogenization process was originally carried out for a matrix with no hardening. However, from a number of recent studies (e.g., see Danas and Aravas (2012), Cao et al. (2015), Papadioti et al. (2016), Cheng et al. (2017)), this approximation was shown to deliver fairly accurate results and thus is adopted in here as well.

Considering now the limiting case of rate-independent plasticity, expression (2.14) becomes:

$$u^{hom}(\boldsymbol{\sigma}; \mathbf{q}) = \begin{cases} 0, & \text{if } \Sigma^{hom} \leq \sigma_y \\ \infty & \text{otherwise} \end{cases} \tag{2.15}$$

which implies that the *effective* yield function for the porous material with the unidirectional porous microstructure is defined as:

$$\Phi^{\text{M}}(\boldsymbol{\sigma}, \mathbf{q}) = \Sigma^{hom}(\boldsymbol{\sigma}; \mathbf{q}) - \sigma_y \tag{2.16}$$

Determination of the macroscopic behavior of the porous material requires the explicit calculation of u^{hom} or in the case of rate-independent plasticity, of the effective equivalent stress Σ^{hom}. However, albeit the general form of the nonlinear stress potential is given by (2.12), determination of the precise expression requires the solution of the variational problem (2.6)-(2.7) which is very difficult to solve. This is attributed to the fact that a system of nonlinear partial differential equations with randomly oscillating coefficients would need to be solved in this case (Ponte Castañeda (2002a)).

In order to calculate approximate *bounds* or *estimates* for the nonlinear effective stress potential u^{hom}, the variational procedures proposed by Ponte Castañeda (Ponte Castañeda,

1991, 1996) can be used. These methods are based on the utilization of a "linear comparison composite" (LCC) with the same microstructure as the nonlinear composite and are in the spirit of the general "comparison medium" variational principles proposed earlier by Talbot and Willis Talbot and Willis (1985). The common goal of these methods is to replace the original optimization problem (2.6)–(2.7) with respect to the stress $\boldsymbol{\sigma}^*$ (which is rather difficult to solve) with an equivalent optimization problem for the phases of the LCC. As pointed out in Mbiakop et al. (2015b), the advantage of this procedure lies in the fact that, instead of trying to find an optimal stress field which needs to satisfy certain boundary conditions and constrains (imposed by (2.7)), one needs to solve an *unconstrained* optimization problem for the moduli of the LCC. A brief outline of the method is given in the following[2].

First notice that the nonlinear stress potential $u^*(\boldsymbol{\sigma}^*)$ for the matrix material can be re-written in terms of a *linear* stress potential u_L^* characterizing the matrix in the LCC:

$$u^*(\boldsymbol{\sigma}^*) = u_L^*(\boldsymbol{\sigma}^*, \boldsymbol{\mathcal{M}}_L) + [u^*(\boldsymbol{\sigma}^*) - u_L^*(\boldsymbol{\sigma}^*, \boldsymbol{\mathcal{M}}_L)] \tag{2.17}$$

where $\boldsymbol{\mathcal{M}}_L = \boldsymbol{\mathcal{M}}_L(\mathbf{x})$ is the fourth-order compliance tensor of the yet unspecified LCC in respect to which the optimization will take place and the subscript "L" is used to denote quantities associated with the LCC. Substitution of (2.17) into $(2.6)_2$ yields

$$\begin{aligned} u^{hom}(\boldsymbol{\sigma};\mathbf{q}) &= (1-f) \inf_{\boldsymbol{\sigma}^* \in \mathcal{S}(\boldsymbol{\sigma})} \langle u^*(\boldsymbol{\sigma}^*)\rangle^{(1)} \\ &= (1-f) \inf_{\boldsymbol{\sigma}^* \in \mathcal{S}(\boldsymbol{\sigma})} \langle u_L^*(\boldsymbol{\sigma}^*, \boldsymbol{\mathcal{M}}_L) + [u^*(\boldsymbol{\sigma}^*) - u_L^*(\boldsymbol{\sigma}^*, \boldsymbol{\mathcal{M}}_L)]\rangle^{(1)} \\ &\geq u_L^{hom}(\boldsymbol{\sigma}, \boldsymbol{\mathcal{M}}_L; \mathbf{q}) + (1-f) \inf_{\boldsymbol{\sigma}^* \in \mathcal{S}(\boldsymbol{\sigma})} \langle u^*(\boldsymbol{\sigma}^*) - u_L^*(\boldsymbol{\sigma}^*, \boldsymbol{\mathcal{M}}_L)\rangle^{(1)} \end{aligned} \tag{2.18}$$

with

$$u_L^{hom}(\boldsymbol{\sigma}, \boldsymbol{\mathcal{M}}_L; \mathbf{q}) = (1-f) \inf_{\boldsymbol{\sigma}^* \in \mathcal{S}(\boldsymbol{\sigma})} \langle u_L^*(\boldsymbol{\sigma}^*, \boldsymbol{\mathcal{M}}_L)\rangle^{(1)} \tag{2.19}$$

being the homogenized stress potential for the *porous LCC*. The variational problem (2.19) corresponds to a linear material and thus any available linear homogenization technique can be used for its evaluation. The inequality in (2.18) suggests that the expression on the right-hand side is, in general, a *lower bound* for the effective stress potential of the original nonlinear composite. However, this problem is still difficult to solve since it still requires the optimization of the nonlinear stress potential with respect to the stress field. Following Ponte Castañeda (2002a) and more recently Mbiakop et al. (2015b), by relaxing the constraint $\boldsymbol{\sigma}^* \in \mathcal{S}(\boldsymbol{\sigma})$ with the more broad one of *constant stress fields* (i.e., $\boldsymbol{\sigma}^* \in \{\boldsymbol{\sigma} : \boldsymbol{\sigma}^*(\mathbf{x}) = \hat{\boldsymbol{\sigma}} = \text{ct}\}$), the second term in (2.18) can be simplified as:

$$\begin{aligned} \inf_{\boldsymbol{\sigma}^* \in \mathcal{S}(\boldsymbol{\sigma})} \langle u^*(\boldsymbol{\sigma}^*) - u_L^*(\boldsymbol{\sigma}^*, \boldsymbol{\mathcal{M}}_L)\rangle^{(1)} &\geq \inf_{\hat{\boldsymbol{\sigma}}} [u^*(\hat{\boldsymbol{\sigma}}) - u_L^*(\hat{\boldsymbol{\sigma}}, \boldsymbol{\mathcal{M}}_L)] = \\ &= -\sup_{\hat{\boldsymbol{\sigma}}} [u_L^*(\hat{\boldsymbol{\sigma}}, \boldsymbol{\mathcal{M}}_L) - u^*(\hat{\boldsymbol{\sigma}})] \\ &\equiv -v(\boldsymbol{\mathcal{M}}_L) \end{aligned} \tag{2.20}$$

where $v(\boldsymbol{\mathcal{M}}_L)$ can be thought of as an "error function" in the sense that it serves as a measure of the nonlinearity of the real porous material. Substitution of (2.20) into (2.18) now yields:

$$u^{hom}(\boldsymbol{\sigma};\mathbf{q}) \geq u_L^{hom}(\boldsymbol{\sigma}, \boldsymbol{\mathcal{M}}_L; \mathbf{q}) - (1-f)v(\boldsymbol{\mathcal{M}}_L) \tag{2.21}$$

[2] In the derivations, use is made of the properties $\inf_{\mathbf{x}\in\mathcal{A}}[f(\mathbf{x}) + g(\mathbf{x})] \geq \inf_{\mathbf{x}\in\mathcal{A}} f(\mathbf{x}) + \inf_{\mathbf{x}\in\mathcal{A}} g(\mathbf{x})$, $\inf_{\mathbf{x}\in\mathcal{A}} f(-\mathbf{x}) = -\sup_{\mathbf{x}\in\mathcal{A}} f(\mathbf{x})$ and $\mathcal{A} \subseteq \mathcal{B} \Rightarrow \inf_{\mathbf{x}\in\mathcal{A}} f(\mathbf{x}) \geq \inf_{\mathbf{x}\in\mathcal{B}} f(\mathbf{x})$

Remark 1. As explained in Ponte Castañeda (1991), the character of the result on the right-hand side of (2.21) depends on the character of the result used for the determination of $u_L^{hom}(\boldsymbol{\sigma}, \boldsymbol{\mathcal{M}}_L; \mathbf{q})$. More specifically, if u_L^{hom} is a *bound* then the right-hand side of (2.21) will retain its bound character for the nonlinear effective stress potential. On the other hand, if an *estimate* is used for u_L^{hom}, then the right-hand side of (2.21) will serve as an estimate for the effective potential of the nonlinear material.

It should be noted that, due to the convexity of the assumed nonlinear local potential $u^*(\boldsymbol{\sigma}^*)$, the homogenized stress potential $u^{hom}(\boldsymbol{\sigma}; \mathbf{q})$ will also be convex[3]. Thus, it is desired that the right-hand side of (2.21) is also convex (Ponte Castañeda, 1991). The convexity of this expression ultimately depends on the convexity of $u_L^*(\hat{\boldsymbol{\sigma}}, \boldsymbol{\mathcal{M}}_L)$ which is associated with the selection of the linear comparison composite. As pointed out in Idiart and Ponte Castañeda (2007) the additional constraint for convexity is the *positive-definitiveness* of the fourth-order compliance tensor $\boldsymbol{\mathcal{M}}_L$. In this regard, the *most optimal lower bound* from (2.21) can be obtained by taking the supremum over all positive-definite fourth-order compliance tensors $\boldsymbol{\mathcal{M}}_L$, i.e.,

$$u^{hom}(\boldsymbol{\sigma}; \mathbf{q}) \geq u_-^{hom}(\boldsymbol{\sigma}; \mathbf{q}) \equiv \sup_{\boldsymbol{\mathcal{M}}_L(\mathbf{x})>\mathbf{0}} \{u_L^{hom}(\boldsymbol{\sigma}, \boldsymbol{\mathcal{M}}_L; \mathbf{q}) - (1-f)v(\boldsymbol{\mathcal{M}}_L)\} \tag{2.22}$$

In order to get explicit expressions for $u_-^{hom}(\boldsymbol{\sigma}; \mathbf{q})$, a specific choice has to be made for the stress potential u_L^* and the compliance tensor $\boldsymbol{\mathcal{M}}_L$ characterizing the matrix of the LCC. The "original" variatiational (VAR) method (also known as the "secant method") presented in Ponte Castañeda (1991) proposes the LCC matrix to be taken as *linear-elastic* and *isotropic* being characterized by a quadratic stress potential, i.e.,

$$u_{L,VAR}^*(\boldsymbol{\sigma}^*, \boldsymbol{\mathcal{M}}_L) = \frac{1}{2}\boldsymbol{\sigma}^* : \boldsymbol{\mathcal{M}}_L : \boldsymbol{\sigma}^*, \qquad \boldsymbol{\mathcal{M}}_L(\mathbf{x}) \equiv \boldsymbol{\mathcal{M}}_L = \frac{1}{2\mu_L}\boldsymbol{\mathcal{K}} + \frac{1}{3\kappa_L}\boldsymbol{\mathcal{J}}, \tag{2.23}$$

where μ_L, κ_L are the shear and bulk modulus of the LCC respectively. Another option would be to use a Taylor-like expansion of the stress potential of the matrix material of the nonlinear composite around a reference stress state as proposed in the so-called "second-order" (SOM) method (also known as the "tangent method") (Ponte Castañeda, 1996). The stress potential characterizing the matrix material in this case is given as

$$u_{L,SOM}^*(\boldsymbol{\sigma}^*, \check{\boldsymbol{\sigma}}^*, \boldsymbol{\mathcal{M}}_L) = u^*(\check{\boldsymbol{\sigma}}^*) + \frac{\partial u^*(\check{\boldsymbol{\sigma}}^*)}{\partial \boldsymbol{\sigma}^*} : (\boldsymbol{\sigma}^* - \check{\boldsymbol{\sigma}}^*) + \frac{1}{2}(\boldsymbol{\sigma}^* - \check{\boldsymbol{\sigma}}^*) : \boldsymbol{\mathcal{M}}_L : (\boldsymbol{\sigma}^* - \check{\boldsymbol{\sigma}}^*), \tag{2.24}$$

$$\boldsymbol{\mathcal{M}}_L(\mathbf{x}) \equiv \boldsymbol{\mathcal{M}}_L = \frac{1}{2\lambda_L}\boldsymbol{\mathcal{E}} + \frac{1}{2\mu_L}\boldsymbol{\mathcal{F}} + \frac{1}{3\kappa_L}\boldsymbol{\mathcal{J}}, \qquad \boldsymbol{\mathcal{E}} = \frac{3}{2(\check{\sigma}_{eq}^*)^2}\check{\mathbf{s}}^*\check{\mathbf{s}}^*, \qquad \boldsymbol{\mathcal{F}} = \boldsymbol{\mathcal{K}} - \boldsymbol{\mathcal{E}} \tag{2.25}$$

where $u^*(\boldsymbol{\sigma}^*)$ is the stress potential in the nonlinear matrix, $\check{\boldsymbol{\sigma}}^*$, is a reference stress tensor, λ_L is an additional modulus associated with the LCC and $(\boldsymbol{\mathcal{E}}, \boldsymbol{\mathcal{F}})$ are projection tensors. As mentioned in Ponte Castañeda (1996) (see also Danas (2008)), equations (2.24)–(2.25) can be identified with a *thermo-elastic* and *anisotropic* matrix material for the LCC. In any case, since the matrix material in the actual composite is assumed to be incompressible, the limit $\kappa_L \to \infty$ (or equivalently $\nu_{\mathtt{m},L} = 1/2$) has to be considered in either approach. By

[3]This can be readily proved by starting from the definition of a convex function and taking into account that equation $(2.6)_2$ holds (e.g., see Appendix A in Ponte Castañeda and Willis (1988)).

choosing the LCC proposed in (2.23) it follows from the results presented in Section 2.1.2 that the bound (2.10) can be used for u_L^{hom} and a fully explicit expression for the yield function of the porous material can be derived. It is worth mentioning that although use of the LCC proposed by the SOM method can generally lead to more accurate description of the effective response, the resulting formulation is more complicated; the solution of a set of nonlinear equations is required for the determination of the effective stress potential and the corresponding yield function is not explicit in this case (Danas et al., 2008a; Danas, 2008).

Finally, substituting all the involved expressions and carrying out the relevant optimizations in (2.22), one can get to the following result for the effective homogenized stress Σ_{VAR}^{hom} (Kailasam et al., 1997; Aravas and Ponte Castañeda, 2004):

$$\Sigma_{VAR}^{hom} = \sqrt{\frac{\boldsymbol{\sigma} : \mathbb{m}^{\mathtt{w}} : \boldsymbol{\sigma}}{1-f}}, \qquad \mathbb{m}^{\mathtt{w}} = \frac{3}{2}\boldsymbol{\mathcal{K}} + \frac{3f}{1-f}\boldsymbol{\mathcal{Q}}^{-1}(1/2, w_a, \mathbf{n}^{(i)}) \tag{2.26}$$

and the corresponding yield criterion can be written as

$$\frac{\boldsymbol{\sigma} : \mathbb{m}^{\mathtt{w}} : \boldsymbol{\sigma}}{1-f} - \sigma_y^2 = 0, \tag{2.27}$$

where $\mathbb{m}^{\mathtt{w}}$ is the fourth-order plastic compliance tensor for the the porous material with unidirectional microstructure. Notice that $\boldsymbol{\mathcal{Q}}$ in $(2.26)_2$ is evaluated for a Poisson's ratio $\nu_{\mathtt{m}} = 1/2$ accounting for the incompressibility of the LCC. It is important to emphasize that, the tensors $\boldsymbol{\mathcal{M}}^{\mathtt{w}}$ and $\mathbb{m}^{\mathtt{w}}$ which describe the elastic and plastic behaviors of the porous material are in general *anisotropic* except for the special case of spherical voids. This is due to the fact that, the microstructure assumed in this case comprises a random distribution of voids which are all characterized by the *same shape and orientation*.

2.2 Equivalence between orientation averaging and isotropic projection

In order to reduce the complexity of material models or to fit a given data set to the known symmetry of the material at hand, "projections" between spaces of material symmetry can be employed (Moakher and Norris, 2006). For instance, the Euclidean projection (i.e., distance based on the Euclidean norm) has been employed to reduce material symmetry in the context of elasticity (Gazis et al., 1963) or to fit rock data to particular material symmetries in the context of geomechanics (Arts et al., 2005; Helbig, 1996). On the other hand, in the context of mechanics of composites, various authors (Gatt et al., 2005; Vincent and Monerie, 2008; Shen et al., 2011) have proposed the use of orientational averaging techniques; these make use of estimates for the effective behavior of composites with lower material symmetry (e.g., orthotropic, transversely isotropic etc.) to derive estimates for isotropic composites. Such a procedure allows for the transition from a material with "aligned" constituents to a material whose constituents are distributed with random orientations. As it is proved in the following, an equivalence exists between the projection of tensors of lower symmetry into isotropic space and orientation averaging, allowing for efficient implementation of such an approach. In particular, we show that the projection operation in the isotropic space, which is used in Section 2.3, is equivalent to averaging over all possible orientations, provided the fourth-order tensor to be projected possess the minor symmetries. The proof is as follows.

Let $A'_{\kappa_1\kappa_2\cdots\kappa_n}$ be the components of a n$^{\text{th}}$-order tensor of *even* rank with respect to a local coordinate system (e.g., a system which is defined by the orientation vectors $\mathbf{n}^{(i)}$ of the principal axes of the voids) and $A_{\lambda_1\lambda_2\cdots\lambda_n}$ the components of the tensor with respect to a global (fixed) coordinate system. Then, the components with respect to the fixed system can be related to the components of the local system through the corresponding direction cosines $Q_{\kappa_i\lambda_i}$, i.e.,

$$A_{\kappa_1\kappa_2\cdots\kappa_n} = Q_{\kappa_1\lambda_1}Q_{\kappa_2\lambda_2}\cdots Q_{\kappa_n\lambda_n}A'_{\lambda_1\lambda_2\cdots\lambda_n}. \tag{2.28}$$

The direction cosines $Q_{\kappa_i\lambda_i}$ can be expressed in terms of three Euler angles (θ,ϕ,ψ), so that the orientation average of a tensor can be calculated as an average over (θ,ϕ,ψ) (e.g., Andrews (2004))[4]:

$$\langle A_{\kappa_1\kappa_2\cdots\kappa_n}\rangle = \underbrace{\frac{1}{8\,\pi^2}\int_{\psi=0}^{2\pi}\left[\int_{\phi=0}^{2\pi}\left(\int_{\theta=0}^{\pi} Q_{\kappa_1\lambda_1}Q_{\kappa_2\lambda_2}\cdots Q_{\kappa_n\lambda_n}\,\sin\theta\,d\theta\right)d\phi\right]d\psi}_{=I_{\kappa_1\kappa_2\cdots\kappa_n|\lambda_1\lambda_2\cdots\lambda_n}\equiv I^{(n)}} A'_{\lambda_1\lambda_2\cdots\lambda_n}, \tag{2.29}$$

where $I^{(n)}$ is the rotational average of the direction cosines and can be thought of as an orientation averaging operator acting on an n$^{\text{th}}$-order tensor. By making use of Weyl's theorem (Weyl, 1946), it can be shown that $I^{(n)}$ can be expressed as the sum of Q_n linearly independent isotropic tensors of order n, i.e., it will be of the form (Andrews and Thirunamachandran, 1977)

$$I^{(n)} = \underset{1\times Q_n}{\left\lfloor f^{(n)}\right\rfloor}\underset{Q_n\times Q_n}{\left[M^{(n)}\right]}\underset{Q_n\times 1}{\left\{g^{(n)}\right\}}, \qquad Q_n = \sum_{r=0}^{n/2}\frac{n!(3r-n+1)}{(n-2r)!r!(r+1)!}, \tag{2.30}$$

where $\left\{f^{(n)}\right\}$ and $\left\{g^{(n)}\right\}$ are sets containing the components of linearly independent tensors of order n with respect to the fixed and the material coordinate systems respectively and $\left[M^{(n)}\right]$ is a coefficients matrix which can be calculated as

$$\underset{Q_n\times Q_n}{\left[M^{(n)}\right]} = \underset{Q_n\times Q_n}{\left[S^{(n)}\right]^{-1}}, \qquad \underset{Q_n\times Q_n}{\left[S^{(n)}\right]} = \underset{Q_n\times 1}{\left\{f^{(n)}\right\}}\underset{1\times Q_n}{\left\lfloor f^{(n)}\right\rfloor} = \underset{Q_n\times 1}{\left\{g^{(n)}\right\}}\underset{1\times Q_n}{\left\lfloor g^{(n)}\right\rfloor}, \tag{2.31}$$

under the assumption that $\left[S^{(n)}\right]$ is invertible. For even ranked tensors, each element of the aforementioned sets is a product of Kronecker deltas comprising $n/2$ factors (i.e., they are of the form $\delta_{\kappa_1\kappa_2}\cdots\delta_{\kappa_{n-1}\kappa_n}$). In the special case of fourth-order tensors (i.e., $n=4$, $\{\kappa_1,\kappa_2,\kappa_3,\kappa_4\}\to\{i,j,k,l\}$, $\{\lambda_1,\lambda_2,\lambda_3,\lambda_4\}\to\{p,q,r,s\}$), it follows from $(2.30)_2$ that $Q_4=3$ and the expressions for the quantities $\left\{f^{(n)}\right\}$, $\left\{g^{(n)}\right\}$ and $\left[S^{(n)}\right]$ read

$$\underset{3\times 1}{\left\{f^{(4)}\right\}} = \begin{Bmatrix}\delta_{ij}\delta_{kl}\\ \delta_{ik}\delta_{jl}\\ \delta_{il}\delta_{jk}\end{Bmatrix}, \qquad \underset{3\times 1}{\left\{g^{(4)}\right\}} = \begin{Bmatrix}\delta_{pq}\delta_{rs}\\ \delta_{pr}\delta_{qs}\\ \delta_{ps}\delta_{qr}\end{Bmatrix}, \qquad \underset{3\times 3}{\left[S^{(4)}\right]} = \begin{bmatrix}9 & 3 & 3\\ 3 & 9 & 3\\ 3 & 3 & 9\end{bmatrix} \tag{2.32}$$

[4]The angles ϕ and θ define the location of one of the global axes with respect to the local system and the angle ψ defines the orientation of the other two global axes. Averaging is carried out over a unit sphere, to cover all possible (ϕ,θ) orientations, and over ψ.

From (2.30)–(2.32), after some lengthy but straightforward calculations, one ends up with the following expression

$$I^{(4)} \equiv \mathbb{I}_{ijklpqrs} = \mathbb{O}_{ijklpqrs} + \mathbb{S}^a_{ijklpqrs}, \tag{2.33}$$

$$\mathbb{O} \equiv \mathbb{P}\mathbf{roj}_{\{\mathcal{K},\mathcal{J}\}}, \qquad \mathbb{S}^a_{ijklpqrs} = \frac{1}{12}(\delta_{il}\delta_{jk} - \delta_{ik}\delta_{jl})(\delta_{ps}\delta_{qr} - \delta_{pr}\delta_{qs}), \tag{2.34}$$

where the eighth-order "isotropic projection tensor" $\mathbb{P}\mathbf{roj}_{\{\mathcal{K},\mathcal{J}\}}$ is defined as (Gatt et al., 2005)

$$\mathbb{P}\mathbf{roj}_{\{\mathcal{K},\mathcal{J}\}} \equiv \frac{1}{\mathcal{K} :: \mathcal{K}}\mathcal{K}\,\mathcal{K} + \frac{1}{\mathcal{J} :: \mathcal{J}}\mathcal{J}\,\mathcal{J} = \frac{1}{5}\mathcal{K}\,\mathcal{K} + \mathcal{J}\,\mathcal{J}, \tag{2.35}$$

Substitution of (2.33) into (2.29) yields

$$\langle \mathcal{A}_{ijkl} \rangle = \mathbb{I}_{ijklpqrs}\,\mathcal{A}'_{pqrs} = \mathbb{O}_{ijklpqrs}\,\mathcal{A}'_{pqrs} + \mathbb{S}^a_{ijklpqrs}\,\mathcal{A}'_{pqrs}. \tag{2.36}$$

If the fourth-order tensor $\boldsymbol{\mathcal{A}}$ possesses the *minor* symmetries, using $(2.34)_2$ one can show that the second term in (2.36) vanishes, so that

$$\langle \mathcal{A}_{ijkl} \rangle = \mathbb{O}_{ijklpqrs}\,\mathcal{A}'_{pqrs}, \tag{2.37}$$

i.e., orientation averaging of $\boldsymbol{\mathcal{A}}$ equals its projection on the space of fourth-order symmetric isotropic tensors.

Remark 2. It can be proved that the following identities hold between the fourth-order projection tensor $\boldsymbol{\mathcal{I}}, \boldsymbol{\mathcal{J}}$ and $\boldsymbol{\mathcal{K}}$

$$\begin{aligned} &\mathcal{K} :: \mathcal{K} = 5, \qquad \mathcal{J} :: \mathcal{J} = 1, \qquad \mathcal{K} :: \mathcal{J} = \mathcal{J} :: \mathcal{K} = 0, \\ &\mathcal{I} :: \mathcal{I} = 6, \qquad \mathcal{I} :: \mathcal{K} = \mathcal{K} :: \mathcal{I} = 5, \qquad \mathcal{I} :: \mathcal{J} = \mathcal{J} :: \mathcal{I} = 1. \end{aligned}$$

which imply also that

$$\mathbb{P}\mathbf{roj}_{\{\mathcal{K},\mathcal{J}\}} :: \mathbb{P}\mathbf{roj}_{\{\mathcal{K},\mathcal{J}\}} = \mathbb{P}\mathbf{roj}_{\{\mathcal{K},\mathcal{J}\}}, \tag{2.38}$$

$$\mathbb{P}\mathbf{roj}_{\{\mathcal{K},\mathcal{J}\}} :: \left(\mathbb{P}\mathbf{roj}_{\{\mathcal{K},\mathcal{J}\}} :: \boldsymbol{\mathcal{A}}\right) = \mathbb{P}\mathbf{roj}_{\{\mathcal{K},\mathcal{J}\}} :: \boldsymbol{\mathcal{A}}, \tag{2.39}$$

for all fourth-order tensors $\boldsymbol{\mathcal{A}}$ that possess major and minor symmetries. In addition, the last two relations are satisfied by all "projection operators" (e.g., see Meyer (2000), p. 386) and state the fact that the projection of a projection equals the original projection; all projection operators are "idempotent", i.e., they can be applied multiple times without changing the result beyond the initial application.

Remark 3. In general, given a fourth-order tensor $\boldsymbol{\mathcal{A}}$ of arbitrary material symmetry, the definition of projection consists in finding the tensor $\boldsymbol{\mathcal{A}}_{sym}$ of a particular symmetry which minimizes a distance function (norm) between $\boldsymbol{\mathcal{A}}$ and $\boldsymbol{\mathcal{A}}_{sym}$. Examples of such distance functions include the Euclidean (or Frobenius), log-Euclidean and Riemannian norms defined respectively as:

$$d_E(\boldsymbol{\mathcal{A}}_1, \boldsymbol{\mathcal{A}}_2) = ||\boldsymbol{\mathcal{A}}_1 - \boldsymbol{\mathcal{A}}_2||, \tag{2.40}$$

$$d_{LE}(\boldsymbol{\mathcal{A}}_1, \boldsymbol{\mathcal{A}}_2) = ||\log(\boldsymbol{\mathcal{A}}_1) - \log(\boldsymbol{\mathcal{A}}_2)||, \tag{2.41}$$

$$d_R(\boldsymbol{\mathcal{A}}_1, \boldsymbol{\mathcal{A}}_2) = ||\log(\boldsymbol{\mathcal{A}}_2^{-1/2} : \boldsymbol{\mathcal{A}}_2 : \boldsymbol{\mathcal{A}}_1^{-1/2})||, \tag{2.42}$$

where $\boldsymbol{\mathcal{A}}_1, \boldsymbol{\mathcal{A}}_2$ are two forth-order tensors. For the sake of simplicity, in this work we make use of the eighth-order isotropic projection tensor defined in (2.35) which is based on the minimization of the *Euclidean* norm (2.40). An alternative approach would be to use an isotropic projection tensor based on either the log-Euclidean or the Riemmanian norms given by (2.41) and (2.42) respectively, which are also known to be invariant to inversion. For instance, using the *log-Euclidean* norm, it can be shown that the corresponding projected moduli would be given as (e.g. see (Moakher and Norris, 2006), p. 29)

$$3\kappa^{LE} = \exp[\mathrm{tr}(\mathcal{J}_{ipqr}(\log \boldsymbol{\mathcal{A}})_{pqrj})], \qquad 2\mu^{LE} = \exp[\frac{1}{5}\mathrm{tr}(\mathcal{K}_{ipqr}(\log \boldsymbol{\mathcal{A}})_{pqrj})]. \tag{2.43}$$

Notice, however, that in this case the calculations could become more involved since the logarithm of a fourth-order tensor is required in the evaluation of the corresponding projected moduli in expressions (2.43).

2.3 The local "Isotropic Projection" model

In the following, we describe the main ingredients of the proposed analytical model. Since metallic materials are of interest in this work, the small elastic strain hypothesis holds and an additive decomposition of the Eulerian total rate-of-deformation tensor $\mathbf{D}$ into an elastic and a plastic part is adopted:

$$\mathbf{D} = \mathbf{D}^e + \mathbf{D}^p \tag{2.44}$$

Since only monotonic loading paths are considered in the study, the constitutive equations for the elastic and plastic behavior are treated in a decoupled manner (Aravas and Ponte Castañeda, 2004; Danas and Aravas, 2012; Cao et al., 2015; Cheng et al., 2017; Papadioti et al., 2019; Aravas and Papadioti, 2021) and are later combined in order to yield the total homogenized elastic-plastic response of the porous material.

2.3.1 Microstructure description

We consider porous metals with random microstructures that contain $N_{\mathtt{fam}}$ families of randomly distributed ellipsoidal voids of different shapes and orientations embedded in an isotropic elasto-plastic matrix (to be defined explicitly later). We follow the definitions introduced in Anoukou et al. (2018): each family contains voids with the same aspect ratios and orientation but possibly different sizes, e.g., polydisperse microstructures (Lopez-Pamies et al., 2013). The features of the vacuous phase can be described by the following set of microstructural variables (see Fig. 2.1):

- The current void volume fraction or (Eulerian) porosity $f = \mathcal{V}^v/\mathcal{V}$, where $\mathcal{V}^v$ denotes the current volume occupied by the voids and $\mathcal{V}$ the total current volume of the specimen. The volume fraction of the matrix is $1 - f$.

- Two aspect ratios that characterize the shape of the ellipsoidal voids for each void family: $w_1^{\mathtt{I}} = a_3/a_1$ and $w_2^{\mathtt{I}} = a_3/a_2$ with $\mathtt{I} = 1, \cdots, N_{\mathtt{fam}}$.

- A set of three mutually orthogonal unit vectors that define the orientation of the principal axes in the ellipsoidal voids of each void family: $\{\mathbf{n}_{\mathtt{I}}^{(1)}, \mathbf{n}_{\mathtt{I}}^{(2)}, \mathbf{n}_{\mathtt{I}}^{(3)}\}$ with $\mathtt{I} = 1, \cdots, N_{\mathtt{fam}}$.

It has been shown recently that such microstructures may be directly realized by the use of 3D-printers (Zerhouni et al., 2019; Tarantino et al., 2019; Hooshmand-Ahoor et al., 2022).

We consider the geometries described above as idealized microstructures for low-porosity metallic materials. Actual metallic materials do not have such regular quadric pore shapes (Limodin et al., 2023); nevertheless, over the last fifty years, such idealized geometries have been used extensively to adequately account for the main effects of porosity on ductile fracture (Gurson, 1977; Tvergaard and Needleman, 1984; Kailasam and Ponte Castañeda, 1998; Danas and Ponte Castañeda, 2009a; Madou and Leblond, 2012a; Danas and Aravas, 2012; Morin et al., 2016). These involve the first order porosity effect as well as the local *average* pore-induced morphological anisotropy due to random grain distributions and precipitates. An ellipsoidal void should be regarded as a locally orthotropic soft heterogeneity, which describes the average response over a neighborhood of voided regions. Any attempt to connect the actual local microstructure of a real material with such idealized void shape distributions is irrelevant. A local pore description requires a practically unattainable meshing effort and extremely heavy numerical simulations that would not even allow for large strains at the macroscopic scale. In turn, the idealized average ellipsoidal voids allow for the development of simple models that can be calibrated and used to address boundary value problems at the scale of structural components (Danas and Aravas, 2012; Morin et al., 2017).

A priori, the linear comparison composite (LCC) homogenization models proposed by Ponte Castañeda and co-workers (Ponte Castañeda, 1991, 1996, 2002a) may deal with such ideal microstructures and any number $N_{\mathtt{fam}}$ of families (see for instance Papadioti et al. (2016)), owing mainly to the corresponding linear composite estimates they depend on (Willis, 1981).

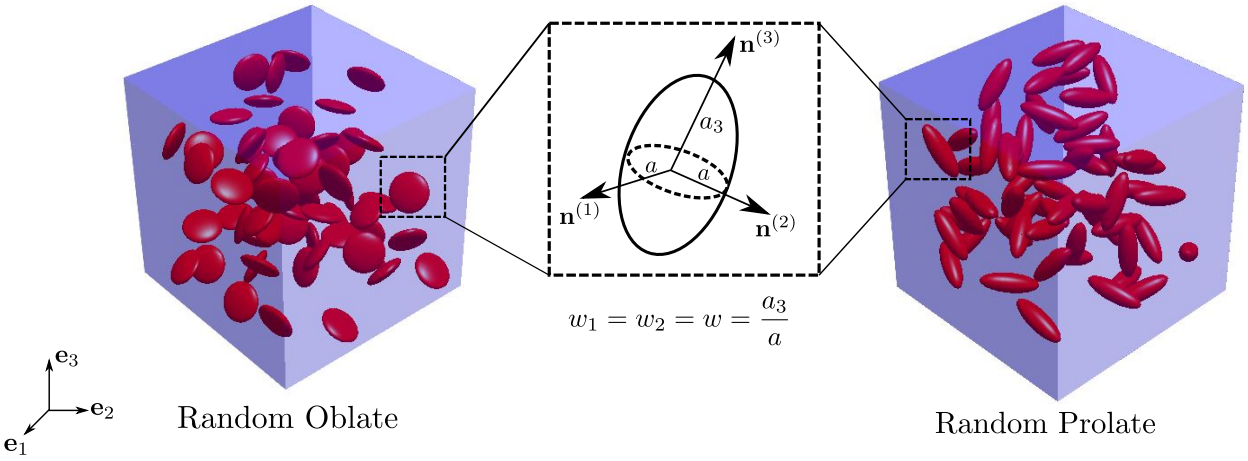

Figure 2.1 – Illustration of porous microstructures consisting of N_{fam} randomly oriented and randomly distributed spheroidal voids (shown in red). The aspect ratio is $w = 0.3$ in the oblate and $w = 5$ in the prolate voids.

Using the same viewpoint, we simplify further the microstructure descriptors in an attempt to propose a fully analytical and explicit, *isotropic* model. The simplifications introduced are as follows.

- All void families have the same shape, i.e., $w_1^{\mathtt{I}} = w_1$ and $w_2^{\mathtt{I}} = w_2$ (for all $\mathtt{I} = 1, \cdots, N_{\mathtt{fam}}$), but not the same orientation.

- All voids are assumed spheroidal, i.e., $w_1 = w_2 = w$, so that the semi-axes become $a_1 = a_2 = a$. The cases of $w = 1$, $w > 1$, and $w < 1$ correspond to spherical, prolate, and oblate spheroidal voids respectively. This additional specification allows for the development of a fully explicit model of the Gurson type, since the Eshelby–Hill tensors (Eshelby (1957); Hill (1963)) involved in the homogenization estimates can now be determined analytically as described in Appendix A. The special cases $w_1 = a_3/a_1 = 1$ and $w_2 \neq 1$ (or $w_1 \neq 1$ and $w_2 = a_3/a_2 = 1$) also correspond to spheroidal voids rotated by 90° about $\mathbf{e}_1$ (or $\mathbf{e}_2$) and are therefore included by default in the formulation. Note that the approach discussed in this work can be easily generalized to consider ellipsoidal voids (i.e., $w_1 \neq w_2$); in this case however, as discussed in Section 2.1.2, computation of the Eshelby–Hill tensors is more involved requiring the numerical evaluation of elliptic integrals.

- We consider a spatially uniform (isotropic) random distribution of orientations of the spheroidal voids leading to an overall isotropic elasto-plastic response of the porous material. In the analytical treatment of the model presented in Section 2.3, an infinite number of orientations is considered by taking advantage of the equivalence between an integral orientation average and projection into isotropic space as discussed in Section 2.2. In the numerical microstructure generation of a representative volume element, a finite number $N_{\texttt{fam}}$ of families with random orientations is used (see Anoukou et al. (2018)). The number of voids deemed sufficient for a fairly isotropic average RVE response is decided by simulating RVEs with progressively more voids until the response does not change in the three principal directions beyond a small percentage. This important point is discussed in more detail in Section 3.3.1.

A representation of such random porous (or more generally particulate) microstructures with oblate (i.e., $w = 0.3$) and prolate (i.e., $w = 5$) voids is shown in Fig. 2.1.

Remark 4. It should be noted at this point that, for the sake of deriving a fully explicit and computationally efficient analytical homogenization model, only microstructures with statistically uniform distribution of voids will be considered. Clustering effects at microstructural level, such as the ones discussed in the work of Bilger et al. (2007) and more recently Holte et al. (2023), will not be taken into account. However, the present model can account for such effects at a macroscopic level in an average sense since non-uniform initial porosity distributions can be readily implemented in codes used for structural calculations (see for instance Srivastava et al. (2014)).

2.3.2 Elasticity

The *homogenized* elastic behavior of the porous material is described by a hypoelastic constitutive equation of the form

$$\mathbf{D}^e = \boldsymbol{\mathcal{M}} : \overset{\nabla}{\boldsymbol{\sigma}}, \qquad \boldsymbol{\mathcal{M}} = \frac{1}{2\,\mu}\boldsymbol{\mathcal{K}} + \frac{1}{3\,\kappa}\boldsymbol{\mathcal{J}}, \qquad \boldsymbol{\mathcal{J}} = \frac{1}{3}\boldsymbol{\delta}\,\boldsymbol{\delta}, \qquad \boldsymbol{\mathcal{K}} = \boldsymbol{\mathcal{I}} - \boldsymbol{\mathcal{J}}, \tag{2.45}$$

where, $\overset{\nabla}{\boldsymbol{\sigma}}$ is the co-rotational Jaumann derivative of the Cauchy stress $\boldsymbol{\sigma}$. In turn, $\boldsymbol{\mathcal{M}}$ is the fourth-order *isotropic* incremental elastic compliance tensor, and (κ, μ) are the effective incremental elastic bulk and shear moduli of the porous material with an infinite number

of randomly oriented pore families ($N_{\mathtt{fam}} \to \infty$), which all have the same aspect ratio w, as discussed in the previous section.

Specifically, the incremental elastic moduli (κ, μ) (and thus $\boldsymbol{\mathcal{M}}$) are calculated using the methodology of Gatt et al. (2005) (see also Anoukou et al. (2018)), who proposed the use of an "isotropic projection" of the well-known anisotropic Hashin and Shtrikman (1963) estimates, and take the final compact and explicit form

$$\frac{1}{3\,\kappa} = \frac{1}{3}\mathcal{M}^{\mathtt{w}}_{iijj} \qquad \text{and} \qquad \frac{1}{2\,\mu} = \frac{1}{5}\left(\mathcal{M}^{\mathtt{w}}_{ijij} - \frac{1}{3\,\kappa}\right). \tag{2.46}$$

In this expression, $\boldsymbol{\mathcal{M}}^{\mathtt{w}}$ is the effective compliance tensor defined in (2.10) corresponding to a single family of unidirectional ellipsoidal voids, $(\mu_{\mathtt{m}}, \kappa_{\mathtt{m}})$ are the shear modulus and bulk modulus of the matrix, $\nu_{\mathtt{m}} = (3\,\kappa_{\mathtt{m}} - 2\,\mu_{\mathtt{m}})/(6\,\kappa_{\mathtt{m}} + 2\,\mu_{\mathtt{m}})$ is the matrix Poisson ratio, and $\boldsymbol{\mathcal{Q}}$ is the fourth-order "microstructural" tensor (generally anisotropic) defined in (2.11). In order to obtain the final expression (2.46) we identify $\boldsymbol{\mathcal{M}}$ with the isotropic projection $\mathbb{Proj}_{\{\mathcal{K},\mathcal{J}\}} :: \boldsymbol{\mathcal{M}}^{\mathtt{w}}$ of $\boldsymbol{\mathcal{M}}^{\mathtt{w}}$, i.e.,

$$\boldsymbol{\mathcal{M}} = \mathbb{Proj}_{\{\mathcal{K},\mathcal{J}\}} :: \boldsymbol{\mathcal{M}}^{\mathtt{w}} = \boldsymbol{\mathcal{M}}^{\mathtt{w}} :: \mathbb{Proj}_{\{\mathcal{K},\mathcal{J}\}} \equiv \frac{1}{2\,\mu}\boldsymbol{\mathcal{K}} + \frac{1}{3\,\kappa}\boldsymbol{\mathcal{J}}, \tag{2.47}$$

leading to (κ, μ) defined in (2.46). This final result is obtained by direct algebraic manipulations and the use of the identities between the fourth-order hydrostatic and deviatoric tensor given in Remark 2.

Based on the discussion of Section 2.2, since the effective compliance tensor $\boldsymbol{\mathcal{M}}^{\mathtt{w}}$ possesses the "minor" symmetries $\mathcal{M}^{\mathtt{w}}_{ijkl} = \mathcal{M}^{\mathtt{w}}_{jikl} = \mathcal{M}^{\mathtt{w}}_{ijlk} = \mathcal{M}^{\mathtt{w}}_{jilk}$, the isotropic projection operation is equivalent to orientational averaging over all directions of $\boldsymbol{\mathcal{M}}^{\mathtt{w}}$. Therefore, the effective elastic shear and bulk moduli (κ, μ) of the isotropic porous material resulting from the isotropic projection (2.47) of $\boldsymbol{\mathcal{M}}^{\mathtt{w}}$ are independent of the orientation vectors $\mathbf{n}^{(i)}$ and depend only on the elastic properties of the matrix ($\mu_{\mathtt{m}}$, $\kappa_{\mathtt{m}}$), on porosity f, and on the void aspect ratio w, as expected.

Figure 2.2 shows the variation of the effective elastic moduli (μ, κ), determined from (2.46), with the aspect ratio w of the spheroidal voids and the bulk modulus $\kappa_{\mathtt{m}}$ of the matrix. All moduli in Fig. 2.2 are normalized with the shear modulus $\mu_{\mathtt{m}}$ of the matrix material; the horizontal axes are in a logarithmic scale.

Figure 2.2a shows the effect of the aspect ratio w on the normalized effective shear $\mu/\mu_{\mathtt{m}}$ and bulk $\kappa/\mu_{\mathtt{m}}$ moduli of the porous material for a matrix with a ratio of bulk to shear modulus $\kappa_{\mathtt{m}}/\mu_{\mathtt{m}} = 2.17$ (corresponding to a Poisson's ratio of $\nu_{\mathtt{m}} = 0.3$). There is a significant drop in both the effective shear and bulk moduli for values of $w < 0.1$ (i.e., for penny shaped voids), whereas the stiffest response corresponds to spherical voids ($w = 1$). In the limit $w \to 0$ for fixed porosity, both the effective shear and bulk moduli (μ, κ) become asymptotically zero. This may be interpreted by observing that, in the limiting case of $w \to 0$ with finite porosity, the porous material reaches a laminated type microstructure (with random orientations) and a plane of voided material may span the entire volume leading to zero resistance to deformation. These results are in agreement with the earlier numerical and theoretical homogenization studies of Gatt et al. (2005) and Anoukou et al. (2018).

The effect of the matrix bulk modulus $\kappa_{\mathtt{m}}$ on the effective elastic properties is shown in Fig. 2.2b for three different oblate void shapes at a fixed porosity value $f = 3\%$. Both the

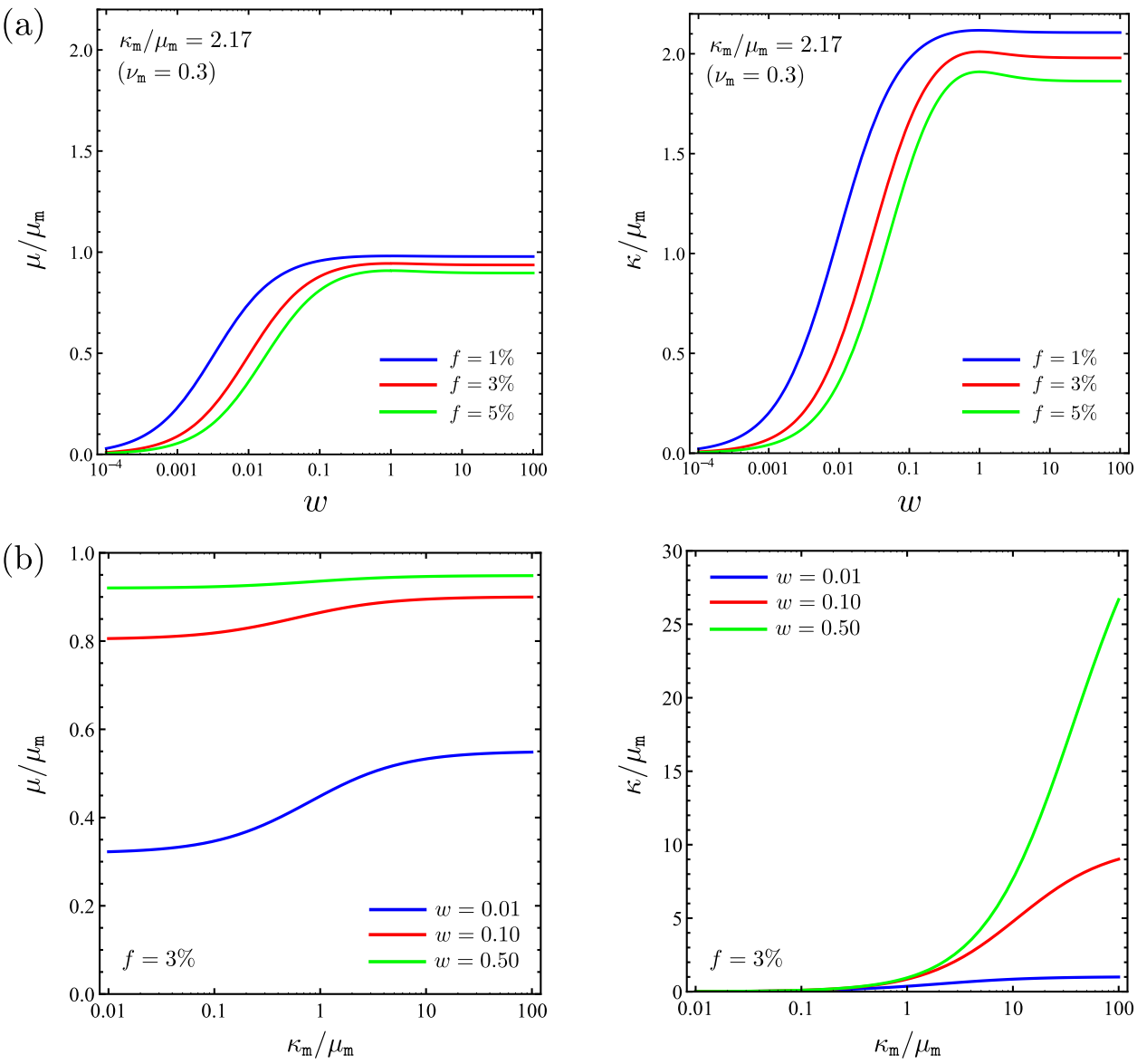

Figure 2.2 – Variation of the effective elastic shear and bulk moduli (μ, κ) with (a) the aspect ratio w of the spheroidal voids for $\nu_m = 0.3$ and for porosities 1%, 3% and 5%, and (b) the bulk modulus κ_m of the matrix material for a porosity of 3% and for aspect ratios $w = 0.01$, 0.10, and 0.50. All moduli are normalized with the shear modulus μ_m of the matrix material, and a logarithmic scale is used on the horizontal axes. Note the different scales used on the vertical axes in Fig. 2.2b.

effective shear and bulk moduli (μ, κ) increase with increasing κ_m. However, the effective bulk modulus κ is much more sensitive to κ_m compared to the effective bulk modulus μ (note the different scales used on the vertical axes in Fig. 2.2b). For a fixed value of porosity ($f = 3\%$ in Fig. 2.2b), when κ_m takes large values, i.e., as the matrix approaches the incompressible limit, the effective bulk modulus κ defined in (2.46) reaches a finite value, which is an increasing function of w. In other words, as the aspect ratio w of the voids increases, the compressibility of the composite decreases. The limiting case in which both $w \to 0$ and $f \to 0$ corresponds to a compressible cracked material and can be treated by using similar methods as the ones presented in the works of Willis (Willis, 1977, 1980c, 1981); the details of such calculation are not discussed here and are left for future work. Qualitatively similar results to those of

Fig. 2.2b were found to hold for prolate voids (i.e., for $w > 1$), the only difference being that the effects of $\kappa_{\mathtt{m}}$ on the effective elastic moduli (μ, κ) remained the same with increasing w and are not presented here for brevity.

Finally, it is noted that this work deals with monotonic loads and thus porosity evolution during elastic loads is ignored since it is negligible. Nevertheless, possible extension of this model in the case of cyclic loads requires to consider porosity evolution in the elasticity regime. This may be added in the present model in a straightforward manner following the works of Cheng et al. (2017) or more recently Remmal and Leblond (2024).

2.3.3 Plasticity and evolution of microstructure

In this section, we extend the previous ideas of void orientational averaging in the context of plasticity. In previous works, a form of orientational averaging was used by Vincent and Monerie (2008) and Shen et al. (2011) to derive the yield criterion for the case of a rigid-perfectly plastic porous material comprising randomly oriented and distributed spheroidal voids. These models are based on a limit analysis approach and were found to be fairly accurate when compared to numerical yield surface estimates, but have not been as yet used to predict porosity evolution in the material.

The present study is based on utilizing estimates for the effective response of porous materials with aligned microstructures as generated using the "secant" variational method (Ponte Castañeda, 1991) along with the isotropic projection technique in order to derive explicit estimates for the effective plastic response of an isotropic composite with the microstructure described in Section 2.3.1. Calculation of porosity evolution is then a straightforward operation.

2.3.3.1 Yield function

For the determination of the yield function, the concept of isotropic projection, which was used in the description of the elastic constitutive equations, is now employed in a similar manner by making use of the nonlinear estimate given in Section 2.1.3. More specifically, in this work, we propose a Gurson-type yield function, which however is obtained by use of the LCC homogenization method and in particular of the estimates for porous materials originally proposed in Kailasam et al. (1997). The Hashin-Shtrikman character of these estimates implies that interaction between the randomly oriented voids is accounted for in the sense of one- and two-point correlation functions. In this regard, it was shown in earlier studies that such estimates are sufficiently accurate for porosities up to $15 - 20\%$ (see for instance Lopez-Pamies et al. (2013), Papadioti et al. (2016), Anoukou et al. (2018), Luo et al. (2023)), which is more than sufficient for the purposes of the present study. The derivation of the yield criterion for the new model is described in the following.

First recall that the yield criterion for the porous material with unidirectional voids based on the "secant" variational method can be written in the explicit form (2.27), i.e.,

$$\frac{\boldsymbol{\sigma} : \mathit{m}^{\mathtt{w}} : \boldsymbol{\sigma}}{1-f} - \sigma_y^2 = 0, \tag{2.48}$$

where $\mathit{m}^{\mathtt{w}}$ is the effective microstructural fourth-order tensor (anisotropic and compressible in general) defined in (2.26) and σ_y is the yield stress of the matrix, which can in general be a function of the accumulated plastic strain $\bar{\varepsilon}^p$ of the matrix phase (i.e., $\sigma_y = \sigma_y(\bar{\varepsilon}^p)$). It is worth noting that when the matrix includes no voids (i.e., for $f = 0$), the above criterion

becomes identically that of J_2 von Mises plasticity. In the present model, the effective compliance tensor $\mathbb{m}^{\mathtt{w}}$ is proposed to be replaced by its isotropic projection $\mathbb{m}$, which reads

$$\mathbb{m} = \mathbb{Proj}_{\{\mathcal{K},\mathcal{J}\}} :: \mathbb{m}^{\mathtt{w}} = \frac{1}{2\,m_{\mathcal{K}}}\mathcal{K} + \frac{1}{3\,m_{\mathcal{J}}}\mathcal{J}. \tag{2.49}$$

By performing the algebra, in accordance to the elastic case, one obtains two homogenized coefficients $(m_{\mathcal{K}}, m_{\mathcal{J}})$ that characterize the effective plastic response of the material and are given as

$$\frac{1}{3\,m_{\mathcal{J}}(f,w)} = \frac{m^{\mathtt{w}}_{ijkl}\,\mathcal{J}_{ijkl}}{\mathcal{J}_{mnpq}\,\mathcal{J}_{mnpq}} = \frac{1}{3}m^{\mathtt{w}}_{iijj}, \tag{2.50}$$

$$\frac{1}{2\,m_{\mathcal{K}}(f,w)} = \frac{m^{\mathtt{w}}_{ijkl}\,\mathcal{K}_{ijkl}}{\mathcal{K}_{mnpq}\,\mathcal{K}_{mnpq}} = \frac{1}{5}\left(m^{\mathtt{w}}_{ijij} - \frac{1}{3m_{\mathcal{J}}}\right). \tag{2.51}$$

Using equation (2.49) for the projected effective compliance tensor, the yield criterion (2.48) may be written directly in terms of the von Mises equivalent stress and the hydrostatic stress to take the form

$$\frac{1}{1-f}\left(\frac{\sigma_e^2}{3\,m_{\mathcal{K}}} + \frac{p^2}{m_{\mathcal{J}}}\right) - \sigma_y^2 = 0. \tag{2.52}$$

Since the latter result is derived from the corresponding estimate of the "secant" variational method, the new estimate for the present isotropic projection model inherits the significantly stiff response for the nonlinear behavior in the case of isotropic matrix and hydrostatic stress states when compared to numerical calculations of representative volume elements (RVEs) (Michel and Suquet, 1992). To improve upon this behavior, following Danas and Aravas (2012) and Mbiakop et al. (2015b), we introduce the correction factor $q^2_{\mathcal{J}}$ in the second term (hydrostatic part) of (2.52) and the yield criterion takes the form

$$\frac{1}{3\,m_{\mathcal{K}}}\left(\frac{\sigma_e}{\sigma_y}\right)^2 + q^2_{\mathcal{J}}\frac{4}{9\,m_{\mathcal{J}}}\left(\frac{3\,p}{2\,\sigma_y}\right)^2 - (1-f) = 0, \qquad q_{\mathcal{J}} = \frac{1-f}{\sqrt{f}\,\ln\frac{1}{f}}. \tag{2.53}$$

The value of the correction factor $q_{\mathcal{J}}$ in $(2.53)_2$ is determined so that the exact results of the "Composite Sphere and Cylinder Assemblages" (CSA & CCA) of Hashin and of the original Gurson (Gurson, 1977) model can be recovered for the special case of spherical ($w = 1$) and cylindrical voids with circular cross-section ($w \to \infty$) respectively, when the stress state is purely hydrostatic (see Danas et al. (2008a), Danas and Aravas (2012), and Mbiakop et al. (2015a)) Specifically, in the case of spherical voids, one has (Bele et al., 2017)

$$m_{\mathcal{K}}(f) = \frac{1-f}{3+2\,f}, \qquad m_{\mathcal{J}}(f) = \frac{4(1-f)}{9\,f}. \tag{2.54}$$

and for purely hydrostatic loading (i.e., for $\sigma_e = 0$), the required hydrostatic stress for yielding is

$$\frac{|p|}{\sigma_y} = \frac{2}{3}\ln\frac{1}{f}, \tag{2.55}$$

a value consistent with the corresponding prediction of the Gurson model and the rigorous bound of Ponte Castañeda (2012). Expression (2.53) is expected to give fairly accurate results at high stress triaxialities and moderate to high porosities. At low porosities and

for spherical voids, earlier studies (Cao et al., 2015) have found that porosity f exhibits an exponential dependence on the hydrostatic stress p. To obtain such a dependence, one may consider the Taylor expansion of $\cosh x$ and ignore higher order terms, i.e.,

$$\cosh\left(\frac{3\,p}{2\,\sigma_y}\right) = 1 + \frac{1}{2}\left(\frac{3\,p}{2\,\sigma_y}\right)^2 + O\left[\left(\frac{3\,p}{2\,\sigma_y}\right)^4\right] \quad \text{or} \quad \left(\frac{3\,p}{2\,\sigma_y}\right)^2 \cong 2\left[\cosh\left(\frac{3\,p}{2\,\sigma_y}\right) - 1\right]. \tag{2.56}$$

Finally, driven by numerical results and the fact that porosity, even if it starts at low values, may eventually evolve to larger ones, we substitute the quadratic hydrostatic stress term in $(2.53)_1$ by a linear combination of $(3\,p/(2\,\sigma_y))^2$ and the right-hand-side of $(2.56)_2$ to arrive at the following final form of the yield criterion:

$$\begin{aligned}&\frac{1}{3\,m_{\mathcal{K}}(f,w)}\left(\frac{\sigma_e}{\sigma_y}\right)^2 + \\ &+ \frac{4}{9\,m_{\mathcal{J}}(f,w)}\left[(1-\alpha(f,w))\,q_{\mathcal{J}}^2(f)\left(\frac{3\,p}{2\,\sigma_y}\right)^2 + 2\,\alpha(f,w)\left(\cosh\frac{3\,p}{2\,\sigma_y} - 1\right)\right] - (1-f) = 0.\end{aligned} \tag{2.57}$$

The corresponding fully explicit isotropic yield function for the porous material then reads

$$\begin{aligned}\Phi(\sigma_e, p, \bar{\varepsilon}^p, f, w) = &\frac{1}{3\,m_{\mathcal{K}}(f,w)}\left(\frac{\sigma_e}{\sigma_y}\right)^2 + \\ &+ \frac{4}{9\,m_{\mathcal{J}}(f,w)}\left[(1-\alpha(f,w))\,q_{\mathcal{J}}^2(f)\left(\frac{3\,p}{2\,\sigma_y}\right)^2 + 2\,\alpha(f,w)\left(\cosh\frac{3\,p}{2\,\sigma_y} - 1\right)\right] - \\ &- (1-f).\end{aligned} \tag{2.58}$$

This combination of terms allows to have a fairly accurate description at small, moderate, and larger porosities, which is necessary in high stress triaxiality loads where porosity can evolve significantly during the deformation process.

In the case of spherical voids ($w = 1$), when $\alpha = 0$, the proposed yield criterion reduces to that of the MVAR (Modified VARariational) model of Danas and Aravas (2012), whereas, for $\alpha = 1$, to that of the GVAR (Gurson VARiational) model of Cao et al. (2015) (which coincides with that of the original Gurson's model (Gurson, 1977)). It should be noted that, these two models take into account the evolution of porosity as well as the evolution of the aspect ratios and the orientations of the voids. Therefore, even when they are initially isotropic, they eventually develop a deformation-induced *anisotropy*, in general. To keep the proposed new model sufficiently accurate and, at the same time, as simple a possible, we consider only the evolution of the porosity and assume that change of the void aspect ratio w has a negligible effect, so that the model is always ***isotropic***; i.e., we adopt a formulation similar to the Gurson model, which is now enriched with an additional microstructural parameter, the fixed aspect ratio w of the voids.

Finally, the interpolation function $\alpha(f,w)$ in (2.58) is introduced to allow for a better calibration of the proposed model with corresponding finite element (FE) representative volume element (RVE) simulations conducted in Section 3.2. In particular, α should be chosen so that:

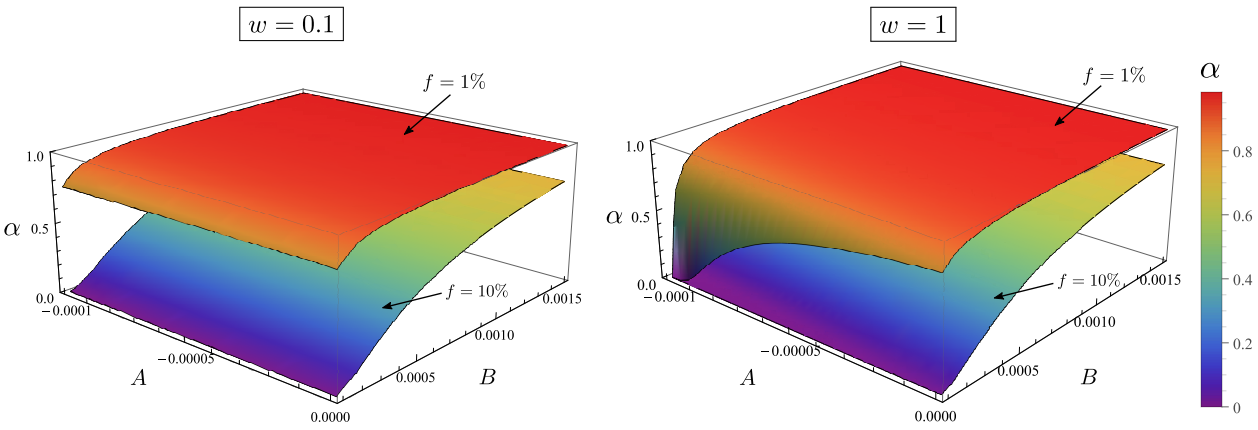

Figure 2.3 – Variation of the proposed interpolation function α with parameters A, B for a microstructure comprising flat oblate ($w = 0.1$) and spherical voids (i.e., $w = 1$) at two different porosity levels, $f = 1\%, 10\%$. In both cases the minimum porosity parameter is taken as $f_{min} = 0.5\%$.

- $\alpha = 1$ when f is lower than a prescribed minimum porosity f_{min}, thus leading to a "cosh" type response in the hydrostatic limit, similar to that of the Gurson model. Cao et al. (2015) have shown that, when the voids are initially spherical, the "cosh" functional form is more accurate for porosities less than 1%.

- $\alpha = 0$ as $f \to 1$. The rate at which α goes to zero for larger porosities depends on the aspect ratio w and in general is slower as $w \to 0$, i.e., for small values of w, the weight of the "cosh" term is larger than that of the quadratic term in (2.58).

In view of the above, we propose the following exponential expression for α, i.e.,

$$\alpha(f, w) = \begin{cases} 1, & f < f_{\min}, \\ e^{-\frac{f_{\min}}{k(w)}(f - f_{min})}, & f \geq f_{\min}, \end{cases} \qquad \text{and} \qquad k(w) = A\,w + B, \tag{2.59}$$

Parameter f_{min} defines the minimum void volume fraction above which porosity evolution is considered to exhibit a quadratic dependence on the hydrostatic stress. Parameters A and B are related to the rate of exponential decay k, i.e., the rate of transition between exponential and quadratic dependence on the hydrostatic stress. In this work, a good fit with FE calculations was found if this rate was assumed to exhibit a linear dependence on the aspect ratio w.

To better illustrate the effect of parameters A, B on the interpolation function α, contours of the latter are presented in Fig. 2.3 for both spherical (i.e., $w = 1$) and oblate voids with an aspect ratio $w = 0.1$ for a fixed value of $f_{min} = 0.5\%$. Contours of α are shown at different porosity levels to also examine the variation of α as porosity evolves. In the case of oblate voids with a low aspect ratio, it can be seen that α appears to be more sensitive to parameter B than A, especially for higher porosity values. Lower values of B lead to substantial reduction of α inducing a strongly quadratic dependence of porosity evolution on hydrostatic stress. The effect of parameter B remains essentially the same for the case of spherical voids. However, in this case there is also increased sensitivity on parameter A as well. Selection of lower negative values of A can lead to substantial reduction of α even at relatively lower porosity levels. Such qualitative analysis can serve as an indicator on the choice of these parameters.

In all subsequent calculations the values of $A = -8.6 \times 10^{-4}, B = 1.06 \times 10^{-3}$ and $f_{\min} = 0.5\%$ are used. For these values, the predictions of the proposed model are found to best fit the corresponding numerical FE calculations for the stress and porosity evolution presented in Section 3.3.2. In general, $\alpha(f, w)$ can be used as a calibration function to fit numerical or experimental data.

Remark 5. It should be pointed out that, in the case of spherical voids (i.e., for $w = 1$) and $\alpha \neq 1$, the predictions of the new isotropic projection model will generally be different than those of the corresponding *original* Gurson's model (except for purely hydrostatic stress states). This is due to the existence of the interpolation parameter α in the yield function (2.58) which in turn affects porosity evolution through the associated flow rule (see equations (2.60) and (2.63) below).

Remark 6. The yield condition (2.58) can be written alternatively in terms of an "effective stress" Σ, such that

$$\Phi(\boldsymbol{\sigma}, \bar{\varepsilon}^p, f, w) = \Sigma(\sigma_e, p, f, w) - \sigma_y(\bar{\varepsilon}^p) = 0,$$

where Σ is now defined *implicitly* from the condition

$$\frac{1}{3\,m_{\mathcal{K}}}\left(\frac{\sigma_e}{\Sigma}\right)^2 + \frac{4}{9\,m_{\mathcal{J}}}\left[(1-\alpha)\,q_{\mathcal{J}}^2\left(\frac{3\,p}{2\,\Sigma}\right)^2 + 2\,\alpha\left(\cosh\frac{3\,p}{2\,\Sigma} - 1\right)\right] - (1-f) = 0.$$

This form of the yield condition is convenient, when a viscoplastic (rate-dependent) version of the model is of interest. In such a case, the flow stress σ_y depends on both $\bar{\varepsilon}^p$ and the plastic strain-rate $\dot{\bar{\varepsilon}}^p$ and an "overstress" can be defined in terms of the effective stress Σ. An alternative and perhaps more rigorous way to include rate-dependency is the use of the corresponding viscoplastic LCC estimates (Danas, 2008; Danas et al., 2008b). This, however, is beyond the scope of the present study.

Remark 7. We remark here that an alternative realistic modeling approach would be to extend the models of Kailasam et al. (1997), Danas and Ponte Castañeda (2009a) or Danas and Aravas (2012) and consider a finite number of void families with the same shape but different orientations. In such a case, the general homogenization theory of Kailasam and Ponte Castañeda (1998) for multiple-phase composites could be used. This, however, would lead to a large number of microstructural variables, along with corresponding evolution equations, and would render the model unnecessarily complicated and difficult to implement numerically or calibrate in real-life applications. As will be discussed in Section 3.2, the proposed isotropic model, with the appropriate choice of the fitting parameters A, B, and f_{min} in the interpolation function $\alpha(f, w)$, is able to reproduce very well the results of detailed unit cell FE simulations.

Figure 2.4 shows the variation of the effective plastic coefficients $m_{\mathcal{K}}$ and $m_{\mathcal{J}}$ with the void aspect ratio w for three values of porosity ($f = 1\%, 3\%, 5\%$). Note the different scales used on the vertical axes. In Section 2.3.3.2 that follows, it is shown that the deviatoric and volumetric parts of the plastic deformation rate $\mathbf{D}^p$ are inversely proportional to $m_{\mathcal{K}}$ and $m_{\mathcal{J}}$, respectively (eqns (2.60)–(2.61) below). The results shown in Fig. 2.4 indicate that a porous material whose microstructure consists of isotropically distributed and randomly orientated oblate voids with low aspect ratios ($w \leq 0.1$) would exhibit a much *softer plastic response* compared to porous materials with spherical or prolate voids. It is also interesting to note

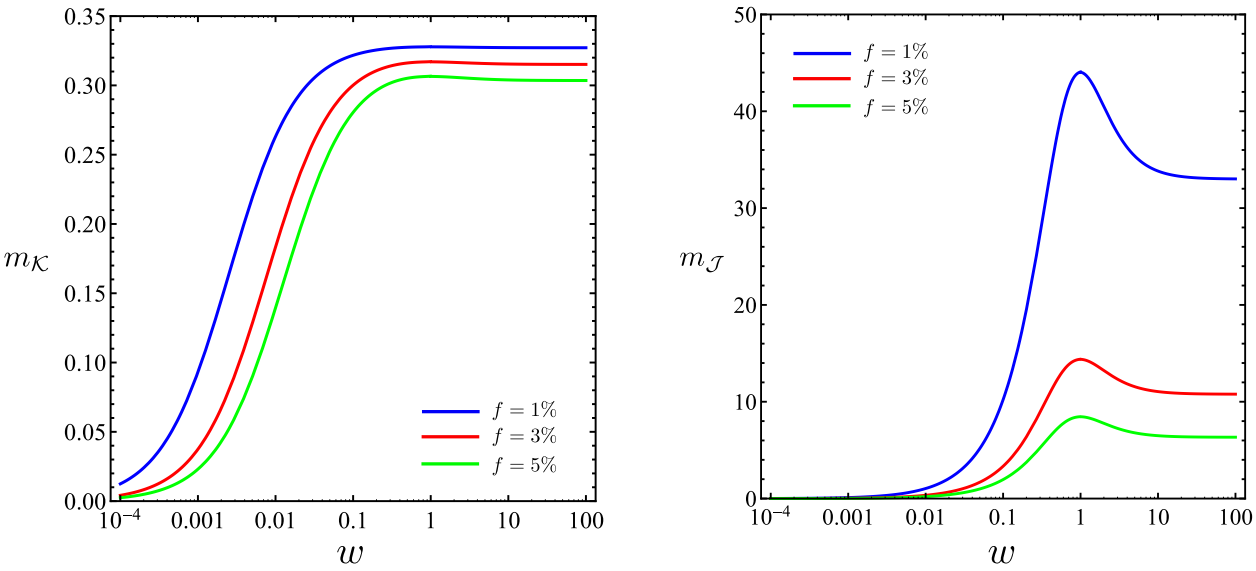

Figure 2.4 – Variation of the normalized effective plastic coefficients with void aspect ratio w (logarithmic scale) at three different porosity levels ($f = 1\%, 3\%, 5\%$). Note the different scales used on the vertical axes.

that the effective plastic coefficient $m_{\mathcal{J}}$ associated with the hydrostatic response appears to be more sensitive to the shape of the voids compared to the effective plastic shear coefficient $m_{\mathcal{K}}$, especially at lower porosity levels. This implies that, for low values of porosity, the void shape affects strongly the plastic dilatational behavior of the material and, consequently, the corresponding porosity evolution during plastic deformation.

2.3.3.2 Flow rule and evolution equations

The plastic part of the rate-of-deformation tensor is given by the *associated flow rule* ("normality"), i.e.,

$$\mathbf{D}^p = \dot{\lambda}\,\mathbf{N}, \qquad \mathbf{N} \equiv \frac{\partial \Phi}{\partial \boldsymbol{\sigma}} = \frac{3}{2\,\sigma_e}\frac{\partial \Phi}{\partial \sigma_e}\mathbf{s} + \frac{1}{3}\frac{\partial \Phi}{\partial p}\boldsymbol{\delta}, \tag{2.60}$$

where $\dot{\lambda} \geq 0$ is the "plastic multiplier", which vanishes when the response is elastic and is determined from the "consistency condition" $\dot{\Phi} = 0$ during plastic flow. The derivatives $\partial\Phi/\partial\sigma_e$ and $\partial\Phi/\partial p$ are calculated from (2.58):

$$\frac{\partial \Phi}{\partial \sigma_e} = \frac{2}{3\,m_{\mathcal{K}}}\frac{\sigma_e}{\sigma_y^2}, \qquad \frac{\partial \Phi}{\partial p} = \frac{4}{3\,m_{\mathcal{J}}}\frac{1}{\sigma_y}\left[(1-\alpha)q_{\mathcal{J}}^2\frac{3\,p}{2\,\sigma_y} + \alpha\sinh\left(\frac{3\,p}{2\,\sigma_y}\right)\right]. \tag{2.61}$$

In the present model, two variables evolve during plastic flow: i) the accumulated plastic strain $\bar{\varepsilon}^p$ upon which depends the yield stress of the matrix σ_y and ii) the porosity f. The first is an internal variable serving to characterize the plastic state in the matrix phase, and the second is a microstructural variable that characterizes the void volume fraction in the porous material.

For the evolution of $\bar{\varepsilon}^p$, we consider that the macroscopic plastic power $\boldsymbol{\sigma} : \mathbf{D}^p$ in the porous material is dissipated entirely in the plastic deformation of the matrix and equals the microscopic plastic power $(1-f)\sigma_y\,\dot{\bar{\varepsilon}}^p$, which leads to (Tvergaard and Needleman, 1984)

$$\dot{\bar{\varepsilon}}^p = \frac{\boldsymbol{\sigma} : \mathbf{D}^p}{(1-f)\sigma_y(\bar{\varepsilon}^p)} = \dot{\lambda}\frac{\boldsymbol{\sigma} : \mathbf{N}}{(1-f)\sigma_y(\bar{\varepsilon}^p)} \equiv \dot{\lambda}\,g_{\bar{\varepsilon}^p}. \tag{2.62}$$

The porosity evolution in the plastic regime is derived from mass conservation by ignoring the contribution of elasticity and taking into account the plastic incompressibility of the matrix material, such that

$$\dot{f} = (1-f)D^p_{kk} = \dot{\lambda}(1-f)N_{kk} \equiv \dot{\lambda}\, g_f. \tag{2.63}$$

2.3.4 The local elastic-plastic tangent modulus

In the present section, we determine the local elasto-plastic tangent modulus $\boldsymbol{\mathcal{L}}^{\mathrm{loc}}$, which is a fourth-order tensor that relates the Jaumann (or co-rotational) rate of the Cauchy stress $\overset{\nabla}{\boldsymbol{\sigma}}$ to the total rate-of-deformation tensor $\mathbf{D}$.

During plastic flow, $\mathbf{D}^e = \mathbf{D} - \mathbf{D}^p = \mathbf{D} - \dot{\lambda}\,\boldsymbol{\mathcal{L}} : \mathbf{N}$ and the elastic constitutive equation $(2.45)_1$ becomes

$$\overset{\nabla}{\boldsymbol{\sigma}} = \boldsymbol{\mathcal{L}} : \mathbf{D}^e = \boldsymbol{\mathcal{L}} : \mathbf{D} - \dot{\lambda}\,\boldsymbol{\mathcal{L}} : \mathbf{N}, \qquad \boldsymbol{\mathcal{L}} = \boldsymbol{\mathcal{M}}^{-1} = 2\,\mu\,\boldsymbol{\mathcal{K}} + 3\,\kappa\,\boldsymbol{\mathcal{J}} \tag{2.64}$$

where μ and κ are defined in (2.46). The consistency condition $\dot{\Phi} = 0$ is written as

$$\dot{\Phi} = \frac{\partial \Phi}{\partial \boldsymbol{\sigma}} : \overset{\nabla}{\boldsymbol{\sigma}} + \frac{\partial \Phi}{\partial \bar{\varepsilon}^p}\dot{\bar{\varepsilon}}^p + \frac{\partial \Phi}{\partial f}\dot{f} = \mathbf{N} : (\boldsymbol{\mathcal{L}} : \mathbf{D} - \dot{\lambda}\,\boldsymbol{\mathcal{L}} : \mathbf{N}) + \dot{\lambda}\,\frac{\partial \Phi}{\partial \bar{\varepsilon}^p} g_{\bar{\varepsilon}^p} + \dot{\lambda}\,\frac{\partial \Phi}{\partial f} g_f = 0$$

where $(2.64)_1$, (2.62), and (2.63) have been taken into account and the derivatives $\partial\Phi/\partial\bar{\varepsilon}^p$ and $\partial\Phi/\partial f$ can be calculated from (2.58). The last equation yields

$$\dot{\lambda} = \frac{1}{L^{\mathrm{loc}}}\mathbf{N} : \boldsymbol{\mathcal{L}} : \mathbf{D}, \qquad \text{where} \quad L^{\mathrm{loc}} = \mathbf{N} : \boldsymbol{\mathcal{L}} : \mathbf{N} + H^{\mathrm{loc}} \quad \text{with} \quad H^{\mathrm{loc}} = -\left(\frac{\partial \Phi}{\partial \bar{\varepsilon}^p} g_{\bar{\varepsilon}^p} + \frac{\partial \Phi}{\partial f} g_f\right). \tag{2.65}$$

The sign of the effective "hardening modulus" H^{loc} of the local model determines whether the porous material is hardening ($H^{\mathrm{loc}} > 0$) or softening ($H^{\mathrm{loc}} < 0$) at the given stress state and internal and microstructural variables. Substitution of (2.65) in $(2.64)_1$ yields the local elasto-plastic tangent modulus $\boldsymbol{\mathcal{L}}^{\mathrm{loc}}$, which reads

$$\overset{\nabla}{\boldsymbol{\sigma}} = \boldsymbol{\mathcal{L}}^{\mathrm{loc}} : \mathbf{D}, \qquad \boldsymbol{\mathcal{L}}^{\mathrm{loc}} = \boldsymbol{\mathcal{L}} - \frac{1}{L^{\mathrm{loc}}}(\boldsymbol{\mathcal{L}} : \mathbf{N})(\boldsymbol{\mathcal{L}} : \mathbf{N}). \tag{2.66}$$

Note that $\boldsymbol{\mathcal{L}}^{\mathrm{loc}}$ has both the minor ($\mathcal{L}^{\mathrm{loc}}_{ijkl} = \mathcal{L}^{\mathrm{loc}}_{jikl} = \mathcal{L}^{\mathrm{loc}}_{ijlk}$) and major ($\mathcal{L}^{\mathrm{loc}}_{ijkl} = \mathcal{L}^{\mathrm{loc}}_{klij}$) symmetries.

At this point, it useful to make a comment regarding the qualitative behavior of the hardening modulus H^{loc}. For a hardening matrix material and during plastic flow the yield surface increases in size with increasing equivalent plastic strain (i.e., $\partial\Phi/\partial\bar{\varepsilon}^p < 0$) and $g_{\bar{\varepsilon}^p} > 0$ holds. Also, in porous metals, for loadings where the hydrostatic component of the stress is positive, porosity increases (i.e., $g_f > 0$); the yield surface shrinks with increasing porosity implying that $\partial\Phi/\partial f > 0$ (see p. 6 in Aravas and Papadioti (2021)). Based on these observations, equation $(2.65)_3$ implies that in the case of the local model, the hardening modulus H^{loc} is in general a decreasing function of porosity and *may become negative* during loading. This result is important in the discussion of the mathematical character of the governing equations which is presented in Section 4.3.

2.4 Analytical yield surfaces

To illustrate the effect of the void shape on the plastic behavior of the porous material, instantaneous yield curves on the normalized "meridonial" $p-\sigma_e$ plane are shown in Figs 2.5–2.8. Since the isotropic yield function is independent of the Lode parameter (Danas et al., 2008b), only the results for the first quadrant are presented on the $p-\sigma_e$ plane.

For later reference, we define the stress triaxiality and Lode angle[5] as

$$X_\Sigma = \frac{p}{\sigma_e}, \qquad \theta = \frac{1}{3}\arcsin\left(-\frac{27}{2}\frac{\det \mathbf{s}}{\sigma_e^3}\right), \qquad \mathbf{s} = \boldsymbol{\sigma} - p\boldsymbol{\delta} \tag{2.67}$$

and the strain triaxiality as

$$X_E = \frac{E_m}{E_{eq}}, \qquad E_m = \frac{E_{kk}}{3}, \qquad E_{eq} = \sqrt{\frac{2}{3}\,\mathbf{E}^d : \mathbf{E}^d} \tag{2.68}$$

where E_m, E_{eq} are norms associated with the hydrostatic and deviatoric ($\mathbf{E}^d$) parts of the logarithmic strain tensor $\mathbf{E}$.

Figure 2.5a shows the effect of the void shape on the effective yield curves for two different porosity values, $f = 1\%$ and 5%, and three different aspect ratios, $w = 0.01$, 0.10, and 1. Therein, we observe that as the aspect ratio w decreases from 1 to 0.01 (i.e., as voids change from spherical to flat penny shaped ones), the yield surfaces shrink significantly, especially at stress states near the "hydrostatic" point (the point on the curve corresponding to $\sigma_e = 0$ on the hydrostatic stress axis). It should be also noted that, as the aspect ratio w decreases from 1 to 0.01, the hydrostatic point decreases faster than the corresponding "shear" point (the point on the curve corresponding to $p = 0$ on the σ_e-axis). Also, for a fixed value of the aspect ratio w, the yield surface shrinks with increasing porosity, as expected.

Figure 2.5b shows the effects of stress triaxiality on the normalized volumetric plastic strain-rate $N_{kk} = D^p_{kk}/\dot{\lambda} = \partial\Phi/\partial p$, which is proportional to $\dot{f}$ and controls the evolution of porosity during plastic flow (see (2.60) and (2.63)). As the aspect ratio w decreases, the corresponding value for N_{kk} increases significantly for higher stress triaxialities, with the effect being more pronounced at higher porosities. This implies that, during plastic deformation and especially at high stress triaxiality conditions, porosity is expected to increase rapidly for microstructures consisting of flat oblate voids. Such effects are less important for prolate voids ($w > 1$) and are not shown here for brevity.

Figure 2.6 shows the normalized hydrostatic p/σ_y and shear σ_e/σ_y points, respectively, as a function of the void aspect ratio w at three different porosity values $f = 1\%$, 3%, and 5%. As w decreases, both the hydrostatic and shear points decrease rapidly, with the former being more sensitive to the void shape changes. Once again, this behavior confirms the non-trivial dependence of the plastic response on the void shape parameter.

Figure 2.7 showcases the paramount differences between microstructures with spherical and oblate voids. More specifically, we show the yield curves for a random distribution of (a) oblate voids ($w = 0.05$) with $f = 1\%$, (b) spherical voids at a low porosity of $f = 2.6\%$, and (c) spherical voids at a high porosity of $f = 7.7\%$. In cases (b) and (c) with spherical voids, the values of porosity were chosen so that the corresponding yield surfaces have the same

[5] It should be noted here that alternative definitions for θ can be found in the literature (see for instance Danas et al. (2008b) and Danas and Ponte Castañeda (2009a)) and any of them can be adopted, as long as consistency is kept in subsequent calculations.

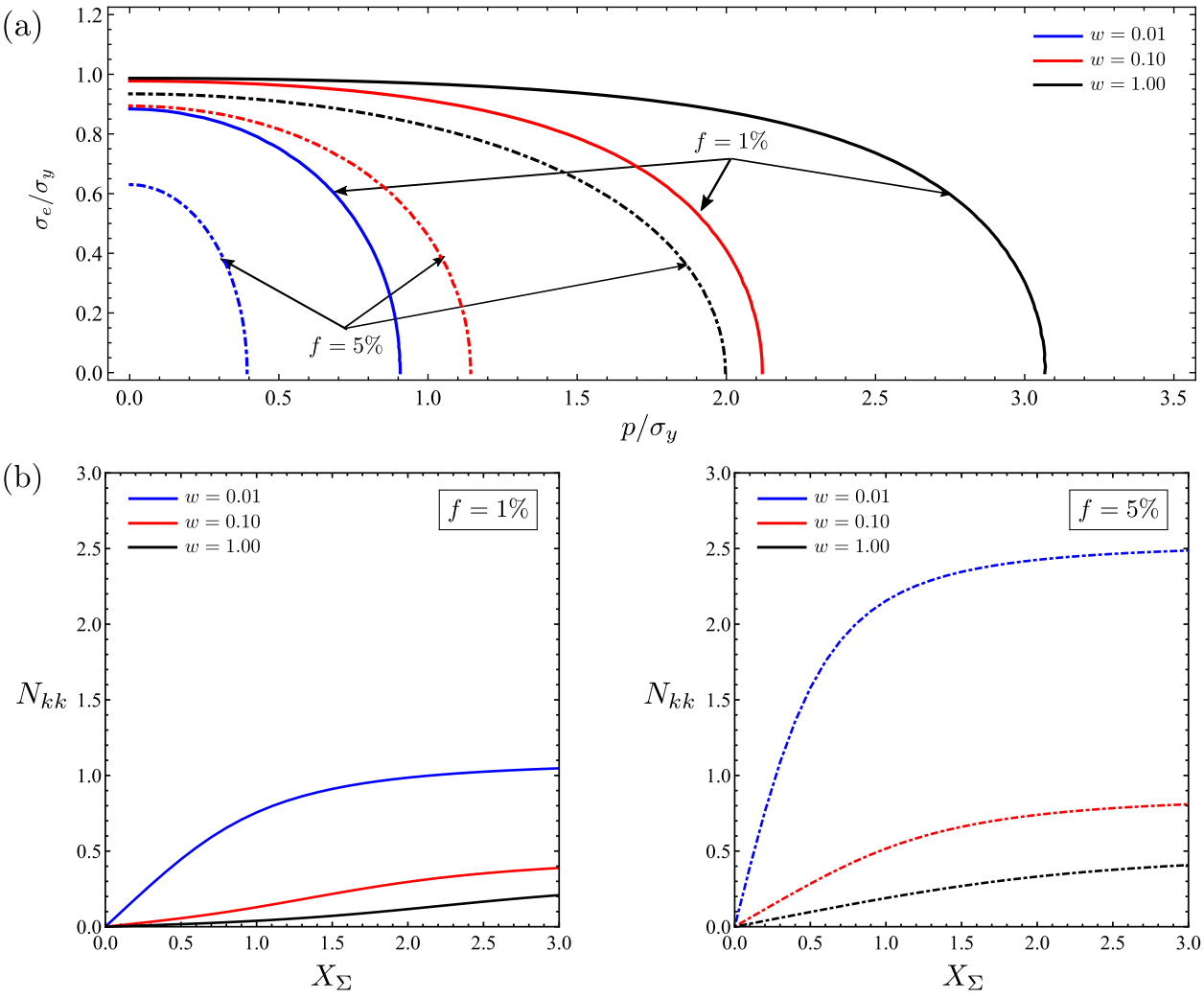

Figure 2.5 – (a) Yield curves on the normalized $p - \sigma_e$ plane. (b) Influence of void aspect ratio w on the variation of normalized volumetric plastic strain-rate N_{kk}; results are shown for porosities $f = 1\%$ (solid lines) and $f = 5\%$ (dashed lines).

hydrostatic ($f = 7.7\%$) and shear points ($f = 2.6\%$) as the yield surface of the microstructure comprising oblate voids with $f = 1\%$. Comparison of the results for microstructures (a) and (b) shows that the response of a material whose microstructure consists of oblate voids is much more compliant than that with spherical voids, especially for stress states in which the hydrostatic component dominates ($p \gg \sigma_e$). On the other hand, comparison of the results for microstructures (a) and (c) shows that a material comprising a random distribution of oblate voids with $f = 1\%$ and $w = 0.05$ exhibits fairly similar behavior with a material consisting of spherical voids with approximately eight times higher porosity, i.e., $f = 7.7\%$ and $w = 1$. Such results are indicative of the fact that, even at low porosities, the existence of flat voids (the shape of which deviates considerably from spherical) can have a detrimental effect on the effective plastic response of the porous material.

We conclude this section with a parametric analysis of the effects of function $k(w)$, used in (2.59) to define the interpolation parameter $\alpha(f, w)$, on the predictions of the model. Figure 2.8 shows the influence of k on the shape and size of the yield surface and on the volumetric plastic strain-rate N_{kk}. For demonstration purposes, fixed values for the void

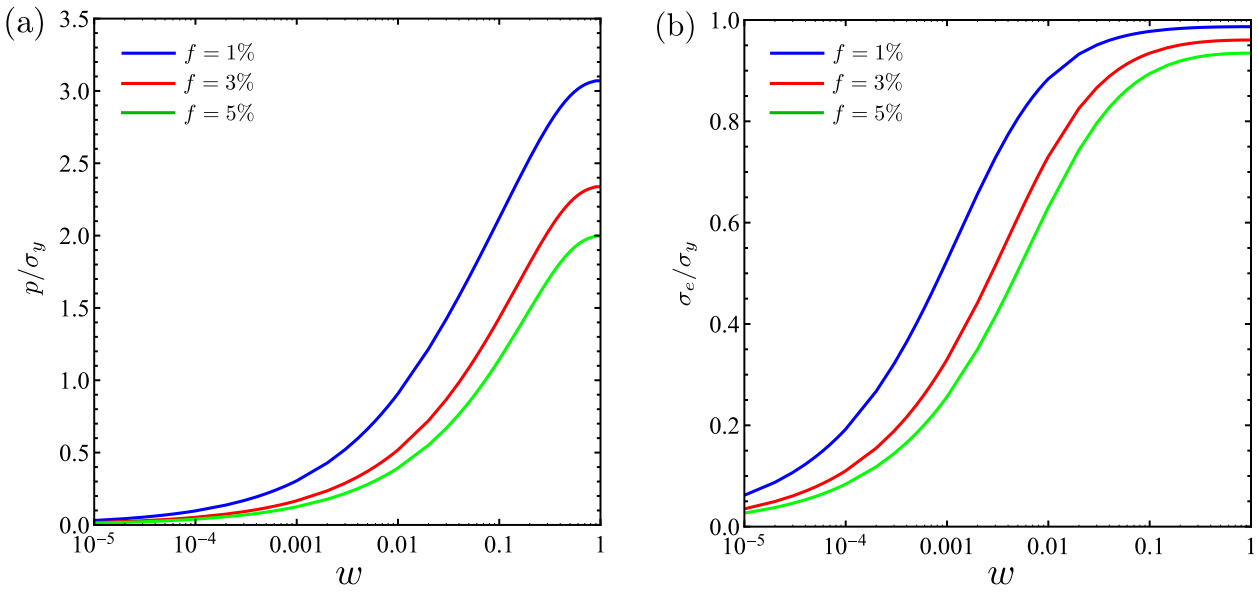

Figure 2.6 – Normalized (a) "hydrostatic" and (b) "shear" points as functions of the aspect ratio w (logarithmic scale) at three different porosity levels ($f = 1\%$, 3%, and 5%).

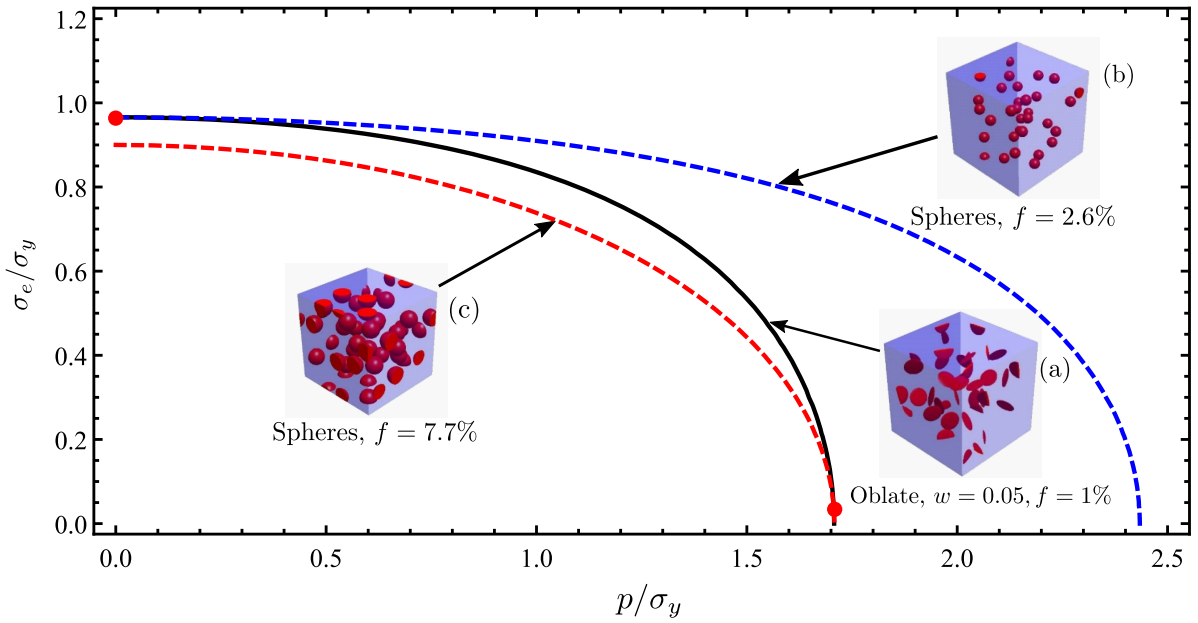

Figure 2.7 – Yield curves on the normalized $p - \sigma_e$ plane for a random distribution of oblate voids ($w = 0.05$) with $f = 1\%$, spherical voids at a low porosity of $f = 2.6\%$ and spherical voids at a high porosity of $f = 7.7\%$.

aspect ratio ($w = 0.10$) and porosity ($f = 5\%$) are used. As the value of k increases, the hydrostatic point moves "outwards", thus making the response stiffer for stress states with $p \gg \sigma_e$, whereas the material response in shear is marginally affected (Fig. 2.8a). Accordingly, the corresponding values of N_{kk} decrease as k increases, and this leads to reduced porosity growth, especially at higher stress triaxialities. We also note that the parameter $k(w)$ does not affect the hydrostatic point when $w = 1$ (spherical voids). Also, in this special case of spherical voids ($w = 1$) and purely hydrostatic stress states (i.e., for $\sigma_e = 0$), the model recovers the Gurson hydrostatic point irrespective of the value of

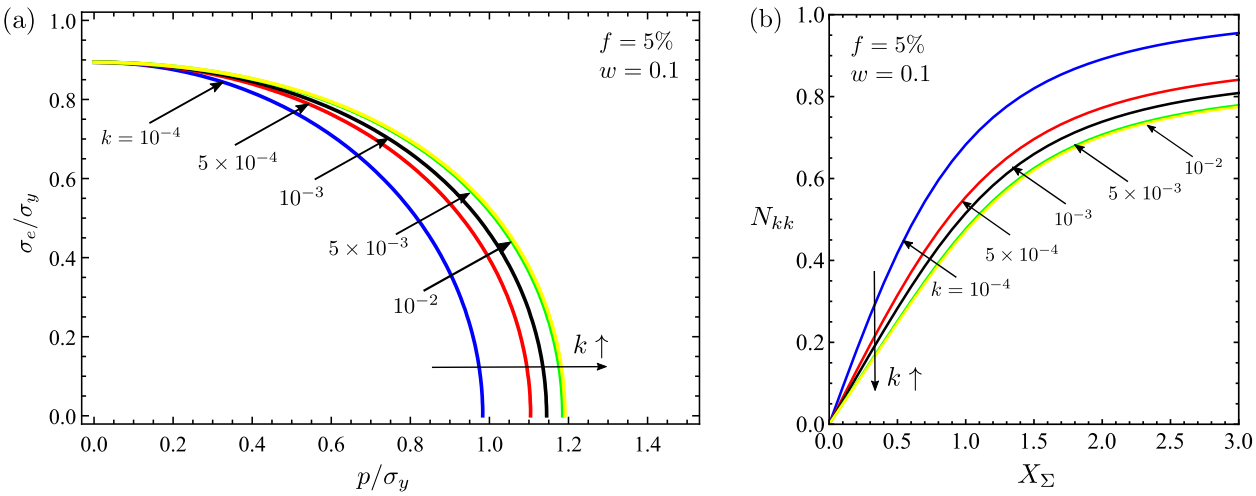

Figure 2.8 – Influence of parameter k on (a) the yield curve on the normalized $p - \sigma_e$ plane and (b) the variation of the normalized volumetric plastic strain-rate N_{kk} with stress triaxiality X_Σ.

$k(w = 1)$ and α. Nonetheless, the rate at which the yield curve approaches that point is obviously affected by α (see discussion in Mbiakop et al. (2015b)).

2.5 Concluding remarks

In this chapter, the isotropic projection approach has been employed in conjunction with Hashin-Shtrikmann type estimates for porous materials with unidirectional microstructures to derive estimates for the effective elastic-plastic response of porous material with randomly oriented voids. In order to derive a fully explicit and computationally efficient model, only spheroidal voids are considered, which are all characterized by the same shape parameter, the aspect ratio w, but different orientations. Microstructural changes are assumed to be characterized by the matrix equivalent plastic strain and porosity evolution while the effect of void shape evolution to the macroscopic response is assumed negligible. Also, a simple interpolation is used based on past numerical studies (Cao et al., 2015; Mbiakop et al., 2015a,b) to accurately capture porosity evolution for both low and high initial porosity microstructures. These assumptions result in a formulation that possesses the advantages of the isotropic Gurson's model while incorporating at the same time critical void shape effects through homogenization.

Examination of the various parameters in the analytical model gives rise to interesting implications for the effective response of materials with the proposed microstructure. Overall, the effect of initial void shape is found to be stronger than that of void volume fraction. In particular, the effect of oblate voids (i.e., voids with aspect ratios $w < 1$) is indicated to be much stronger on both the elastic and the plastic response of porous materials compared to spherical or prolate voids (i.e., voids with $w \geq 1$). Microstructures comprising penny-shaped microvoids of low aspect ratios ($w \leq 0.5$) are expected to exhibit highly compliant homogenized responses, especially at high stress triaxiality states. This is also indicated by the instantaneous yield curves as predicted by the analytical model for various microstructures where the hydrostatic point is found to be more sensitive to the aspect ratio parameter compared to the corresponding shear point.

CHAPTER 3

Numerical Homogenization and Model Assessment

Chapter summary: This chapter deals with the assessment of the fully analytical model presented previously through the use of a numerical RVE homogenization framework. First, a general methodology for the implementation of periodic boundary conditions and loading under constant, predefined, macroscopic stress ratios is presented. Then, we discuss the results from numerical FE calculations of 3D representative unit cells which comprise random distributions of randomly oriented spheroidal voids at different initial porosities and are loaded under different combinations of average stress triaxiality and Lode angle. The analytical model is subsequently aligned with the predictions for the average RVE response through the use of a small number of fitting parameters. The calibrated analytical homogenization model is utilized to examine the evolution of microstructure by assuming different void shapes and average stress states.

Contents

3.1 Loading of 3D RVEs under periodic boundary conditions

In the context of analytical model assessment through numerical homogenization, it is desirable to carry out finite element calculations on Representative Volume Elements (RVEs)

which are loaded in such a way so that some predefined ratios of the components of the average stress tensor remain constant throughout the loading program. The way to achieve this condition is by no means trivial since, in the case of RVEs with periodic B.C., this requires the applied displacement fields that drive the solution to be defined in a special manner. A methodology for the implementation of such complex loading conditions has been discussed for the special case of *principal loading* by several authors in the literature (see for example the works of Barsoum and Faleskog (2007), Dunand and Mohr (2014) or Mbiakop et al. (2015b)). Herein, we present a methodology which generalizes the techniques presented usually in the literature to loadings that may include all the components of the average stress tensor and consider triaxial loading as a special case. In what follows, a superposed "ˆ" is used to denote vector or matrix representations of tensors whose corresponding ranks are indicated by the context.

3.1.1 Application of periodic boundary conditions

In this section, the application of the periodic boundary conditions which are necessary for the unit cell calculations presented in Section 3.2 is discussed. A more detailed description of the properties of periodic stress and strain fields can be found in Michel et al. (1999). Let us consider a cubic RVE with edge size $L_i, i = 1, 2, 3$ as the one shown in Fig. 3.1. The definition of periodicity implies that the displacement field $\mathbf{u}(\mathbf{X})$ can be written in terms of a periodic displacement $\bar{\mathbf{u}}(\mathbf{X})$ with zero mean strain in the RVE (Suquet (1987)) as:

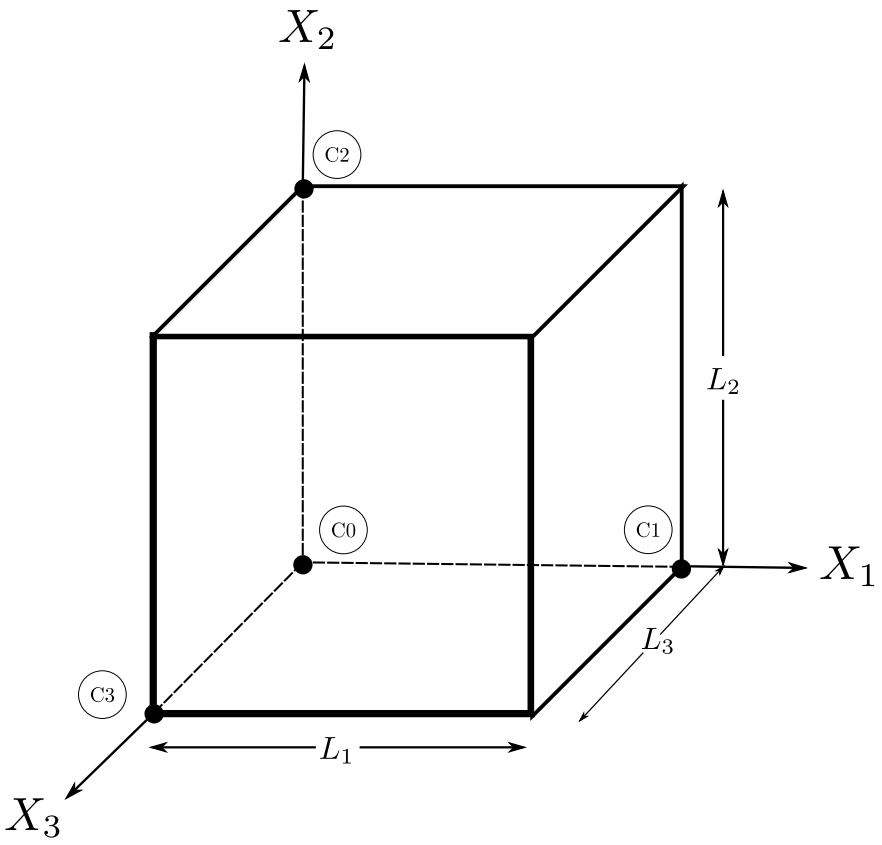

Figure 3.1 – Schematic representation of the cubic cell and depiction of corner nodes.

$$\mathbf{u}(\mathbf{X}) = (\mathbf{F} - \boldsymbol{\delta}) \cdot \mathbf{X} + \bar{\mathbf{u}}(\mathbf{X}), \qquad \int_{\mathcal{V}_{RVE}} (\nabla \bar{\mathbf{u}} + \bar{\mathbf{u}} \nabla) d\mathcal{V} = \mathbf{0} \tag{3.1}$$

where $\mathbf{X}$ is a position vector of a material point in the undeformed configuration, $\mathbf{F}$ is the average (macroscopic) *applied* deformation gradient, and $\mathcal{V}_{RVE}$ is the volume of the RVE. Since $\bar{\mathbf{u}}(\mathbf{X})$ is periodic it follows that it takes the same values on opposite sides of the RVE, i.e., the following conditions hold

$$\bar{\mathbf{u}}(L_1, X_2, X_3) = \bar{\mathbf{u}}(0, X_2, X_3), \quad \bar{\mathbf{u}}(X_1, L_2, X_3) = \bar{\mathbf{u}}(X_1, 0, X_3), \quad \bar{\mathbf{u}}(X_1, X_2, L_3) = \bar{\mathbf{u}}(X_1, X_2, 0) \tag{3.2}$$

In order to eliminate rigid body motions and rotations about each of the axes shown in Fig. 3.1, the following constraints are applied in finite element calculations:

$$\mathbf{u}^{C0} \equiv \mathbf{u}(\mathbf{0}) = \mathbf{0} \quad \text{and} \quad u_2^{C1} = u_3^{C1} = u_3^{C2} = 0 \tag{3.3}$$

In view of the conditions (3.2), by substracting the nodal displacements on opposite boundary sides we can arrive to the following kinematic constraints for the corner nodes of the cubic cell:

$$\mathbf{u}(L_1, 0, 0) - \mathbf{u}(\mathbf{0}) = (\mathbf{F} - \boldsymbol{\delta}) \cdot (L_1 \mathbf{e}_1) \quad \text{or} \quad \mathbf{u}^{C1} = L_1 (\mathbf{F} - \boldsymbol{\delta}) \cdot \mathbf{e}_1 \tag{3.4}$$

$$\mathbf{u}(0, L_2, 0) - \mathbf{u}(\mathbf{0}) = (\mathbf{F} - \boldsymbol{\delta}) \cdot (L_2 \mathbf{e}_2) \quad \text{or} \quad \mathbf{u}^{C2} = L_2 (\mathbf{F} - \boldsymbol{\delta}) \cdot \mathbf{e}_2 \tag{3.5}$$

$$\mathbf{u}(0, 0, L_3) - \mathbf{u}(\mathbf{0}) = (\mathbf{F} - \boldsymbol{\delta}) \cdot (L_3 \mathbf{e}_3) \quad \text{or} \quad \mathbf{u}^{C3} = L_3 (\mathbf{F} - \boldsymbol{\delta}) \cdot \mathbf{e}_3 \tag{3.6}$$

where the notation $\mathbf{u}^{C1}, \mathbf{u}^{C2}, \mathbf{u}^{C3}$ is used to indicate the applied displacement fields at the corner nodes of the cell. Equations (3.4)–(3.6) establish a relation between the average applied deformation gradient $\mathbf{F}$ and the applied corner displacement fields. Writing now the constraints for all nodes lying at the same position in opposite sides of the cube, and by accounting for the periodicity of $\bar{\mathbf{u}}(\mathbf{X})$, we arrive at:

$$\mathbf{u}(L_1, X_2, X_3) - \mathbf{u}(0, X_2, X_3) = (\mathbf{F} - \boldsymbol{\delta}) \cdot (L_1 \mathbf{e}_1) = \mathbf{u}^{C1} \tag{3.7}$$

$$\mathbf{u}(X_1, L_2, X_3) - \mathbf{u}(X_1, 0, X_3) = (\mathbf{F} - \boldsymbol{\delta}) \cdot (L_2 \mathbf{e}_2) = \mathbf{u}^{C2} \tag{3.8}$$

$$\mathbf{u}(X_1, X_2, L_3) - \mathbf{u}(X_1, X_2, 0) = (\mathbf{F} - \boldsymbol{\delta}) \cdot (L_3 \mathbf{e}_3) = \mathbf{u}^{C3} \tag{3.9}$$

Relations (3.7)–(3.9) show that the linear periodic constraints for all nodes located at the same position of opposite sides of the cubic RVE can be written in terms of the applied displacement fields at the three corner nodes (i.e., $\mathbf{u}^{C1}, \mathbf{u}^{C2}, \mathbf{u}^{C3}$). In a finite element setting, given $\mathbf{F}$, one only needs to impose boundary conditions for the aforementioned corner nodes C1, C2, C3 and the origin node C0; periodicity conditions for each "opposite" node is then enforced through the linear constraints defined by equations (3.7)–(3.9).

For later reference it should be noted that, for the derivation of the constraints which are necessary to impose the desired constant macroscopic stress state loading, it is useful to express the average *applied* rate-of-deformation tensor $\mathbf{D}$ in terms the applied displacement fields at the corner nodes. This can be done by using equations (3.4)–(3.6) to write $\mathbf{F}$ in terms of the displacement fields $\mathbf{u}^{C1}, \mathbf{u}^{C2}, \mathbf{u}^{C3}$, so that the applied rate-of-deformation tensor $\mathbf{D}$ can then be given as:

$$\mathbf{D} = \frac{1}{2}(\mathbf{L} + \mathbf{L}^T), \qquad \mathbf{L} = \dot{\mathbf{F}} \cdot \mathbf{F}^{-1} \tag{3.10}$$

3.1.2 Nonlinear constraints for stress ratio control

Consider that loading is applied to the RVE in a manner so that the components of the average stress tensor follow the proportional history:

$$\begin{aligned} \sigma_{11} &= \sigma n_1, \quad \sigma_{22} = \sigma n_2, \quad \sigma_{33} = \sigma n_3 \\ \sigma_{12} &= \sigma s_1, \quad \sigma_{13} = \sigma s_2, \quad \sigma_{23} = \sigma s_3 \end{aligned} \tag{3.11}$$

where $n_i, s_i,\ i = 1, 2, 3$ denote the ratios of macroscopic stress components and σ could be any of the six independent stress components σ_{ij}. This identification of σ implies that in the most general loading case only five stress ratios will be independent since one stress ratio will always be equal to unity depending on the choice of σ. Let $\hat{\boldsymbol{\Sigma}}, \hat{\mathbf{D}}$ denote the reduced (six-dimensional) vectors of the average stress and rate-of-deformation tensors $\boldsymbol{\sigma}, \mathbf{D}$. The components of $\hat{\boldsymbol{\Sigma}}, \hat{\mathbf{D}}$ with respect to a base spanned by the vectors $\{\mathbf{e}_I\},\ I = 1, \cdots, 6$ can be written as:

$$\underset{6\times1}{\left\{\hat{\Sigma}\right\}}_{\mathbf{e}_I} \equiv \begin{Bmatrix} \hat{\Sigma}_1 \\ \hat{\Sigma}_2 \\ \hat{\Sigma}_3 \\ \hat{\Sigma}_4 \\ \hat{\Sigma}_5 \\ \hat{\Sigma}_6 \end{Bmatrix} = \begin{Bmatrix} \sigma_{11} \\ \sigma_{22} \\ \sigma_{33} \\ \sigma_{12} \\ \sigma_{13} \\ \sigma_{23} \end{Bmatrix} = \sigma \begin{Bmatrix} n_1 \\ n_2 \\ n_3 \\ s_1 \\ s_2 \\ s_3 \end{Bmatrix} \quad \text{and} \quad \underset{6\times1}{\left\{\hat{D}\right\}}_{\mathbf{e}_I} \equiv \begin{Bmatrix} \hat{D}_1 \\ \hat{D}_2 \\ \hat{D}_3 \\ \hat{D}_4 \\ \hat{D}_5 \\ \hat{D}_6 \end{Bmatrix} = \begin{Bmatrix} D_{11} \\ D_{22} \\ D_{33} \\ 2D_{12} \\ 2D_{13} \\ 2D_{23} \end{Bmatrix} \tag{3.12}$$

where using (3.10), one can derive explicit expressions for the components of $\hat{\mathbf{D}}$ in terms of the nodal velocities of the corner nodes:

$$\underset{6\times1}{\left\{\dot{U}\right\}} = \underset{6\times6}{\left[Q\right]} \underset{6\times1}{\left\{\hat{D}\right\}} \quad \text{or} \quad \underset{6\times1}{\left\{\hat{D}\right\}} = \underset{6\times6}{\left[Q\right]}^{-1} \underset{6\times1}{\left\{\dot{U}\right\}}$$

$$\underset{6\times1}{\left\{\dot{U}\right\}} \equiv \begin{Bmatrix} \dot{U}_1 \\ \dot{U}_2 \\ \dot{U}_3 \\ \dot{U}_4 \\ \dot{U}_5 \\ \dot{U}_6 \end{Bmatrix} = \begin{Bmatrix} \dot{u}_1^{C1} \\ \dot{u}_1^{C2} \\ \dot{u}_2^{C2} \\ \dot{u}_1^{C3} \\ \dot{u}_2^{C3} \\ \dot{u}_3^{C3} \end{Bmatrix}, \quad \underset{6\times6}{\left[Q\right]} = \begin{bmatrix} L_1+U_1 & 0 & 0 & 0 & 0 & 0 \\ 0 & L_2+U_2 & 0 & 0 & 0 & 0 \\ 0 & 0 & L_3+U_3 & 0 & 0 & 0 \\ U_4 & 0 & 0 & L_2+U_2 & 0 & 0 \\ U_5 & 0 & 0 & U_6 & L_3+U_3 & 0 \\ 0 & U_6 & 0 & U_6 & 0 & L_3+U_3 \end{bmatrix} \tag{3.13}$$

The average stress vector $\hat{\boldsymbol{\Sigma}}$ can be written equivalently in terms of a "generalized force" vector $\hat{\mathbf{P}}$ reading:

$$\mathcal{V}_{RVE}\hat{\boldsymbol{\Sigma}} = \bar{\boldsymbol{\mathcal{L}}} \cdot \hat{\mathbf{P}} \quad \text{or} \quad \mathcal{V}_{RVE} \underset{6\times1}{\left\{\hat{\Sigma}\right\}} = \underset{6\times6}{\left[\bar{\mathcal{L}}\right]} \underset{6\times1}{\left\{\hat{P}\right\}} \tag{3.14}$$

with $\bar{\boldsymbol{\mathcal{L}}}$ being an arbitrary matrix with dimensions of length and $\mathcal{V}_{RVE}$ being the volume of the RVE. Let $\boldsymbol{\Delta}$ be the vector of "generalized displacemenets" conjugate to $\hat{\mathbf{P}}$, i.e.,

$$\dot{W} = \hat{\mathbf{P}} \cdot \dot{\boldsymbol{\Delta}} = \underset{1\times6}{\left\lfloor \hat{P} \right\rfloor} \underset{6\times1}{\left\{\dot{\Delta}\right\}}, \quad \underset{1\times6}{\lfloor \Delta \rfloor} = \lfloor \Delta_1 \ \Delta_2 \ \Delta_3 \ \Delta_4 \ \Delta_5 \ \Delta_6 \rfloor \tag{3.15}$$

The components of $\boldsymbol{\Delta}$ can be identified as the degrees of freedom of two fictitious nodes in the model. We introduce at this point an auxiliary orthonormal base spanned by the vectors $\{\mathbf{a}^{(I)}\}, I = 1, \cdots, 6$ which are defined in such a way so that $\hat{\boldsymbol{\Sigma}}$ is aligned with $\{\mathbf{a}^{(1)}\}$ as follows:

For $n_1^2 + n_2^2 \neq 0$:

$$\underset{6\times1}{\left\{\mathbf{a}^{(1)}\right\}} = \frac{1}{\Pi_1}\begin{Bmatrix} n_1 \\ n_2 \\ n_3 \\ s_3 \\ s_2 \\ s_3 \end{Bmatrix}, \quad \underset{6\times1}{\left\{\mathbf{a}^{(2)}\right\}} = \frac{1}{\Pi_2}\begin{Bmatrix} -n_2 \\ n_1 \\ 0 \\ 0 \\ 0 \\ 0 \end{Bmatrix}, \quad \underset{6\times1}{\left\{\mathbf{a}^{(3)}\right\}} = \frac{1}{\Pi_3}\begin{Bmatrix} -n_1 n_3 \\ -n_2 n_3 \\ n_1^2 + n_2^2 \\ 0 \\ 0 \\ 0 \end{Bmatrix}$$

$$\underset{6\times1}{\left\{\mathbf{a}^{(4)}\right\}} = \frac{1}{\Pi_4}\begin{Bmatrix} -n_1 s_1 \\ -n_2 s_1 \\ -n_3 s_1 \\ \sum_{i=1}^{3} n_i^2 \\ 0 \\ 0 \end{Bmatrix}, \quad \underset{6\times1}{\left\{\mathbf{a}^{(5)}\right\}} = \frac{1}{\Pi_5}\begin{Bmatrix} -n_1 s_2 \\ -n_2 s_2 \\ -n_3 s_2 \\ -s_1 s_2 \\ \sum_{i=1}^{3} n_i^2 + s_1^2 \\ 0 \end{Bmatrix}, \quad \underset{6\times1}{\left\{\mathbf{a}^{(5)}\right\}} = \frac{1}{\Pi_6}\begin{Bmatrix} -n_1 s_3 \\ -n_2 s_3 \\ -n_3 s_3 \\ -s_1 s_3 \\ -s_2 s_3 \\ \sum_{i=1}^{3} n_i^2 + s_1^2 + s_2^2 \end{Bmatrix} \tag{3.16}$$

where the corresponding coefficents Π_I $(I = 1, \cdots, 6)$ are given as:

$$\begin{aligned} \Pi_1 &= \sqrt{\sum_{i=1}^{3}\left(n_i^2 + s_i^2\right)}, \quad \Pi_2 = \sqrt{n_1^2 + n_2^2}, \quad \Pi_3 = \sqrt{\left(n_1^2 + n_2^2\right)\sum_{i=1}^{3} n_i^2} \\ \Pi_4 &= \sqrt{\sum_{i=1}^{3} n_i^2 \left(\sum_{i=1}^{3} n_i^2 + s_1^2\right)}, \quad \Pi_5 = \sqrt{\left(\sum_{i=1}^{3} n_i^2 + s_1^2\right)\left(\sum_{i=1}^{3} n_i^2 + s_1^2 + s_2^2\right)} \\ \Pi_6 &= \sqrt{\left(\sum_{i=1}^{3} n_i^2 + s_1^2 + s_2^2\right)\left(\sum_{i=1}^{3}\left(n_i^2 + s_i^2\right)\right)} \end{aligned} \tag{3.17}$$

For $n_1 = n_2 = 0$ and $n_3^2 + s_1^2 \neq 0$:

$$\left\{\mathbf{a}^{(2)}\right\} = \left\{\mathbf{e}_1\right\}, \quad \left\{\mathbf{a}^{(3)}\right\} = \left\{\mathbf{e}_2\right\}, \quad \left\{\mathbf{a}^{(1)}\right\}, \left\{\mathbf{a}^{(4)}\right\}, \left\{\mathbf{a}^{(5)}\right\}, \left\{\mathbf{a}^{(6)}\right\} \text{ from (3.16)} \tag{3.18}$$

For $n_1 = n_2 = n_3 = s_1 = 0$ and $s_2^2 + s_3^2 \neq 0$:

$$\begin{aligned} &\left\{\mathbf{a}^{(2)}\right\} = \left\{\mathbf{e}_1\right\}, \quad \left\{\mathbf{a}^{(3)}\right\} = \left\{\mathbf{e}_2\right\}, \quad \left\{\mathbf{a}^{(4)}\right\} = \left\{\mathbf{e}_3\right\}, \quad \left\{\mathbf{a}^{(5)}\right\} = \left\{\mathbf{e}_4\right\}, \\ &\left\{\mathbf{a}^{(1)}\right\}, \left\{\mathbf{a}^{(6)}\right\} \text{ from (3.16)} \end{aligned} \tag{3.19}$$

The vectors $\hat{\boldsymbol{\Sigma}}, \hat{\mathbf{D}}, \hat{\mathbf{P}}, \boldsymbol{\Delta}$ can then be expressed in the new base as:

$$\hat{\boldsymbol{\Sigma}} = \hat{\Sigma}_1'\left\{\mathbf{a}^{(1)}\right\}, \quad \hat{\mathbf{D}} = \sum_{I=1}^{6} \hat{D}_I'\left\{\mathbf{a}^{(I)}\right\}, \quad \hat{\mathbf{P}} = \sum_{I=1}^{6} \hat{P}'\left\{\mathbf{a}^{(I)}\right\}, \quad \boldsymbol{\Delta} = \sum_{I=1}^{6} \Delta_I'\left\{\mathbf{a}^{(I)}\right\} \tag{3.20}$$

where

$$\underset{6\times1}{\left\{\hat{\Sigma}'\right\}} = \underset{6\times6}{\left[C\right]}^{T}\underset{6\times1}{\left\{\hat{\Sigma}\right\}}, \quad \underset{6\times1}{\left\{\hat{D}'\right\}} = \underset{6\times6}{\left[C\right]}^{T}\underset{6\times1}{\left\{\hat{D}\right\}}, \quad \underset{6\times1}{\left\{\hat{P}'\right\}} = \underset{6\times6}{\left[C\right]}^{T}\underset{6\times1}{\left\{\hat{P}\right\}}, \quad \underset{6\times1}{\left\{\Delta'\right\}} = \underset{6\times6}{\left[C\right]}^{T}\underset{6\times1}{\left\{\Delta\right\}}, \tag{3.21}$$

$$\underset{6\times6}{\left[C\right]} = \left[\underset{6\times1}{\left\{\mathbf{a}^{(1)}\right\}} \; \underset{6\times1}{\left\{\mathbf{a}^{(2)}\right\}} \; \underset{6\times1}{\left\{\mathbf{a}^{(3)}\right\}} \; \underset{6\times1}{\left\{\mathbf{a}^{(4)}\right\}} \; \underset{6\times1}{\left\{\mathbf{a}^{(5)}\right\}} \; \underset{6\times1}{\left\{\mathbf{a}^{(6)}\right\}}\right] \tag{3.22}$$

Loading at constant stress ratios can then be achieved by enforcing the following conditions:

$$\Delta'_1 = \bar{\Delta}' = \text{known} \quad \text{and} \quad \hat{\Sigma}'_2 = \hat{\Sigma}'_3 = \hat{\Sigma}'_4 = \hat{\Sigma}'_5 = \hat{\Sigma}'_6 = 0 \tag{3.23}$$

which lead to the expressions (3.11) for the desired average stress aspect ratios. In view of expressions (3.14), (3.13) and (3.20), coupling of the components of $\boldsymbol{\Delta}$ with the physical degrees of freedom that drive the solution can be achieved by comparing the total work rate on the RVE ($= \mathcal{V}_{RVE}\boldsymbol{\sigma} : \mathbf{D} = \mathcal{V}_{RVE}\hat{\boldsymbol{\Sigma}} \cdot \hat{\mathbf{D}}$) with (3.15), yielding:

$$\underset{6\times1}{\left\{\dot{\Delta}'\right\}} = \underset{6\times6}{\left[C\right]}^{T}\underset{6\times6}{\left[\bar{\mathcal{L}}\right]}\underset{6\times6}{\left[Q\right]}^{-1}\underset{6\times1}{\left\{\dot{U}\right\}} \quad \text{or} \quad \underset{6\times1}{\left\{\dot{U}\right\}} = \underset{6\times6}{\left[Q\right]}\underset{6\times6}{\left[\bar{\mathcal{L}}\right]}^{-1}\underset{6\times6}{\left[C\right]}\underset{6\times1}{\left\{\dot{\Delta}'\right\}} \tag{3.24}$$

Equation $(3.24)_2$ defines a set of nonlinear kinematic constraints associating the degrees of freedom of the nodes related to the application of the periodic boundary conditions with the degrees of freedom of two fictitious nodes. Satisfaction of this constraint at every increment of the numerical solution ensures that the loading follows the desired proportional history defined by the stress ratios in (3.11). In the special case of *principal* loading, the desired constant stress state can be established through two stress invariants, namely the average stress triaxiality X_Σ and Lode angle θ as follows. Using equations (3.11), it can be shown that the average stress triaxiality and Lode angle can be given as functions of the stress ratios:

$$X_\Sigma = \frac{p}{\sigma_e} = \frac{A_1(n_i, s_i)}{3A_2(n_i, s_i)}, \qquad \theta = \frac{1}{3}\arcsin\left(-\frac{27}{2}\frac{\det(\mathbf{s})}{\sigma_e^3}\right) = \frac{1}{3}\arcsin\left(-\frac{A_3(n_i, s_i)}{2\left[A_2(n_i, s_i)\right]^3}\right) \tag{3.25}$$

$$\begin{aligned}
A_1 &= n_1 + n_2 + n_3, \\
A_2 &= \sqrt{n_1^2 + n_2^2 + n_3^2 - (n_1n_2 + n_1n_3 + n_2n_3) + 3\left(s_1^2 + s_2^2 + s_3^2\right)} \\
A_3 &= 2\left(n_1^2 + n_2^2 + n_3^2\right) - 3\{\left(n_1^2 + n_2n_3\right)(n_2 + n_3) - n_1\left(n_2^2 - 4n_2n_3 + n_3^2\right), \\
&\quad + 3\left[(n_2 - 2n_3)s_1^2 + (n_3 - 2n_2)s_2^2 + (n_2 + n_3)s_3^2 + 6s_1s_2s_3 + n_1\left(s_1^2 + s_2^2 - 2s_3^2\right)\right]\}
\end{aligned} \tag{3.26}$$

For principal loading (i.e., for $s_i = 0$, $i = 1, 2, 3$), equations (3.25) can be used to express any of the two remaining independent stress ratios n_α as functions of the average stress triaxiality and Lode angle, i.e., a relation of the following form can be written:

$$n_\alpha = n_\alpha(X_\Sigma, \theta) \tag{3.27}$$

where $\alpha = 2, 3$ if $\sigma \equiv \sigma_1$, $\alpha = 1, 3$ if $\sigma \equiv \sigma_2$, and $\alpha = 1, 2$ if $\sigma \equiv \sigma_3$, with σ_i, $i = 1, 2, 3$ denoting the principal stresses. One can also show that in this case, the principal stresses can be given explicitly as functions of stress triaxiality and Lode angle as:

$$\frac{\sigma_i}{\sigma_e} = \frac{2}{3}\cos\theta_i + X_\Sigma, \qquad \theta_i = \theta + (5 - 4i)\frac{\pi}{6}, \qquad i = 1, 2, 3 \tag{3.28}$$

Since the average stress triaxility and Lode angle can be used as measures that characterize the type of the applied *macroscopic* loading, equations (3.25) and (3.28) show that specific choice for the stress ratios n_α corresponds to a specific macroscopic loading stress state and vice versa.

To summarize the procedure, in a finite element setting, the condition $(3.23)_1$ is enforced on a fictitious node and the periodic B.C.s are enforced at each increment of the solution through $(3.24)_2$; this implies that the desired stress ratios defined by (3.11) are kept constant throughout the loading program. In the general case of *multi-axial* proportional loading, the nonlinear constraints $(3.24)_2$ will be functions of all stress ratios. In the special case of *principal* loading, the nonlinear constraints $(3.24)_2$ can defined as a functions of the desired constant average stress triaxiality X_Σ and Lode angle θ based on their functional dependence concisely expressed by (3.27).

3.2 Unit cell calculations

Concerning validation techniques at the *material (constitutive) level*, the numerical periodic homogenization method may be used as a test-bed to assess the predictions of analytical homogenization models. The methodology used in this study for the case of a two-phase, porous material can be summarized as follows. A suitably chosen RVE containing randomly oriented and distributed with uniform probability spheroidal voids of predefined initial volume fraction is loaded and periodic boundary conditions are applied. The finite element method is used to determine the *local*[1] displacement, strain, and stress fields in the RVE. The local fields are then used to calculate the corresponding *average* fields. The fitting parameters A, B, and f_{min} used in the interpolation function α in (2.59), are then adjusted to align the predictions of the analytical model with the average numerical results.

In this work, cubic unit cells with side lengths $L_1 = L_2 = L_3 = 1$ and initial volume $\mathcal{V}_0 = L_1\, L_2\, L_3 = 1$ are filled with uniform distributions of randomly oriented voids of the same spheroidal shapes and initial porosities as shown in Fig. 3.2. The unit cells are subjected to constant average stress triaxiality X_Σ and Lode angle θ under periodic boundary conditions, using the procedure described in Section 3.1. Using as an indicator both previous numerical results (Danas and Aravas, 2012; Cao et al., 2015; Anoukou et al., 2018; Zerhouni et al., 2021) and the results presented in Section 2.4, only oblate and spherical voids (i.e., $w \leq 1$) are considered in the RVE calculations, since prolate voids exhibit substantially weaker effects on the effective response. The geometry of the unit cells is generated using the Random Sequential Adsorption (RSA) method discussed in Anoukou et al. (2018). Therein, ellipsoidal voids (or inclusions in the general case) of the same or different size are sequentially added in the unit cell imposing a non-overlapping condition based on distance evaluation of quadric objects of general shape. When the desired volume fraction (porosity) is reached, periodic images of any "incomplete" voids at the cube boundaries are added.

In all numerical calculations, the matrix material is assumed to be isotropic with Young's modulus $E = 300\,\sigma_0$, Poisson's ratio $\nu = 0.3$, and a flow stress following power law isotropic

[1]It should be recalled that in the context of homogenization theory, these are the fields that develop at the scale of the various heterogeneities as opposed to the (measurable) fields at the scale of the applied macroscopic loads.

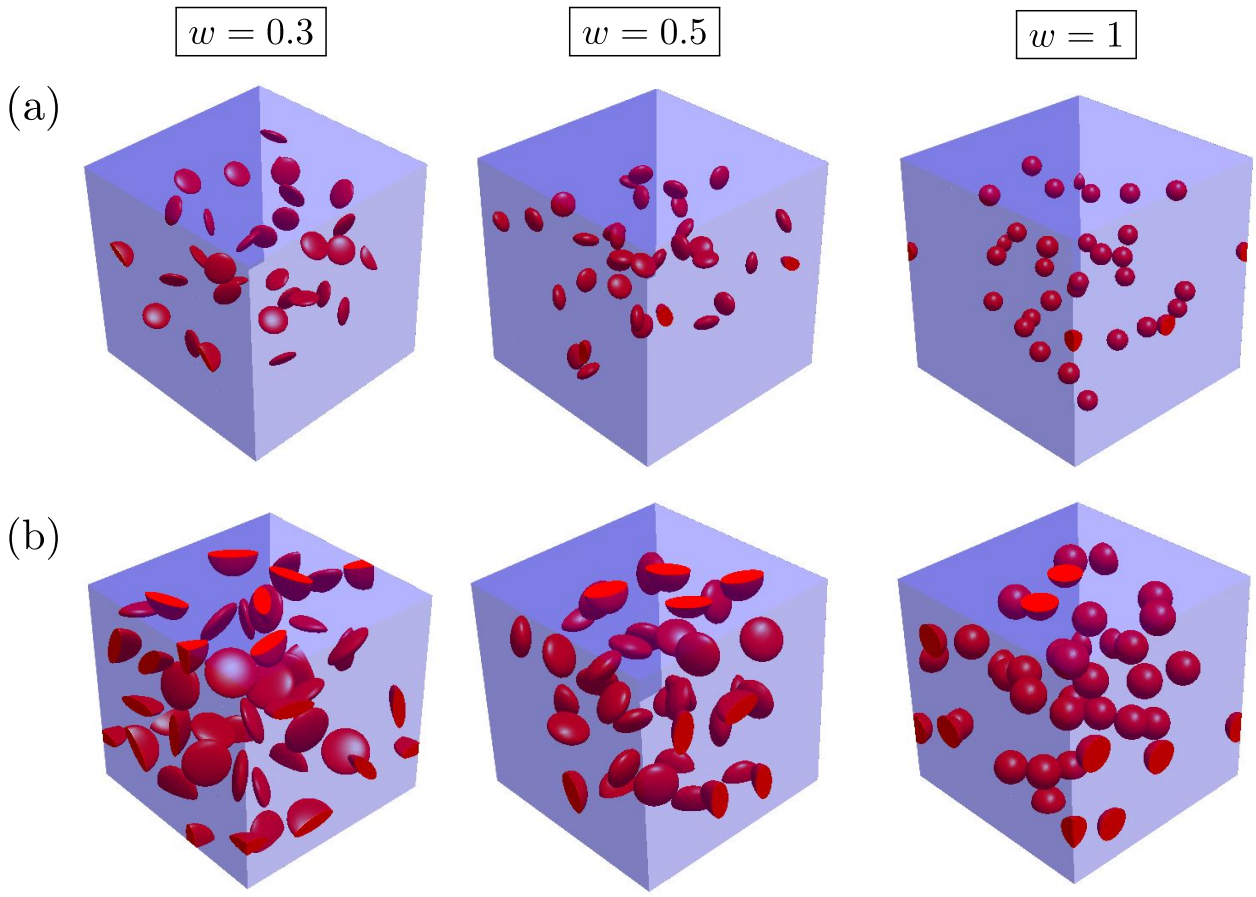

Figure 3.2 – Cubic unit cells used in the numerical homogenization calculations containing randomly oriented and distributed oblate voids of various shapes at an initial volume fraction (a) $f_0 = 1\%$ and (b) $f_0 = 5\%$.

hardening[2] of the form

$$\sigma_y(\bar{\varepsilon}^p) = \sigma_0 \left(1 + \frac{\bar{\varepsilon}^p}{\varepsilon_0}\right)^{1/n}, \tag{3.29}$$

is used, where $n \geq 1$ is the hardening exponent and $\varepsilon_0 = \sigma_0/E$. A hardening exponent of $n = 10$ is used in all numerical homogenization calculations. The average porosity in the unit cell is calculated using the corresponding average deformation gradient as

$$f = \frac{\mathcal{V}^{\mathrm{v}}}{\mathcal{V}} = \frac{\det \mathbf{F} - \mathcal{V}^{\mathrm{m}}/\mathcal{V}_0}{\det \mathbf{F}}, \qquad \det \mathbf{F} = \frac{\mathcal{V}}{\mathcal{V}_0}, \qquad \mathcal{V} = \mathcal{V}^{\mathrm{m}} + \mathcal{V}^{\mathrm{v}}, \tag{3.30}$$

where $\mathbf{F}$ is the average deformation gradient, $\mathcal{V}^{\mathrm{m}}$ is the current matrix volume, $\mathcal{V}^{\mathrm{v}}$ the current volume of the voids, and $\mathcal{V}$ the current total volume of the RVE.

3.2.1 Computational aspects of RVE simulations

The FE calculations are carried out using the commercial finite element program ABAQUS/Standard (Abaqus, 2021). The power-law isotropic hardening model for the matrix material is

[2] Any other hardening law including kinematic hardening as discussed in Cheng et al. (2017) may be used if required. This is however beyond the scope of the present study.

implemented via a User HARDening (UHARD) user-subroutine provided by ABAQUS/Standard. Loading under constant stress triaxiality and Lode angle is achieved by employing the time-dependent nonlinear constraint $(3.24)_2$, which is enforced at every increment using the Multiple Point Constraint (MPC) user-subroutine provided by ABAQUS/Standard.

All meshes are generated with the mesh generation program NETGEN[3] (https://ngsolve.org). Ten-node quadratic tetrahedral hybrid elements with constant pressure are used in the simulations (C3D10H in ABAQUS/Standard). Mesh convergence studies (concerning both local and average fields) of microstructures with oblate voids show that the number of required elements vary from 8.5×10^5 to 1.5×10^6, depending on the initial porosity and, more importantly, on the void shape; as the value of the aspect ratio w decreases, the number of required elements increases. It is worth noting that, in the case of spherical voids ($w = 1$), convergence of the effective behavior can be achieved with mesh densities in the range of 2×10^5 elements, depending on the value of the initial porosity; these numbers are much smaller than the number of elements required for oblate voids with an aspect ratio $w = 0.3$ for the same initial volume fractions.

The simulations are carried out using parallel computing (20 cpus per simulation) on a high-performance computing (HPC) cluster; for oblate voids with low aspect ratios ($w \leq 0.5$), the average computation time per simulation ranges from 24 to 48 hours depending on the mesh density. A python script was then used for post-processing of the results in order to calculate the average fields of interest. It should be pointed-out that simulations for $w \leq 0.2$ could not be performed, mainly due to significant meshing quality problems. Also, based on the computational times required for $w = 0.3$, we expect very high computational times to be required for such calculations.

3.3 RVE calculations and model calibration

3.3.1 RVE determination and convergence study

It has become clear from previous (e.g., Suquet (1987), Kanit et al. (2003)) and more recent numerical homogenization studies (Lopez-Pamies et al., 2013; Benhizia et al., 2014; El Moumen et al., 2014, 2015a,b; Bensaada et al., 2022; Luo et al., 2023) on porous and particle-reinforced materials that determination of an appropriate RVE requires to investigate the convergence of the average material behavior with respect to a number of parameters in the RVE. In porous materials, these include the number of voids, different realizations of the same microstructures (i.e., different spatial distribution of voids with the same shape and volume fraction), and, for the model considered in this work, examination of the RVE's isotropy. To this end, a systematic investigation for the determination of RVE characteristics is carried out. Unit cell calculations are performed at a constant stress triaxiality $X_\Sigma = 1$, since moderate to high triaxialities are of interest. Dependence on the Lode parameter (or equivalently the third invariant J_3 of the deviatoric stress) is examined through variation of the Lode angle θ. Results for oblate microstructures with an aspect ratio $w = 0.3$ are presented in the following. Due to severe mesh distortion issues with progressing deformation, the calculations were terminated at moderate average strain levels in this case.

Figure 3.3 shows results of the convergence analysis for different *number of voids* N_p. Cross-plots for the average von Mises stress and porosity as functions of Lode angle θ (in

[3]Alternatively, it is also possible to use the open-source, 3D mesh generation software GMSH (https://gmsh.info), as discussed recently in Luo et al. (2023).

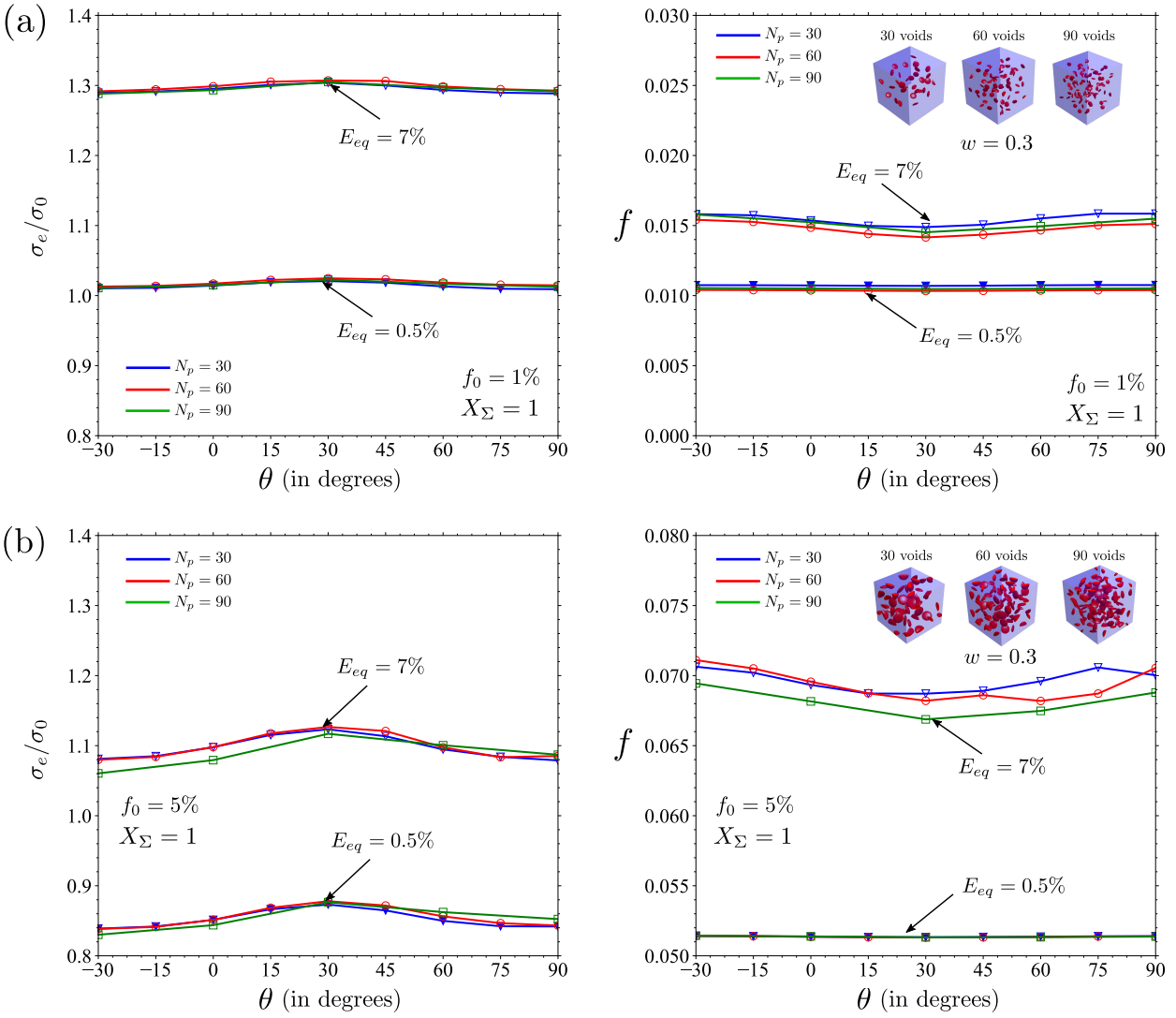

Figure 3.3 – Cross-plots of average normalized von Mises stress σ_{eq}/σ_0 and porosity f as functions of Lode angle θ for $w = 0.3$ and for three different number of voids ($N_p = 30$, 60, and 90), at an initial porosity level (a) $f_0 = 1\%$ and (b) $f_0 = 5\%$.

degrees) at strain levels $E_{eq} = 0.5\%$ and 7% are presented for microstructures comprising three different void numbers ($N_p = 30$, 60, and 90). Note that the vertical axes do not start at the value of zero. A Lode angle range of $\Delta\theta = 120°$ (as opposed to 60°) was intentionally scanned in these series of calculations, to verify the validity of the material isotropy hypothesis of the unit cells. It can be seen from Fig. 3.3a that, for a low initial porosity $f_0 = 1\%$, the scatter in the prediction of the overall porosity evolution is small at all strain levels, leading to an almost identical behavior for the average von Mises stress for all microstructures. A qualitatively similar response is observed for the higher initial porosity of $f_0 = 5\%$ (Fig. 3.3b). Very good agreement can be observed in the results for the microstructures comprising $N_p = 30$ and $N_p = 60$ voids, while a small deviation exists for the microstructures with $N_p = 90$ voids; this difference is more pronounced at the larger average strain of $E_{eq} = 7\%$.

The dependence of the results on the Lode angle is rather weak, at least for the range of strains considered. Examination of the predictions for the effective von Mises stress as

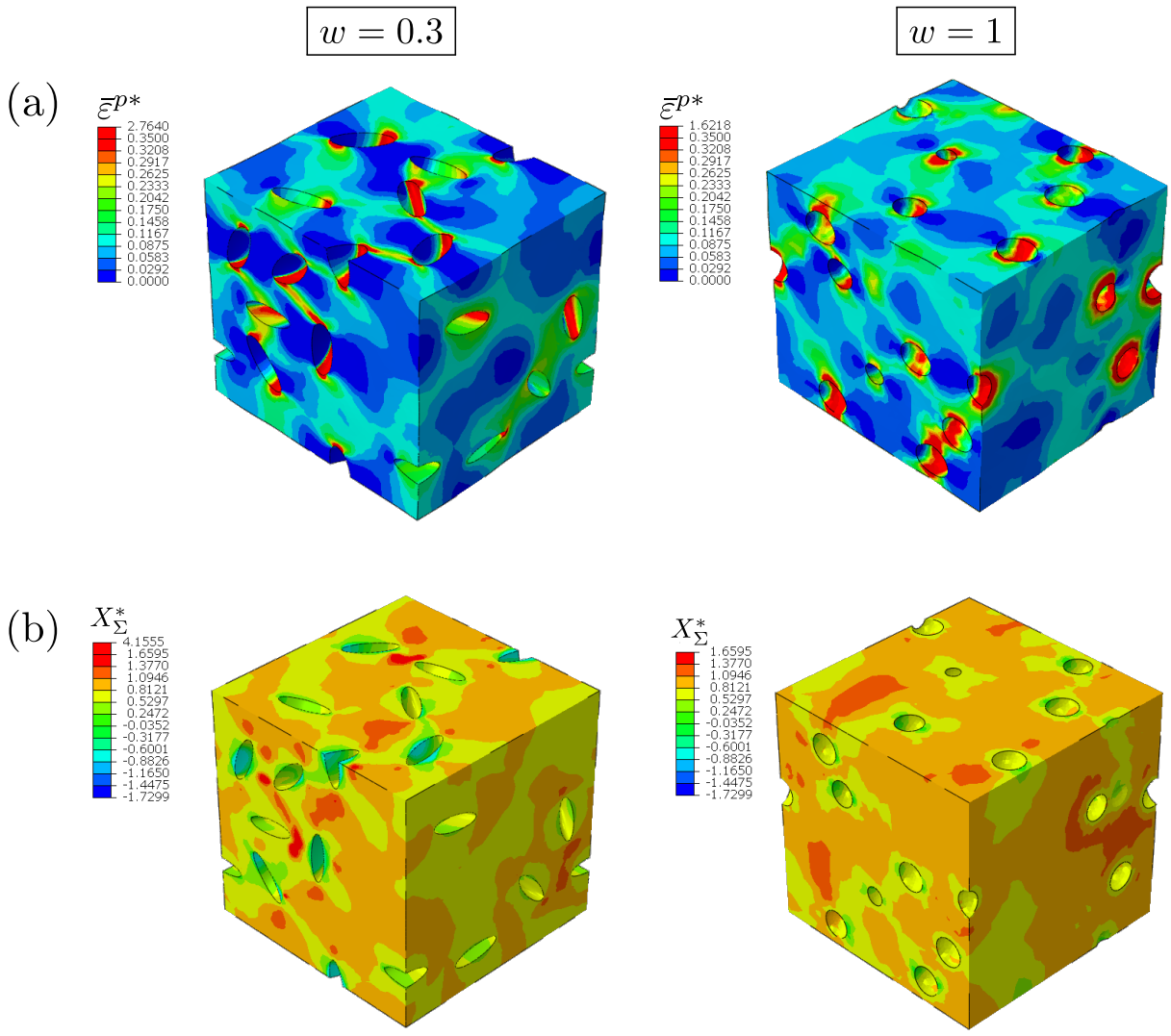

Figure 3.4 – Contour plots of *local* (a) equivalent plastic strain ($\bar{\varepsilon}^{p*}$) and (b) stress triaxiality (X^*_Σ) fields corresponding to a loading with *average* stress triaxiality $X_\Sigma = 1$ and Lode angle $\theta = -30°$. Distributions for two microstructures, one comprising random oblate voids with aspect ratio $w = 0.3$ and another comprising spherical voids (i.e., $w = 1$) are shown. The initial void volume fraction is $f_0 = 5\%$ in both cases.

a function of the Lode angle [4] reveals that for all microstructures considered, there exists approximately a 60° symmetry with respect to $\theta = 30°$ with maximum differences between corresponding points being less than 2%; this indicates that the unit cells can be considered, to within this approximation, as close to isotropic and be used for a fair comparison with the analytical model. Also, the results depicted in Fig. 3.3 show that a distribution of $N_p = 30$ voids provides sufficient convergence of the effective behavior. For computational efficiency, all subsequent unit cell calculations are carried out with a number of $N_p = 30$ voids.

Figure 3.4 depicts the distributions of the *local* equivalent plastic strain ($\bar{\varepsilon}^{p*}$) and stress triaxiality (X^*_Σ) fields that develop at the scale of the voids corresponding to a loading with

[4] Recall that a relation of the form $\sigma_e = \sigma_e(\theta)$ describes the corresponding yield curve on the so-called Π-plane (Danas et al., 2008b).

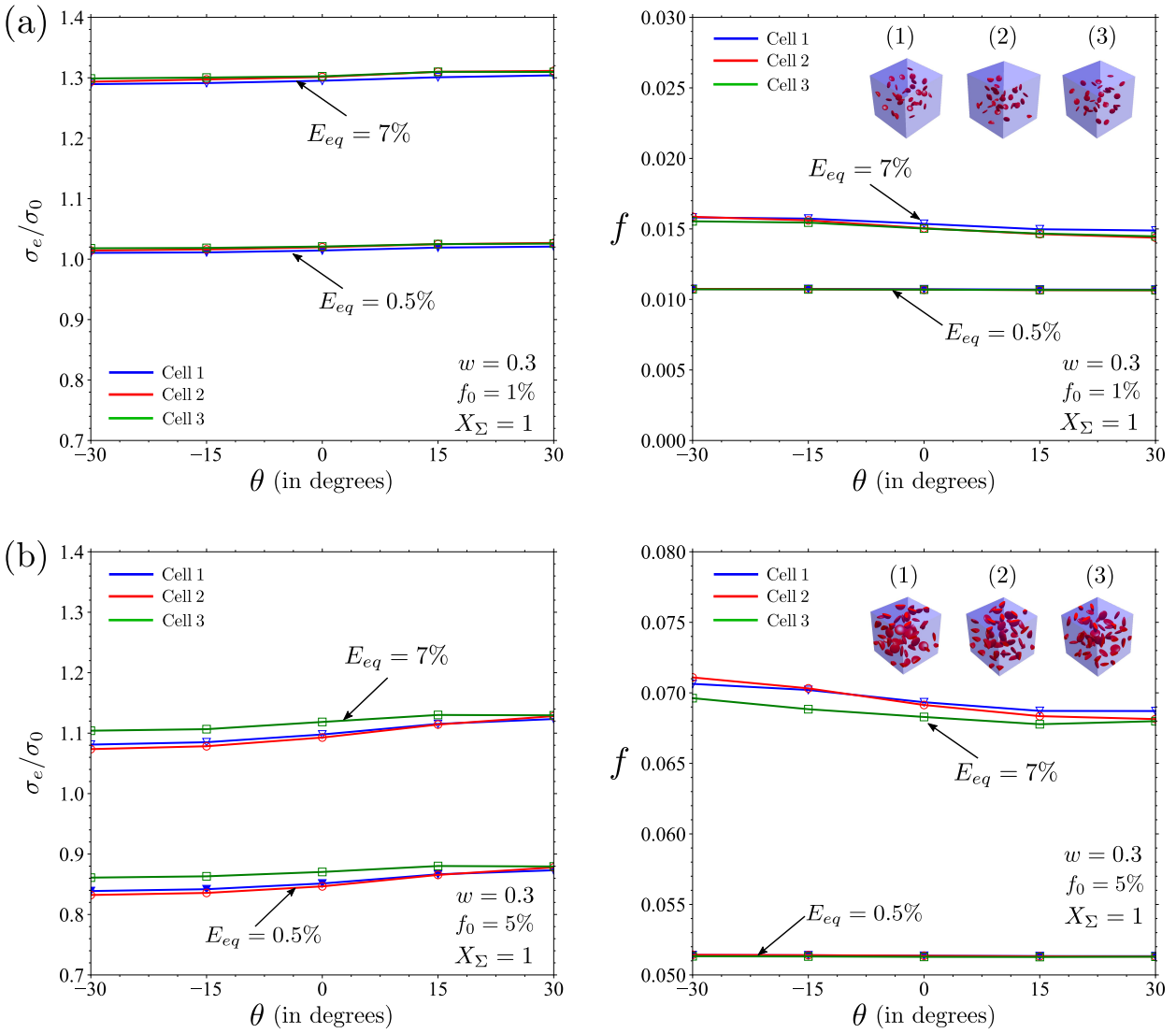

Figure 3.5 – Cross-plots of average normalized von Mises stress σ_{eq}/σ_0 and porosity f as functions of Lode angle θ for three different cell realizations at an initial porosity level (a) $f_0 = 1\%$ and (b) $f_0 = 5\%$.

an *average* stress triaxiality $X_\Sigma = 1$ and a Lode angle $\theta = -30°$. The results for two different microstructures are shown, one with oblate voids of aspect ratio $w = 0.3$ and another with spherical voids (i.e., $w = 1$). As one can see from Fig. 3.4a, plastic strains concentrate mostly in the ligaments between the voids in the microstructure comprising oblate voids with the corresponding distribution being more diffuse in the microstructure with spherical voids. Also, the highest plastic strains develop at the free surfaces of the voids and are much higher in the case of oblate voids compared to spherical ones. Regions of high and low stress triaxiality appear to form in the case of oblate voids as shown in Fig. 3.4b; relatively high local stress triaxiality conditions ($X^*_\Sigma \geq 1.4$) develop at the region in front of the high curvature side of the voids while lower local stress triaxialities (in the range of $X^*_\Sigma = 0.3-0.6$) develop at the areas surrounding the low curvature (more flat) side of the voids' surfaces. Overall, lower local stress triaxiality conditions with more diffuse distribution are observed in the microstructure with spherical voids.

Figure 3.5 shows the results from the convergence analysis with respect to three different realizations of the same microstructure comprising $N_p = 30$ voids. The RSA algorithm is used to generate multiple random microstructures with a given initial porosity, void shape, and number of voids, but with *different spatial position* of the voids in the matrix material. Again, we present cross-plots for the average von-Mises stress and porosity as functions of the Lode angle at different levels of straining. The range of $\theta \in [-30°, 30°]$ was examined in this series of calculations. In the case of an initial porosity $f_0 = 1\%$, Fig. 3.5a shows a good agreement among the predictions of the three realizations at the strain levels considered. A similar behavior is observed at the higher initial porosity of $f_0 = 5\%$ (Fig. 3.5b). Once again, there exists only a weak variation of the effective behavior with the Lode angle.

Based on these results, it is reasonable to assume that the Lode parameter has a weak effect on the effective plastic response of a porous material especially at the smaller values of w considered here. Therefore, plasticity is assumed to be independent of the Lode angle in the present analytical model.

Remark 8. Nevertheless, if deemed absolutely necessary, extension of the present model to include Lode angle-dependence could be employed through various approaches. One possibility would be to include in the evolution equation of porosity (2.63) an additional term that depends on the third invariant of the stress deviator, as suggested by Nahshon and Hutchinson (2008). Another approach could be the introduction of an additional, Lode angle-dependent, shear-induced damage variable along with a corresponding evolution law as proposed by Zhou et al. (2014a). Also, in the spirit of the model proposed by Bai and Wierzbicki (2008), a Lode angle dependent factor could be introduced directly into the yield function. Finally, one could of course bring the proposed isotropic projection approach in more elaborate homogenization methods (e.g., Danas and Ponte Castañeda (2009a), Agoras and Ponte Castañeda (2014), Song and Ponte Castañeda (2018)), which naturally include dependence on the Lode parameter.

3.3.2 Fitting between the homogenization model and average RVE response

Alignment of the analytical model with the average RVE response is achieved through variation of the fitting parameters A, B and f_{min} of the interpolation function α in (2.59). In particular, we calibrate directly those parameters by repeatedly carrying out calculations with the analytical model using the same material parameters and loading conditions as in the RVE simulations until adequate agreement is found with the average RVE predictions. We find that the evolution of the average von Mises stress and porosity, as predicted by the analytical model, for different values of the void aspect ratio w and initial porosities, fits well the average RVE response for $A = -8.6 \times 10^{-4}$, $B = 1.06 \times 10^{-3}$ and $f_{min} = 0.5\%$ in equation (2.59). It should be mentioned however that this comparison is not exhaustive; more rigorous fitting techniques (e.g., statistical methods such as regression analysis) or even machine learning approaches could be utilized, depending on data availability.

To illustrate the variation in the effective response with the aspect ratio w, results are presented for two different microstructures: one consisting of oblate voids with aspect ratio $w = 0.3$ and another with spherical voids ($w = 1$) for two different initial porosities, $f_0 = 1\%$ and $f_0 = 5\%$. Figures 3.6a-d show the comparison between numerical homogenization results and the predictions of the analytical model for an initial porosity of $f_0 = 1\%$ and a triaxiality $X_\Sigma = 1$. The shaded areas in Fig. 3.6 indicate fluctuations of the effective behavior from

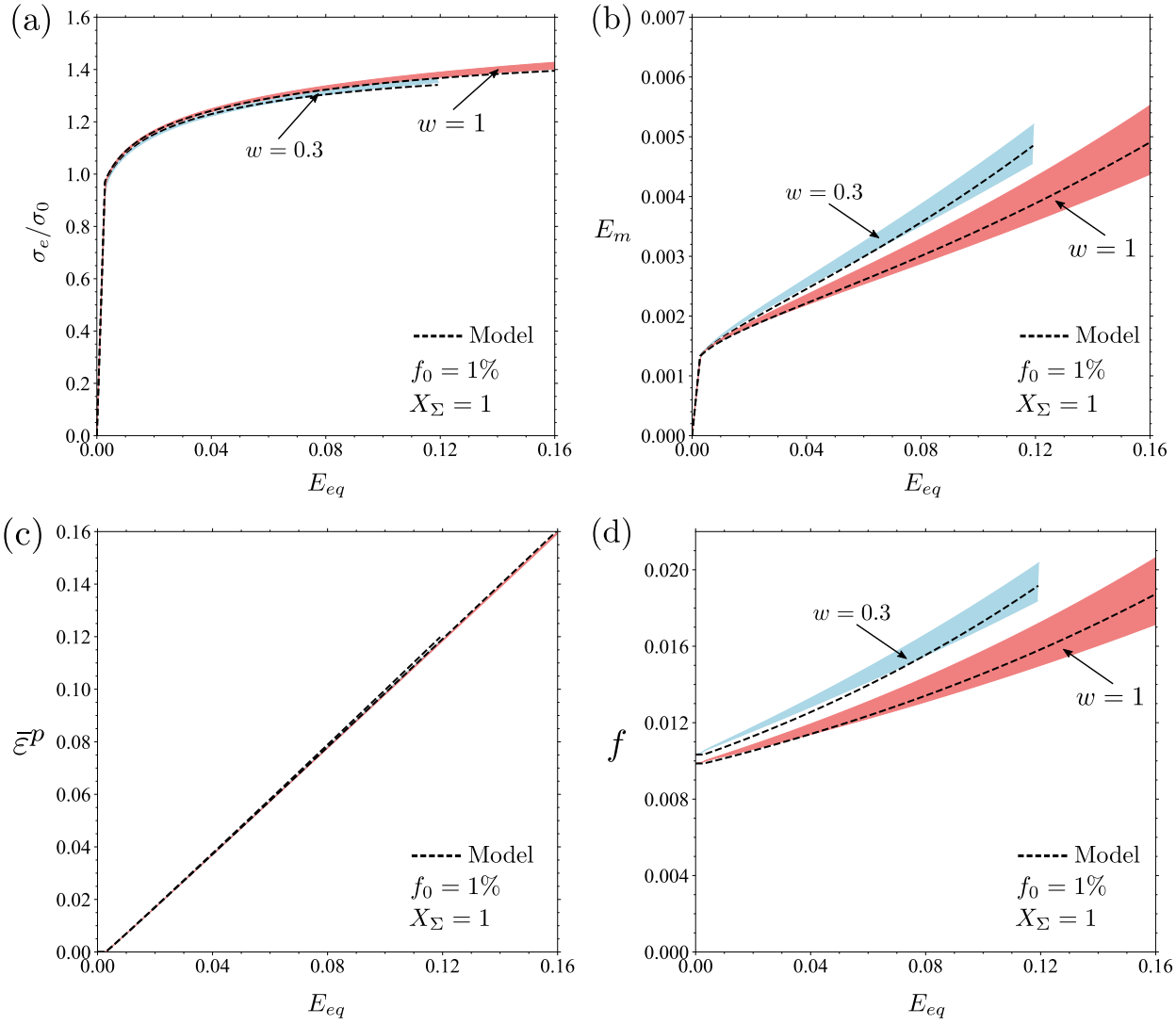

Figure 3.6 – Comparison of average RVE response with the corresponding predictions of the homogenization model for an initial porosity $f_0 = 1\%$ at a constant stress triaxiality $X_\Sigma = 1$. The shaded areas indicate the scatter of the RVE response over different Lode angles $\theta \in [-30°, 30°]$.

the unit cell calculations with respect to different values of the Lode angle in the range $\theta \in [-30°, 30°]$; blue color corresponds to oblate voids with an aspect ratio $w = 0.3$ and red color corresponds to spherical voids ($w = 1$). The black dashed curve corresponds to the predictions of the proposed analytical model, which does not have any dependence on the Lode angle. It is observed that the average hydrostatic strain shown in Fig. 3.6b as well as the porosity evolution shown in Fig. 3.6d are higher in the case of voids with an aspect ratio of $w = 0.3$ compared to a microstructure with spherical voids. The effect of higher porosity in the former case is reflected in the corresponding average stress-strain response (Fig. 3.6a); this effect is weak though, due to the overall small porosity levels developed. It is also interesting to emphasize that the numerical and analytical results for the equivalent plastic strain in the matrix coincide and are independent of the assumed void shape (Fig. 3.6c).

Comparisons between numerical and analytical homogenization results were also carried out for microstructures with an initial volume fraction $f_0 = 5\%$ as shown in Figs. 3.7a-d. The same values for the fitting parameters A, B and f_{min} as in the case of the lower initial

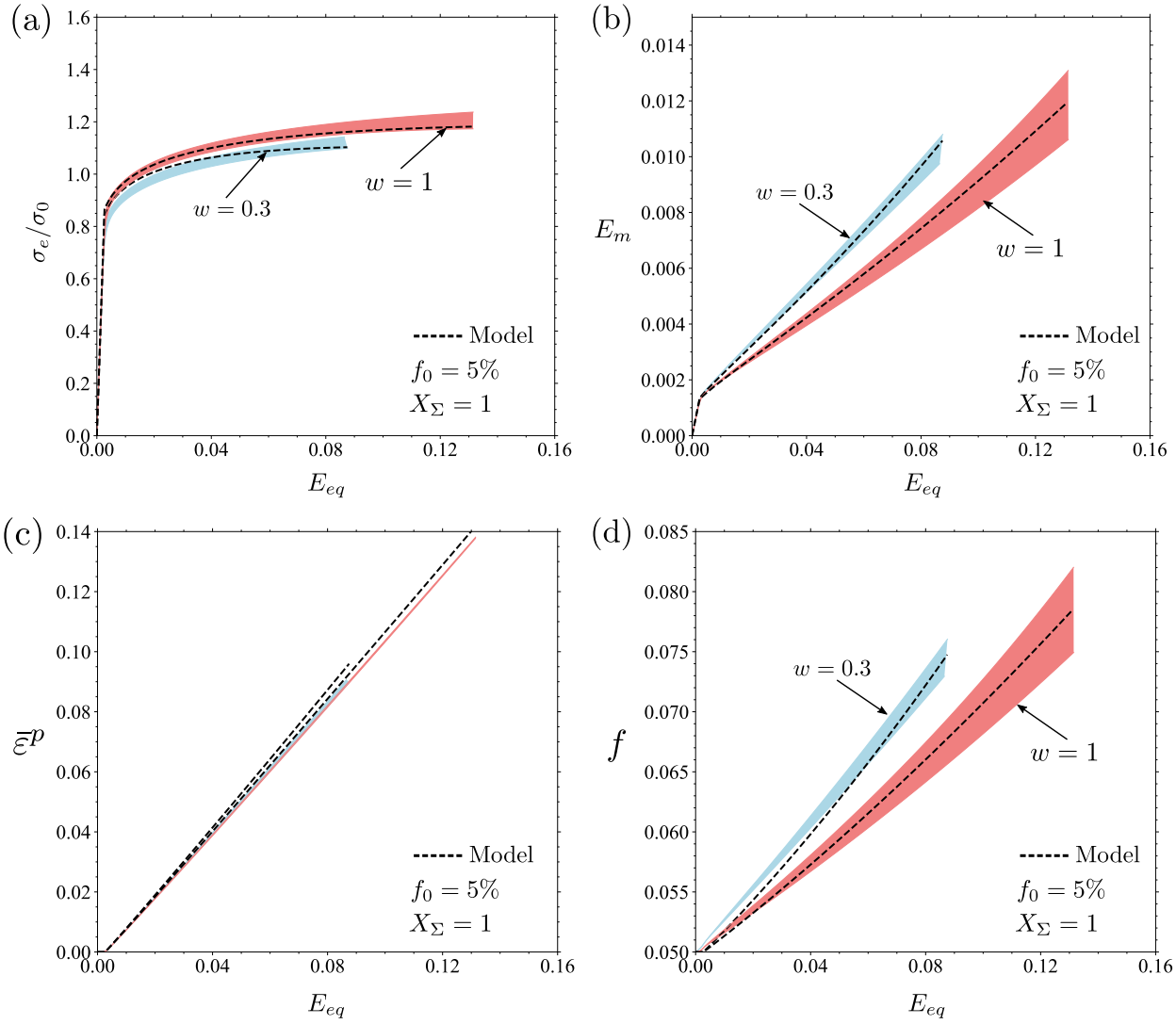

Figure 3.7 – Comparison of average RVE response with the corresponding predictions of the homogenization model for an initial porosity $f_0 = 5\%$ at a constant stress triaxiality $X_\Sigma = 1$. The shaded areas indicate the scatter of the RVE response over different Lode angles $\theta \in [-30°, 30°]$.

porosity were used in the analytical model. As it can be seen the effective stress-strain response is more compliant due to the higher initial porosity assumed in this case. Overall, the analytical model is in good agreement with the corresponding average RVE behavior and similar qualitative observations can be made as in the case of $f_0 = 1\%$. Such results verify the validity of the proposed calibrated model for microstructures with low to moderate initial volume fractions.

Remark 9. Due to approximations introduced during the meshing of the voided unit cells, the resulting numerical meshed initial porosity is slightly higher ($f_0 \cong 0.0104$) for oblate voids and slightly lower ($f \cong 0.0098$) for spherical voids than the prescribed value of $f_0 = 0.010$.

For both the low and high initial porosities considered in these calculations we observe that the largest fluctuations in the scatter of the effective RVE response with respect to the Lode angle appear in the porosity evolution of initially spherical voids. This dependence on the Lode angle, although weak overall, becomes more important with progressing defor-

mation, which was known from previous studies such as Danas et al. (2008b) and Danas and Ponte Castañeda (2012). This may be attributed to the fact that, although both microstructures are initially isotropic, their evolution in the case of finite deformations is rather different. In the case of $w = 1$, the initially spherical voids change their shape in the same *average* way. This leads to deformation-induced anisotropic effective behavior at higher strains. On the other hand, in the case of randomly oriented spheroids, the voids are not expected to all evolve in the same manner, since deformation of each void will ultimately depend on its relative orientation with respect to the applied load. In this latter case, the microstructure is able to retain fairly well its initial isotropy, even at larger strains, showing less sensitivity to the Lode angle parameter.

Overall good agreement is achieved on average between the numerical and analytical results, both for oblate and spherical voids, up to the strain levels attained. This study shows that the proposed analytical model, together with the appropriate choice of the fitting parameters in the interpolation function introduced in (2.59), can capture well the stress and porosity evolution, when compared to full-field numerical results from RVE calculations. In any case, this comparison is not meant to be exhaustive, but it can be used to gain intuition on the effect of the void shape upon the effective response of the porous material.

3.4 Model predictions: Evolution of microstructure

In order to investigate the predictions of the new model, material point (constitutive) calculations for various microstructural configurations and different stress states (defined by the stress triaxiality parameter) are carried out. We consider three different microstructures consisting of spherical voids (i.e., $w = 1$) and oblate voids with aspect ratios $w = 0.3$ and $w = 0.1$ respectively at constant low ($X_\Sigma = 1/3$) and high ($X_\Sigma = 3$) stress triaxiality. The matrix material is characterized by a Young's modulus $E = 300\,\sigma_0$ and a Poisson's ratio $\nu = 0.3$ in all calculations. Also, for comparison purposes, the same calculations are repeated using the well-known "Gurson–Tvergaard–Needleman" (GTN) model (Gurson, 1977; Chu and Needleman, 1980; Tvergaard and Needleman, 1984) with a yield function of the form:

$$\Phi^{\mathrm{GTN}}(\sigma_e, p, \bar{\varepsilon}^p, f) = \left(\frac{\sigma_e}{\sigma_y(\bar{\varepsilon}^p)}\right)^2 + 2\,f\,q_1\,\cosh\left(\frac{3\,q_2}{2}\frac{p}{\sigma_y(\bar{\varepsilon}^p)}\right) - (1 + q_3\,f^2), \tag{3.31}$$

where (q_1, q_2, q_3) are calibration parameters. For $q_1 = q_2 = q_3 = 1$, equation (3.31) reduces to the original Gurson's yield function. Following Tvergaard (1981), we use the values $q_1 = 1.5$, $q_2 = 1$, and $q_3 = q_1^2 = 2.25$ in subsequent calculations. We recall that the GTN model, originating from a modification of the Gurson model, is valid for spherical voids that remain spherical at finite strains. We show that the aspect ratio w can be viewed as a calibration parameter for the newly proposed homogenization model, similar to the aforementioned (q_1, q_2, q_3) calibration parameters in the GTN model. In this set of calculations, σ_e and p are increased in proportion according to the desired stress triaxiality, and the solution is developed incrementally.

Figures 3.8a,b show the stress-strain response and the corresponding porosity evolution for the three different microstructures with $w = 0.1$, 0.3, and 1, and triaxialities $X_\Sigma = 1/3$ and 3. At very high stress triaxiality $X_\Sigma = 3$, the effective response appears very sensitive to w and the material becomes gradually softer for lower values of the aspect ratio. Porosity

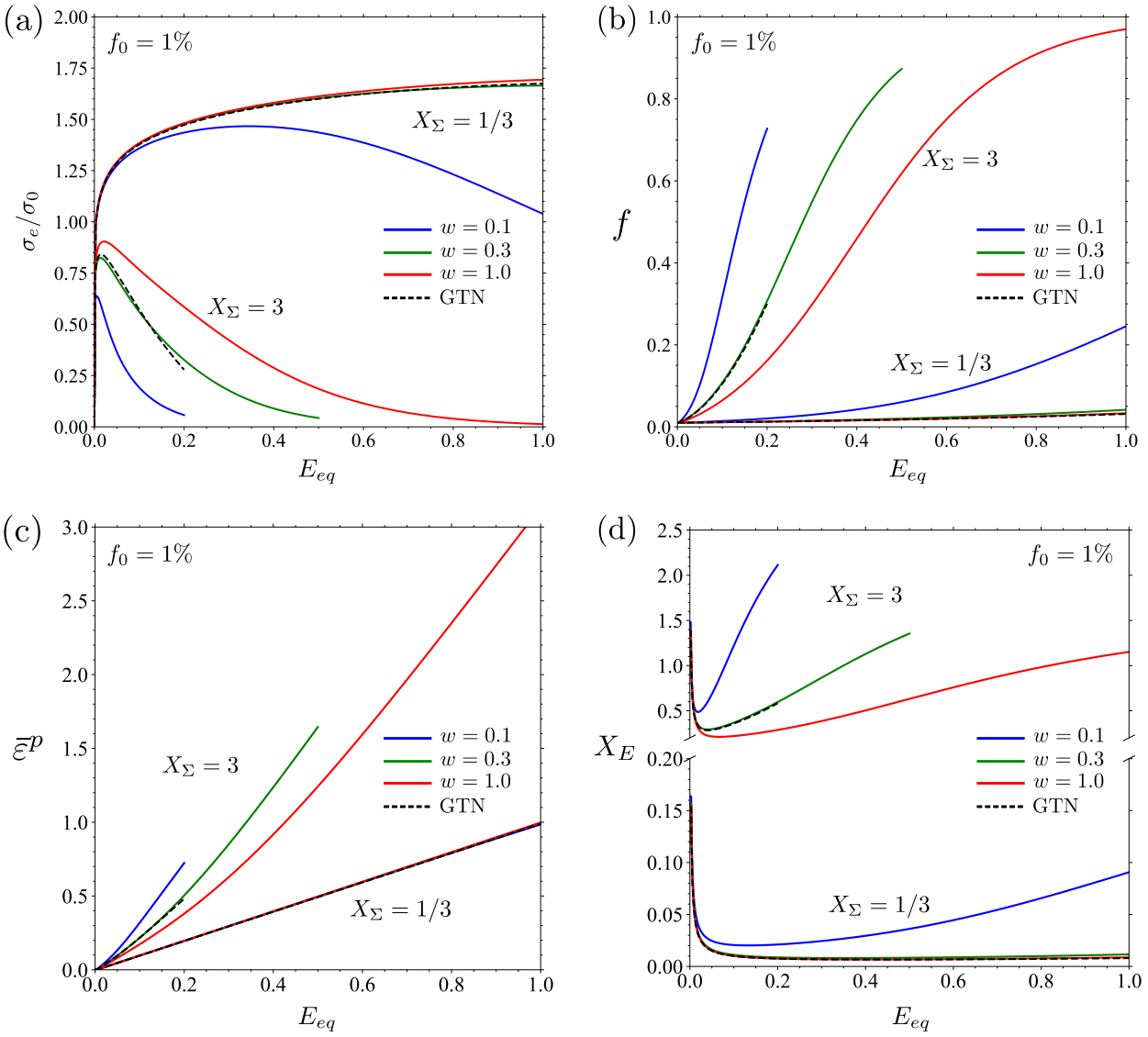

Figure 3.8 – Results from microstructural evolution calculations regarding the effective elastic-plastic response as predicted by the proposed homogenization model showcasing the effect of the aspect ratio parameter. Plots of (a) the normalized von Mises stress σ_e/σ_0, (b) porosity f, (c) equivalent plastic strain $\bar{\varepsilon}^p$, and (d) strain triaxiality X_E are shown for different values of the aspect ratio w both at low and high stress triaxialities. The dashed black line corresponds to the predictions of the isotropic GTN model with $q_1 = 1.5$, $q_2 = 1$, and $q_3 = q_1^2 = 2.25$.

evolves rapidly to extremely large values for all w, and increases faster at lower strain levels for oblate voids with smaller aspect ratios. On the other hand, at a stress triaxiality of $X_\Sigma = 1/3$, the response appears almost insensitive to the aspect ratio for spherical and oblate voids with an aspect ratio $w = 0.3$, whereas a fast increase of porosity is predicted for $w = 0.1$. The latter leads to a substantial drop in the corresponding stress-strain response as shown in Fig. 3.8a. This observation suggests that the initial void shape alone is a predominant variable and can induce local softening even at loads with a *small hydrostatic component*. This effect is highly nonlinear with respect to w and tends to become stronger for $w < 0.5$.

Figures 3.8c,d show the evolution of the equivalent plastic strain and strain triaxiality.

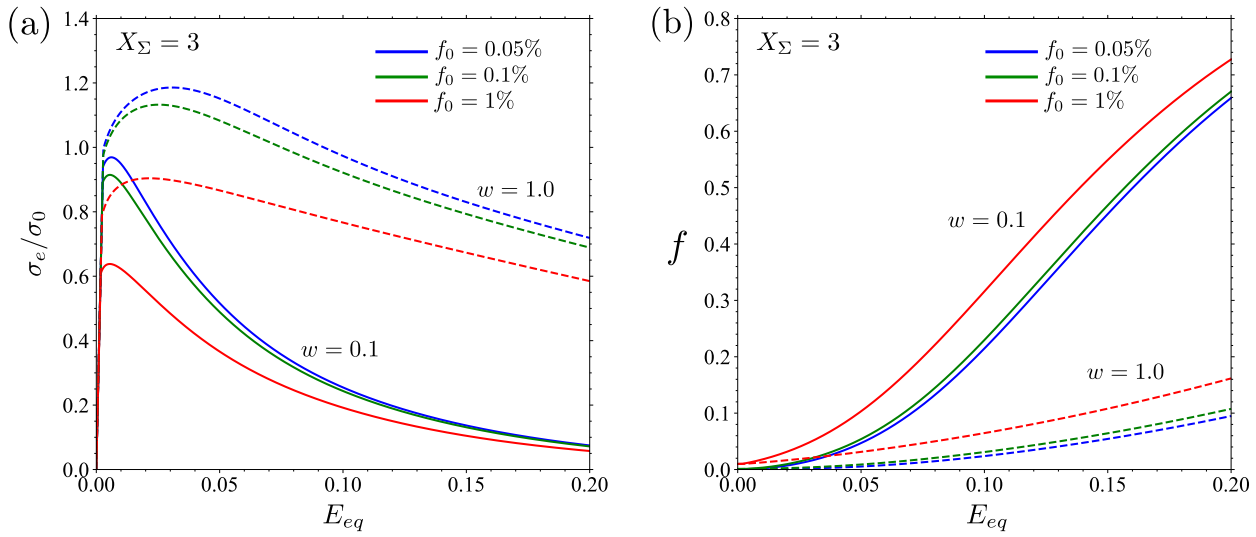

Figure 3.9 – Results from microstructural evolution calculations regarding the effective elastic-plastic response as predicted by the proposed model showcasing the effect of initial porosity. Plots of (a) the normalized von Mises stress σ_e/σ_0 and (b) porosity f are shown for different values of initial porosity f_0 at a high stress triaxiality $X_\Sigma = 3$. Solid lines correspond to an aspect ratio of $w = 0.1$ and dashed lines with same color correspond to respective initial porosity with $w = 1$.

For a stress triaxiality of $X_\Sigma = 3$, the aspect ratio w does affect the accumulated plastic strain in the matrix, whereas this effect becomes stronger for lower values of w. Also, strain triaxiality reaches higher values at lower overall strains as the void aspect ratio decreases, thus indicating that very high dilatational strains develop for microstructures containing flat oblate voids. At a low stress triaxiality of $X_\Sigma = 1/3$, the aspect ratio does not affect the equivalent plastic strain in the matrix, whereby higher strain triaxiality is only obtained for the case of $w = 0.1$, which is consistent with the corresponding porosity evolution shown in Fig. 3.8b.

It is also interesting to note that the predictions of the GTN model are very close to those of the proposed new model with $w = 0.3$ in the case of the high triaxiality $X_\Sigma = 3$. In turn, at the lower triaxiality of $X_\Sigma = 1/3$, the GTN predictions are close to those of the proposed model with $w = 1$. This indicates that the proposed new model is able to reproduce such results with a variation of only one parameter (the aspect ratio w) that nevertheless incorporates a physical meaning related to the microstructure.

Figures 3.9a,b showcase the effect of initial porosity on the stress-strain response and porosity evolution for the three different initial porosity distributions $f_0 = 0.05\%$, 0.1%, and 1% at a stress triaxiality $X_\Sigma = 3$. Solid lines correspond to microstructures comprising oblate voids with an aspect ratio $w = 0.1$; for reference, microstructures with the same initial volume fractions of spherical voids (i.e., with $w = 1$) are also shown with dashed lines of corresponding color. It can be seen in all cases that for initial porosities 0.05% and 0.1% porosity evolution is relatively the same while a substantial increase in the rate of porosity evolution is observed for an initial porosity $f_0 = 1\%$. As expected, softening response initiates at lower strain levels for very flat oblate voids when compared to spherical voids at the same initial void volume fraction; also, for strain levels above 5%, porosity grows to substantially higher values at corresponding strains and initial porosities for voids with $w = 0.1$. It is interesting to also note that, up to relatively small strains of 2.5%, the effective

response of a material with a microstructure consisting of penny-shaped voids with $w = 0.1$ exhibits similar behavior with a material comprising spherical voids that had 20 times more initial volume fraction in the matrix; this indicates once again the strong effect of the shape parameter in accelerating porosity evolution relative to the initial porosity content.

3.5 Concluding remarks

In the present chapter we employed the numerical 3D RVE homogenization approach as a test bed in order to assess the predictions of the new analytical homogenization model proposed in this study. The modified RSA algorithm of Anoukou et al. (2018) was used to generate unit cells comprising randomly distributed and randomly orientated spheroidal voids of various shapes and initial volume fraction in a von Mises matrix. The cells were loaded at different constant macroscopic stress states under periodic boundary conditions and a convergence study with respect to the number of voids, microstructural realizations and isotropy was carried out. These results from micromechanics calculations were subsequently used to calibrate the analytical model by using a small number of fitting parameters.

The convergence analysis has shown that unit cells with as low as 30 randomly oriented and distributed spheroidal voids are enough to be used as RVEs for the microstructures assumed in this work, exhibiting an effective response sufficiently close to isotropic. Examination of the fields at the level of the voids reveals that higher local plastic strains and stress triaxialities develop in microstructures that consist of low aspect ratio oblate voids compared to ones with almost spherical or spherical voids. Moreover, variation of the effective RVE behavior with the Lode angle was found to be small and thus such a dependence was also neglected in the analytical model. Spherical voids are found to exhibit a higher sensitivity to the Lode angle parameter compared to oblate voids. In any case, if deemed necessary, J_3 dependence can be incorporated either by using more general LCC homogenization estimates or, more easily, through simple heuristic modifications of the present constitutive equations. Using the calibrated model, we have also investigated the effects of microstructural configurations and stress states on the effective response and evolution of microstructure. Material point calculations verify the strong effect of the initial void shape parameter on the effective response; lower aspect ratios lead to increased porosity evolution and softening at both lower and higher stress triaxiality states. Also, the effect of initial porosity content is found to be weaker compared to that of the shape of the microvoids.

CHAPTER 4

Mathematical Issues and Regularization Methods

Chapter summary: In this chapter the computational issues related to the FE implementation of rate-independent constitutive models with softening are discussed in detail and a regularized version of the new isotropic model is proposed. First, a review of the various non-local regularization methods proposed in the context of solid mechanics is given followed by the general definition of a non-local field. Subsequently, we focus our attention to the implicit non-local (gradient) formulation used in this work, which results in an additional PDE for the non-local porosity variable. The constitutive equations presented in Chapter 2 are then modified accordingly resulting in a regularized formulation. The mathematical character of both local and non-local problems is then analyzed in detail. The effects of the non-local formulation on strain localization and post-bifurcation response are numerically investigated using the well-known Rice's localization analysis (Rice, 1976) under plane strain conditions.

Contents

4.1 Introduction to non-local theories

A well-known problem in the finite element implementation of rate-independent constitutive models that can lead to softening behavior is the mesh-dependency of the corresponding numerical solutions. For instance, as it is pointed out in Pijaudier-Cabot and Bažant (1987), implementation of damage and crack propagation simulations using standard continuum mechanics models results in unrealistic failure predictions in the sense that the corresponding material fails immediately slightly after peak load with zero energy dissipation and with deformation localized in a zone of zero width.

From a mechanics perspective, softening behavior suggests a form of *material instability* and is closely related to *strain localization phenomena* that can appear, under certain conditions, within a structure. The term "localization" in the sense of Rice (1976) refers to the emergence of regions of specific size where all further deformation of the structure tends to concentrate (i.e., localize) regardless of the fact that the loading program may remain unaltered. Classical examples of localization phenomena in metals include the formation of '*shear bands* or the process of *void nucleation, growth and coalescence* in ductile fracture with their interaction critically affecting the final failure mode of the structure (Tekoğlu et al., 2015).

This ill-posed behavior is common to all such models (e.g., porous plasticity, continuum damage models etc.) that are based on classical or *local* continuum mechanics formulations and do not incorporate a characteristic length scale (see p. 517 in Jirásek and Bažant (2002)). Local models neglect long-range material point interactions assuming that the fields at any material point of the body depend solely on the loading history at that specific point. Deformation history of the material at any time is then characterized by the current values of the internal variables of the model, excluding higher order gradients that would incorporate non-local effects. In practice, local continuum models are sufficiently accurate to be used in problems where the strain distribution remains smooth (even if it becomes non-homogeneous) and no discontinuities are present.

The mathematical reason for this behavior is the *loss of ellipticity* of the governing partial differential equations (PDEs), which allows for the development of non-smooth solutions, such as shear bands of zero thickness. Since spatially discontinuous velocity gradients can develop only across characteristic surfaces (or curves in 2D) and elliptic problems have no real characteristics, all solutions of elliptic problems are smooth functions (e.g., see p. 135 in Zauderer (2006)); even when non-smooth boundary conditions are used, the elliptic operators smooth out the solution in the interior of the problem domain. In *elliptic* problems, shear bands can still initiate at imperfections and appear as highly strained regions of *finite width* in a *smooth* solution and can be accurately represented by finite element numerical calculations, which converge as the mesh is refined.

In order to overcome the numerical difficulties associated with loss of ellipticity, the governing equations need to be "regularized". In solid mechanics, a solution to overcoming the aforementioned difficulties can be achieved by enhancing the classical models so as to include long-range interactions at all material points. The non-local effects can be incorporated either through differential operators (non-local models of the *gradient* type) or through (weighted) spatial averaged fields (non-local models of the *integral* type). Based on the type of enrichment, non-local theories can be classified into two major groups:

- Theories that enhance the *kinematic equations*, in the sense that they incorporate higher order gradients or non-local averages of the strain field. For instance, the

models proposed by Fleck and co-workers (Fleck and Hutchinson, 1993; Fleck et al., 1994; Fleck and Hutchinson, 1997, 2001), Leblond and co-workers (Bergheau et al., 2014), and Gurtin and co-workers (Gurtin, 2003; Gurtin and Anand, 2005; Gurtin et al., 2010) which fit into the fraimwork laid down in the works of Mindlin (Mindlin, 1964; Mindlin and Eshel, 1968) fall in this category.

- Theories that enhance the *constitutive equations* by considering gradients or non-local averages of the internal variables. Examples of models that fall in this class include the ones proposed by Aifantis (Aifantis, 1984, 1987, 1992, 1999), Bažant and co-workers (Bažant et al., 1984; Bažant and Pijaudier-Cabot, 1988), Leblond et al. (1994a), Needleman and Tvergaard (1998), Peerlings and co-workers (Peerlings et al., 1995, 1996), Geers et al. (2001), Engelen et al. (2003), and more recently Enakoutsa (2014), Papadioti et al. (2019), Aravas and Papadioti (2021).

Several of these non-local models can be recovered by using a more rigorous thermodynamic framework as shown in the work of Forest (2009), based on the ideas of a "micromorphic" medium which was first introduced by Eringen and Suhubl (Eringen and Suhubl, 1964a,b). In the case of gradient non-local theories belonging to the second group, these can be further classified into *explicit* or *implicit* depending on how the higher order gradients of the internal variables are introduced in the formulation. In explicit gradient models, gradients of one or more internal variables enter directly the formulation, for instance in the yield function. In implicit gradient models, higher order gradients are introduced through the definition of one or more non-local fields which satisfy the so-called *modified Helmholtz* partial differential equation, as will be shown in Section 4.2.

In the following, the general definition of a non-local field is given. Let $\mathbf{a}(\mathbf{x})$ be a local field that may represent any quantity of the problem that is meaningful to define a corresponding non-local quantity (i.e., it may refer to strain or any other scalar, vector or tensor internal variable). Then, the corresponding weighted spatial average or non-local average $\mathbf{a}^{\mathrm{nl}}(\mathbf{x})$, of the field $\mathbf{a}(\mathbf{x})$ is defined as (Pijaudier-Cabot and Bažant, 1987; Bažant and Pijaudier-Cabot, 1988):

$$\mathbf{a}^{\mathrm{nl}}(\mathbf{x}) = \frac{1}{W(\mathbf{x})}\int_{\mathcal{V}} g(\mathbf{x},\mathbf{y})\mathbf{a}(\mathbf{y})d\mathcal{V}(\mathbf{y}) \qquad \text{with} \qquad W(\mathbf{x}) = \int_{\mathcal{V}} g(\mathbf{x},\mathbf{y})d\mathcal{V}(\mathbf{y}) \tag{4.1}$$

where $g(\mathbf{x},\mathbf{y})$ is a properly selected weight function and $\mathbf{y}$ is the position vector of the infinitesimal material volume $d\mathcal{V}(\mathbf{y})$. The weight function g is usually of the Gaussian type and can be stated in the general form (see p. 10 in Rolshoven (2003)):

$$g(\mathbf{x},\mathbf{y}) = \frac{1}{c^G}\exp\left(-\frac{|\mathbf{x}-\mathbf{y}|^2}{2\ell^2}\right) \qquad \text{where} \qquad c^G = \begin{cases} (2\pi)^{1/2}\ell & \text{for 1D} \\ 2\pi\ell^2 & \text{for 2D} \\ (2\pi)^{3/2}\ell^3 & \text{for 3D} \end{cases} \tag{4.2}$$

with ℓ being a constant with *dimensions of length* which is referred to as the "characteristic length". It should be noted here that, the normalizing factor W in $(4.1)_2$ is defined in such a way so that as $\ell \to 0$ or for a homogeneous local field variable, the non-local formulation reduces to the local one. Non-local models that fit in the formalism defined by (4.1) are considered *strongly non-local* in the sense that the non-local variable is calculated using information from all material points included in the domain $\mathcal{V}$ of integration.

It should be noted that the characteristic length ℓ is a calibration parameter introduced by the non-local formulation and is identified with reference to a microstructural dimension (e.g., several times the grain size in a polycrystal material or the void spacing in a voided material). In the context of continuum damage mechanics, various calibration methods have been proposed in the literature for the estimation of the characteristic material length. For instance, energetic approaches (Bažant and Pijaudier-Cabot, 1989), inverse calibration based on experimental or numerical structural results (Bellégo et al., 2003; Jiràsek et al., 2004; Iacono et al., 2006) and more recently the use of surface roughness experimental measurements for quasi-brittle materials (Xenos et al., 2015) have been proposed.

4.2 The implicit non-local Isotropic Projection model

4.2.1 Definition of the non-local porosity

The ideas of Peerlings and co-workers (Peerlings et al., 1995, 1996), Geers et al. (2001), and Engelen et al. (2003) are used to define the "non-local" porosity field $f^{\mathrm{nl}}(\mathbf{x})$ in terms of the "local" porosity field $f(\mathbf{x})$. At any given material point with current position $\mathbf{x}$, the non-local porosity $f^{\mathrm{nl}}(\mathbf{x})$ is defined as the average value of the local porosity $f(\mathbf{x})$ over a sphere $\Omega_R(\mathbf{x})$ of radius R centered at $\mathbf{x}$:

$$f^{\mathrm{nl}}(\mathbf{x}) \equiv \frac{1}{\mathcal{V}} \int\limits_{\Omega_R(\mathbf{x})} f(\mathbf{y})\, d\mathcal{V}(\mathbf{y}), \tag{4.3}$$

where $\mathcal{V} = 4\,\pi\,R^3/3$ is the volume of Ω_R. The radius R can be identified with a microstructural dimension (e.g., a few times the average grain size in a metal). The expression used in (4.3) to define the non-local porosity is different from the corresponding definition (4.1) in that i) it involves a volume integral in the neighborhood of the point under consideration (as opposed to an integral over the whole body) and ii) the weight function used in (4.3) equals unity (i.e., a volume average is calculated locally instead of a weighted-average). However, this definition proves useful for establishing a physical interpretation of the "characteristic length" that naturally appears in the formulation as will be discussed in the following. It is shown next that the non-local porosity defined in (4.3) satisfies the so-called modified Helmholtz equation to a first approximation.

If $f(\mathbf{y})$ is a smooth function of position, use of a Taylor series expansion around $\mathbf{x}$ in (4.3) yields

$$\begin{aligned} f^{\mathrm{nl}}(\mathbf{x}) = f(\mathbf{x}) &+ \frac{1}{\mathcal{V}} \frac{\partial f(\mathbf{x})}{\partial x_i} \int\limits_{\Omega_R(\mathbf{x})} (y_i - x_i)\, d\mathcal{V}(\mathbf{y}) + \\ &+ \frac{1}{2!\,\mathcal{V}} \frac{\partial^2 f(\mathbf{x})}{\partial x_i\, \partial x_j} \int\limits_{\Omega_R(\mathbf{x})} (y_i - x_i)\,(y_j - x_j)\, d\mathcal{V}(\mathbf{y}) + \\ &+ \frac{1}{3!\,\mathcal{V}} \frac{\partial^3 f(\mathbf{x})}{\partial x_i\, \partial x_j\, \partial x_k} \int\limits_{\Omega_R(\mathbf{x})} (y_i - x_i)\,(y_j - x_j)\,(y_k - x_k)\, d\mathcal{V}(\mathbf{y}) + \\ &+ \frac{1}{4!\,\mathcal{V}} \frac{\partial^4 f(\mathbf{x})}{\partial x_i\, \partial x_j\, \partial x_k\, \partial x_q} \int\limits_{\Omega_R(\mathbf{x})} (y_i - x_i)\,(y_j - x_j)\,(y_k - x_k)\,(y_q - x_q)\, d\mathcal{V}(\mathbf{y}) + \cdots, \end{aligned} \tag{4.4}$$

where the summation convention is used on repeated Latin indices. Let (r, θ, ϕ) be spherical coordinates with origin at $\mathbf{x}$. Then, $d\mathcal{V} = r^2 \sin\theta \, dr \, d\theta \, d\phi$ and

$$y_1 - x_1 = r\cos\phi \, \sin\theta, \qquad y_2 - x_2 = r \sin\phi \, \sin\theta, \qquad y_3 - x_3 = r\cos\theta, \tag{4.5}$$

$$\int\limits_{\Omega_R(\mathbf{x})} A(r,\theta,\phi)\, d\mathcal{V} = \int\limits_{\phi=0}^{2\pi} \left\{ \int\limits_{\theta=0}^{\pi} \left[\int\limits_{r=0}^{R} A(r,\theta,\phi)\, r^2 \, dr \right] \sin\theta \, d\theta \right\} d\phi, \tag{4.6}$$

where $A(r, \theta, \phi)$ is an arbitrary function. Substitution of (4.5) and (4.6) into (4.4) and a lengthy but straightforward evaluation of the integrals lead to the following expression (see also Mühlhaus and Alfantis (1991)):

$$f^{\mathrm{nl}}(\mathbf{x}) = f(\mathbf{x}) + \ell^2 \, \nabla^2 f(\mathbf{x}) + O(\ell^4 \, \nabla^4 f), \tag{4.7}$$

where

$$\ell = \frac{R}{\sqrt{10}} = 0.316\, R \qquad \text{or} \qquad R = \ell\,\sqrt{10} = 3.162\,\ell\,.$$

Equation (4.7) shows that the quantity $\ell^2 \, \nabla^2 f$ is, to leading order, a measure of the difference between the local value f and the neighborhood average f^{nl}. Also, equation (4.7) implies that

$$\ell^2 \, \nabla^2 f^{\mathrm{nl}}(\mathbf{x}) = \ell^2 \, \nabla^2 f(\mathbf{x}) + O(\ell^4 \, \nabla^4 f). \tag{4.8}$$

Combination of (4.8) and (4.7) leads to

$$f^{\mathrm{nl}}(\mathbf{x}) - \ell^2 \, \nabla^2 f^{\mathrm{nl}}(\mathbf{x}) = f(\mathbf{x}) + O(\ell^4 \, \nabla^4 f). \tag{4.9}$$

If terms of order $\ell^4 \, \nabla^4 f$ or smaller are ignored, equations (4.7) and (4.9) can be thought of as PDEs that define $f^{\mathrm{nl}}(\mathbf{x})$ in terms of $f(\mathbf{x})$ and vice versa. In the following, the assumption is made that terms of $O(\ell^4 \, \nabla^4 f)$ are negligible. It is also assumed that the normal derivative of the non-local porosity $\partial f^{\mathrm{nl}}/\partial n$ vanishes on the boundary of the elastoplastic body. Then, the non-local porosity field $f^{\mathrm{nl}}(\mathbf{x})$ can be determined in terms of the local quantity $f(\mathbf{x})$ by the following boundary value problem (BVP):

$$f^{\mathrm{nl}} - \ell^2 \, \nabla^2 f^{\mathrm{nl}} = f \qquad \text{in} \quad \Omega \tag{4.10}$$

$$\frac{\partial f^{\mathrm{nl}}}{\partial n} \equiv \mathbf{n} \cdot \nabla f^{\mathrm{nl}} = 0 \qquad \text{on} \quad \partial\Omega, \tag{4.11}$$

where Ω is the domain occupied by the elastoplastic body in the deformed configuration, $\partial\Omega$ its boundary, and $\mathbf{n}$ the unit outward normal vector to $\partial\Omega$. Equation (4.10) is sometimes referred to as the *modified Helmholtz equation*.

It is emphasized that the BVP (4.10)–(4.11) is solved in the *entire problem domain* Ω of the elastoplastic body and not just inside the plastic zone; i.e., the BVP (4.10)–(4.11) defines the non-local porosity $f^{\mathrm{nl}}(\mathbf{x})$ everywhere in Ω and not just inside the plastic zone (Peerlings et al., 2001; Engelen et al., 2003). Also, the homogeneous boundary condition (4.11) guarantees that the "total values" of f^{nl} and f in Ω coincide, i.e.,

$$\int\limits_{\Omega} f^{\mathrm{nl}} \, d\Omega = \int\limits_{\Omega} f \, d\Omega. \tag{4.12}$$

It should be noted that more general, non-homogeneous Neumann boundary conditions can be used, in which the flux $\partial f^{\mathrm{nl}}/\partial n$ in (4.11) can take non-zero values on the boundary $\partial\Omega$. If the physical problem is such that it is acceptable, Dirichlet boundary conditions could also be considered. The form of the boundary conditions in (4.11) however does not affect the mathematical character of the problem.

In the non-local constitutive model presented in the following section, the non-local porosity $f^{\mathrm{nl}}(\mathbf{x})$ is defined from the solution of the BVP (4.10)–(4.11), as opposed to equation (4.3). The derivation of (4.10) clearly shows that the non-local porosity $f^{\mathrm{nl}}(\mathbf{x})$ defined by the BVP (4.10)–(4.11) is essentially the *average value of the local porosity* $f(\mathbf{x})$ *over a sphere of radius* $R = \sqrt{10}\,\ell = 3.16\,\ell \cong 3\,\ell$ *centered at* $\mathbf{x}$. Obviously, this interpretation breaks down for material points near the boundary $\partial\Omega$, where part of the material sphere of radius R centered at the point under consideration lies outside the domain Ω occupied by the elastoplastic body. Also, as pointed out by Huerta and Pijaudier-Cabot (1994), in regions of very steep gradients, where terms $O(\ell^4\,\nabla^4 f)$ may not be negligible, the above interpretation is not valid.

In the case of two dimensional problems, similar calculations lead to the conclusion that the non-local porosity $f^{\mathrm{nl}}(\mathbf{x})$ in (4.10) is essentially the average value of the local porosity f over a *circle* of radius $R = 2\sqrt{2}\,\ell = 2.83\,\ell \cong 3\,\ell$ centered at $\mathbf{x}$.

Remark 10. The modified Helmholtz equation (4.10) has also been derived by Forest (2009) using his micromorphic approach. In particular, if the free energy density is assumed to be a quadratic function of the "relative porosity" $f - f^{\mathrm{nl}}$ and the gradient of the non-local porosity ∇f^{nl}, the generalized balance of micromomentum in isotropic materials leads to the modified Helmholtz equation (4.10) (see p. 119 in Forest (2009)).

4.2.2 Non-local formulation of the Isotropic Projection model

In the implicit non-local (gradient) version of the Isotropic Projection model, following Aravas and Papadioti (2021), it is proposed that the local porosity f be replaced with its non-local counterpart f^{nl} in the calculation of the incremental effective elastic moduli (κ, μ), the plastic coefficients $(m_{\mathcal{K}}, m_{\mathcal{J}})$ as well as in the homogenized yield function Φ. In this case, the non-local porosity f^{nl} is calculated in terms of the local porosity f from the coupled solution of the BVP (4.10)–(4.11) along with the usual static (or dynamic) equilibrium equations. The formulation is outlined in the following.

The homogenized elastic behavior of the porous material is still described by a hypoelastic constitutive equation of the form (2.45) with the difference that the fourth-order isotropic effective elastic compliance tensor $\boldsymbol{\mathcal{M}}$ now depends on the non-local porosity f^{nl} instead of the local f, i.e.,

$$\mathbf{D}^e = \boldsymbol{\mathcal{M}} : \overset{\nabla}{\boldsymbol{\sigma}}, \quad \boldsymbol{\mathcal{M}} = \frac{1}{2\,\mu}\boldsymbol{\mathcal{K}} + \frac{1}{3\,\kappa}\boldsymbol{\mathcal{J}}, \quad \frac{1}{3\,\kappa} = \frac{1}{3}\mathcal{M}^{\mathtt{w}}_{iijj} \quad \text{and} \quad \frac{1}{2\,\mu} = \frac{1}{5}\left(\mathcal{M}^{\mathtt{w}}_{ijij} - \frac{1}{3\,\kappa}\right) \tag{4.13}$$

where

$$\boldsymbol{\mathcal{M}}^{\mathtt{w}}(\mu_{\mathtt{m}}, \kappa_{\mathtt{m}}, \nu_{\mathtt{m}}, f^{\mathrm{nl}}, w, \mathbf{n}^{(i)}) = \frac{1}{2\,\mu_{\mathtt{m}}}\boldsymbol{\mathcal{K}} + \frac{1}{3\,\kappa_{\mathtt{m}}}\boldsymbol{\mathcal{J}} + \frac{f^{\mathrm{nl}}}{(1-f^{\mathrm{nl}})\mu_{\mathtt{m}}}\boldsymbol{\mathcal{Q}}^{-1}(\nu_{\mathtt{m}}, w, \mathbf{n}^{(i)}), \tag{4.14}$$

The yield function of the non-local model is now also defined explicitly by substituting the local porosity f with the corresponding non-local porosity f^{nl} in equations (2.50)–(2.51)

and (2.58), i.e.,

$$\Phi(\sigma_e, p, \bar{\varepsilon}^p, f^{\rm nl}, w) = \frac{1}{3\,m_{\mathcal{K}}(f^{\rm nl}, w)}\left(\frac{\sigma_e}{\sigma_y}\right)^2 + \\ + \frac{4}{9\,m_{\mathcal{J}}(f^{\rm nl}, w)}\left[(1-\alpha(f^{\rm nl}, w))\,q^2_{\mathcal{J}}(f^{\rm nl})\left(\frac{3\,p}{2\,\sigma_y}\right)^2 + 2\,\alpha(f^{\rm nl}, w)\left(\cosh\frac{3\,p}{2\,\sigma_y} - 1\right)\right] - \\ - (1 - f^{\rm nl}). \tag{4.15}$$

with

$$\frac{1}{3\,m_{\mathcal{J}}(f^{\rm nl}, w)} = \frac{1}{3}m^{\mathtt{w}}_{iijj}, \qquad \frac{1}{2\,m_{\mathcal{K}}(f^{\rm nl}, w)} = \frac{1}{5}\left(m^{\mathtt{w}}_{ijij} - \frac{1}{3\,m_{\mathcal{J}}}\right), \qquad q_{\mathcal{J}}(f^{\rm nl}) = \frac{1 - f^{\rm nl}}{\sqrt{f^{\rm nl}}\,\ln\frac{1}{f^{\rm nl}}}. \tag{4.16}$$

As is the case in the corresponding local model, the effective homogenized coefficients $(m_{\mathcal{K}}, m_{\mathcal{J}})$ result from the isotropic projection of the microstructural fourth-order tensor $\mathbb{m}^{\mathtt{w}}$ which is now assumed to depend on the non-local porosity $f^{\rm nl}$, i.e.,

$$\mathbb{m}^{\mathtt{w}}(f^{\rm nl}, w) = \frac{3}{2}\boldsymbol{\mathcal{K}} + \frac{3f^{\rm nl}}{1 - f^{\rm nl}}\boldsymbol{\mathcal{Q}}^{-1}(1/2, w), \tag{4.17}$$

The plastic part of the rate-of-deformation tensor $\mathbf{D}^p$ in the non-local model is given by an associated flow rule as in (2.60)

$$\mathbf{D}^p = \dot{\lambda}\,\mathbf{N}, \qquad \mathbf{N} \equiv \frac{\partial\Phi}{\partial\boldsymbol{\sigma}} = \frac{3}{2\,\sigma_e}\frac{\partial\Phi}{\partial\sigma_e}\mathbf{s} + \frac{1}{3}\frac{\partial\Phi}{\partial p}\boldsymbol{\delta}, \tag{4.18}$$

The derivatives $\partial\Phi/\partial\sigma_e$ and $\partial\Phi/\partial p$ are calculated from (4.15) and now depend on the non-local porosity $f^{\rm nl}$:

$$\frac{\partial\Phi}{\partial\sigma_e} = \frac{2}{3\,m_{\mathcal{K}}(f^{\rm nl}, w)}\frac{\sigma_e}{\sigma_y^2}, \qquad \frac{\partial\Phi}{\partial p} = \frac{4}{3\,m_{\mathcal{J}}(f^{\rm nl}, w)}\frac{1}{\sigma_y}\left[(1-\alpha)q^2_{\mathcal{J}}(f^{\rm nl}, w)\frac{3\,p}{2\,\sigma_y} + \alpha\sinh\left(\frac{3\,p}{2\,\sigma_y}\right)\right]. \tag{4.19}$$

As in the local model, only two variables evolve during plastic flow in the non-local model; the accumulated plastic strain $\bar{\varepsilon}^p$ and the *local* porosity f. The corresponding evolution equations are of the same form as (2.62) and (2.63) the only difference being that the local porosity f is substituted with its non-local counterpart $f^{\rm nl}$ in the right-hand side of the aforementioned expressions, i.e.,

$$\dot{\bar{\varepsilon}}^p = \frac{\boldsymbol{\sigma} : \mathbf{D}^p}{(1 - f^{\rm nl})\sigma_y(\bar{\varepsilon}^p)} = \dot{\lambda}\frac{\boldsymbol{\sigma} : \mathbf{N}}{(1 - f^{\rm nl})\sigma_y(\bar{\varepsilon}^p)} \equiv \dot{\lambda}\,g_{\bar{\varepsilon}^p}. \tag{4.20}$$

$$\dot{f} = (1 - f^{\rm nl})D^p_{kk} = \dot{\lambda}(1 - f^{\rm nl})N_{kk} \equiv \dot{\lambda}\,g_f. \tag{4.21}$$

The "plastic multiplier", $\dot{\lambda} \geq 0$ of the implicit non-local model is determined from the "consistency condition" $\dot{\Phi} = 0$ by using expression (4.15) instead of (2.58); as will be seen in the upcoming sections, this difference ultimately affects the mathematical character of the governing equations in the non-local formulation.

4.2.3 The non-local elastic-plastic tangent modulus

In the case of the non-local model, the consistency condition $\dot{\Phi} = 0$ is written using (4.15) as

$$\dot{\Phi} = \frac{\partial \Phi}{\partial \boldsymbol{\sigma}} : \overset{\nabla}{\boldsymbol{\sigma}} + \frac{\partial \Phi}{\partial \bar{\varepsilon}^p} \dot{\bar{\varepsilon}}^p + \frac{\partial \Phi}{\partial f^{\mathrm{nl}}} \dot{f}^{\mathrm{nl}} = \mathbf{N} : (\boldsymbol{\mathcal{L}} : \mathbf{D} - \dot{\lambda}\, \boldsymbol{\mathcal{L}} : \mathbf{N}) + \dot{\lambda} \frac{\partial \Phi}{\partial \bar{\varepsilon}^p} g_{\bar{\varepsilon}^p} + \frac{\partial \Phi}{\partial f^{\mathrm{nl}}} \dot{f}^{\mathrm{nl}} = 0$$

where $(2.64)_1$ and (2.62) have been taken into account. Last equation yields

$$\dot{\lambda} = \frac{1}{L^{\mathrm{nl}}} \left(\mathbf{N} : \boldsymbol{\mathcal{L}} : \mathbf{D} + \frac{\partial \Phi}{\partial f^{\mathrm{nl}}} \dot{f}^{\mathrm{nl}} \right), \quad \text{where} \quad L^{\mathrm{nl}} = \mathbf{N} : \boldsymbol{\mathcal{L}} : \mathbf{N} + H^{\mathrm{nl}} \quad \text{with} \quad H^{\mathrm{nl}} = -\frac{\partial \Phi}{\partial \bar{\varepsilon}^p} g_{\bar{\varepsilon}^p}. \tag{4.22}$$

where the derivatives $\partial\Phi/\partial\bar{\varepsilon}^p$ and $\partial\Phi/\partial f^{\mathrm{nl}}$ can be calculated from (4.15). Substitution of $(4.22)_1$ in equation $(2.64)_1$ yields the elasto-plastic tangent modulus $\boldsymbol{\mathcal{L}}^{\mathrm{nl}}$ for the non-local model, which reads

$$\overset{\nabla}{\boldsymbol{\sigma}} = \boldsymbol{\mathcal{L}}^{\mathrm{nl}} : \mathbf{D} + \mathbf{A} \dot{f}^{\mathrm{nl}}, \quad \boldsymbol{\mathcal{L}}^{\mathrm{nl}} = \boldsymbol{\mathcal{L}} - \frac{1}{L^{\mathrm{nl}}} (\boldsymbol{\mathcal{L}} : \mathbf{N})(\boldsymbol{\mathcal{L}} : \mathbf{N}), \quad \mathbf{A} = -\frac{1}{L^{\mathrm{nl}}} \frac{\partial \Phi}{\partial f^{\mathrm{nl}}} \boldsymbol{\mathcal{L}} : \mathbf{N}. \tag{4.23}$$

Also, expression $(4.22)_1$ for the plastic multiplier can be substituted in the evolution equations $(4.20)_3$ and $(4.21)_3$ (i.e., in $\dot{\bar{\varepsilon}}^p = \dot{\lambda} g_{\bar{\varepsilon}^p}$ and $\dot{f} = \dot{\lambda} g_f$) yielding

$$\dot{\bar{\varepsilon}}^p = \mathbf{C}^{\mathrm{nl}} : \mathbf{D} + M \dot{f}^{\mathrm{nl}} \qquad \text{where} \qquad \mathbf{C}^{\mathrm{nl}} = \frac{g_{\bar{\varepsilon}^p}}{L^{\mathrm{nl}}} \boldsymbol{\mathcal{L}} : \mathbf{N}, \qquad M = \frac{g_{\bar{\varepsilon}^p}}{L^{\mathrm{nl}}} \frac{\partial \Phi}{\partial f^{\mathrm{nl}}}. \tag{4.24}$$

$$\dot{f} = \mathbf{B}^{\mathrm{nl}} : \mathbf{D} + K \dot{f}^{\mathrm{nl}} \qquad \text{where} \qquad \mathbf{B}^{\mathrm{nl}} = \frac{g_f}{L^{\mathrm{nl}}} \boldsymbol{\mathcal{L}} : \mathbf{N}, \qquad K = \frac{g_f}{L^{\mathrm{nl}}} \frac{\partial \Phi}{\partial f^{\mathrm{nl}}}. \tag{4.25}$$

Using equations $(2.65)_3$ and $(4.22)_3$, the hardening modulus H^{nl} of the non-local model can be written in terms of the corresponding hardening modulus of the local model H^{loc} as

$$H^{\mathrm{nl}} = H^{\mathrm{loc}} + \frac{\partial \Phi}{\partial f} g_f. \tag{4.26}$$

where $\partial\Phi/\partial f > 0$ and $\partial\Phi/\partial\bar{\varepsilon}^p < 0$ as mentioned in Subsection 2.3.4. Examination of equations $(4.22)_3$ and (4.26) leads to two results which will be useful in the discussion of the mathematical character of the governing equations in the case of the non-local formulation; the former implies that during plastic loading (i.e., when $g_{\bar{\varepsilon}^p} > 0$) for a material with a strain hardening matrix, the hardening modulus of the corresponding non-local model *is always positive*. The latter shows that the hardening modulus H^{nl} *is always larger* than that of the associated local model H^{loc} for loading programs where the local porosity increases (i.e., when $g_f > 0$).

4.3 Mathematical character of the governing equations

In this section we examine the mathematical character of the incremental (or rate) quasi-static elastic-plastic problem for the local and implicit non-local isotropic projection models. The mathematical character of the problem determines whether the solution can have spatial discontinuities. For example, in second order PDEs, continuous weak solutions may have discontinuous first derivatives across characteristic surfaces (or curves in two dimensions) (e.g.,

see p. 347 in Zauderer (2006)). Elliptic equations have no real characteristics. Therefore, in elliptic problems, any boundary data discontinuities must be confined to the boundary and the interior solutions are smooth; this excludes, for example, the formation of "shear bands" with zero thickness in elliptic problems. We note that all quasi-static problems of infinitesimal linear elastostatics have smooth solutions, since the corresponding governing equations are known to be elliptic (e.g., see p. 128 in Fraeijs de Veubeke (1979)). When the material deforms plastically, the equations may lose ellipticity and become hyperbolic; in such cases, the development of weak solutions with discontinuous gradients becomes possible.

4.3.1 The local problem

We consider the velocity field $\mathbf{v}$ as the primary unknown of the quasi-static elastoplastic incremental problem. Let $\mathbf{v}(\mathbf{x},t)$ and $\boldsymbol{\sigma}(\mathbf{x},t)$ be the Eulerian description of the velocity and stress fields respectively, where $\mathbf{x}$ is position of a material point in the deformed configuration and t is a time-like parameter. The corresponding primary equations are the incremental equilibrium equations, which, in the absence of body forces, can be written in the form (e.g., see Appendix A in Aravas and Papadioti (2021))

$$\frac{\partial \dot{\sigma}_{ij}}{\partial x_j} - \frac{\partial \sigma_{iq}}{\partial x_p}\frac{\partial v_p}{\partial x_q} = 0 \qquad \text{or} \qquad \frac{\partial}{\partial x_j}\left(\overset{\nabla}{\sigma}_{ij} + \mathcal{B}_{ijpq}\frac{\partial v_p}{\partial x_q}\right) - \frac{\partial \sigma_{iq}}{\partial x_p}\frac{\partial v_p}{\partial x_q} = 0, \tag{4.27}$$

where

$$\mathcal{B}_{ijpq}(\boldsymbol{\sigma}) = \frac{1}{2}\left(-\sigma_{ip}\,\delta_{jq} + \sigma_{iq}\,\delta_{jp} + \delta_{ip}\,\sigma_{jq} - \delta_{iq}\,\sigma_{jp}\right) = \mathcal{B}_{jipq} = -\mathcal{B}_{ijqp}. \tag{4.28}$$

The $\mathcal{B}$-terms in $(4.27)_2$ are of order stress, are due to the rotational effects in the stress rate, and appear when the material derivative $\dot{\boldsymbol{\sigma}}$ in $(4.27)_1$ is written in terms of the Jaumann derivative $\overset{\nabla}{\boldsymbol{\sigma}}$.

In continuing plastic flow, the Jaumann stress rate $\overset{\nabla}{\boldsymbol{\sigma}}$ is defined in terms of the spatial gradient of the velocity field $\mathbf{v}$ by equation $(2.66)_1$:

$$\overset{\nabla}{\sigma}_{ij} = \mathcal{L}^{\text{loc}}_{ijpq}\,D_{pq} = \mathcal{L}^{\text{loc}}_{ijpq}\frac{\partial v_p}{\partial x_q}, \tag{4.29}$$

where the symmetry $\mathcal{L}^{\text{loc}}_{ijpq} = \mathcal{L}^{\text{loc}}_{ijqp}$ has been taken into account. Substitution of the last equation into the incremental equilibrium equations $(4.27)_2$ yields the governing equations of the rate problem in terms of the velocity field $\mathbf{v}$:

$$\underbrace{\left(\mathcal{L}^{\text{loc}}_{ijpq} + \mathcal{B}_{ijpq}\right)\frac{\partial^2 v_p}{\partial x_j\,\partial x_q}}_{\text{principal part}} + \left[\frac{\partial}{\partial x_j}\left(\mathcal{L}^{\text{loc}}_{ijpq} + \mathcal{B}_{ijpq}\right) - \frac{\partial \sigma_{iq}}{\partial x_p}\right]\frac{\partial v_p}{\partial x_q} = 0. \tag{4.30}$$

Equations (4.30) define a linear second order system of PDEs for the velocity field $\mathbf{v}$[1]. The *principal part* of the equations involves the terms of the highest derivatives of $\mathbf{v}$ (second order) and can be written in matrix form as

$$\underset{3\times 3}{\left[\hat{\mathbf{P}}\right]}\,\underset{3\times 1}{\{\mathbf{v}\}} = \underset{3\times 1}{\{\mathbf{0}\}}, \qquad \text{where} \qquad \hat{P}_{ip} = \left(\mathcal{L}^{\text{loc}}_{jipq} + \mathcal{B}_{jipq}\right)\frac{\partial^2}{\partial x_j\,\partial x_q}\,. \tag{4.31}$$

[1]The possible non-linearity in the constitutive equation due to neutral loading or elastic unloading is not considered here. This is equivalent to using the "linear comparison solid" introduced by Hill (1958).

To form the *matrix symbol* $[\mathbf{\Lambda}^{pr}]$ of the principal part of the system, the partial derivatives $\partial/\partial x_p$ are replaced by the Fourier variables $i\,\xi_p$ in the operator matrix $[\hat{\mathbf{P}}]$, where $i=\sqrt{-1}$ is the imaginary unit (e.g., see p. 215 in Joseph and Saut (1990) and p. 43 in Renardy and Rogers (2004)). This leads to the following matrix with quadratic entries in the real variables ξ_p:

$$\underset{3\times3}{[\mathbf{\Lambda}^{\rm pr}]} \equiv -\underset{3\times3}{[\mathbf{P}]}, \qquad \text{where} \qquad P_{ip}=\left(\mathcal{L}^{\rm loc}_{jipq}+\mathcal{B}_{jipq}\right)\xi_j\,\xi_q. \tag{4.32}$$

The system of equations is elliptic when the determinant of $[\mathbf{\Lambda}^{pr}]$ is non-zero for all real $\boldsymbol{\xi}$; this means that the system of PDEs has no real characteristic surfaces and the solution cannot have discontinuous spatial derivatives (e.g., see p. 135 in Zauderer (2006)). Ellipticity is lost when $\det[\mathbf{\Lambda}^{pr}]=0$, i.e., when

$$\det\left[\left(\mathcal{L}^{\rm loc}_{jipq}+\mathcal{B}_{jipq}\right)\xi_j\,\xi_q\right]=0 \quad \text{for some real vector} \quad \boldsymbol{\xi}\neq\mathbf{0}. \tag{4.33}$$

The loss of ellipticity condition (4.33) can be written in the equivalent form

$$\det\left[n_j\left(\mathcal{L}^{\rm loc}_{jipq}+\mathcal{B}_{jipq}\right)n_q\right]\equiv\det\left[\mathbf{n}\cdot\left(\boldsymbol{\mathcal{L}}^{\rm loc}+\boldsymbol{\mathcal{B}}\right)\cdot\mathbf{n}\right]=0 \quad \text{for some } \textit{unit} \text{ vector } \mathbf{n} \tag{4.34}$$

where $\boldsymbol{\mathcal{L}}^{\rm loc}$ is defined in $(2.66)_2$ and $\boldsymbol{\mathcal{B}}$ is defined in (4.28).

It should be noted that in elastic-plastic problems of metallic materials, the governing incremental equations are initially elliptic, and ellipticity is first lost at the earliest stage of deformation history at which (4.34) is satisfied. As discussed at the end of Section 2.3.4 since the hardening modulus $H^{\rm loc}$ of the local model is a decreasing function of porosity it reduces gradually as the material deforms plastically and porosity increases. The elastic-plastic tangent moduli $\mathcal{L}^{\rm loc}_{ijkl}$ also change, and at some stage of the deformation history an $\mathbf{n}$ may exist so that (4.34) is satisfied and ellipticity is lost. Rice (1976) showed that, when condition (4.34) is satisfied for some unit vector $\mathbf{n}$, the corresponding value of the hardening modulus is (see also Appendix B in Aravas and Papadioti (2021))

$$H^{\rm loc}=-\mathbf{N}:\boldsymbol{\mathcal{L}}^{\rm loc}:\mathbf{N}+[\mathbf{n}\cdot(\boldsymbol{\mathcal{L}}:\mathbf{N})]\cdot[\mathbf{n}\cdot(\boldsymbol{\mathcal{L}}+\boldsymbol{\mathcal{B}})\cdot\mathbf{n})]^{-1}\cdot[\mathbf{n}\cdot(\boldsymbol{\mathcal{L}}:\mathbf{N})]. \tag{4.35}$$

The right hand side of (4.35) defines the value of the hardening modulus $H^{\rm loc}$ when ellipticity of the governing equations is lost. Determination of the orientation $\mathbf{n}$ that maximizes the right hand side of (4.35) defines the "critical" value $H^{\rm loc}_{\rm cr}$ of the hardening modulus, i.e., the maximum possible value of the hardening modulus $H^{\rm loc}$ at which ellipticity is lost for the first time (Rudnicki and Rice, 1975; Stören and Rice, 1975; Bigoni and Hueckel, 1991). Rice (1976) used (4.35) to prove that, if the following three conditions are satisfied:

i. $\boldsymbol{\mathcal{L}}^{\rm loc}$ is of the form $(2.66)_2$ ("normality"),

ii. the incremental elasticity tensor $\boldsymbol{\mathcal{L}}$ is isotropic (equation $(2.64)_2$), and

iii. the rotational effects in the stress rate are neglected ($\boldsymbol{\mathcal{B}}=\mathbf{0}$ in (4.34) and (4.35)),

then the critical hardening modulus is *non-positive*, i.e.,

$$H^{\rm loc}_{\rm cr}\leq 0. \tag{4.36}$$

Therefore, in such a case, the condition $H^{\rm loc}>0$ guarantees the ellipticity of the problem and eliminates the possibility of shear bands.

Remark 11. When (4.34) is satisfied for some $\mathbf{n}$ and ellipticity is lost, the vector $\mathbf{n}$ is normal to the corresponding characteristic surface (or curve in 2D). That is, the characteristic surfaces $\phi(\mathbf{x}) = 0$ of the problem are such that the functions $\phi(\mathbf{x})$ satisfy the equation $\det[(\mathcal{L}^{\rm loc}_{jipq} + \mathcal{B}_{jipq})\frac{\partial\phi}{\partial x_j}\frac{\partial\phi}{\partial x_q}] = 0$.

Remark 12. If rotational effects in the stress rate are neglected in the constitutive equation, i.e., if we replace $\overset{\nabla}{\boldsymbol{\sigma}}$ with $\dot{\boldsymbol{\sigma}}$ in $(2.66)_1$, the loss of ellipticity condition takes the form of equation (4.34) with $\boldsymbol{\mathcal{B}} = \mathbf{0}$.

Remark 13. When the incremental behavior of the material point under consideration is *elastic*, $\boldsymbol{\mathcal{L}}^{\rm loc}$ is replaced by the elasticity tensor $\boldsymbol{\mathcal{L}}$ in (4.34), and the loss of ellipticity condition becomes

$$\det\left[n_j\left(\mathcal{L}_{jipq} + \mathcal{B}_{jipq}\right)n_q\right] \equiv \det\left[\mathbf{n}\cdot\left(\boldsymbol{\mathcal{L}} + \boldsymbol{\mathcal{B}}\right)\cdot\mathbf{n}\right] = 0. \tag{4.37}$$

Since $\boldsymbol{\mathcal{L}}$ is positive definite, it can be readily shown that $\det[n_j\,\mathcal{L}_{jipq}\,n_q] > 0\ \forall\ \mathbf{n}$, and since $\boldsymbol{\mathcal{B}}$ is of order $\boldsymbol{\sigma}$, (4.37) is satisfied only if the stresses become of order elastic modulus, which can never happen in metallic materials. Therefore, when the incremental response of the material point under consideration is elastic, the equations are always elliptic.

Remark 14. Rice (1976) considered a homogeneously and quasi-statically deforming elastic-plastic solid and determined the conditions under which a bifurcation in the form of a planar shear band can develop (continuous velocity field with a jump in the spatial velocity gradient $\partial v_i/\partial x_j$ across the band). He concluded that condition (4.34) (i.e., loss of ellipticity) is a *necessary* condition for such a bifurcation to be possible. This conclusion is consistent with the general mathematical result that discontinuous weak solutions are not possible in elliptic problems, which are known to always have smooth solutions. The aforementioned detailed analysis of planar shear bands does not require additional necessary conditions apart from the general condition of loss of ellipticity, which is known to be required for the development of general discontinuous weak solutions. It should be emphasized that condition (4.34) is *not sufficient* for plastic flow localization. For example, Santisi d'Avila et al. (2016) considered an infinite layered non-linear hyperelastic solid under axial plane strain compression along the lamination direction and showed that there exist homogenized post-bifurcated equilibrium paths with no localization of deformation for macroscopic strains well above the one corresponding to loss of ellipticity.

4.3.2 The implicit non-local problem

The primary unknowns of the quasi-static incremental problem are now the velocity field $\mathbf{v}(\mathbf{x},t)$ and the material derivative of the non-local porosity field $\dot{f}^{\rm nl}(\mathbf{x},t)$. The corresponding primary equations are the incremental form of the equilibrium equations and the equation that results when the material time derivative of the modified Helmholtz equation (4.10) is taken. These equations are (e.g., see Appendix A in Aravas and Papadioti (2021))

$$\frac{\partial}{\partial x_j}\left(\overset{\nabla}{\sigma}_{ij} + \mathcal{B}_{ijpq}\frac{\partial v_p}{\partial x_q}\right) - \frac{\partial\sigma_{iq}}{\partial x_p}\frac{\partial v_p}{\partial x_q} = 0, \tag{4.38}$$

$$\dot{f}^{\rm nl} - \ell^2\left(\nabla^2\dot{f}^{\rm nl} - \frac{\partial f^{\rm nl}}{\partial x_i}\nabla^2 v_i - 2\,\frac{\partial^2 f^{\rm nl}}{\partial x_i\,\partial x_j}\frac{\partial v_i}{\partial x_j}\right) = \dot{f}, \tag{4.39}$$

where $\boldsymbol{\mathcal{B}}$ is defined in (4.28).

The Jaumann derivative of stress $\overset{\nabla}{\boldsymbol{\sigma}}$ and the material derivative of the local porosity field $\dot{f}$ in the non-local model are defined in terms of the primary unknowns $(\mathbf{v}, \dot{f}^{\mathrm{nl}})$ in equations (4.23) and (4.25), which can be written as

$$\overset{\nabla}{\sigma}_{ij} = \mathcal{L}^{\mathrm{nl}}_{ijpq}\, D_{pq} + A_{ij}\, \dot{f}^{\mathrm{nl}} = \mathcal{L}^{\mathrm{nl}}_{ijpq}\, \frac{\partial v_p}{\partial x_q} + A_{ij}\, \dot{f}^{\mathrm{nl}}, \qquad \mathbf{A} = -\frac{1}{L^{\mathrm{nl}}} \frac{\partial \Phi}{\partial f^{\mathrm{nl}}}\, \boldsymbol{\mathcal{L}} : \mathbf{N}$$

$$\dot{f} = B^{\mathrm{nl}}_{ij}\, D_{ij} + K\, \dot{f}^{\mathrm{nl}} = B^{\mathrm{nl}}_{ij}\, \frac{\partial v_i}{\partial x_j} + \frac{g_f}{L^{\mathrm{nl}}} \frac{\partial \Phi}{\partial f^{\mathrm{nl}}}\, \dot{f}^{\mathrm{nl}}, \qquad \mathbf{B}^{\mathrm{nl}} = \frac{g_f}{L^{\mathrm{nl}}} \boldsymbol{\mathcal{L}} : \mathbf{N}.$$

where the symmetries $\mathcal{L}^{\mathrm{nl}}_{ijpq} = \mathcal{L}^{\mathrm{nl}}_{ijqp}$ and $B^{\mathrm{nl}}_{ij} = B^{\mathrm{nl}}_{ji}$ have been taken into account. Substitution of the last two constitutive equations into (4.38) and (4.39) yields the governing equations of the incremental problem for $(\mathbf{v}, \dot{f}^{\mathrm{nl}})$:

$$\underbrace{\left(\mathcal{L}^{\mathrm{nl}}_{ijpq} + \mathcal{B}_{ijpq}\right) \frac{\partial^2 v_p}{\partial x_j\, \partial x_q}}_{\text{principal part}} + \left[\frac{\partial}{\partial x_j}\left(\mathcal{L}^{\mathrm{nl}}_{ijpq} + \mathcal{B}_{ijpq}\right) - \frac{\partial \sigma_{iq}}{\partial x_p}\right] \frac{\partial v_p}{\partial x_q} + \frac{\partial}{\partial x_j}\left(A_{ij}\, \dot{f}^{\mathrm{nl}}\right) = 0, \tag{4.40}$$

$$\underbrace{\left(\ell^2 \frac{\partial f^{\mathrm{nl}}}{\partial x_i}\right) \frac{\partial^2 v_i}{\partial x_j \partial x_j} - \ell^2 \frac{\partial^2 \dot{f}^{\mathrm{nl}}}{\partial x_j \partial x_j}}_{\text{principal part}} - \left(B^{\mathrm{nl}}_{ij} - 2\,\ell^2 \frac{\partial^2 f^{\mathrm{nl}}}{\partial x_i\, \partial x_j}\right) \frac{\partial v_i}{\partial x_j} + \left(1 - \frac{g_f}{L^{\mathrm{nl}}} \frac{\partial \Phi}{\partial f^{\mathrm{nl}}}\right) \dot{f}^{\mathrm{nl}} = 0. \tag{4.41}$$

Equations (4.40) and (4.41) define a linear second order system of PDEs for $\mathbf{v}(\mathbf{x}, t)$ and $\dot{f}^{\mathrm{nl}}(\mathbf{x}, t)$. The principal part of the equations involves the terms with the highest derivatives (second order) of $\mathbf{v}$ and $\dot{f}^{\mathrm{nl}}$, and can be written in matrix form as

$$\begin{bmatrix} \underset{3\times3}{\left[\hat{\mathbf{P}}^{\mathrm{nl}}\right]} & \underset{3\times1}{\{\mathbf{0}\}} \\ \underset{1\times3}{\ell^2 \lfloor \mathbf{r} \rfloor\, \hat{d}} & \underset{1\times1}{-\ell^2\, \hat{d}} \end{bmatrix} \begin{Bmatrix} \underset{3\times1}{\{\mathbf{v}\}} \\ \underset{1\times1}{\dot{f}^{\mathrm{nl}}} \end{Bmatrix} = \begin{Bmatrix} \underset{3\times1}{\{\mathbf{0}\}} \\ \underset{1\times1}{0} \end{Bmatrix}, \tag{4.42}$$

where $r_i = \partial f^{\mathrm{nl}} / \partial x_i$ and the following operators have been defined:

$$\hat{P}^{\mathrm{nl}}_{ip} = \left(\mathcal{L}^{\mathrm{nl}}_{jipq} + \mathcal{B}_{jipq}\right) \frac{\partial^2}{\partial x_j\, \partial x_q}, \qquad \hat{d} = \nabla^2 = \frac{\partial^2}{\partial x_j \partial x_j}\,. \tag{4.43}$$

To form the corresponding matrix symbol $[\boldsymbol{\Lambda}^{\mathrm{pr}}]$ of the principal part of the system, the partial derivatives $\partial / \partial x_p$ are replaced by the Fourier variables $i\,\xi_p$ in the operator matrix. This leads to the following matrix with quadratic entries in the real variables ξ_p:

$$\underset{4\times4}{\left[\boldsymbol{\Lambda}^{\mathrm{pr}}\right]} = \begin{bmatrix} \underset{3\times3}{-\left[\mathbf{P}^{\mathrm{nl}}\right]} & \underset{3\times1}{\{\mathbf{0}\}} \\ \underset{1\times3}{-\ell^2 \lfloor \mathbf{r} \rfloor\, d} & \underset{1\times1}{\ell^2\, d} \end{bmatrix}, \quad \text{where} \quad P^{\mathrm{nl}}_{ip} = \left(\mathcal{L}^{\mathrm{nl}}_{jipq} + \mathcal{B}_{jipq}\right) \xi_j\, \xi_q, \qquad d = \xi_j\, \xi_j = |\boldsymbol{\xi}|^2\,. \tag{4.44}$$

The system of equations is elliptic when the determinant of $[\boldsymbol{\Lambda}^{\mathrm{pr}}]$ is non-zero for all real $\boldsymbol{\xi}$; this means that the system of PDEs has no real characteristic surfaces and the solution cannot have discontinuous spatial derivatives. Ellipticity is lost when $\det\left[\boldsymbol{\Lambda}^{\mathrm{pr}}\right] = 0$, i.e., when

$$\det\left[\boldsymbol{\Lambda}^{\mathrm{pr}}\right] = -\ell^2\, d\, \det\left[\mathbf{P}^{\mathrm{nl}}\right] = -\ell^2\, |\boldsymbol{\xi}|^2\, \det\left[\left(\mathcal{L}^{\mathrm{nl}}_{jipq} + \mathcal{B}_{jipq}\right) \xi_j\, \xi_q\right] = 0 \tag{4.45}$$

for some real vector $\boldsymbol{\xi} \neq \mathbf{0}$. The loss of ellipticity condition (4.45) can be written in the equivalent form

$$\det\left[n_j\left(\mathcal{L}^{\mathrm{nl}}_{jipq}+\mathcal{B}_{jipq}\right)n_q\right]=0 \quad \text{for some } \boldsymbol{unit} \text{ vector } \mathbf{n}, \tag{4.46}$$

where $\boldsymbol{\mathcal{L}}^{\mathrm{nl}}$ and $\boldsymbol{\mathcal{B}}$ are defined in $(4.23)_2$ and (4.28) respectively. The loss of ellipticity condition (4.46) for the implicit non-local model has the same form as the corresponding condition (4.34) for the local model. In fact, (4.46) results from (4.34) if the substitution $\boldsymbol{\mathcal{L}}^{\mathrm{loc}} \to \boldsymbol{\mathcal{L}}^{\mathrm{nl}}$ is made in (4.34). Since the expression $(4.23)_2$ for $\boldsymbol{\mathcal{L}}^{\mathrm{nl}}$ is obtained from the corresponding expression $(2.66)_2$ for $\boldsymbol{\mathcal{L}}^{\mathrm{loc}}$ when the substitution $H^{\mathrm{loc}} \to H^{\mathrm{nl}}$ is made in $(2.66)_2$, we conclude that the loss of ellipticity condition (4.46) of the implicit non-local problem is obtained from the corresponding expression (4.34) of the local problem when the substitution $H^{\mathrm{loc}} \to H^{\mathrm{nl}}$ is made. Therefore, when, at some loading stage, condition (4.46) is satisfied for some unit vector $\mathbf{n}$, the corresponding value of the non-local hardening modulus H^{nl} is defined by an equation similar to (4.35):

$$H^{\mathrm{nl}} = -\mathbf{N}:\boldsymbol{\mathcal{L}}^{\mathrm{nl}}:\mathbf{N} + [\mathbf{n}\cdot(\boldsymbol{\mathcal{L}}:\mathbf{N})]\cdot[\mathbf{n}\cdot(\boldsymbol{\mathcal{L}}+\boldsymbol{\mathcal{B}})\cdot\mathbf{n})]^{-1}\cdot[\mathbf{n}\cdot(\boldsymbol{\mathcal{L}}:\mathbf{N})]. \tag{4.47}$$

Also, when the three conditions stated in Subsection 4.3.1 are satisfied (with $\boldsymbol{\mathcal{L}}^{\mathrm{loc}}$ replaced by $\boldsymbol{\mathcal{L}}^{\mathrm{nl}}$), the critical hardening modulus in the implicit non-local problem can never be positive, i.e.,

$$H^{\mathrm{nl}}_{\mathrm{cr}} \leq 0. \tag{4.48}$$

The above discussion makes it clear that in general *use of a rate-independent implicit non-local model does not always guarantee the ellipticity of the mathematical problem*; *the character of the equations depends on the value of* H^{nl}. In particular, when $H^{\mathrm{nl}} > 0$, the equations are elliptic, the solution is smooth, and the formation of shear bands with zero thickness is excluded. However, when $H^{\mathrm{nl}} < 0$, it is possible that the problem loses ellipticity and the solution may not be smooth. Since the new porous model is isotropic, plasticity is characterized by an associated flow rule, and the model focuses on porous *metallic* materials (which means that $||\boldsymbol{\mathcal{L}}|| \gg ||\boldsymbol{\mathcal{B}}||$ so that the $\boldsymbol{\mathcal{B}}$ terms can be considered negligible), the three conditions stated in Subsection 4.3.1 are satisfied and the critical hardening modulus is non-positive in this case. Thus, in the case of the implicit gradient model presented in Sections 4.2.2–4.2.3 for which the non-local hardening modulus H^{nl} is always positive, the governing equations remain elliptic, and the non-local formulation regularizes the problem in this case.

As will be shown in Section 4.4, the development of non-smooth solutions is responsible for the mesh dependence in finite element calculations when the local isotropic projection model is used. Use of the corresponding gradient formulation preserves ellipticity and allows for convergence of the results as the finite element mesh is refined. Also, it is should be noted here that the material length scale ℓ does not enter the loss of ellipticity condition (4.46); the value of ℓ does affect the solution but does not influence the mathematical character of the problem.

4.4 Plastic flow localization under plane strain conditions

A well-known problem in the finite element implementation of rate-independent local plasticity models with softening is that numerical solutions depend on the mesh size, when the

material enters the softening region (i.e., when $H^{\text{loc}} < 0$). As already discussed, such difficulties are related to loss of ellipticity, which allows for the development of solutions with discontinuities across the characteristic surfaces (or curves in 2D) of the problem. In finite element solutions, as the mesh is refined, the thickness of the predicted shear band reduces, but is limited by the element size. In other words, as the mesh is refined, the finite element solution does its best, the width of the predicted shear band reduces, but it can never capture a zero-thickness shear band, unless special elements are designed or the element boundaries are perfectly aligned with the direction of the shear band (e.g., Jiràsek (2000)). As a consequence, the finite element solutions appear to be mesh-size dependent. It should be noted that this difficulty is not limited to the finite element method; it appears in all numerical methods that discretize the problem. To overcome this difficulty and regularize the problem, non-local models can be used to restore ellipticity, provided the hardening modulus H^{nl} in the rate-independent implicit non-local model is always greater than the critical value defined by the minimum value of the right hand side of equation (4.47).

In the special case where the conditions stated in Section 4.3.1 are satisfied and the non-local hardening modulus H^{nl} remains positive (which is the case in the implicit gradient porous plasticity model proposed in Section 4.2.2), the corresponding mathematical problem is always elliptic and the solution is smooth. In such cases, intensely strained regions can still develop at some imperfection, but these highly strained regions have finite width and appear as zones of high spatial strain-gradients in the smooth solution. The width of the intensely strained regions scales with the material parameter ℓ of the non-local model. When the finite element mesh is fine enough, i.e., the element size in the intensely strained zone is smaller than ℓ, the numerical solution converges to the correct smooth solution.

All the above are demonstrated in the numerical examples that follow. The problem of plastic flow localization under plane strain tension is solved using the finite element method. The solution for the local model shows strong mesh dependence. However, when the non-local model is used, the problem remains elliptic and the numerical solution converges to the correct smooth solution as the mesh is refined. It is also shown that the value of the characteristic length ℓ does not influence the deformation level at which localization first becomes possible (i.e., the bifurcation point) but only the (finite) width of the highly strained region, at least for the material parameters and microstructural configurations considered in these calculations.

4.4.1 Description of the problem

In this section, the quasi-static problem of plastic flow localization under plane strain conditions is examined. Both the local and implicit non-local isotropic projection models are used and the effect of the regularized model is investigated. The models were implemented using User MATerial (UMAT) subroutines provided by ABAQUS/Standard[2]. Due to symmetry, only one quarter of the specimen is used in the finite element calculations and doubly symmetric solutions are obtained. The matrix material is characterized by a Young's modulus $E = 1000\,\sigma_0$, a Poisson's ratio $\nu = 0.3$ and the flow stress is assumed to follow a power law of the form (3.29). An initial porosity of $f_0 = 5\%$ is assumed in all cases.

Figure 4.1 shows a schematic representation of one quarter of the specimen along with the geometric boundary conditions imposed. The right side of the specimen is traction free

[2]The procedure used for the efficient implementation of implicit non-local models in ABAQUS is described in more detail in Section 5.3.

and the top side is subjected to a prescribed displacement δ. The length of the one quarter of the specimen is $L = 2W$, where W is the corresponding width. To trigger the initiation of non-uniform deformation, an imperfection in the material properties is introduced over a small square region of side $d = 0.10W$ at the center of the specimen, as shown (with red color) in Fig. 4.1; the flow stress σ_0 is replaced by $0.99\sigma_0$ in the imperfect region. The meshes

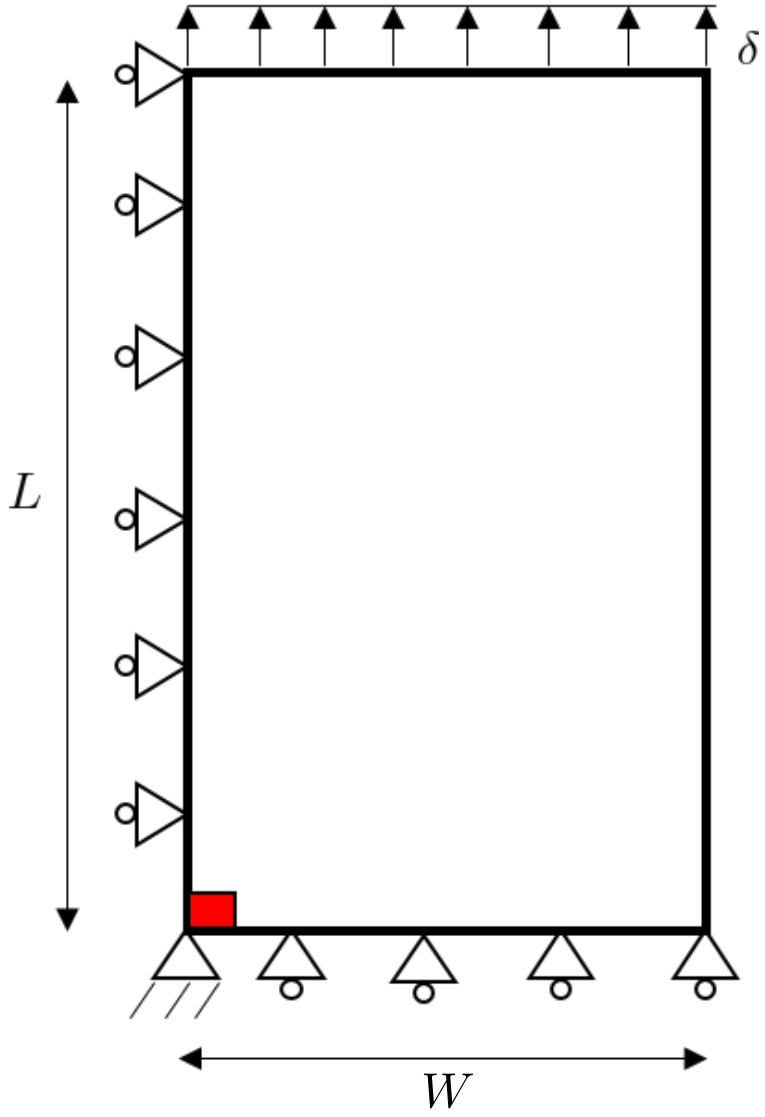

Figure 4.1 – Schematic representation of one quarter of the plane strain tension specimen.

used consist of 4-node linear, plane strain CPE4H (local model) and CPE4HT (non-local model) coupled temperature-displacement hybrid elements with constant pressure provided by ABAQUS/Standard. The elements are square and equally spaced in the undeformed configuration. Three different meshes are used with number of elements 20×40, 40×80 and 80×160, where the first and second numbers denote the number of elements in the W and L directions respectively. The corresponding initial size of the square elements is $e = W/20$, $e = W/40$ and $e = W/80$ respectively.

The critical strain at which localization is first possible is determined by using the methodology of Rice and co-workers (Rudnicki and Rice, 1975; Rice, 1976). For plane strain

problems, it can be shown that the conditions (4.34) or (4.46) for plastic flow localization in a shear band can be written in the following form[3]

$$\det\left[n_j\left(\mathcal{L}_{jipq}+\mathcal{B}_{jipq}\right)n_q\right]\equiv C=C_{11}C_{22}-C_{21}C_{12}=0 \tag{4.49}$$

$$C_{11}=\mathcal{L}_{1111}n_1^2+\sigma_{12}n_1n_2+\left(\mathcal{L}_{1212}-\frac{\sigma_{11}-\sigma_{22}}{2}\right)n_2^2 \tag{4.50}$$

$$C_{22}=\left(\mathcal{L}_{1212}+\frac{\sigma_{11}-\sigma_{22}}{2}\right)n_1^2+\mathcal{L}_{2222}n_2^2+\sigma_{12}n_1n_2 \tag{4.51}$$

$$C_{12}=-\sigma_{12}n_1^2+\left(\mathcal{L}_{1122}+\mathcal{L}_{1212}+\frac{\sigma_{11}-\sigma_{22}}{2}\right)n_1n_2 \tag{4.52}$$

$$C_{21}=-\sigma_{12}n_2^2+\left(\mathcal{L}_{2211}+\mathcal{L}_{1212}-\frac{\sigma_{11}-\sigma_{22}}{2}\right)n_1n_2 \tag{4.53}$$

where $\mathcal{L}_{ijkl}$ are the components of the appropriate fourth-order elastic-plastic *tangent* modulus with respect to the global coordinate system, i.e., $\mathcal{L}_{ijkl}=\mathcal{L}^{\text{loc}}_{ijkl}$ for the local model and $\mathcal{L}_{ijkl}=\mathcal{L}^{\text{nl}}_{ijkl}$ for the non-local model. Determination of the critical strain for localization is carried out using a semi-analytical approach as follows. Let $(\mathbf{e}_1,\mathbf{e}_2)$ be the unit vectors defining the global coordinate system in the plane of loading and $\mathbf{e}_2$ the corresponding direction of loading. Constitutive calculations using a single finite element loaded in tension under plane strain conditions are performed incrementally in ABAQUS/Standard module. At each stage of deformation, within UMAT and after the integration of the constitutive equations is completed, the unit vector $\mathbf{n}$ is written in the form $\mathbf{n}(\psi)=cos\psi\mathbf{e}_1+sin\psi\mathbf{e}_2$, where ψ defines the orientation of the band with respect to axis $\mathbf{e}_1$. The quantity $C=C_{11}C_{22}-C_{21}C_{12}$ is determined by scanning the range $0^\circ\leq\psi\leq 90^\circ$ and its minimum and maximum values C_{min} and C_{max} in that range of ψ are found. The value of C_{min} is initially positive and decreases with increasing logarithmic axial strain E_2; if, at some stage of deformation, a change of sign of C_{min} is detected and the condition $C_{min}C_{max}<0$ also holds, the corresponding value of E_2 defines the strain E_2^{cr} at which localization is first possible and the value of ψ defines the corresponding orientation of the shear band.

4.4.2 Solution using the local model

In this section, the results regarding the predictions of the local model are discussed in detail. To showcase the numerical issues related with the use of a non-regularized model when softening behavior is present, a mesh convergence analysis is first carried out. Also, the effect of void shape and hardening of the matrix material (i.e., the effect of microstructural components) to the critical strain for localization is investigated.

Figure 4.2 shows the results for the mesh convergence analysis, where a microstructure with an aspect ratio $w=0.1$ is assumed. Particularly, on the left part of Fig. 4.2 the calculated normalized "load-extension" curves for the three different meshes in the local model are presented. The dashed line corresponds to the uniform solution when there is no imperfection, and the dark circle on the curve indicates the point of the predicted localization initiation from the loss of ellipticity condition (4.49). Fig. 4.2 also shows the contours of plastic zones (in red) as predicted by the three meshes at a macroscopic axial logarithmic strain $E_2=0.10$ (where the whole specimen is shown for visualization purposes). As it can

[3]for $\sigma_{22}=\sigma_{12}=0$ the following expressions reduce to those found in the works of Aravas and co-workers (Aravas and Ponte Castañeda, 2004; Aravas and Papadioti, 2021).

be seen, the numerical solutions for the three different discretizations agree initially; but, after the shear band is formed, the "load-extension" curves and the predicted width of the shear band become mesh-dependent. Loss of ellipticity allows for discontinuous solutions (shear bands) and, as the mesh is refined, the finite element solution tends to reproduce the "zero thickness" of the shear band.

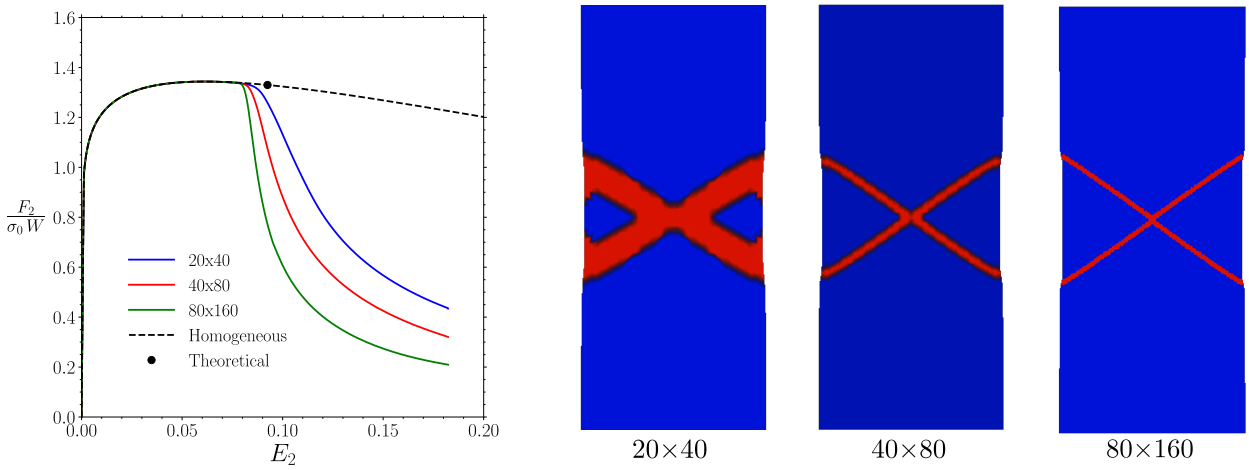

Figure 4.2 – Variation of the normalized total force per unit out-of-plane thickness $F_2/(\sigma_0 W)$ with macroscopic axial logarithmic strain $E_2 = \ln\left(1 + \frac{u_2}{L}\right)$ (left) and plastic zones (in red) for the local model with an aspect ratio $w = 0.1$ at a strain $E_2 = 0.10$ (right). Whole specimen is shown.

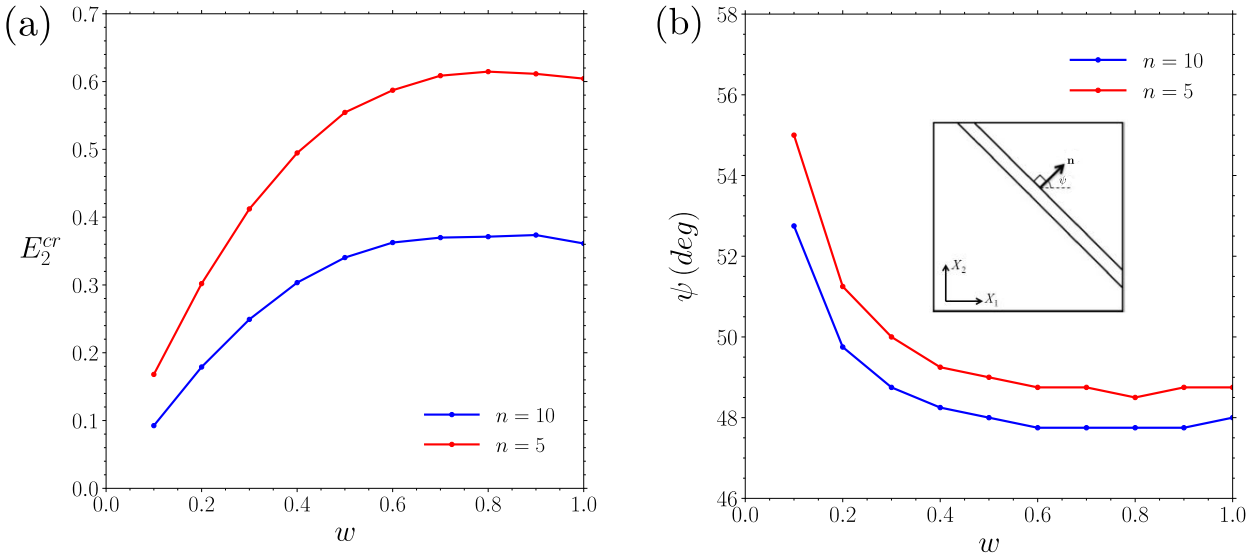

Figure 4.3 – Variation of (a) critical axial logarithmic strain for localization E_2^{cr} and (b) shear band orientation angle ψ with respect to the aspect ratio of the voids w for two different hardening exponents.

The effect of the shape of the voids and matrix hardening on the critical strain to localization and the corresponding shear band orientation are shown in Figure 4.3. Again, based on previous numerical results only oblate voids are considered (i.e., $w \leq 1$). Figure 4.3a shows that the critical strain to localization is an increasing function of the aspect ratio of

the voids; the critical strain at which localization is first possible is substantially higher for microstructures that consist of almost spherical or spherical voids ($0.5 \leq w \leq 1$) compared to those that consist of oblate voids with lower aspect ratios (i.e., for $w \leq 0.5$). A possible interpretation for this behavior is that, microstructures comprising penny-shaped oblate voids lead to significantly higher rates of porosity evolution and thus softening behavior occurs at lower strain levels promoting earlier strain localization. In this regard, the void aspect ratio w can be viewed as parameter in the model that controls the *bifurcation point* at which the solution switches to a highly localized, non-homogeneous strain distribution pattern. Also, it should be noted that critical localization strains for a material with increased hardening capacity (i.e., for $n = 5$) are higher compared to those for a material with less matrix hardening (i.e., for $n = 10$) for corresponding void shapes. This is due to the fact that, matrix hardening acts as a competitive mechanism to softening due to porosity evolution implying that higher hardening capacity leads to delayed onset of strain localization.

Figure 4.3b presents the variation of the predicted shear band orientation (which is defined by the angle ψ) with respect to the void aspect ratio parameter. For the microstructural configurations examined, the angle ψ is a decreasing function of void aspect ratio with possible orientations falling in the range $\psi \in [48°, 55°]$. Materials with microstructures consisting of very flat oblate voids ($w \leq 0.3$) exhibit a higher sensitivity with more inclined bands while microstructures comprising voids of higher aspect ratios show less sensitivity and less steep bands with respect to the $\mathbf{e}_1$ direction.

4.4.3 Solution using the non-local model

Calculations were repeated using the implicit gradient isotropic projection model and the results are discussed in the following. Figure 4.4 shows the results for the mesh convergence

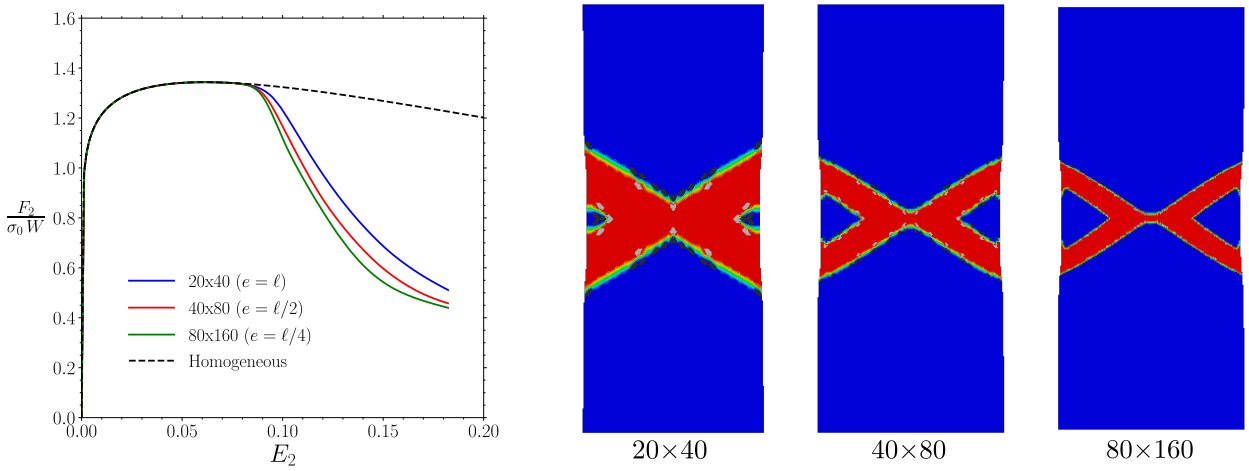

Figure 4.4 – Variation of the normalized total force per unit out-of-plane thickness $F_2/(\sigma_0 W)$ with macroscopic axial logarithmic strain $E_2 = \ln\left(1 + \frac{u_2}{L}\right)$ for the non-local model with $\ell = 0.05W$. A value of $w = 0.1$ is used in the calculations.

analysis, where again a microstructure with an aspect ratio $w = 0.1$ is assumed and the characteristic length is taken to be $\ell = 0.05W$. The corresponding normalized "load-extension" curves for the three different meshes using the implicit non-local model are presented on the left part of Fig. 4.4. The dashed line corresponds to the uniform solution when there is no imperfection. The right part of Fig. 4.4 also shows the contours of plastic zones (in red) while

Fig. 4.5 depicts the equivalent plastic strain and non-local porosity distributions in the three meshes at a macroscopic axial logarithmic strain $E_2 = 0.10$. In this case, the equations are always elliptic and the solution is continuous at all deformation levels. The condition (4.49) does not predict the occurrence of localization in the case of the implicit gradient model. It is evident from Figs. 4.4 and 4.5 that, as the finite element mesh is refined, the numerical solution becomes mesh-independent and converges. The initial size e of the square elements becomes a smaller fraction of the material parameter ℓ as the finite element mesh is refined: $e = \ell$ (in 20×40), $e = \ell/2$ (in 40×80), and $e = \ell/4$ (in 80×160).

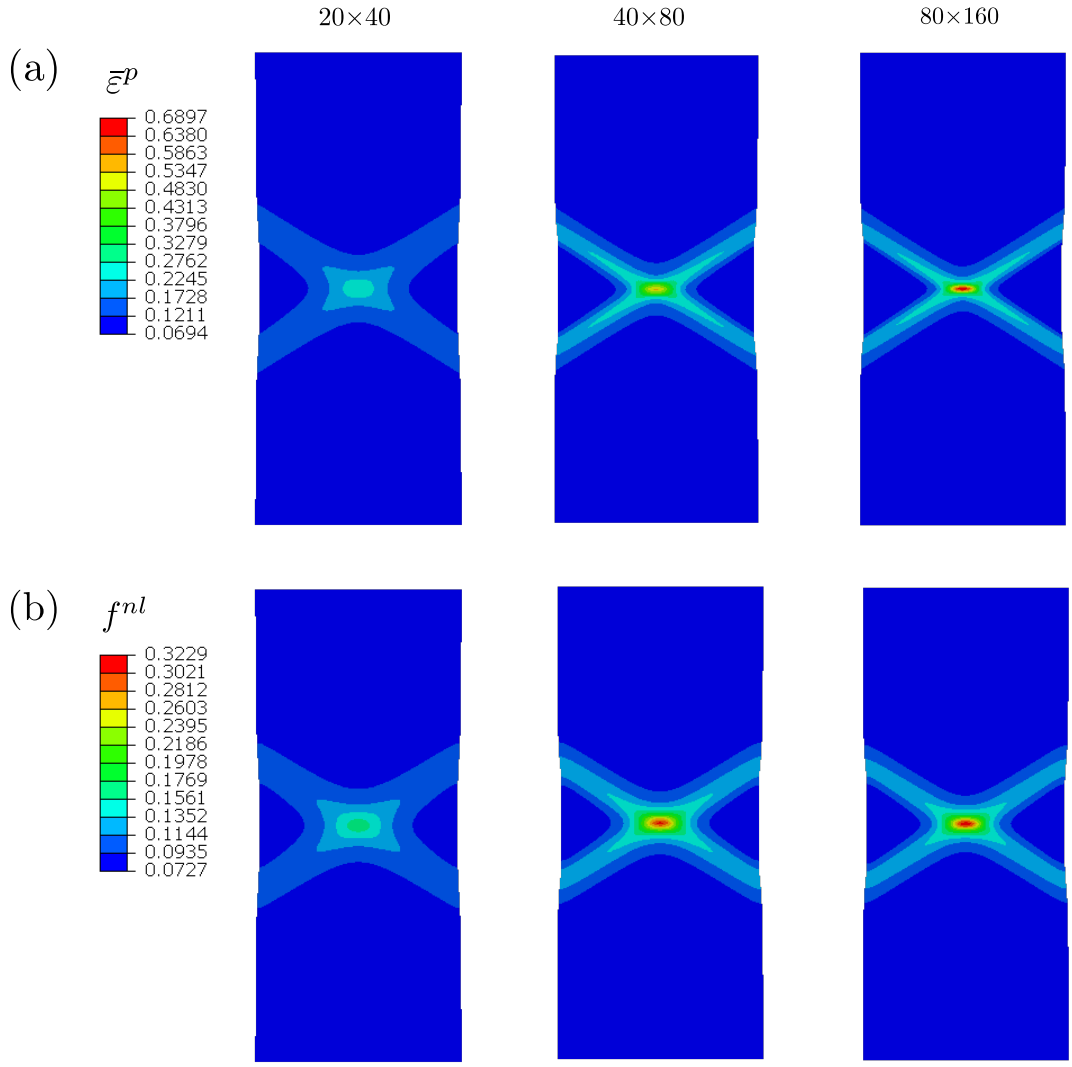

Figure 4.5 – Contours (a) of equivalent plastic strain $\bar{\varepsilon}^p$ and (b) of local porosity for the three meshes at macroscopic axial strain $E_2 = 0.10$, for the non-local model. Whole specimen is shown.

Figure 4.6 shows the "load-extension" curves for the 80×160 mesh in the non-local model for three different values of the characteristic length ℓ ($\ell = 0,01W$, $\ell = 0,05W$ and $\ell = 0,1W$). The black dashed line corresponds to the uniform solution when there is no imperfection. These calculations correspond to a microstructure comprising oblate voids with aspect ratio $w = 0.1$ and an initial porosity of $f_0 = 5\%$. For this particular case it can be seen that the solutions up to the bifurcation point are essentially the same and independent of the value of ℓ. The choice of the characteristic length, however, affects the solution

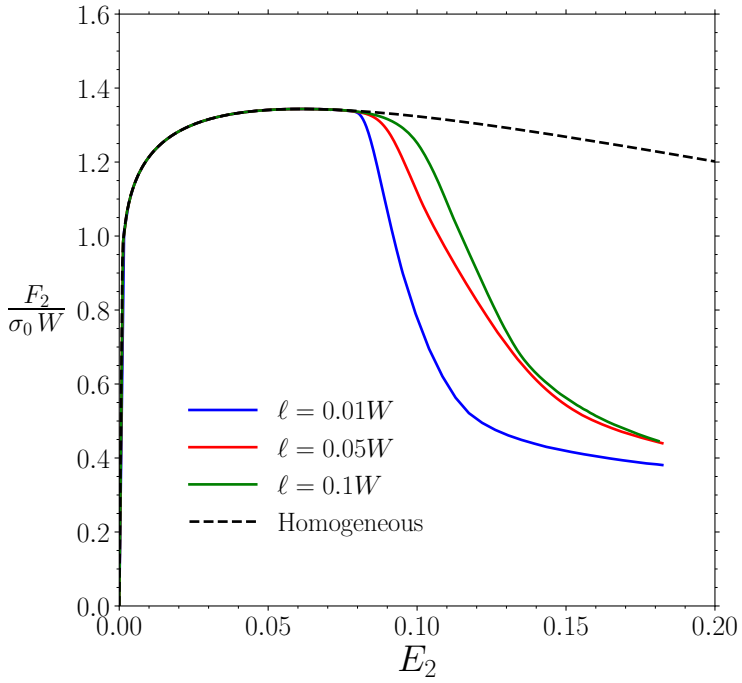

Figure 4.6 – Variation of the normalized "load-extension" curves for the non-local model with the 80×160 mesh for different values of the characteristic length ℓ. A value of $w = 0.1$ is used in the calculations.

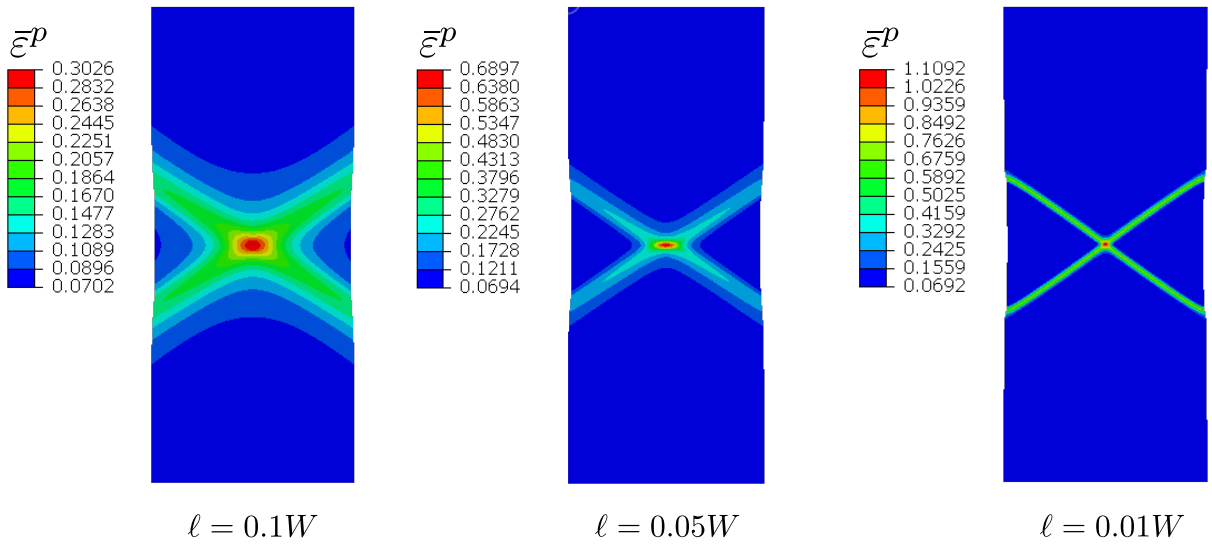

Figure 4.7 – Distribution of the equivalent plastic strain at an axial strain $E_2 = 0.10$ for different values of the characteristic length ℓ. A value of $w = 0.1$ is used in the calculations.

in the post-bifurcation regime; as the value of the characteristic length decreases the slope of the post-bifurcation branch becomes steeper and the width of the corresponding highly strained region reduces, as shown in Fig. 4.7. This numerical result is in agreement with the theoretical analysis of the non-local problem's mathematical character which was discussed in Section 4.3.2. In particular, the characteristic length enters the modified Helmholtz PDE (4.10) multiplying the term of the Laplacian of the non-local porosity. In the post-bifurcation

regime, the fields are highly non-homogeneous and the Laplacian term could affect the solution depending on the value of the characteristic length ℓ. Also, this observation can be used as a guide for the calibration of ℓ based on available experimental results; For instance, for a specific material, numerical simulations can be carried out for various values of the characteristic length until a value that closely fits the experimental stress-strain curves is found. This value of ℓ can then be considered as a parameter for the non-local model which can be used make predictions in structural calculations of the material at hand.

4.5 Concluding remarks

In this chapter, we discuss in detail the computational issues related to the numerical implementation of rate-independent constitutive models that may lead to softening as well as the available regularization solutions proposed in the literature. The mathematical reason for these numerical problems is related to loss of ellipticity of the governing equations. In view of its computational attractiveness, we propose an implicit non-local version of the isotropic projection model developed in this work in order to amend these issues. The formulation remains largely the same with the local version, the main difference being the substitution of the local porosity with its non-local counterpart in the constitutive equations; the non-local porosity is now an additional field variable that is defined by the solution of a modified Helmholtz BVP along with the classical equilibrium equations. Also, a characteristic length is introduced in the formulation and acts as a "localization limiter" to the problem.

Detailed analysis shows that the mathematical character of the problem's governing equations ultimately depends on the value of the material's effective hardening modulus. In general, if the hardening modulus becomes lower than a critical value, the governing equations lose ellipticity and numerical solutions depend on spatial discretization. Conversely, if the hardening modulus remains higher than a critical value during the loading program, equations remain elliptic and solutions are mesh-independent provided that a fine enough mesh is used. For metallic, isotropic materials obeying an associated flow rule (i.e., "normality"), the critical value of the hardening modulus is found to be non-positive. In contrast to the local formulation where the hardening modulus may become negative during loading, the hardening modulus of the corresponding non-local isotropic projection model is always positive preserving thus the elliptic properties of the problem. Rice's localization analysis is then used to investigate the effect of the non-local formulation on the problem of plane strain localization. Numerical examples indicate that the non-local model allows for mesh-independent solutions to be obtained in the post-bifurcation regime as the element size becomes smaller than the value of the material's characteristic length. The void shape parameter is also found to strongly affect the theoretically predicted critical localization strain; microstructures comprising very flat voids of low aspect ratios ($w \leq 0.5$) result in lower critical strains compared to microstructures with almost spherical or spherical voids. We also comment on the possibility of using a simple hybrid numerical-experimental approach in order to calibrate the characteristic length appearing in the non-local formulation.

CHAPTER 5

Numerical Implementation and Simulation of Structural Problems

Chapter summary: In this chapter the local and non-local models developed in this work are used for the numerical solution of various BVPs related to forming processes and ductile fracture phenomena. First, we discuss the details related to the numerical implementation of the non-local model. In particular, the strong and weak formulations of the non-local problem are presented, the FE approximation is introduced, and the corresponding residuals for the mechanical and the non-local porosity BVPs are derived. Also, we present an algorithm for the numerical integration of the non-local constitutive equations which is necessary for the solution of the discretized global equations. Attention is focused on the numerical implementation in the ABAQUS commercial FE software. Next, the industrially relevant problems of the Hole Expansion Test (HET) and Charpy V-notch (CVN) test, the phenomenon of cup-and-cone fracture of round bars and the ductile fracture of the specimen proposed in the first Sandia Fracture Challenge (SFC) are simulated using both ABAQUS/Standard and ABAQUS/Explicit. The main purpose of these simulations is (a) to identify the effects and establish a connection between the models' parameters and the the predicted structural behavior and (b) to assess the capability of the models to qualitatively and/or quantitatively capture experimental observations.

Contents

5.1 Variational formulation of the implicit non-local BVP

Consider a continuum body which in the reference configuration $\mathfrak{B}_0$ at $t = t_0$ occupies volume $\mathcal{V}_0$ bounded by a surface $\partial\mathcal{V}_0$ with a mass density ρ_0. Let also the body be subjected to external body forces per unit mass $\mathbf{b}(\mathbf{x}, t)$, known surface (traction) forces $\hat{\mathbf{t}}$ on part $\partial\mathcal{V}_t$ of its surface and known displacements $\hat{\mathbf{u}}$ on its remaining surface ∂V_u[1] The balance of linear momentum with respect to the current configuration (i.e., Eulerian description) leads to the following set of partial differential equations:

$$\boldsymbol{\nabla}\cdot\boldsymbol{\sigma} + \rho\mathbf{b} = \rho\ddot{\mathbf{u}} \qquad \text{or} \qquad \frac{\partial\sigma_{ij}}{\partial x_j} + \rho b_i = \rho\ddot{u}_i \qquad \text{in} \quad \mathcal{V} \tag{5.1}$$

where $\mathbf{u}(\mathbf{x}, t)$, $\boldsymbol{\sigma}(\mathbf{x}, t)$, and ρ are the displacement field, stress field and mass density with respect to the deformed configuration. In the context of the implicit gradient formulation proposed in Chapter 4, the non-local porosity field $f^{\text{nl}}(\mathbf{x}, t)$ is defined through the solution of the modified Helmholtz equation

$$f^{\text{nl}} - \ell^2\nabla^2 f^{\text{nl}} = f \qquad \text{in} \quad \mathcal{V} \tag{5.2}$$

Furthermore, kinematic (or compatibility) relations read

$$\mathbf{D} \equiv \mathbf{L}^s = \frac{1}{2}\Big(\mathbf{v}\boldsymbol{\nabla} + \boldsymbol{\nabla}\mathbf{v}\Big) \qquad \text{or} \qquad D_{ij} = \frac{1}{2}\left(\frac{\partial v_i}{\partial x_j} + \frac{\partial v_j}{\partial x_i}\right) \tag{5.3}$$

$$\mathbf{W} \equiv \mathbf{L}^a = \frac{1}{2}\Big(\mathbf{v}\boldsymbol{\nabla} - \boldsymbol{\nabla}\mathbf{v}\Big) \qquad \text{or} \qquad W_{ij} = \frac{1}{2}\left(\frac{\partial v_i}{\partial x_j} - \frac{\partial v_j}{\partial x_i}\right) \tag{5.4}$$

where $\mathbf{L}$, $\mathbf{D}$ and $\mathbf{W}$ are the velocity gradient, total rate-of-deformation, and spin tensors respectively and the superscripts "s" and "a" denote the symmetric and skew-symmetric parts of a tensor.

Under the assumption of small elastic strains (as is the case for metallic materials), the constitutive behavior for the non-local model is described by the additive decomposition of the total rate-of-deformation tensor (2.44), the yield condition using (4.15) and the evolution equations for the equivalent plastic strain and the local porosity (4.24)–(4.25), which are recalled here for brevity,

$$\mathbf{D} = \mathbf{D}^e + \mathbf{D}^p \tag{5.5}$$

$$\mathbf{D}^e = \boldsymbol{\mathcal{M}} : \overset{\nabla}{\boldsymbol{\sigma}}, \qquad \boldsymbol{\mathcal{M}} = \frac{1}{2\,\mu}\boldsymbol{\mathcal{K}} + \frac{1}{3\,\kappa}\boldsymbol{\mathcal{J}}, \qquad (\mu, \kappa) = \text{fcn}(\mu_{\text{m}}, \kappa_{\text{m}}, \nu_{\text{m}}, f^{\text{nl}}, w) \tag{5.6}$$

$$\mathbf{D}^p = \dot{\lambda}\,\mathbf{N}, \qquad \mathbf{N} \equiv \frac{\partial\Phi}{\partial\boldsymbol{\sigma}} = \frac{3}{2\,\sigma_e}\frac{\partial\Phi}{\partial\sigma_e}\mathbf{s} + \frac{1}{3}\frac{\partial\Phi}{\partial p}\boldsymbol{\delta}, \tag{5.7}$$

$$\Phi(\sigma_e, p, \bar{\varepsilon}^p, f^{\text{nl}}, w) = 0 \tag{5.8}$$

$$\dot{\bar{\varepsilon}}^p = \mathbf{C}^{\text{nl}} : \mathbf{D} + M\dot{f}^{\text{nl}}, \qquad \dot{f} = \mathbf{B}^{\text{nl}} : \mathbf{D} + K\dot{f}^{\text{nl}} \tag{5.9}$$

[1] Recall that $\partial\mathcal{V}_t \cup \partial\mathcal{V}_u = \partial\mathcal{V}V$ while $\partial\mathcal{V}_t \cap \partial\mathcal{V}_u = \varnothing$.

The BVP is completed with the addition of boundary conditions. For the mechanical problem, both displacement and traction boundary conditions on the corresponding parts of the total boundary can be prescribed while Neumann boundary conditions on the external boundary ∂V for the non-local porosity f^{nl} are assumed:

$$\mathbf{u} = \hat{\mathbf{u}} = \text{known}, \qquad \text{on } \partial\mathcal{V}_u \tag{5.10}$$

$$\mathbf{t} = \boldsymbol{\sigma}\cdot\mathbf{n} = \hat{\mathbf{t}} = \text{known}, \qquad \text{on } \partial\mathcal{V}_t \tag{5.11}$$

$$\boldsymbol{\nabla} f^{\text{nl}}\cdot\mathbf{n} = 0 \qquad \text{or} \qquad \frac{\partial f^{\text{nl}}}{\partial n} = 0 \qquad \text{on } \partial\mathcal{V} \tag{5.12}$$

The field equations (5.1), (5.2) along with the kinematic equations (5.3), (5.4), the constitutive equations (5.5)–(5.9), and the boundary conditions (5.10)–(5.12) suggest the Eulerian *strong form* of the implicit gradient isotropic projection model. The coupled BVP is nonlinear and is solved numerically using the finite element method. Implementation into FE commercial codes (e.g., ABAQUS, FeniCS etc.) requires first the problem to be restated in a variational form as discussed in the following.

The primary unknowns of the problem are the displacement field $\mathbf{u}(\mathbf{x},t)$ and the non-local porosity field $f^{\text{nl}}(\mathbf{x},t)$. The variational formulation of the problem can be stated as follows:
Find $\mathbf{u}(\mathbf{x},t)\in H^2$ *satisfying* (5.10) *and* $f^{\text{nl}}(\mathbf{x},t)\in H^2$ *such that for all* $\boldsymbol{\upsilon}^\star,\mathbf{v}^\star\in L^2$ *satisfying the homogeneous B.C.'s* $\boldsymbol{\upsilon}^\star=\mathbf{0},\mathbf{v}^\star=\mathbf{0}$ *on* $\partial\mathcal{V}_u$ *and for all* $f^\star,\gamma^\star\in L^2$*:*

$$\int_{\mathcal{V}(t)}(\boldsymbol{\nabla}\cdot\boldsymbol{\sigma}+\rho\mathbf{b}-\rho\mathbf{a})\cdot\boldsymbol{\upsilon}^\star d\mathcal{V}+\int_{\partial\mathcal{V}_t(t)}(\boldsymbol{\sigma}\cdot\mathbf{n}-\hat{\mathbf{t}})\cdot\mathbf{v}^\star d\mathcal{S}=0 \tag{5.13}$$

$$\int_{\mathcal{V}(t)}(f^{\text{nl}}-\ell^2\nabla^2 f^{\text{nl}}-f)f^\star d\mathcal{V}+\int_{\partial\mathcal{V}(t)}(\boldsymbol{\nabla}f^{\text{nl}}\cdot\mathbf{n})\gamma^\star d\mathcal{S}=0 \tag{5.14}$$

where H^k denotes the space of functions with square-integrable derivatives through order k, L^2 denotes the space of square-integrable functions, and $\boldsymbol{\upsilon}^\star,\mathbf{v}^\star,f^\star,\gamma^\star$ are test functions. Integration by parts and use of the Gauss theorem leads to the following equivalent variational statement:
Find $\mathbf{u}(\mathbf{x},t)\in H^2$ *satisfying* (5.10) *and* $f^{\text{nl}}(\mathbf{x},t)\in H^1$ *such that for all* $\boldsymbol{\upsilon}^\star\in H^1$ *satisfying the homogeneous B.C.* $\boldsymbol{\upsilon}^\star=\mathbf{0}$ *on* $\partial\mathcal{V}_u$ *and for all* $f^\star\in H^1$*:*

$$W_u(\mathbf{u},f^{\text{nl}})=\int_{\mathcal{V}(t)}\rho\mathbf{b}\cdot\boldsymbol{\upsilon}^\star d\mathcal{V}+\int_{\partial\mathcal{V}_t(t)}\hat{\mathbf{t}}\cdot\boldsymbol{\upsilon}^\star d\mathcal{S}-\int_{\mathcal{V}(t)}\boldsymbol{\sigma}:\mathbf{D}^\star d\mathcal{V}-\int_{V(t)}\rho\ddot{\mathbf{u}}\cdot\boldsymbol{\upsilon}^\star d\mathcal{V}=0 \tag{5.15}$$

$$W_f(\mathbf{u},f^{\text{nl}})=\int_{\mathcal{V}(t)}\left[(f^{\text{nl}}-f)f^\star+\ell^2\boldsymbol{\nabla}f^{\text{nl}}\cdot\boldsymbol{\nabla}f^\star\right]d\mathcal{V}=0 \tag{5.16}$$

where $\boldsymbol{\sigma}=\boldsymbol{\sigma}(\mathbf{u},f^{\text{nl}})$, $f=f(\mathbf{u},f^{\text{nl}})$ and $\mathbf{D}^\star=(\boldsymbol{\upsilon}^\star\boldsymbol{\nabla}+\boldsymbol{\nabla}\boldsymbol{\upsilon}^\star)/2$. Equations (5.15), (5.16) suggest the *weak formulation* of the coupled BVP, which can now be used to introduce the finite element approximation.

5.2 Finite element approximation

In the context of the finite element method, the continuous domain of solution $\mathcal{V}$ is discretized into finite elements and the primary unknown fields of the problem, $\mathbf{u}$ and f^{nl}, are

approximated within each element using appropriately selected shape functions; the original BVP is reduced to the solution of an algebraic system of nonlinear equations which are solved incrementally for the nodal displacements and nodal values of the non-local porosity. In every element at every time instant, one can write the following interpolations:

$$\underset{M\times 1}{\left\{u(\mathbf{x})\right\}} = \underset{M\times n}{\left[N_u(\mathbf{x})\right]}\underset{n\times 1}{\left\{d^e\right\}}, \qquad \underset{M\times 1}{\left\{\ddot{u}(\mathbf{x})\right\}} = \underset{M\times n}{\left[N_u(\mathbf{x})\right]}\underset{n\times 1}{\left\{\ddot{d}^e\right\}}, \qquad \underset{M\times 1}{\left\{\upsilon^\star(\mathbf{x})\right\}} = \underset{M\times n}{\left[N_u(\mathbf{x})\right]}\underset{n\times 1}{\left\{d^{e^\star}\right\}} \tag{5.17}$$

$$f^{\mathrm{nl}}(\mathbf{x}) = \underset{1\times n}{\lfloor N_f(\mathbf{x})\rfloor}\underset{n\times 1}{\left\{d^e\right\}}, \qquad f^\star(\mathbf{x}) = \underset{1\times n}{\lfloor N_f(\mathbf{x})\rfloor}\underset{n\times 1}{\left\{d^{e^\star}\right\}} \tag{5.18}$$

so that

$$\underset{N\times 1}{\left\{D(\mathbf{x})\right\}} = \underset{N\times n}{\left[B_u(\mathbf{x})\right]}\underset{n\times 1}{\left\{d^e\right\}}, \qquad \underset{N\times 1}{\left\{D^\star(\mathbf{x})\right\}} = \underset{N\times n}{\left[B_u(\mathbf{x})\right]}\underset{n\times 1}{\left\{d^{e^\star}\right\}} \tag{5.19}$$

$$\underset{M\times 1}{\left\{\nabla f^{\mathrm{nl}}(\mathbf{x})\right\}} = \underset{M\times n}{\left[B_f(\mathbf{x})\right]}\underset{n\times 1}{\left\{d^e\right\}}, \qquad \underset{M\times 1}{\left\{\nabla f^\star(\mathbf{x})\right\}} = \underset{M\times n}{\left[B_f(\mathbf{x})\right]}\underset{n\times 1}{\left\{d^{e^\star}\right\}} \tag{5.20}$$

where $M = 1, N = 1$, for one-dimensional problems, $M = 2, N = 4$ for two-dimensional, $M = 3, N = 6$ for three-dimensional problems and n is the number of the total nodal unknowns of the element. In the latter expressions, $[N_u(\mathbf{x})]$, $\lfloor N_f(\mathbf{x})\rfloor$ denote the matrices of the shape functions, $[B_u(\mathbf{x})]$, $[B_f(\mathbf{x})]$ are the matrices of the shape functions' spatial derivatives, and $\left\{d^e\right\}$, $\left\{\ddot{d}^e\right\}$, $\left\{d^{e^\star}\right\}$ denote the vectors of nodal unknowns, nodal accelerations and virtual nodal unknowns respectively.

Introducing now the vector $\lfloor X^\star\rfloor$ of global virtual unknowns, the matrix mappings of the rest of the quantities in the weak formulation, i.e.,

$$\boldsymbol{\sigma} \to \underset{N\times 1}{\left\{\sigma\right\}} \quad , \quad \hat{\mathbf{t}} \to \underset{M\times 1}{\left\{\hat{t}\right\}} \quad , \quad \mathbf{b} \to \underset{M\times 1}{\left\{b\right\}} \tag{5.21}$$

and substituting (5.17)–(5.20) and (5.21) into (5.15)–(5.16), one arrives at the following expressions:

$$W_u = \underset{1\times N_T}{\lfloor X^\star\rfloor} \mathop{\mathrm{A}}_{e=1}^{\mathrm{NELEM}} \left\{ \int_{\mathcal{V}^e} \underset{n\times M}{\left[N_u\right]^T}\underset{M\times 1}{\left\{b\right\}} d\mathcal{V} + \int_{\partial\mathcal{V}^e} \underset{n\times M}{\left[N_u\right]^T}\underset{M\times 1}{\left\{\hat{t}\right\}} d\mathcal{S} - \int_{\mathcal{V}^e} \underset{n\times M}{\left[B_u\right]^T}\underset{N\times 1}{\left\{\sigma\right\}} d\mathcal{V} - \right.$$
$$\left. - \int_{\mathcal{V}^e} \left(\rho \underset{n\times M}{\left[N_u\right]^T}\underset{M\times n}{\left[N_u\right]} d\mathcal{V} \right) \underset{n\times 1}{\left\{d^e\right\}} \right\} = 0 \tag{5.22}$$

$$W_f = \underset{1\times N_T}{\lfloor X^\star\rfloor} \mathop{\mathrm{A}}_{e=1}^{\mathrm{NELEM}} \left\{ \int_{\mathcal{V}^e} \left[\left(\underset{1\times n}{\lfloor N_f\rfloor}\underset{n\times 1}{\left\{d^e\right\}} - f \right) \underset{n\times 1}{\left\{N_f\right\}} + \ell^2 \underset{n\times M}{\left[B_f\right]^T}\underset{M\times n}{\left[B_f\right]}\underset{n\times 1}{\left\{d^e\right\}} \right] d\mathcal{V} \right\} = 0 \tag{5.23}$$

where N_T denotes the total number of nodal degrees of freedom in the model, NELEM the total number of elements in the mesh, and "A_e" denotes the assembly operator. Since

expressions (5.22), (5.23) hold $\forall\ \lfloor X^\star \rfloor$, then we arrive at the following discretized problem

$$\underset{N_T\times 1}{\left\{R_u\right\}} = \overset{\text{NELEM}}{\underset{e=1}{\mathbf{A}}} \left\{ \underset{n\times 1}{\left\{f^e_{\text{ext}}\right\}} - \underset{n\times 1}{\left\{f^e_{\text{int}}\right\}} - \underset{n\times n}{\left[m^e\right]} \underset{n\times 1}{\left\{d^e\right\}} \right\} = \underset{N_T\times 1}{\left\{0\right\}} \tag{5.24}$$

$$\underset{N_T\times 1}{\left\{R_f\right\}} = \overset{\text{NELEM}}{\underset{e=1}{\mathbf{A}}} \underset{n\times 1}{\left\{r^e_f\right\}} = \underset{N_T\times 1}{\left\{0\right\}} \tag{5.25}$$

with

$$\underset{n\times n}{\left[m^e\right]} = \int_{\mathcal{V}^e} \rho \underset{n\times M}{\left[N_u\right]}^T \underset{M\times n}{\left[N_u\right]} d\mathcal{V} \tag{5.26}$$

$$\underset{n\times 1}{\left\{f^e_{\text{ext}}\right\}} = \int_{\mathcal{V}^e} \underset{n\times M}{\left[N_u\right]}^T \underset{M\times 1}{\left\{b\right\}} d\mathcal{V} + \int_{\partial\mathcal{V}^e} \underset{n\times M}{\left[N_u\right]}^T \underset{M\times 1}{\left\{\hat{t}\right\}} d\mathcal{S}, \qquad \underset{n\times 1}{\left\{f^e_{\text{int}}\right\}} = \int_{\mathcal{V}^e} \underset{n\times N}{\left[B_u\right]}^T \underset{N\times 1}{\left\{\sigma\right\}} d\mathcal{V} \tag{5.27}$$

$$\underset{n\times 1}{\left\{r^e_f\right\}} = \int_{\mathcal{V}^e} \left[\left(\underset{n\times 1}{\left\{N_f\right\}} \underset{1\times n}{\lfloor N_f \rfloor} + \ell^2 \underset{n\times M}{\left[B_f\right]}^T \underset{M\times n}{\left[B_f\right]} \right) \underset{n\times 1}{\left\{d^e\right\}} - f \underset{n\times 1}{\left\{N_f\right\}} \right] d\mathcal{V} \tag{5.28}$$

where $[m^e]$ is the element mass matrix, $\left\{f^e_{\text{ext}}\right\}, \left\{f^e_{\text{int}}\right\}$ are the vectors of the element "external" and "internal" forces respectively and $\left\{r^e_f\right\}$ is the element residual vector for the modified Helmholtz problem. Equations (5.24)–(5.25) are sets of nonlinear equations for the global nodal unknowns of the problem. If an *implicit* scheme is used, these equations are solved in each increment using an iterative algorithm (e.g., Newton-Raphson) until specific convergence criteria are met; in this case, the integration scheme implemented is unconditionally stable but it involves high computational costs, especially for models with a large number of degrees of freedom. In *explicit* integration schemes, no iterations or Jacobians are required but such methods are only conditionally stable. They allow however for the solution of various classes of highly nonlinear problems (i.e., contact problems, forming processes, impact, crack propagation etc.) where implicit methods usually fail to provide a solution due to severe convergence issues of the iterative scheme.

It should be noted that the values of stresses and internal variables are required for the solution of equations (5.24)–(5.25) in each increment; these are provided from the numerical integration of the constitutive equations at the local Gauss integration points of each finite element. In the following we propose an algorithm for the numerical integration of the constitutive equations which is implemented in the general-purpose finite element code ABAQUS .

5.2.1 Numerical integration of the non-local constitutive equations

In the context of finite element analysis, the solution of the corresponding BVP is developed incrementally and the constitutive equations that model the problem have to be integrated numerically at the local Gauss integration points of each finite element. The method of "rotation neutralized" description of the spatial equations (see p. 290 in Simo and Hughes (1998)) is used herein which is proved to ensure the material frame indifference of the constitutive equations. The involved equations result in a form similar to infinitesimal theory,

allowing for easy computational implementation. The numerical integration of the constitutive equations is similar to that used for the Gurson model and is based on the methodology of Aravas (1987). An outline is given in the following.

During a time interval $[t_n, t_{n+1}]$ the deformation gradient, stresses, set of state variables, and the value of the non-local porosity ($\mathbf{F}_n$, $\boldsymbol{\sigma}_n$, $\mathbf{q}_n$, f_n^{nl}) at the beginning of the increment (i.e., at time t_n) as well as the deformation gradient and non-local porosity ($\mathbf{F}_{n+1}$, f_{n+1}^{nl}) at the end of the increment (i.e., at time t_{n+1}) are known and the problem is to determine the solution ($\boldsymbol{\sigma}_{n+1}$, $\mathbf{q}_{n+1}$) at the end of the time increment. In addition, if an implicit scheme is used for the solution of the global problem, the "element Jacobians" $\partial\boldsymbol{\sigma}/\partial\mathbf{E}$, $\partial\boldsymbol{\sigma}/\partial f^{\mathrm{nl}}$, $\partial f/\partial\mathbf{E}$ and $\partial f/\partial f^{\mathrm{nl}}$ at the end of the time increment need to be calculated. These derivatives are necessary for the evaluation of the global problem's Jacobian for the determination of the correction to the global nodal unknowns.

Let $\mathbf{F}$ be the deformation gradient, which is defined relative to the configuration at the beginning of the time increment under consideration. Then, the time variation of $\mathbf{F}$ during the corresponding time increment $[t_n, t_{n+1}]$ can be written as:

$$\mathbf{F}(t) = \Delta\mathbf{F}(t) \cdot \mathbf{F}_n = \mathbf{R}(t) \cdot \mathbf{U}(t) \cdot \mathbf{F}_n \ , \qquad t \in [t_n, t_{n+1}] \tag{5.29}$$

where $\mathbf{R}(t)$, $\mathbf{U}(t)$ are the rotation and stretch tensors of the right polar decomposition associated with $\Delta\mathbf{F}(t)$. Also, the velocity gradient tensor $\mathbf{L}$ can be written in terms of $\mathbf{F}$ as:

$$\mathbf{L}(t) = \dot{\mathbf{F}}(t) \cdot \mathbf{F}^{-1}(t) \tag{5.30}$$

Using (5.30) and (5.29), one can now write the rate-of-deformation $\mathbf{D}(t)$ and spin $\mathbf{W}(t)$ tensors as the symmetric and skew-symmetric parts of the velocity gradient, i.e.,

$$\begin{aligned} \mathbf{D}(t) &\equiv [\dot{\mathbf{F}}(t) \cdot \mathbf{F}^{-1}(t)]^{(s)} = [\Delta\dot{\mathbf{F}}(t) \cdot \Delta\mathbf{F}^{-1}(t)]^{(s)} \\ \mathbf{W}(t) &\equiv [\dot{\mathbf{F}}(t) \cdot \mathbf{F}^{-1}(t)]^{(a)} = [\Delta\dot{\mathbf{F}}(t) \cdot \Delta\mathbf{F}^{-1}(t)]^{(a)} \end{aligned} \tag{5.31}$$

where the superscripts "s" and "a" denote the symmetric and anti-symmetric part of a tensor respectively. If the assumption that the Lagrangian triad associated with $\Delta\mathbf{F}(t)$ (i.e., the eigenvectors of $\mathbf{U}(t)$) remains constant in the time interval $[t_n, t_{n+1}]$ is adopted then, it can be proved that $\mathbf{D}(t)$ and $\mathbf{W}(t)$ can be given in terms of the logarithmic strain $\mathbf{E}^{\ln}(t) \equiv \mathbf{E}(t)$:

$$\mathbf{D}(t) = \mathbf{R}(t) \cdot \dot{\mathbf{E}}(t) \cdot \mathbf{R}^T(t) \qquad \text{and} \qquad \mathbf{W}(t) = \dot{\mathbf{R}}(t) \cdot \mathbf{R}^T(t) \tag{5.32}$$

where $\mathbf{E}(t) = \ln\mathbf{U}(t)$ is defined relative to the configuration at time t_n. Moreover we can define the "rotation neutralized" version of the Cauchy stress as (Nagtegaal and Veldpaus, 1984):

$$\hat{\boldsymbol{\sigma}}(t) = \mathbf{R}^T(t) \cdot \boldsymbol{\sigma}(t) \cdot \mathbf{R}(t) \qquad \text{and} \qquad \hat{\mathbf{n}}^{(i)}(t) = \mathbf{R}^T \cdot \mathbf{n}^{(i)}(t) \tag{5.33}$$

Using now (5.32) and (5.33) one can readily show that the Jaumman stress rate is related to the material derivative of the rotation neutralized stress $\hat{\boldsymbol{\sigma}}$ by the expression:

$$\overset{\nabla}{\boldsymbol{\sigma}}(t) = \mathbf{R}(t) \cdot \dot{\hat{\boldsymbol{\sigma}}}(t) \cdot \mathbf{R}^T(t) \tag{5.34}$$

It should be noted here that at the start of the increment ($t = t_n$), the following relations hold:

$$\mathbf{F}_n = \mathbf{R}_n = \mathbf{U}_n = \boldsymbol{\delta} \ , \ \hat{\boldsymbol{\sigma}}_n = \boldsymbol{\sigma}_n \quad \text{and} \quad \mathbf{E}_n = \mathbf{0} \tag{5.35}$$

whereas at the end of the increment ($t = t_{n+1}$) one has:

$$\Delta\mathbf{F}_{n+1} = \mathbf{F}_{n+1}\cdot\mathbf{F}_n = \mathbf{R}_{n+1}\cdot\mathbf{U}_{n+1} = \text{known}, \qquad \mathbf{U}_{n+1} = \sum_{i=1}^{3}\lambda_i^{(\Delta\mathbf{F})}\mathbf{N}_i^{(\Delta\mathbf{F})}\mathbf{N}_i^{(\Delta\mathbf{F})} = \text{known}$$
$$\mathbf{R}_{n+1} = \Delta\mathbf{F}_{n+1}\cdot\mathbf{U}_{n+1}^{-1} = \text{known}, \qquad \mathbf{E}_{n+1} = \ln\mathbf{U}_{n+1} = \text{known} \tag{5.36}$$

where $\lambda_i^{(\Delta\mathbf{F})}$, $\mathbf{N}_i^{(\Delta\mathbf{F})}$ correspond to the eigenvalues and eigenvectors of $\Delta\mathbf{F}$ respectively. Taking into account the *mathematical isotropy* of the yield function Φ, it follows that $\mathbf{N}$, $g_{\bar{\varepsilon}^p}$ and g_f are also isotropic functions of their arguments, i.e., they are such that:

$$\mathbf{N}(\mathbf{R}\cdot\boldsymbol{\sigma}\cdot\mathbf{R}^T, f; w) = \mathbf{R}\cdot\mathbf{N}(\boldsymbol{\sigma}, f; w)\cdot\mathbf{R}^T \tag{5.37}$$
$$g_{\bar{\varepsilon}^p}(\mathbf{R}\cdot\boldsymbol{\sigma}\cdot\mathbf{R}^T, \bar{\varepsilon}^p, f; w) = g_{\bar{\varepsilon}^p}(\boldsymbol{\sigma}, \bar{\varepsilon}^p, f; w) \tag{5.38}$$
$$g_f(\mathbf{R}\cdot\boldsymbol{\sigma}\cdot\mathbf{R}^T, \bar{\varepsilon}^p, f; w) = g_f(\boldsymbol{\sigma}, \bar{\varepsilon}^p, f; w) \tag{5.39}$$

In view of the above, the non-local elastic-plastic constitutive equations (2.44), (4.15), $(4.18)_1$, (2.64), (4.20) and (4.21) can be written as:

$$\dot{\mathbf{E}} = \dot{\mathbf{E}}^e + \dot{\mathbf{E}}^p \tag{5.40}$$
$$\dot{\mathbf{E}}^p = \dot{\lambda}\mathbf{N}(\hat{\boldsymbol{\sigma}}, f^{\text{nl}}, w) = \dot{\lambda}\hat{\mathbf{N}} \tag{5.41}$$
$$\dot{\hat{\boldsymbol{\sigma}}} = \hat{\boldsymbol{\mathcal{L}}} : \dot{\mathbf{E}} - \hat{\boldsymbol{\mathcal{L}}} : \dot{\mathbf{E}}^p \tag{5.42}$$
$$\dot{\bar{\varepsilon}}^p = \frac{\hat{\boldsymbol{\sigma}} : \dot{\mathbf{E}}^p}{(1 - f^{\text{nl}})\sigma_y(\bar{\varepsilon}^p)} \tag{5.43}$$
$$\dot{f} = (1 - f^{\text{nl}})\dot{E}^p_{kk} \tag{5.44}$$
$$\Phi(\hat{\boldsymbol{\sigma}}, f^{\text{nl}}, \bar{\varepsilon}^p, w) = 0 \tag{5.45}$$

where $\hat{\mathcal{L}}_{ijkl} = R_{mi}R_{nj}R_{pk}R_{ql}\mathcal{L}_{mnpq}$. The constitutive equations (5.40)–(5.45) are now in the rotation-neutralized form and only contain standard material derivatives. This allows for simple numerical schemes to be used for their integration. In the following we use a combination of simple forward and backward Euler schemes to integrate the constitutive equations[2] The procedure is outlined below:

In particular, equation (5.40) can be integrated exactly yielding:

$$\Delta\mathbf{E} = \Delta\mathbf{E}^e + \Delta\mathbf{E}^p \tag{5.46}$$

where the notation $\Delta(\ ) = (\ )_{n+1} - (\ )_n$ is used. A backward Euler scheme is used for the integration of the flow rule (5.41) and the resulting incremental equation can be written in terms of two scalar quantities $\Delta\varepsilon_m$ and $\Delta\varepsilon_{eq}$:

$$\Delta\mathbf{E}^p = \Delta\lambda\hat{\mathbf{N}}_{n+1} = \frac{1}{3}\Delta\lambda\frac{\partial\Phi}{\partial\hat{p}}\bigg|_{n+1}\boldsymbol{\delta} + \Delta\lambda\frac{\partial\Phi}{\partial\hat{\sigma}_e}\bigg|_{n+1}\hat{\mathbf{n}}_{n+1} = \frac{1}{3}\Delta\varepsilon_m\boldsymbol{\delta} + \Delta\varepsilon_{eq}\hat{\mathbf{n}}_{n+1} \tag{5.47}$$
$$\Delta\varepsilon_m = \Delta\lambda\frac{\partial\Phi}{\partial\hat{p}}\bigg|_{n+1}, \qquad \Delta\varepsilon_{eq} = \Delta\lambda\frac{\partial\Phi}{\partial\hat{\sigma}_e}\bigg|_{n+1}, \qquad \hat{\mathbf{n}}_{n+1} = \frac{3}{2\hat{\sigma}_e|_{n+1}}\hat{\mathbf{s}}_{n+1} = \frac{3}{2\hat{\sigma}_e^e}\mathbf{s}^e = \mathbf{n}^e \tag{5.48}$$

[2]In general numerical integration algorithms such as the midpoint rule or other Runge-Kutta methods (e.g., see Cao et al. (2015)) could be used for the integration of the constitutive equations.

where the derivatives $\partial\Phi/\partial\hat{p}$ and $\partial\Phi/\partial\hat{\sigma}_e$ at the end of the increment can be calculated from equations (4.19). A forward Euler scheme is employed for the numerical integration of elasticity equation (5.42):

$$\hat{\boldsymbol{\sigma}}_{n+1} = \boldsymbol{\sigma}_n + \boldsymbol{\mathcal{L}}_n : \Delta\mathbf{E} - \boldsymbol{\mathcal{L}}_n : \Delta\mathbf{E}^p = \frac{2}{3}\hat{\sigma}_e|_{n+1}\hat{\mathbf{n}}_{n+1} + \hat{p}_{n+1}\boldsymbol{\delta} \tag{5.49}$$

$$\hat{p}_{n+1} = p^e - \kappa\Delta\varepsilon_m, \qquad \hat{\sigma}_e|_{n+1} = \sigma_e^e - 3\mu\Delta\varepsilon_{eq} \tag{5.50}$$

where the fact that $\hat{\boldsymbol{\sigma}}_n = \boldsymbol{\sigma}_n$ and $\hat{\boldsymbol{\mathcal{L}}}_n = \boldsymbol{\mathcal{L}}_n$ was taken into account. In equations $(5.48)_3$ and (5.49)–(5.50) $\mathbf{s}^e$, p^e, and σ_e^e denote the deviatoric stress tensor, hydrostatic stress, and von Mises equivalent stress respectively related to the standard "elastic predictor" tensor $\boldsymbol{\sigma}^e = \boldsymbol{\sigma}_n + \boldsymbol{\mathcal{L}}_n : \Delta\mathbf{E}$. Finally, a backward Euler scheme is employed for the numerical integration of the evolution equations (5.43), (5.44) for the equivalent plastic strain and the local porosity:

$$\bar{\varepsilon}^p_{n+1} = \bar{\varepsilon}^p_n + \Delta\bar{\varepsilon}^p, \qquad \Delta\bar{\varepsilon}^p = \frac{\hat{\boldsymbol{\sigma}}_{n+1} : \Delta\mathbf{E}^p}{(1-f^{\mathrm{nl}}_{n+1})\sigma_y|_{n+1}} = \frac{\hat{p}_{n+1}\Delta\varepsilon_m + \hat{\sigma}_e|_{n+1}\Delta\varepsilon_{eq}}{(1-f^{\mathrm{nl}}_{n+1})\sigma_y|_{n+1}} \tag{5.51}$$

$$f_{n+1} = f_n + \Delta f, \qquad \Delta f = (1-f^{\mathrm{nl}}_{n+1})\Delta E^p_{kk} = (1-f^{\mathrm{nl}}_{n+1})\Delta\varepsilon_m \tag{5.52}$$

The primary unknowns are $\Delta\varepsilon_m, \Delta\varepsilon_{eq}$ and the yield criterion (5.45) along with equations $(5.48)_1$ and $(5.48)_2$:

$$F_1(\Delta\varepsilon_m, \Delta\varepsilon_{eq}) \equiv \Phi(\hat{\sigma}_e|_{n+1}, \hat{p}_{n+1}, f^{\mathrm{nl}}_{n+1}, \bar{\varepsilon}^p_{n+1}, w) = 0 \tag{5.53}$$

$$F_2(\Delta\varepsilon_m, \Delta\varepsilon_{eq}) \equiv \Delta\varepsilon_m \left.\frac{\partial\Phi}{\partial\hat{\sigma}_e}\right|_{n+1} - \Delta\varepsilon_{eq} \left.\frac{\partial\Phi}{\partial\hat{p}}\right|_{n+1} = 0 \tag{5.54}$$

are considered as the basic equations, where $\hat{\sigma}_e|_{n+1}, \hat{p}_{n+1}, f_{n+1}, \bar{\varepsilon}^p_{n+1}$ are given in terms of $\Delta\varepsilon_m, \Delta\varepsilon_{eq}$ from equations (5.50), (5.51) and (5.52). Equations (5.53)–(5.54) constitute a system of nonlinear equations for $\Delta\varepsilon_m, \Delta\varepsilon_{eq}$ which is solved using Newton's method. After $\Delta\varepsilon_m, \Delta\varepsilon_{eq}$ are determined, the stress tensor, the equivalent plastic strain and local porosity can be calculated at the end of the increment using equations (5.49)–(5.52).

Remark 15. Alternatively, the implicit numerical integration algorithm proposed recently by Bouby et al. (2023) in the context of Generalized Standard Materials (GSM) could be used. This would require though the introduction of the "Lagrangian porosity" as an additional microstructural variable. In this work, the proposed integration procedure model is efficiently implemented in the general-purpose finite element code ABAQUS.

5.3 An efficient implementation using ABAQUS

Computational implementation of the implicit gradient isotropic projection model using the finite element method would, in principle, require coding both the numerical integration algorithm for the constitutive equations and the discretized equations (5.24)–(5.28) for the determination of the nodal unknowns. In ABAQUS/Standard and ABAQUS/Explicit, this can be done directly by using the User ELement UEL and VUEL user-subroutines respectively which allow to create "custom elements" with additional degrees of freedom in order to simulate complex coupled problems and/or multi-physics phenomena. In practice, the writing of such user-subroutines requires considerable expertise and extensive testing prior

to their use in "real-world" problems. Also, multiple such subroutines might need to be developed if different element types of different interpolation order (i.e., linear, quadratic etc.) are to be considered.

An alternative, more efficient methodology for the implementation of implicit gradient plasticity mechanical models for both quasi-static and dynamic problems using ABAQUS has been recently utilized by several authors (Azinpour et al., 2018; Seupel et al., 2018; Papadioti et al., 2019; Aravas and Papadioti, 2021). The approach is based on the utilization of an analogy between the BVP (4.10)–(4.11) for the non-local porosity field and the heat transfer BVP allowing the use of the built-in coupled temperature-displacement analysis option for the solution of the non-local problem. However, it should be noted that when there is more than one non-local variables in the model (e.g., as in Tuhami et al. (2022)), the corresponding numerical implementation is not as simple, because the thermomechanical analogy cannot be used for the additional non-local variables. In this case, the development of user-defined elements cannot be avoided. This thermomechanical analogy has been also used extensively for the solution of transient stress-diffusion problems in the finite element modeling of hydrogen embrittlement in metals (Oh et al., 2010; Moriconi et al., 2014; Barrera et al., 2016; Charles et al., 2021) as well as for the implementation of phase field fracture models (Azinpour et al., 2018; Wu and Huang, 2020; Navidtehrani et al., 2021).

Since only one non-local variable is introduced in the present formulation, this alternative approach is employed in this work for the implementation of the gradient isotropic projection model using both the implicit (i.e., ABAQUS/Standard) and explicit (i.e., ABAQUS/Explicit) capabilities of ABAQUS FE code. The necessary variable identifications and assumptions in each case are discussed in the following sections.

5.3.1 Implementation in ABAQUS/Standard

In the case of *quasi-static* problems, the non-local model can be introduced through a UMAT user-subroutine along with the input file command *COUPLED TEMPERATURE-DISPLACEMENT and ABAQUS/Standard solver can be used to obtain a solution. The *steady-state* heat transfer BVP for an isotropic material which is solved by ABAQUS in a body with current volume $\mathcal{V}$ bounded by a surface $\partial\mathcal{V}$ reads

$$k\nabla^2 T + r\left(\Delta\mathbf{E}, T\right) = 0, \quad \text{in} \quad \mathcal{V} \tag{5.55}$$

$$k\boldsymbol{\nabla} T \cdot \mathbf{n} = \hat{q}, \quad \text{on} \quad \partial\mathcal{V} \tag{5.56}$$

where T is the temperature, k is the thermal conductivity, r the thermal power per unit volume provided by a heat source in $\mathcal{V}$, $\hat{q}$ the prescribed thermal power per unit area entering $\mathcal{V}$ through $\partial\mathcal{V}$, and $\Delta\mathbf{E}$ a strain increment properly defined in terms of nodal displacements (see ABAQUS manuals and Hughes and Winget (1980)). Comparison of the heat transfer BVP (5.55)–(5.56) with the BVP (4.10)–(4.11) for the non-local problem shows that, the non-local porosity field f^{nl} can be identified with the temperature field in the coupled thermal-mechanical analysis provided that the following correspondence is used[3]:

$$T \leftrightarrow f^{\text{nl}}, \qquad k \leftrightarrow \ell^2, \qquad r\left(\Delta\mathbf{E}(\mathbf{u}), T\right) \leftrightarrow f\left(\mathbf{u}, f^{\text{nl}}\right) - f^{\text{nl}}, \qquad \hat{q} \leftrightarrow 0, \tag{5.57}$$

It should be noted that the characteristic length ℓ is defined for an analysis in the pre-processing stage with the *CONDUCTIVITY input file command (i.e., $\ell = \sqrt{k}$). During

[3]The modified Helmholtz equation can be written in the form $\ell^2\,\nabla^2 f^{\text{nl}} + (f - f^{\text{nl}}) = 0$, which is similar to the steady-state heat transfer equation (5.55).

a time interval $[t_n, t_{n+1}]$ the non-local porosity at the beginning of the increment and its variation $(f_n^{\rm nl}, \Delta f^{\rm nl})$ are given through the variables "TEMP" and "DTEMP" respectively and the thermal power term r can be provided after the integration of the constitutive equations through variable "RPL".

For the solution of the global coupled "thermal-mechanical" problem, ABAQUS/Standard uses the Newton-Raphson iterative method and Jacobians need to be calculated at every increment. For this purpose, the quantities

$$\frac{1}{J}\frac{\partial \Delta\boldsymbol{\tau}}{\partial \Delta\mathbf{E}}, \ \frac{1}{J}\frac{\partial \Delta\boldsymbol{\tau}}{\partial \Delta T}, \ \frac{\partial r}{\partial \Delta\mathbf{E}}, \ \frac{\partial r}{\partial \Delta T}, \qquad \text{(DDSDDE, DDSDDT, DRPLDE, DRPLDT in UMAT)} \tag{5.58}$$

are calculated and stored in UMAT at the end of every increment, where $\boldsymbol{\tau}$ is the Kirchoff stress tensor (i.e., $\boldsymbol{\tau} = J\boldsymbol{\sigma}$) and $J = \det \mathbf{F}$. The derivatives in (5.58) can be approximated to first order by using the expressions derived for the tangent modulus in Section 4.2.3. Using expressions $(4.23)_1$ and $(4.25)_1$ we have that:

$$\overset{\nabla}{\boldsymbol{\tau}} = J\left(\boldsymbol{\mathcal{L}}^{\rm nl} + \boldsymbol{\sigma}\boldsymbol{\delta}\right) : \mathbf{D} + J\mathbf{A}\dot{f}^{\rm nl} \qquad \text{or} \qquad \Delta\boldsymbol{\tau} \approx J\left(\boldsymbol{\mathcal{L}}^{\rm nl} + \boldsymbol{\sigma}\boldsymbol{\delta}\right) : \Delta\mathbf{E} + J\mathbf{A}\,\Delta f^{\rm nl} \tag{5.59}$$

$$\dot{f} = \mathbf{B}^{\rm nl} : \mathbf{D} + K\dot{f}^{\rm nl} \qquad \text{or} \qquad \Delta f \approx \mathbf{B}^{\rm nl} : \Delta\mathbf{E} + K\,\Delta f^{\rm nl} \tag{5.60}$$

In view of equations (5.59), (5.60), the "element Jacobians" (5.58) can be calculated at the end of the increment as:

$$\frac{1}{J}\frac{\partial \Delta\boldsymbol{\tau}}{\partial \Delta\mathbf{E}} = \frac{\partial \boldsymbol{\sigma}_{n+1}}{\partial \mathbf{E}_{n+1}} + \boldsymbol{\sigma}_{n+1}\boldsymbol{\delta} \approx \boldsymbol{\mathcal{L}}^{\rm nl}_{n+1} + \boldsymbol{\sigma}_{n+1}\boldsymbol{\delta}, \qquad \frac{1}{J}\frac{\partial \Delta\boldsymbol{\tau}}{\partial \Delta T} \equiv \frac{1}{J}\frac{\partial \Delta\boldsymbol{\tau}}{\partial \Delta f^{\rm nl}} = \frac{\partial \boldsymbol{\sigma}_{n+1}}{\partial f^{\rm nl}_{n+1}} \approx \mathbf{A}_{n+1} \tag{5.61}$$

$$\frac{\partial r}{\partial \Delta\mathbf{E}} \equiv \frac{\partial f_{n+1}}{\partial \Delta\mathbf{E}_{n+1}} = \mathbf{B}^{\rm nl}_{n+1}, \qquad \frac{\partial r}{\partial \Delta T} \equiv \frac{\partial r}{\partial \Delta f^{\rm nl}} = \frac{\partial f_{n+1}}{\partial f^{\rm nl}_{n+1}} - 1 \approx K_{n+1} - 1 \tag{5.62}$$

Such an approximation for the Jacobians is first order accurate as $\Delta t = t_{n+1} - t_n \to 0$ (i.e., for small time increments). It should be mentioned however that such an approximation only affects the quadratic rate of convergence of the global Newton-Raphson iterations but not the accuracy of the results. A methodology for the derivation of more accurate expressions for these quantities based on the backward Euler scheme proposed for the integration of the constitutive equations is outlined in Appendix B.

5.3.2 Implementation in ABAQUS/Explicit

In the case of *dynamic* problems or quasi-static problems that *cannot be solved using an implicit scheme* due to convergence issues of the global Newton-Raphson method, the non-local model can be alternatively implemented through user-subroutines VUMAT and VDFLUX (or VHETVAL) along with the input file command *DYNAMIC TEMPERATURE-DISPLACEMENT and the ABAQUS/Explicit solver can be used to obtain a solution. The *transient* heat transfer BVP for an isotropic material which is solved by ABAQUS in a body with current volume $\mathcal{V}$ bounded by a surface $\partial\mathcal{V}$ reads

$$k\nabla^2 T + r\left(\Delta\mathbf{E}, T\right) = \rho c\dot{T}, \quad \text{in} \quad \mathcal{V} \tag{5.63}$$

$$k\boldsymbol{\nabla}T \cdot \mathbf{n} = \hat{q}, \quad \text{on} \quad \partial\mathcal{V} \tag{5.64}$$

where c is the specific heat which is defined during the pre-processing stage using the *SPECIFIC HEAT input file command in ABAQUS. Again, comparing the transient heat transfer

BVP (5.63)–(5.64) with the BVP for the non-local porosity field we have that the identifications (5.57) still hold with the additional requirement that $\rho c\dot{T} \to 0$; this implies that, the values of the current density ρ and the specific heat c must be such so that the term on right hand side of (5.63) becomes negligible. Notice that the numerical stability of the solution in this case is proportional to the product ρc. Following Papadioti et al. (2019) and Aravas and Papadioti (2021) the value of c should be chosen so that the following criterion is satisfied at all integration points of all elements throughout an analysis:

$$\rho c \frac{\Delta f^{\mathrm{nl}}}{\Delta t} \leq \mathrm{TOL}, \qquad \mathrm{TOL} \sim O(10^{-4}) \tag{5.65}$$

During a time interval $[t_n, t_{n+1}]$ the non-local porosity at the beginning and at the end of the increment $(f_n^{\mathrm{nl}}, f_{n+1}^{\mathrm{nl}})$ are given through the variables "tempOld" and "tempNew" respectively and the thermal power term r can be calculated after the integration of the constitutive equations. However, r cannot be provided through the VUMAT subroutine and has to be defined as a "non-uniform body force" (BFNU option in the *DFLUX input file command of ABAQUS/Explicit) through the VDFLUX subroutine. Also, no element Jacobians such as the ones in (5.58) need to be calculated in ABAQUS/Explicit since no iterations are performed for the determination of the global solution at each increment.

If the ABAQUS/Explicit solver is used for the solution of *quasi-static* non-local problems that cannot be solved with ABAQUS/Implicit due to convergence issues (i.e., contact problems, forming processes, impact problems, fracture etc.) the user should make sure that, in addition to the criterion (5.65), the kinetic energy E_K in the model is only a small fraction (in practice no more than 5%) of the corresponding strain energy E_{str} throughout the analysis. These energies are calculated by ABAQUS/Explicit for the whole model (variables ALLKE and ALLSE) and are given as (see energy balance section in (Abaqus, 2021)):

$$E_K = \int_{\mathcal{V}} \frac{1}{2}\rho \mathbf{v}\cdot\mathbf{v} d\mathcal{V}, \qquad E_{str} = \int_0^{\tau}\int_{\mathcal{V}} (\boldsymbol{\sigma}\cdot\mathbf{D}\, d\mathcal{V})\, d\tau \tag{5.66}$$

Remark 16. When ABAQUS/Explicit solver is used, since the integration scheme is only conditionally stable, an initial stable time increment estimate Δt_{stable}^{est} is calculated and used for the solution of the dynamic equations. This stable time increment can be chosen to be fixed or allowed to adjust during the solution. In principle, the stability limit for the explicit integration operator (with no damping) is given in terms of the highest frequency of the system. An approximate upper bound to the stability limit can be obtained from the so-called Courant–Friedrichs–Lewy (CFL) condition and is related to the smallest transit time of a dilatational wave across any of the elements in the mesh (see also the documentation of Abaqus (2021)), i.e.,

$$\Delta t_{stable}^{est} \approx \frac{L_{min}^{e}}{v_d}, \qquad v_d = \sqrt{\frac{E}{\rho_0}} \tag{5.67}$$

where L_{min}^{e} is a characteristic dimension of the smallest element in the finite element mesh and v_d is the dilatational wave speed which can be defined in terms of the materials elastic properties and mass density. Last equation shows that, the time increment used is directly proportional to the square root of the material's mass density. If a solution in the natural (true) time scale of the problem is required and the true mass density of the material is used, equation (5.67) suggests that very small time increments should be used to maintain stability; for large models with fine spatial discretizations, this can lead to significant computational

costs. For a given elastic stiffness, larger time increments can be achieved by using the *mass scaling* technique which is equivalent to artificially increasing the mass density of the material. For *quasi-static* problems, the mass density can be safely increased without loss of accuracy as long as the kinetic energy in the model remains small compared to the strain energy. However, for truly *dynamic* problems where inertial terms could potentially be important, mass scaling should be used with caution to avoid erroneous results.

5.4 Material properties used in numerical calculations

The material parameters used in the numerical simulations described in this chapter, unless otherwise specified, are summarized in Table 5.1. These values do not correspond to any particular material but are typical values found in the literature for commonly used structural steels. The value for the initial mass density ρ_0 needs to be defined in all problems used

Table 5.1 – Matrix material properties used in the numerical calculations.

Property	Symbol	Value	Units
Young's modulus	E	207	GPa
Poisson's ratio	ν	0.3	-
Initial yield strength	σ_0	250	MPa
Hardening exponent	n	10	-
Initial mass density	ρ_0	7850	$\frac{kg}{m^3}$
Specific heat	c	4×10^{-9}	$\frac{m^3\, s}{kg\, K}$

in ABAQUS/Explicit and corresponds to the typical density for structural steels, i.e., $\rho_0 = 7850\, kg/m^3$. The value of c shown in Table 5.1 was chosen so that the criterion (5.65) is satisfied at the integration points of all elements in the corresponding finite element mesh. Hardening in the matrix material, unless otherwise stated, is assumed to be described by an isotropic hardening power law of the form (3.29). Also, in the ductile fracture problems examined in this work, the criterion for macroscopic crack initiation is based on a critical value of the non-local porosity. In what follows, a representative value for the critical porosity to failure f_F is selected from the literature (e.g., see Skallerud and Zhang (1997) or more recently Aravas and Papadioti (2021)).

Proper normalization is used for all input properties related to both the mechanical and the "thermal" problem which is used for the determination of the non-local porosity. In particular, Young's modulus E, initial yield stress σ_0, initial mass density ρ_0 and specific heat c are normalized in the pre-processing stage and the corresponding normalized quantities are defined as follows.

$$\hat{E} = \frac{E}{\Sigma_{norm}}, \quad \hat{\sigma}_0 = \frac{\sigma_0}{\Sigma_{norm}}, \quad \hat{\rho}_0 = \frac{\rho_0}{(\Sigma_{norm}\, t_{norm}^2)/L_{norm}^2}, \quad \hat{c} = \frac{c}{L_{norm}/(\Sigma_{norm}\, t_{norm}\, T_{norm})} \tag{5.68}$$

where $\Sigma_{norm}, t_{norm}, L_{norm}$ and T_{norm} are normalizing parameters with dimensions of stress, time, length and temperature respectively. The values of these parameters can be chosen arbitrarily as long as a consistent unit system is used (e.g., SI units for all quantities).

5.5 Simulation of the Hole Expansion Test

The Hole Expansion Test (HET) (ISO 16630:2017 (2017)) is a test used widely in the steel industry for the determination of the local formability of a steel grade, using thin sheets of standardized dimensions. For the test, a hole of predefined diameter is created in a circular thin sheet specimen, which is then clamped between a die and a blank holder. Next, a conical punch of 60° apex angle[4] expands the initial hole until a through-thickness macroscopic crack appears. The relative difference between the diameter after rupture and the initial diameter of the specimen's inner hole defines the Hole Expansion Ratio (HER), which serves as a measure of the formability (or ductility) of the steel grade.

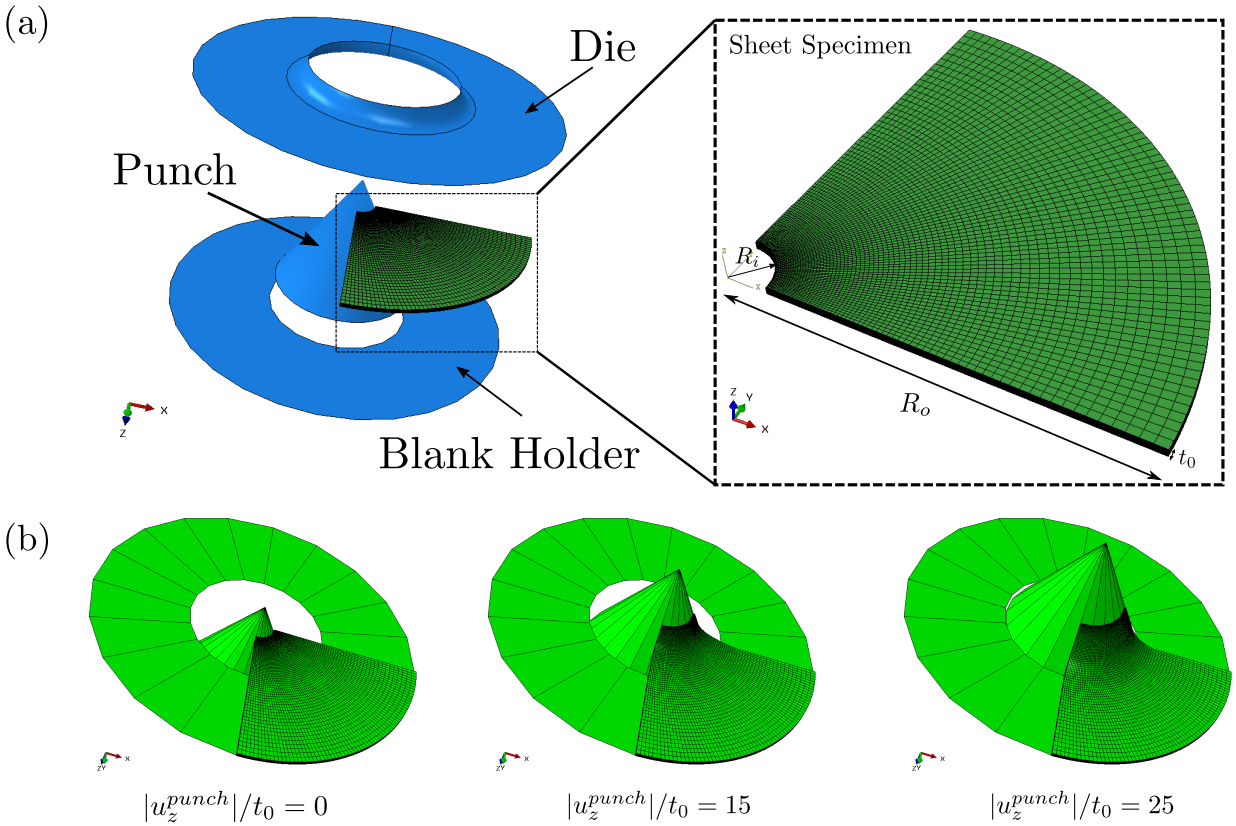

Figure 5.1 – (a) Simulation setup for the HET, which includes the rigid die, blank holder, and conical punch, along with a magnification of the circular specimen showing the mesh density used. (b) The deformed specimen at different stages of the forming process.

Combination of experimental and numerical approaches have been used in the recent years in order to get a better understanding on the parameters affecting the HER as well as the experimentally observed deformation behavior. In particular, numerical simulations have been used to study the effect of anisotropy and material model calibration (Hashimoto et al., 2010; Kuwabara et al., 2011; Lee et al., 2019) on deformation predictions, the effect of hole-edge surface quality and microstructure on the HER (Paul et al., 2014; Barnwal et al., 2020), and the effect of the constitutive model and hardening law on the thinning behavior of sheet specimens (Kim et al., 2021). In what follows, the newly proposed porous plasticity model is used to investigate the effect of different microstructural configurations (through

[4]Also a flat punch is used in other variations of the test.

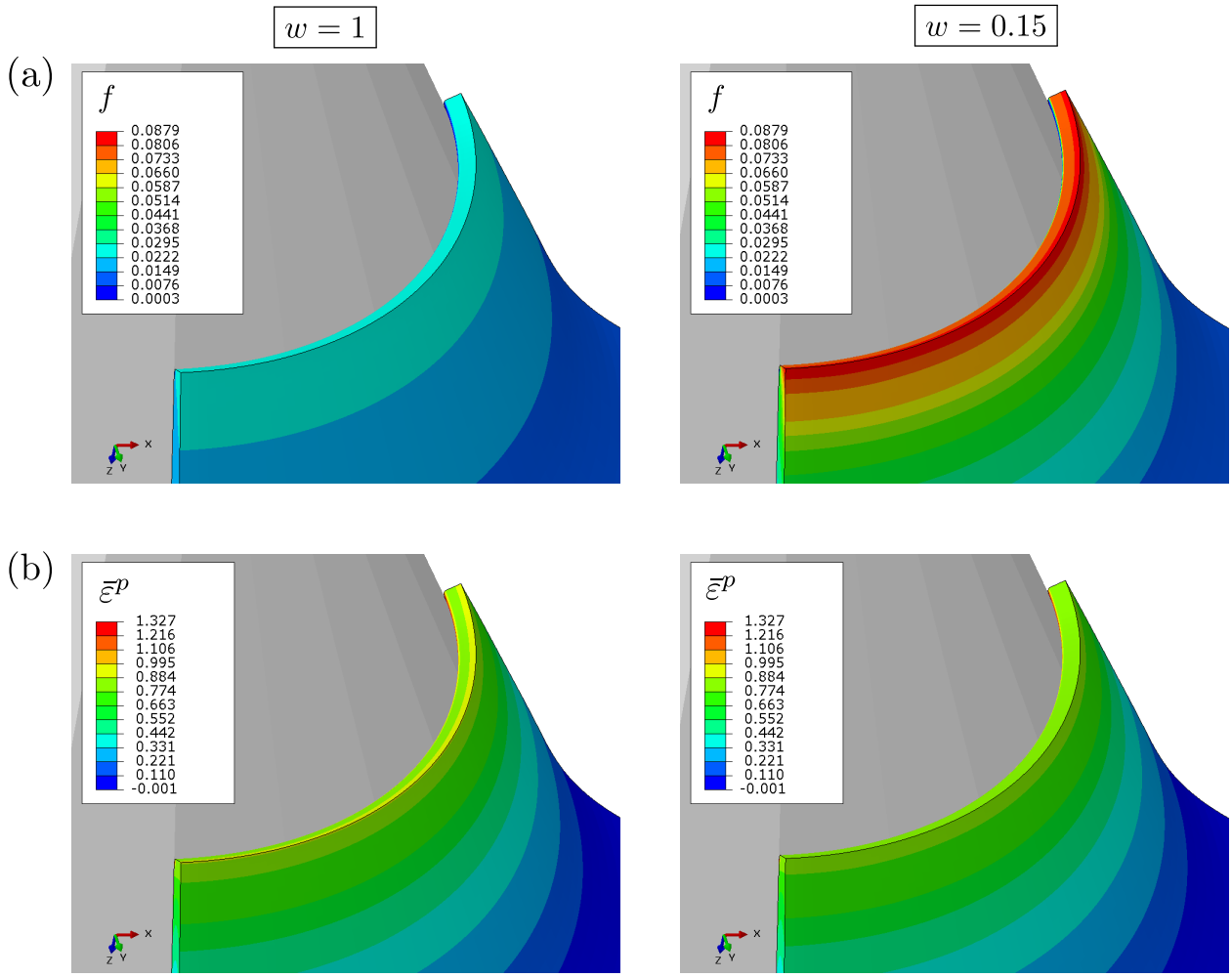

Figure 5.2 – Contours at the end of the analysis of (a) porosity f and (b) equivalent plastic strain $\bar{\varepsilon}^p$ for microstructures consisting of spherical voids ($w = 1$) and oblate voids with aspect ratio $w = 0.15$.

the void shape parameter) on the deformation fields and damage that develop during the HET.

The *local* porous model proposed in Section 2.3 has been implemented using a UMAT user-subroutine provided by the ABAQUS/Standard module allowing to numerically simulate the HET boundary value problem. Although the problem can be treated as axisymmetric, full three-dimensional simulations are intentionally performed, to demonstrate the capabilities and computational efficiency of the proposed model. The setup used for the simulations is shown in Fig. 5.1a. The blank holder, die, and the conical punch are all modeled as rigid bodies. The circular deformable specimen has an initial thickness t_0, an inner radius of $R_i = 5\,t_0$, and an outer radius $R_o = 50\,t_0$. To speed up the calculations, only one quarter of the whole specimen is considered and symmetry conditions are imposed. The mesh used consists of 104 720 eight-node hexahedral, hybrid elements with constant pressure (C3D8H in ABAQUS/Standard) and 20 elements are used throughout the thickness of the specimen. The effect of friction is not investigated here and frictionless contact is assumed between all rigid surfaces and the deformable specimen.

Two different simulations of the HET are carried out; one with a microstructure consisting

of spherical voids ($w = 1$) and another with very flat voids of aspect ratio $w = 0.15$. An initial porosity of $f_0 = 1\%$ is assumed in all cases. The simulation is carried out quasi-statically in two steps. In the first step, which is used to simulate the clamping process, a displacement of $|u_z^{blank}| = 0.011\, t_0$ is imposed on the reference node of the blank holder. During the second step, the forming process is simulated by imposing a total displacement of $|u_z^{punch}| = 25\, t_0$ on the reference node of the rigid punch. The deformed state of the thin sheet during three different stages of the process is shown in 5.1b.

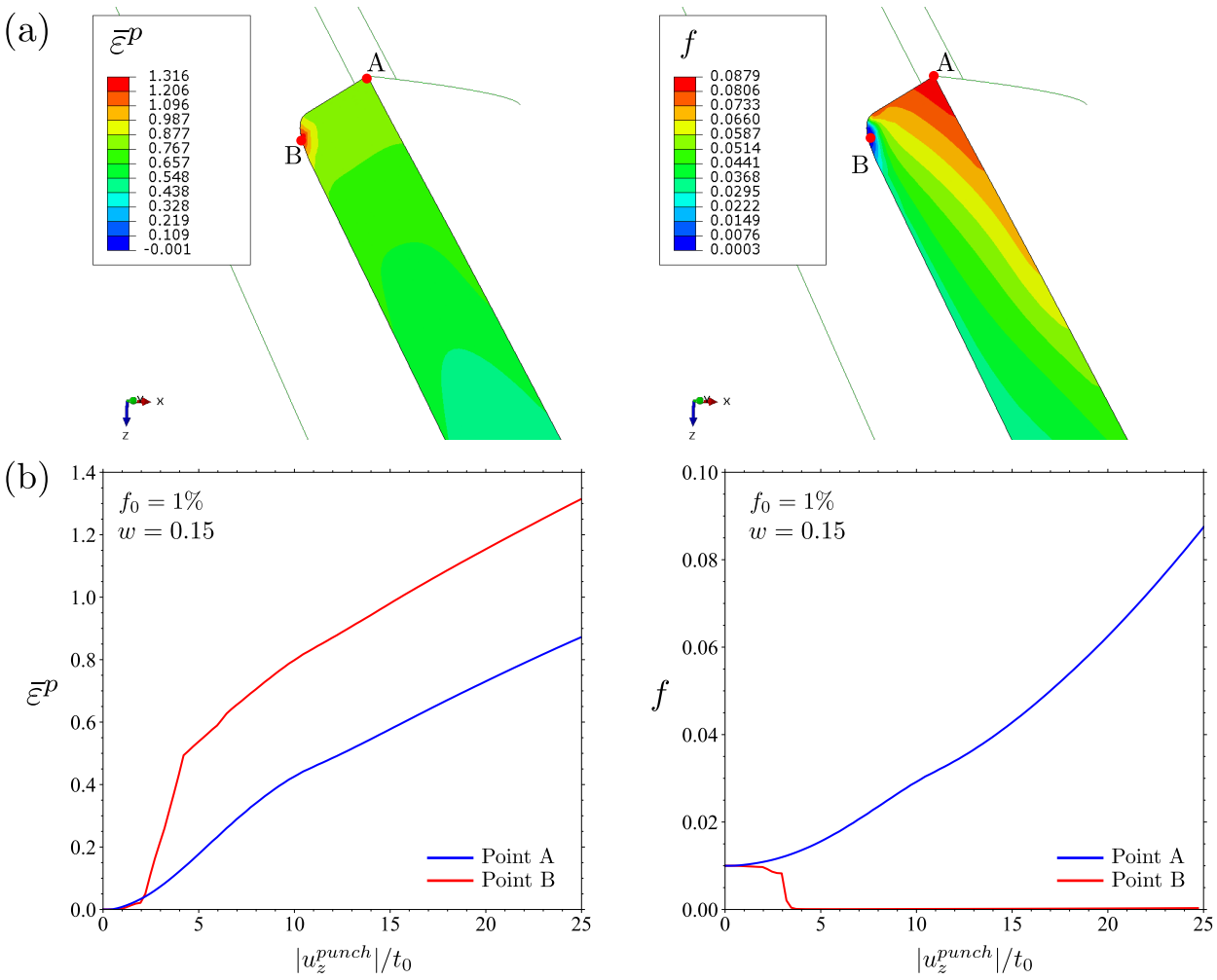

Figure 5.3 – (a) Distributions of the equivalent plastic strain $\bar{\varepsilon}^p$ and porosity f at a cross-section of the specimen at the end of the analysis for the case with aspect ratio $w = 0.15$. (b) Evolution of the corresponding variables during the forming process for points A and B.

Figure 5.2 shows contours of porosity f and equivalent plastic strain $\bar{\varepsilon}^p$ as predicted by the proposed homogenization model, for the two different microstructures, at the end of the corresponding simulations. Figure 5.2a shows that porosity evolution is substantially larger when oblate voids with an aspect ratio $w = 0.15$ are considered, showcasing the strong effect of void shape on material response. It should be also noted that the accumulated plastic strain in the structure remains essentially the same for the two different microstructures considered (Fig. 5.2b). This rather interesting result is not trivial. It indicates that, the equivalent plastic strain can remain insensitive to the underlying microstructural configuration and, thus, it might not be a sufficient measure to solely characterize damage

accumulation in a structure.

This can be further justified by examining the distributions of $\bar{\varepsilon}^p$ and f at a cross section of the specimen. Figure 5.3a shows contour plots of $\bar{\varepsilon}^p$ and f at the end of the simulation for the case with aspect ratio $w = 0.15$. Points A and B, denoted by the red dots in the contours, are the locations of maximum porosity and equivalent plastic strain in the specimen respectively. The highest value of the plastic strain at the end of the simulation is located at the lower (inner) surface of the sheet. At that point, the specimen is in contact with the rigid punch and a compressive stress state is developed. The maximum porosity, however, appears at the upper right corner of the formed collar, which is under tension. In turn, porosity progressively decreases as one moves closer to the inner surface. Also, as shown in Fig. 5.3b, the evolution of $\bar{\varepsilon}^p$ and f during the forming process is quite different at points A and B. At A, porosity progressively increases to high values, while the equivalent plastic strain also increases moderately. At B, however, although the equivalent plastic strain progressively increases to higher values compared to point A, porosity rapidly decreases, since the structure is under compression at that point.

It should be recalled that, in the context of porous plasticity modeling, porosity can be viewed as a degradation (or damage) parameter for the structural load-carrying capacity. In this sense, macroscopic cracks can be identified with the regions of accumulated porosity in the structure. If a loss of stress-carrying capacity criterion was to be used in the model, based on a critical value of the porosity (e.g., Aravas and Papadioti (2021)), then, the numerical simulations predict that crack initiation would take place at the external diameter of the formed collar where porosity takes its maximum value. This prediction of the proposed model is qualitatively consistent with recent results from the experimental realization of the HET (Barlo et al. (2022)).

Such observations verify that selection of the appropriate material model is critical in structural problems involving ductile materials, where complex stress states develop. As shown with this example, standard incompressible plasticity models (such as the von Mises model) or damage models that only consider a critical value of the equivalent plastic strain in the criteria for crack initiation should be used with caution, as they might lead to inaccurate predictions. In case such models are utilized, either more information for the stress state should be included in the definition of the critical strain to failure in a phenomenological sense (e.g., Bai and Wierzbicki (2008)) or models that include more microstructural information (such as the porosity in porous elastic-plastic models) should be alternatively considered.

5.6 Cup-and-cone fracture of a round bar

The cup-and-cone fracture pattern that can be experimentally observed in failure of cylindrical specimens under tensile loading suggests a complex crack propagation phenomenon involving crack branching, which, in principle, is not easy to accurately simulate numerically. In such specimens, macroscopic cracking usually initiates due to void nucleation and growth mechanisms at the center of the bars driven by high stress triaxiality developing in the region. The crack initially propagates in its original plane and as it moves towards the free surface of the specimen, an out-of-plane shift occurs resulting in the experimentally observed slant fracture surface.

The problem was first numerically studied in detail in the work of Tvergaard and Needleman (1984) who used a local version of the modified Gurson's model (GTN) in order to identify the critical parameters affecting the final failure pattern and establish a connection

with the experimentally observed results. The problem was later revisited by Scheider and Brocks (2003) who used the cohesive element approach to predict crack propagation and more recently by several authors (Leclerc et al., 2020; Aravas and Papadioti, 2021; Nikolakopoulos et al., 2021; Tuhami et al., 2022) who used implicit gradient porous plasticity models or the extended finite element method (XFEM) coupled with cohesive zone models to capture the change from flat to slant fracture patterns in both notched and un-notched cylindrical tensile specimens.

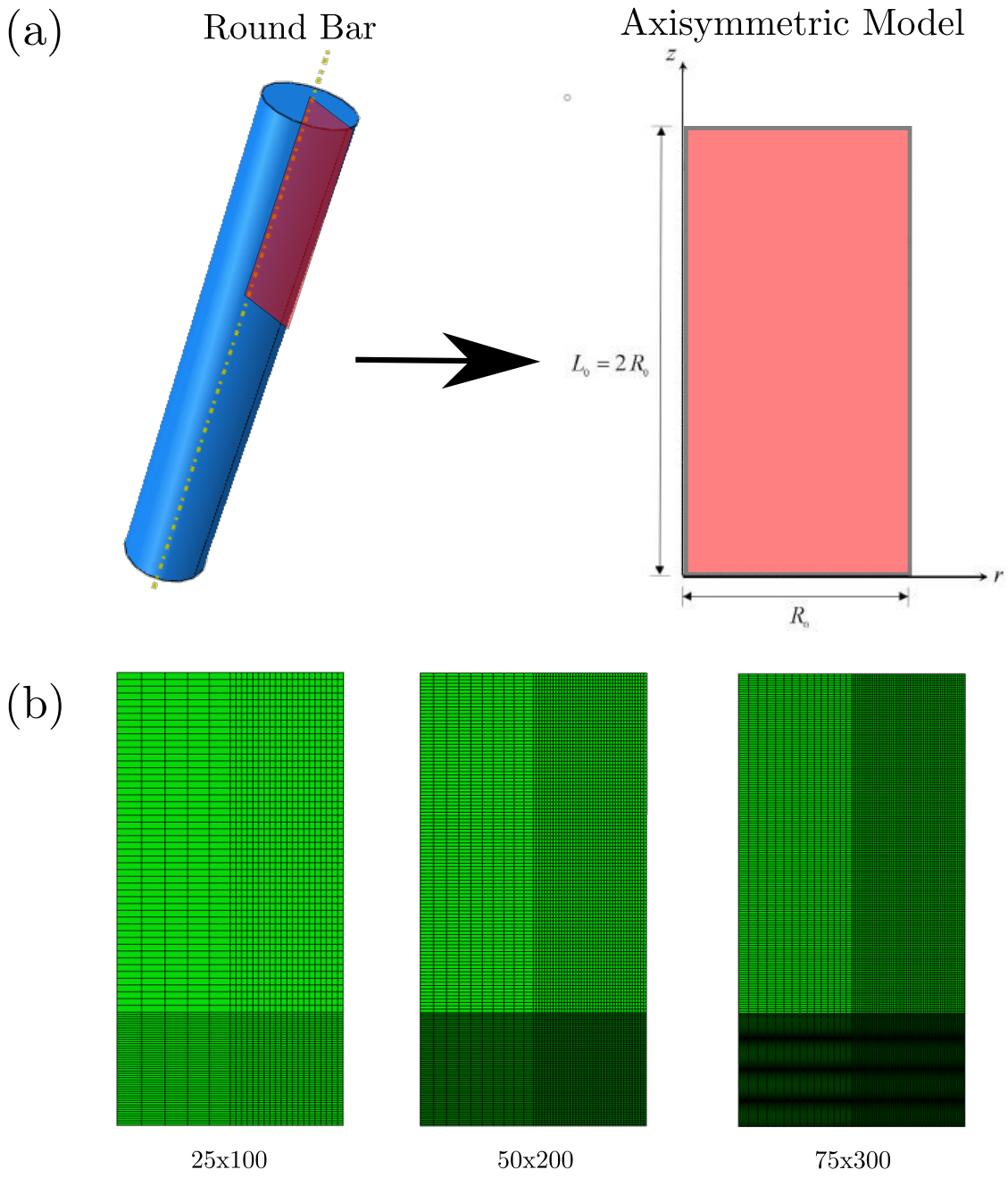

Figure 5.4 – (a) Axisymmetric model for the simulation of the cup-and-cone fracture of a round bar with initial radius R_0 and (b) the three meshes used in the calculations.

The problem of necking and cup-and-cone failure of a cylindrical specimen with circular cross-section quasi-statically loaded axially in tension is studied using both the local

and implicit non-local versions of the isotropic projection model. Due to convergence difficulties associated to modeling crack propagation using an implicit FEM solver, both the local and the non-local model have been implemented in a VUMAT user-subroutine and ABAQUS/Explicit is used to obtain a solution. The modeling approach used is shown in Fig. 5.4a. Due to the cylindrical symmetry of the round bar, the problem is treated as axisymmetric and only a "slice" in the first quadrant of the $r-z$ plane is considered in the simulation with z being the axis of symmetry of the cylinder. The specimen has an aspect ratio $L_0/R_0 = 2$, where L_0 is its initial length and R_0 its initial radius. To promote necking, following Aravas and Papadioti (2021), a small geometric imperfection of the form

$$R(z) = R_0 - \xi\, R_0 \cos\frac{\pi z}{L_0} \tag{5.69}$$

is introduced, where $R(z)$ is the perturbed radius of the specimen and $\xi = 10^{-3}$. All points on the midplane $z = 0$ are constrained to move only in the radial direction (i.e., $u_z(r,0) \equiv u_2(r,0) = 0$) and all points along the z-axis are constrained to have zero radial displacement (i.e., the condition $u_r(0,z) \equiv u_1(0,z) = 0$ is enforced). The lateral cylindrical surface is kept traction-free and the deformation is driven by a uniform prescribed end-displacement $\hat{\delta}$ which is applied incrementally in the z-direction. The values of the normalizing parameters used in all calculations are summarized in Table 5.2.

Table 5.2 – Normalizing parameters used in the cup-and-cone fracture simulations.

Normalizing Property	Symbol	Value	Units
Stress	Σ_{norm}	250	MPa
Length	L_{norm}	1×10^{-3}	m
Time	t_{norm}	1	s
Temperature	T_{norm}	1	K

For the quasi-static simulations, three different meshes are used with $25 \times 100, 50 \times 200$, and 75×300 elements respectively as shown in Fig. 5.4b. In this notation, the first and second numbers indicates the number of elements used in the radial and axial directions $r \equiv 1$ and $z \equiv 2$ respectively All meshes consist of 4-node axisymmetric coupled temperature-displacement elements with reduced integration and "hourglass control" (CAX4RT in ABAQUS/Explicit). The material is assumed to fail locally when the non-local porosity $f^{\rm nl}$ reaches the critical value of $f_F = 0.15$ and the element deletion technique is employed to simulate crack propagation; when this value is reached at an integration point, the material in the element is assumed to lose its load-carrying capacity, all stress components are set to zero, and the element is removed from the mesh. The characteristic length entering the non-local model is chosen as $\ell = 0.01R_0$ and an initial porosity $f_0 = 4\%$ is considered in all cases.

In order to investigate the effect of spatial discretization in the predictability of the cup-and-cone failure pattern, a mesh convergence analysis is carried out using both the local and non-local versions of the new porous plasticity model and the results are presented in Figs. 5.5–5.7. The void shape parameter is set at $w = 0.1$ for this series of calculations.

Variation of the normalized macroscopic axial force $F_2/(\sigma_0 A_0)$ with the macroscopic logarithmic axial strain $E_z \equiv E_2 = \ln(1 + u_2/L_0)$ are shown in Fig. 5.5a and 5.5b for the

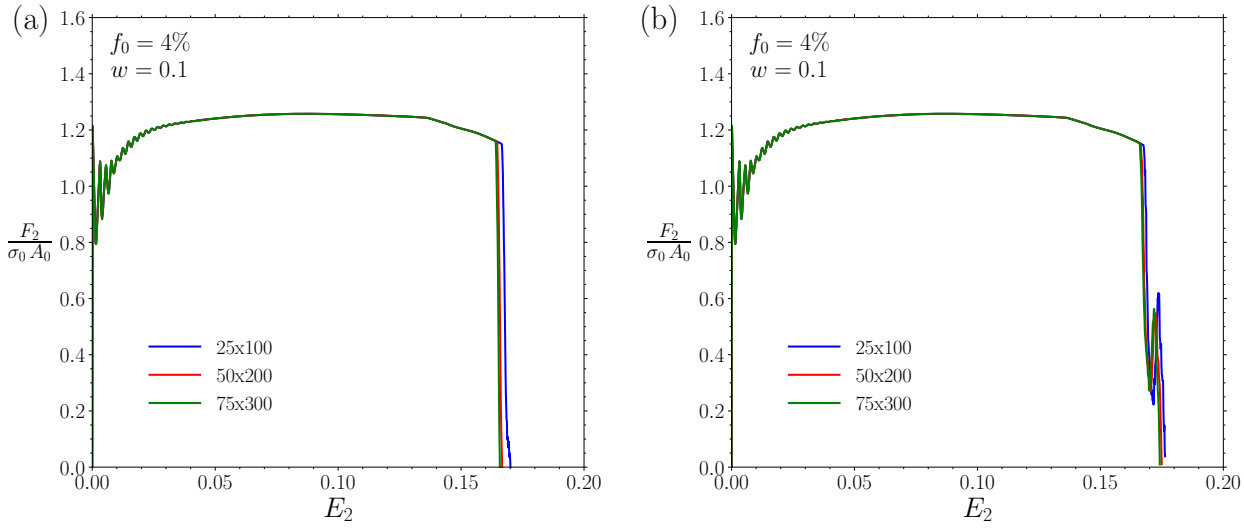

Figure 5.5 – Variation of the normalized total force $F_2/(\sigma_0 A_0)$ with macroscopic axial logarithmic strain $E_2 = \ln\left(1 + \frac{u_2}{L_0}\right)$ for (a) the local model and (b) the non-local model with $\ell = 0.01R_0$ ($A_0 = \pi R_0^2$ is the undeformed cross-sectional area of the round bar).

local and non-local models respectively. The oscillations of the numerical solution in the early stages are due to the explicit scheme used. As it can be seen, the load-deflection curves for both models are qualitatively similar to the ones observed experimentally (see Tvergaard and Needleman (1984)) involving a sharp load drop at the point when the initiation of the central penny-shaped crack takes place. It should be noted that, the normalized force-displacement curves corresponding to the non-local model show a sudden local increase, which takes place just before the crack orientation changes from flat to slant which is followed by quick drop as the crack propagates to the free surface. Also, the force-displacement curves exhibit no-mesh dependency since they converge to a single solution as the mesh is refined.

Figures 5.6 and 5.7 show the distribution of the equivalent plastic strain $\bar{\varepsilon}^p$ in a cross section of the bar at two different axial strain levels (cases (a) and (b)) and after total fracture has occurred (case (c)) as predicted by the local and implicit non-local models respectively. At each strain level (denoted as (a)-(c) in the figures), contour plots are shown for each of the three meshes used. Both the local and non-local models predict that a macroscopic penny shaped crack will initially be formed at the center of the specimen where the plastic strains and stress triaxiality attain their maximum values. However, the final way the cylindrical specimen fails is different depending on whether a regularized model is used or not.

In the case of the local model, the crack remains on its plane (at $z = 0$) in the coarser mesh while a cup-and-cone like fracture is predicted for the finest mesh with a 90° angle turn followed by an approximately 45° turn of the crack until it meets the free surface; the final failure pattern exhibits strong mesh dependency in this case. Conversely, if a non-local formulation is used, the numerical solutions are mesh-independent; the crack initiates at the center and when it grows at a distance approximately $0.47R_0$ it turns out of its plane until it reaches the free surface, a pattern which is predicted by all three meshes. Such results come to verify that, in such material models where softening is present, a regularized formulation is necessary to be used in order to accurately capture the final failure mode of the structure. It should be mentioned that the present calculations assume symmetry about the mid-plane at $z = 0$, so that two symmetrical conical fracture surfaces are predicted; of

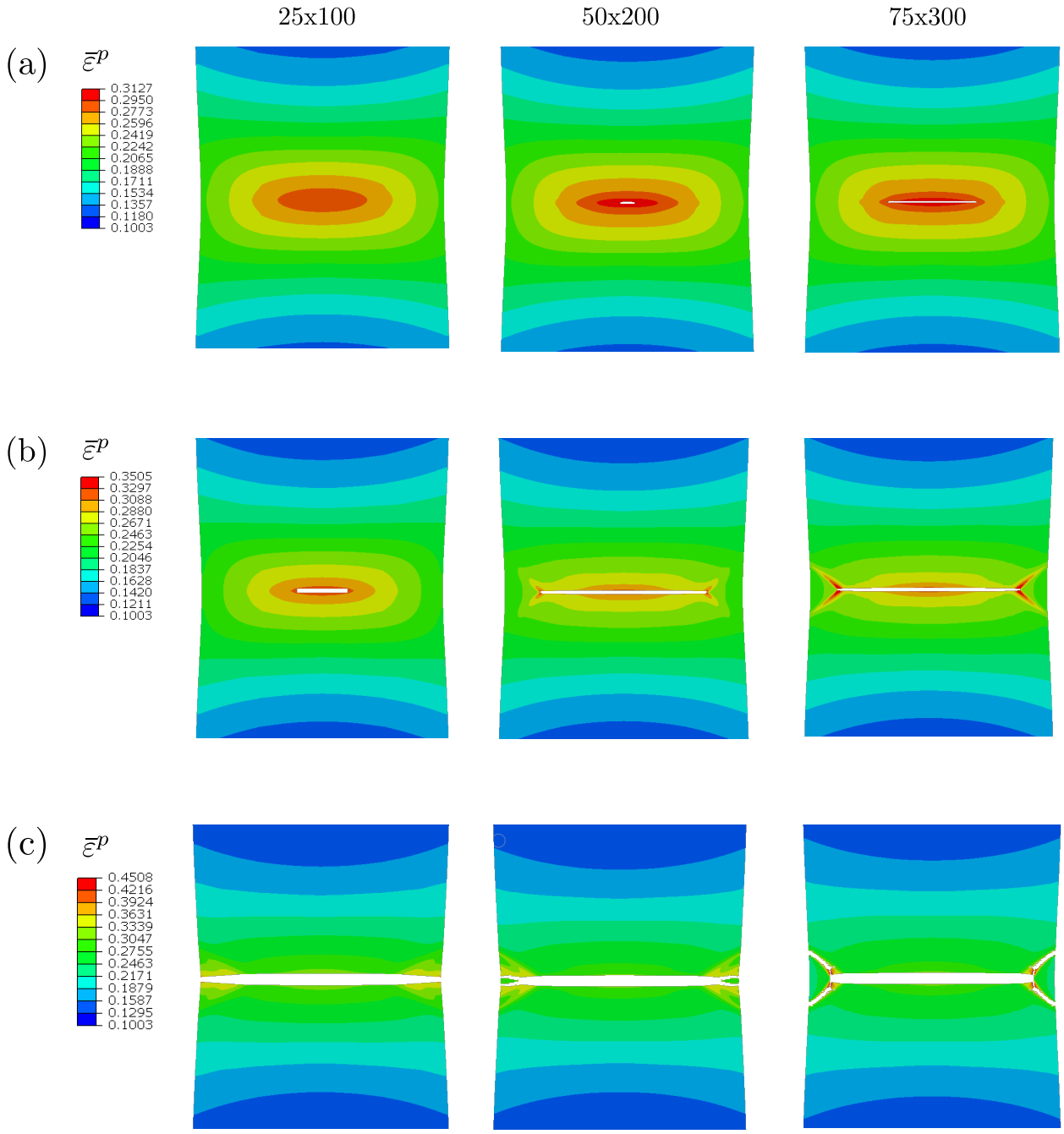

Figure 5.6 – Contours of the equivalent plastic strain $\bar{\varepsilon}^p$ in the round bar as predicted by the local model. Results are shown for values of the macroscopic axial logarithmic strain (a) $E_2 = 0,1629$, (b) $E_2 = 0,1649$ and (c) after a full macroscopic crack has been developed for all meshes. Whole cross-section is shown.

course, in reality, one of the two predicted cracks prevails, giving the cup-and-cone fracture observed in experiments.

The effect of the void shape on fracture was also examined by using the implicit non-local model and the finest of the three meshes comprising 75×300 elements. Figure 5.8 shows the variation of the normalized axial force with the normalized axial strain as predicted by the model for three different values of the aspect ratio parameter $w = 0.1$, $w = 0.2$ and $w = 1$. For comparison purposes, calculations are also carried out by using a non-local

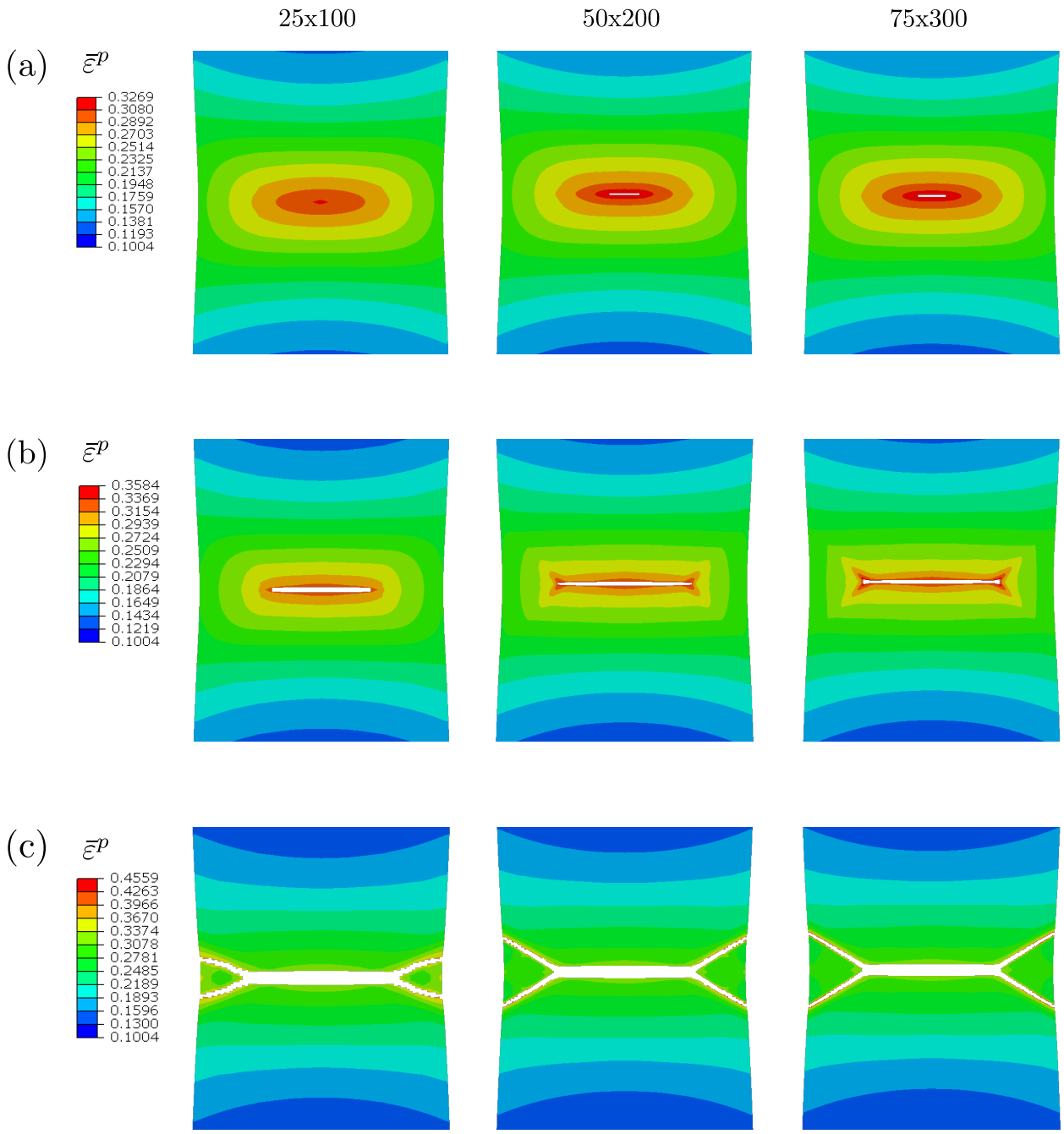

Figure 5.7 – Contours of the equivalent plastic strain $\bar{\varepsilon}^p$ in the round bar as predicted by the implicit non-local model. Results are shown for values of the macroscopic axial logarithmic strain (a) $E_2 = 0,1644$, (b) $E_2 = 0,1667$ and (c) after a full macroscopic crack has been developed for all meshes. Whole cross-section is shown.

version of the *original* Gurson's model (i.e., for $q_1 = q_2 = q_3 = 1$). The final failure patterns are indicated with arrows for each case. As it can be seen, the strain at which the sudden load-drop associated with the formation of the macroscopic penny shaped crack reduces for lower values of the aspect ratio w. This can be explained based on the fact that lower values of the aspect ratio (which would correspond to materials whose microstructures consist of more flat oblate voids) promote significant porosity evolution; this effect is more pronounced under high stress triaxiality conditions, such as the ones developing at the center of the neck

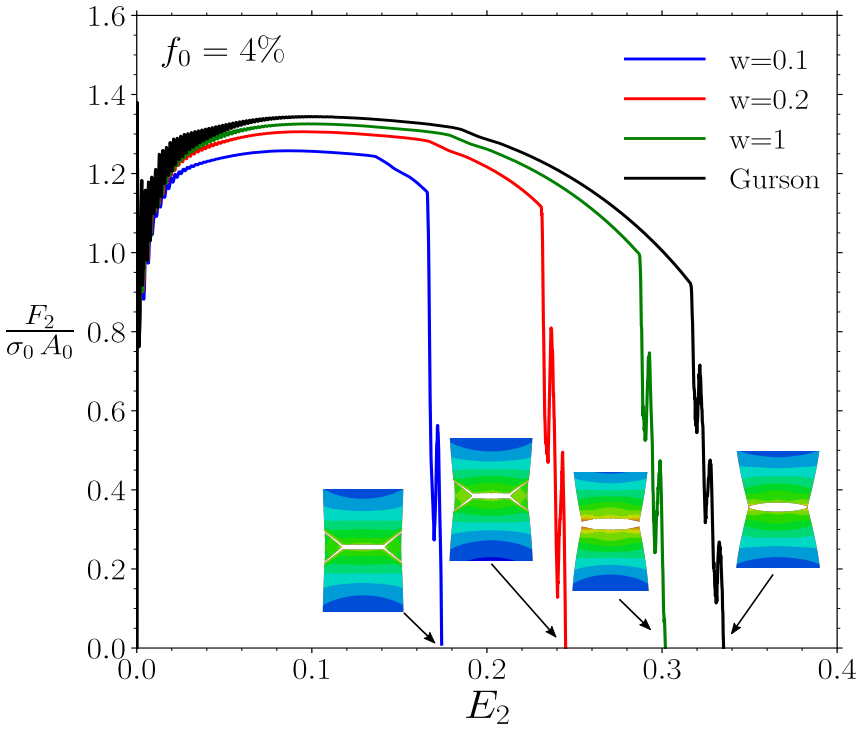

Figure 5.8 – Variation of the normalized total force $F_2/(\sigma_0 A_0)$ with macroscopic axial logarithmic strain $E_2 = \ln\left(1 + \frac{u_2}{L_0}\right)$ and final failure patterns as predicted by the non-local model for various microstructural configurations. A value of $\ell = 0.01 R_0$ is used in all calculations.

region. Again, it should be emphasized that, although both the new model with $w = 1$ and Gurson's model assume microstructures with spherical micro voids, porosity evolution is accelerated due the presence of the interpolation parameter α in the yield function of the isotropic projection model (see $(4.15)_1$); this results in lower macroscopic strain to fracture compared to the original Gurson model. Also, a higher reduction in the cross sectional area of the bar can be observed before the macroscopic crack forms as the aspect ratio of the voids increases; the model predicts that the softening branch of the stress-strain curve is driven by more severe necking for microstructures consisting of spherical voids compared to those consisting of flat penny-shaped voids.

It is worth noting that the shape of the voids also affects the final fracture mode of the bar; the cup-and-cone fracture is predicted for the calculations with $w = 0.1$ and $w = 0.2$ while the analysis with $w = 1$ and the Gurson's model predict that the macroscopic crack propagates in its plane until complete fracture occurs. A possible explanation for this result is that the out-of-plane branching of the macroscopic crack is mostly dominated by shear deformations which are characterized by lower stress triaxiality conditions. The original Gurson's model is known to work poorly under shear dominated conditions (Danas and Aravas, 2012). Under such stress states, damage could be promoted by mechanisms other than porosity evolution alone, such as interactions of neighboring voids due to void rotation or void shape evolution. As discussed in Subsection 3.4, randomly distributed and oriented voids with lower aspect ratio values can induce significant porosity evolution even under low stress triaxiality conditions; although neither void rotation nor void shape evolution are considered in the new model, incorporation of the initial void shape combined with the

random voids' orientations allow for such critical interactions to be taken into account in an implicit manner. In contrast, voids with spherical shapes that do not change their shape or rotate, lead only to moderate porosity evolution and do not perform well under shear dominated stress states. Past experimental and numerical studies (e.g., Bao and Wierzbicki (2004), Barsoum and Faleskog (2007), Dunand and Mohr (2011), Dunand and Mohr (2014)) give supporting evidence that the third invariant J_3 of the stress tensor could be an important parameter in order for more realistic predictions to be made regarding final fracture strains and failure modes under shear dominated stress states. This could also be supported by the results of the micromechanical calculations presented in Section 3.3.2, where it was found that microstructures comprising spherical voids appear to be more sensitive to the Lode angle θ compared to oblate voids of lower aspect ratios.

5.7 Simulation of the Charpy V-notch test

The Charpy V-notch (CVN) test (ISO 148-1:2016, 2016) for metallic materials is a mechanical procedure used to determine (qualitatively or quantitatively) various properties related to fracture behavior such as the impact absorbed energy, ductility, and the ductile-to-brittle transition temperature (DBTT) of welded and non-welded materials. The experimental setup involves metallic specimens with standarized dimensions and a pre-machined notch (see Fig. 5.9a) being placed on the supports of a pendulum impact testing machine, as shown in the schematic representation of Fig. 5.9b. The pendulum is left from a specific height to swing through the specimen, which is positioned on the testing machine so that the notch is across the point at which the center of the hammer strikes. The difference in potential energy of the pendulum before and after the test is then used to measure the absorbed energy of the material during fracture.

The CVN test has been numerically simulated throughout the years by several authors in an effort to estimate the aforementioned fracture related properties and asses the predictability of material models in comparison with experimental findings. In particular, the CVN test was first numerically modeled by Norris (1979) and much later by Tanguy and co-workers (Tanguy et al., 2005a,b; Bouchet et al., 2005) who tried to establish a computational framework for predicting fracture related properties of Charpy specimens failing due to irridiated embrittlement in nuclear reactors. Numerical approaches have also been used to investigate specimen size and inertial effects on the absorbed energy and the DBTT (Benzerga et al., 2002; DeSandre et al., 2004) as well as the effect of weld strength on fracture toughness Tvergaard and Needleman (2005). Ductile fracture in these works was simulated using a porous plasticity approach (a variation of Gurson's model in most cases) with incorporation of additional viscoplastic and/or thermal effects.

In this study, the new implicit gradient isotropic projection model is used to simulate the dynamic Charpy V-notch under plane strain conditions, using the ABAQUS/Explicit solver in conjunction with a VUMAT user-material subroutine. The goal is to investigate the effect of the various model parameters (a) on the prediction of standard macroscopic load-displacement curves and absorbed strain energy associated with the test and (b) on the initiation and propagation of macroscopic cracking. The question of whether brittle or ductile fracture takes place is not addressed here assuming *a priori* that ductile fracture takes place and no thermal or strain rate effects were taken into account. Although important in some cases of interest, such effects were neglected in this first approach to the numerical

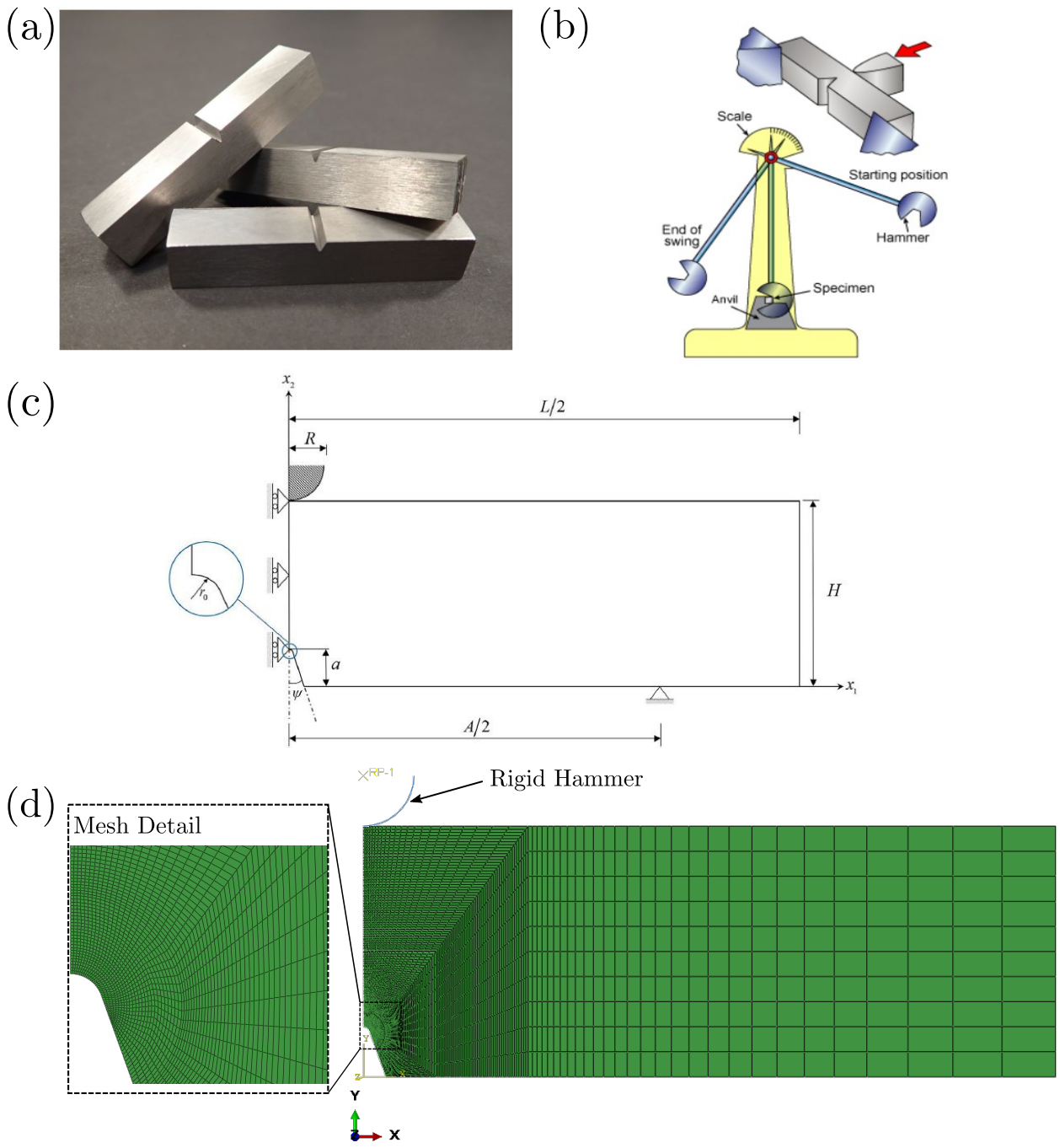

Figure 5.9 – (a) Machined Charpy V-notch specimens, (b) schematic representation of the experimental setup for the Charpy V-notch test, (c) plane strain model of the test with dimension annotations and boundary conditions, and (d) simulation setup which includes the rigid hammer and mesh used along with a magnification of the mesh density near the notch.

simulation of the problem and are left for future work.

Dimensions for the numerical model used in all simulations can be seen in Fig. 5.9c and are taken as proposed in the ISO 148-1:2016 (2016) ISO standard. The specimen has overall initial length $L = 55\,mm$, height $H = 10\,mm$, and thickness $B = 10\,mm$. The notch depth is $a = 2\,mm$ at an angle $2\psi = 45°$ with an initial radius $r_0 = 0.25\,mm$. The specimen's supports are placed at a distance $A = 40\,mm$ apart. Only half of the billet is modeled

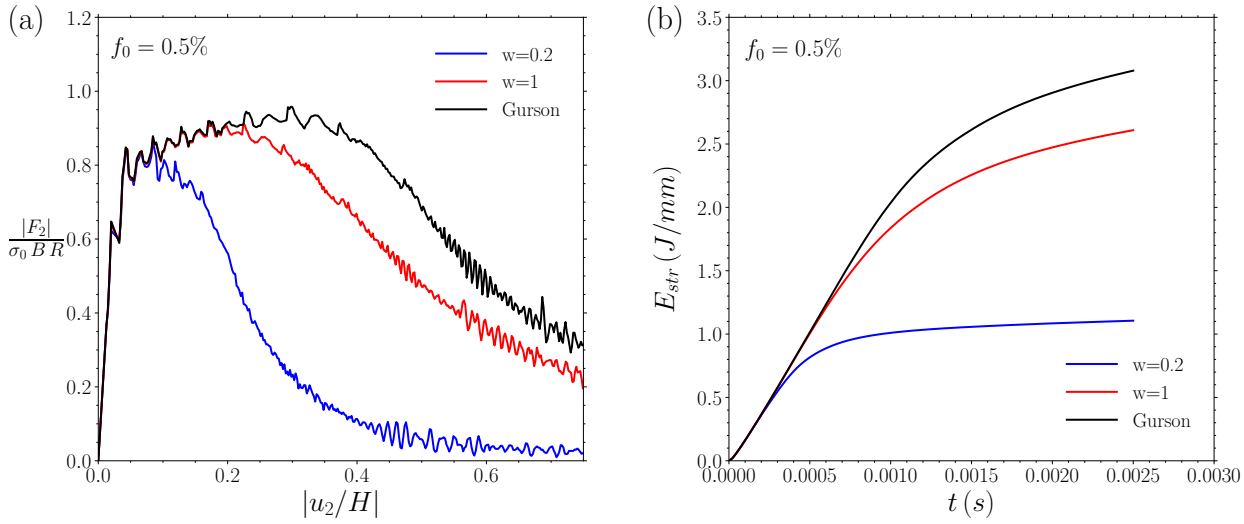

Figure 5.10 – (a) Variation of the normalized contact force $|F_2|/(\sigma_0\, B\, R_0)$ between the mass and the specimen with the normalized vertical displacement of the mass $|u_2/H|$ after it hits the specimen and (b) the absorbed strain energy per unit thickness E_{str}, for two different void shapes. Calculations were also carried out using a non-local version of the original Gurson's model (i.e., with $q_1 = q_2 = q_3 = 1$) for comparison purposes.

and symmetry boundary conditions are imposed. The numerical setup used for for the simulations is presented in Fig. 5.9d. Following Aravas and Papadioti (2021), the pendulum hammer is assumed to have a rounded tip of radius $R = 2\,mm$, a total mass $m = 20\,kg$, and is modeled as a rigid surface on the $x_1 - x_2$ plane so that a contact problem has to be solved. The mass per unit thickness used in the plane strain simulations for the half specimen is $\bar{m} = (m/B)/2 = 1\,kg/mm$. Frictionless contact is assumed between the rigid hammer and the deformable specimen.

The mesh used consists of 4 732 4-node plane strain, coupled temperature-displacement elements with reduced integration and "hourglass control" (CPE4RT in ABAQUS/Explicit). A more focused mesh is used in the vicinity of the notch in order to accurately capture crack propagation, as shown in the magnified region. The rigid hammer is assumed to hit the specimen with an initial velocity $v_2^{ham} = 5\,m/s$ and exert a force of $F_g = \bar{m}g = 9.81\,N/mm$ due to gravity, where $g = 9.81\,m/s^2$ is the acceleration of gravity constant; these conditions are applied on the reference node defining the rigid surface, which is constrained to move only in the vertical direction. To simulate crack propagation, the element deletion technique offered by ABAQUS/Explicit is employed. The material is assumed to fail locally when the non-local porosity at all integration points of an element takes the value $f_F = 0.15$ and the corresponding element is removed from the mesh. The normalizing parameters used are the same as those in Section 5.6 and are given in Table 5.2. An initial porosity $f_0 = 0.5\%$ is considered in all cases and the characteristic length is taken as $\ell = 0.1 r_0 = 25\,\mu m$ (as in Aravas and Papadioti (2021)). The total simulation time is $t = 2.5\,ms$.

Figure 5.10a shows the variation of the normalized contact force $|F_2|/(\sigma_0\, B\, R_0)$ between the hammer and the specimen with the normalized vertical displacement of the hammer $|u_2/H|$ after it hits the specimen. Two different values of the aspect ratio parameter are considered, $w = 0.2$ and $w = 1$. For comparison purposes calculations are also carried out using the *original* Gurson's model (i.e., with $q_1 = q_2 = q_3 = 1$). The load drop in the

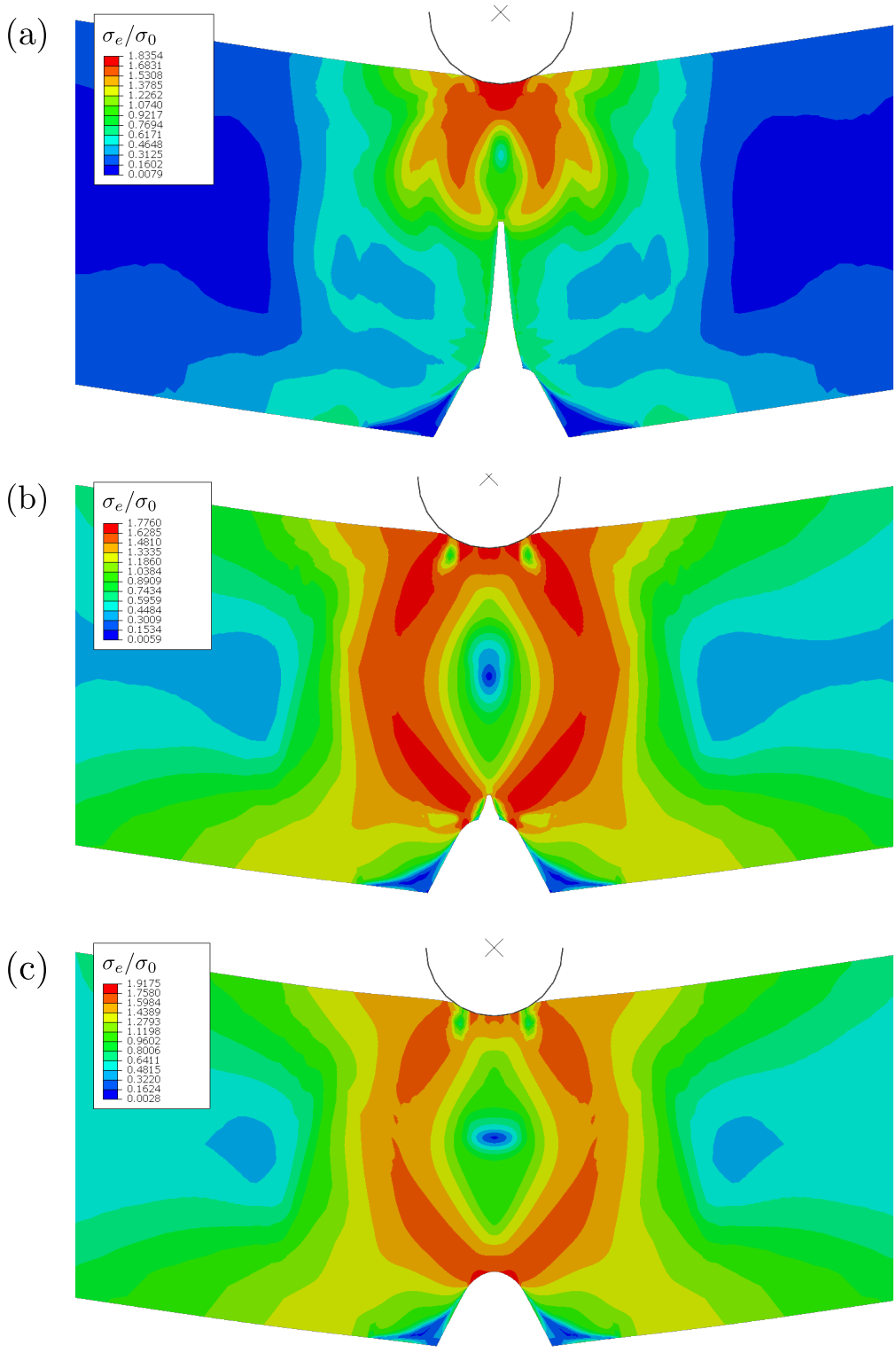

Figure 5.11 – Distribution of the normalized von Mises stress σ_e/σ_0 in the deformed configuration as predicted by (a) the implicit non-local isotropic projection model with $w = 0.2$, (b) the implicit non-local isotropic projection model with $w = 1$, and (c) the implicit non-local Gurson's model. Results are shown at a normalized vertical displacement of the mass $|u_2/H| = 0.3$ in all cases. Whole specimen is shown.

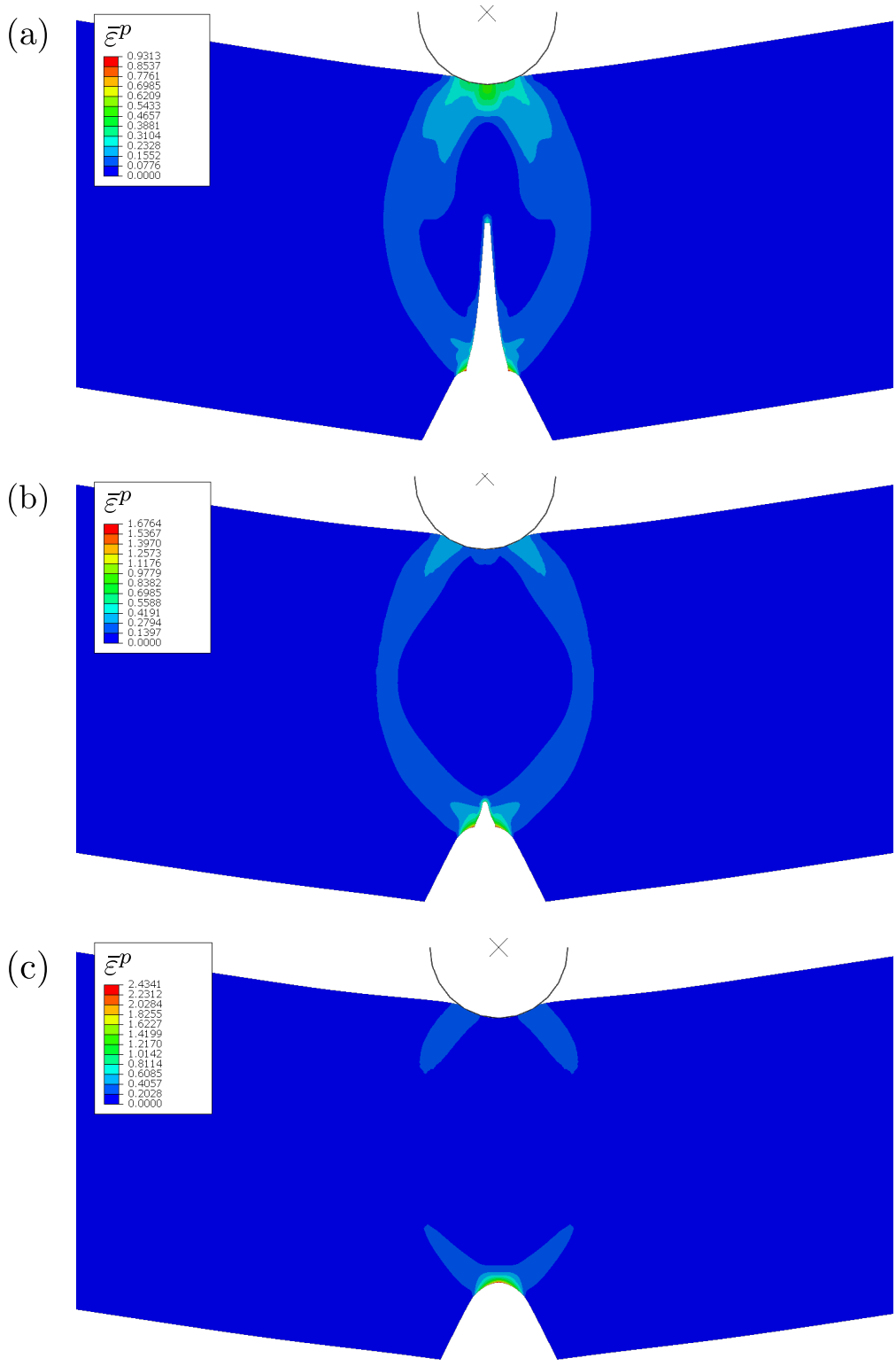

Figure 5.12 – Distribution of the stress triaxiality X_Σ in the deformed configuration as predicted by (a) the implicit non-local isotropic projection model with $w = 0.2$, (b) the implicit non-local isotropic projection model with $w = 1$, and (c) the implicit non-local Gurson's model. Results are shown at a normalized vertical displacement of the mass $|u_2/H| = 0.3$ in all cases. Whole specimen is shown.

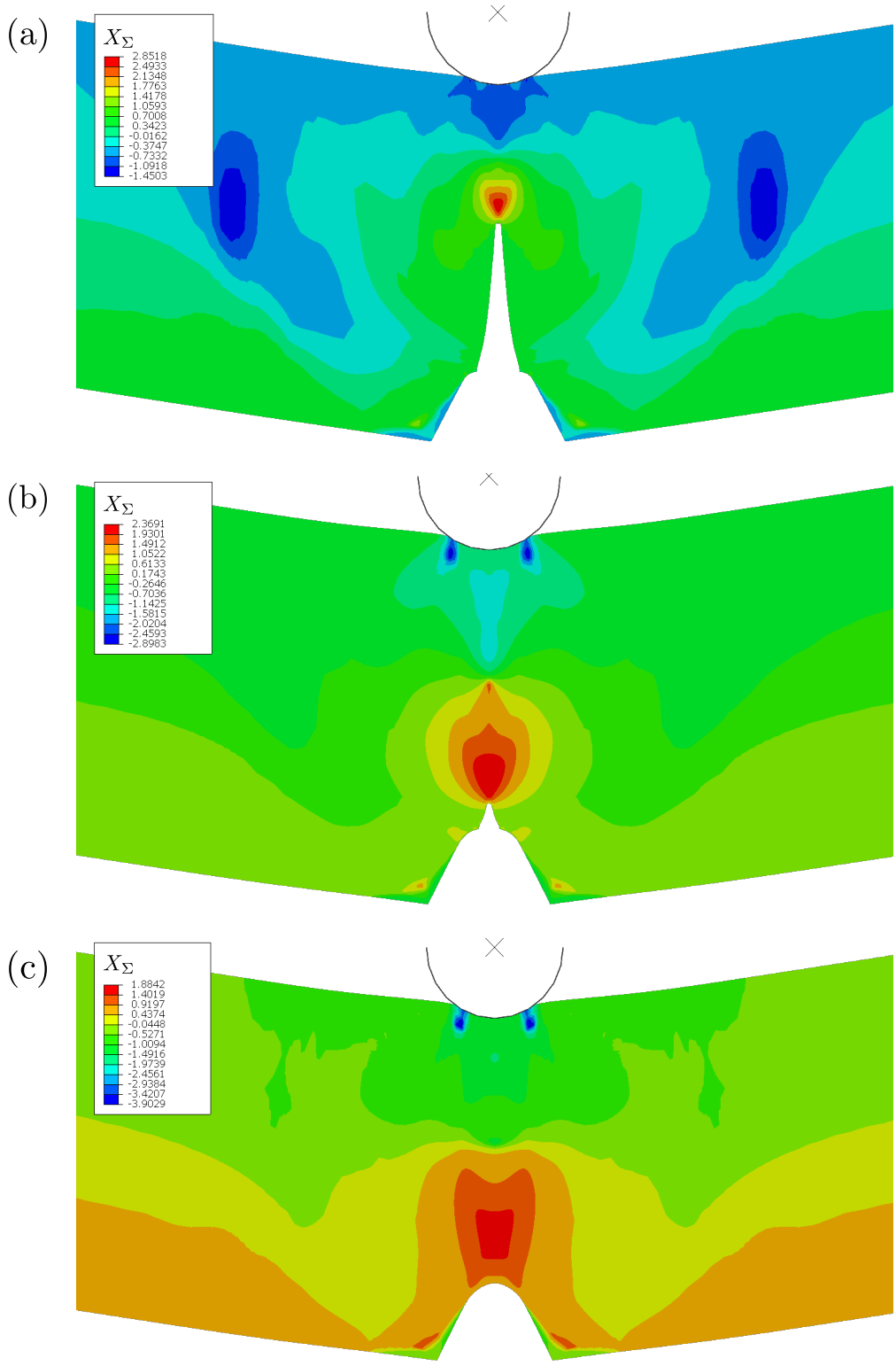

Figure 5.13 – Distribution of the equivalent plastic strain $\bar{\varepsilon}^p$ in the deformed configuration as predicted by (a) the implicit non-local isotropic projection model with $w = 0.2$, (b) the implicit non-local isotropic projection model with $w = 1$, and (c) the implicit non-local Gurson's model. Results are shown at a normalized vertical displacement of the mass $|u_2/H| = 0.3$ in all cases. Whole specimen is shown.

normalized force-displacement curves is associated with the initiation and propagation of a macroscopic crack at the root of the notch. It can be observed that, while the peak force predicted by all models shows little sensitivity to the aspect ratio parameter, the normalized displacement corresponding to crack initiation varies significantly depending the selection of the void shape parameter; for the simulation where the microstructure is assumed to comprise penny-shaped voids (i.e., for $w = 0.2$) crack initiates at a displacement value of $|u_2/H| = 0.087$ whereas the simulation where spherical voids are assumed predicts that a macroscopic crack initiates at a displacement $|u_2/H| = 0.194$. Gurson's model predicts the most delayed crack initiation strain at a normalized hammer displacement of $|u_2/H| = 0.306$. Again, the difference between the isotropic projection model with aspect ratio $w = 1$ and Gurson's model is due to the presence of the interpolation parameter α in (4.15).

Figure 5.10b depicts the strain energy per unit thickness absorbed by the specimen (as calculated by equation $(5.66)_2$ for the whole model by ABAQUS) as a function of the total simulation time for two different values of the aspect ratio parameter, $w = 0.2$ and $w = 1$ and for the analysis using Gurson's model. It is clear that, a material comprising micro-voids with an aspect ratio $w = 0.2$ is able to absorb significantly less energy when compared to a material consisting of spherical voids (i.e., simulation with $w = 1$ and Gurson's model); microstructures that comprise flat oblate micro-voids whose shape significantly deviates from spherical induce a less ductile macroscopic behavior. It should be noted that the corresponding kinetic energy in the specimen was found to be negligible compared to the strain energies shown in Fig. 5.10b for all simulations, i.e., inertial terms do not affect the solution substantially indicating that the analysis is essentially quasi-static.

Figures 5.11–5.13 show the distributions of the normalized von Mises stress σ_e/σ_0, equivalent plastic strain $\bar{\varepsilon}^p$ and stress triaxiality X_Σ in the specimen as predicted by the non-local isotropic projection model for $w = 0.2$, $w = 1$ and the Gurson's model (shown in subfigures (a), (b) and (c) respectively) at a normalized macroscopic displacement $|u_2/H| = 0.3$. Although only half of the specimen was considered in the calculations, the whole specimen is shown for visualization purposes. We observe that at this moment the crack has propagated by a distance $0.45H$ for the simulation with $w = 0.2$, a distance of $0.11H$ for the simulation with $w = 1$ while Gurson's model predicts that no macroscopic crack has formed yet. Due to the substantial crack propagation for the model with $w = 0.2$, a highly stressed region exists in the vicinity of the crack front while most of the specimen unloads elastically, as shown in Fig. 5.11a. Stress distribution is more diffuse in the other two cases where little to no cracking has occurred as depicted in Figs. 5.11b,c. Also, higher plastic strains develop in the region of contact between the rigid hammer and the specimen for the simulation with $w = 0.2$ (Fig. 5.12a) while plasticity appears more concentrated to the notch area for the simulation with $w = 1$ and Gurson's model (Fig. 5.12b,c). This is also reflected to the deformed shape of the notch which has the highest opening in the case of the Gurson's model. Finally, high stress triaxiality conditions ($X_\Sigma \approx 3$) concentrated in the vicinity of the propagating crack front are predicted by the non-local model with $w = 0.2$ (Fig. 5.13a); a less intensive profile for $w = 1$ (Fig. 5.13b) and a much more diffuse stress triaxiality distribution is predicted by the Gurson's model (Fig. 5.13c).

5.8 The first Sandia Fracture Challenge revisited

Over the course of the last decade, Sandia Laboratories has issued a number of "challenges" (Boyce et al., 2014, 2016; Kramer et al., 2019) in order to investigate the capability of the

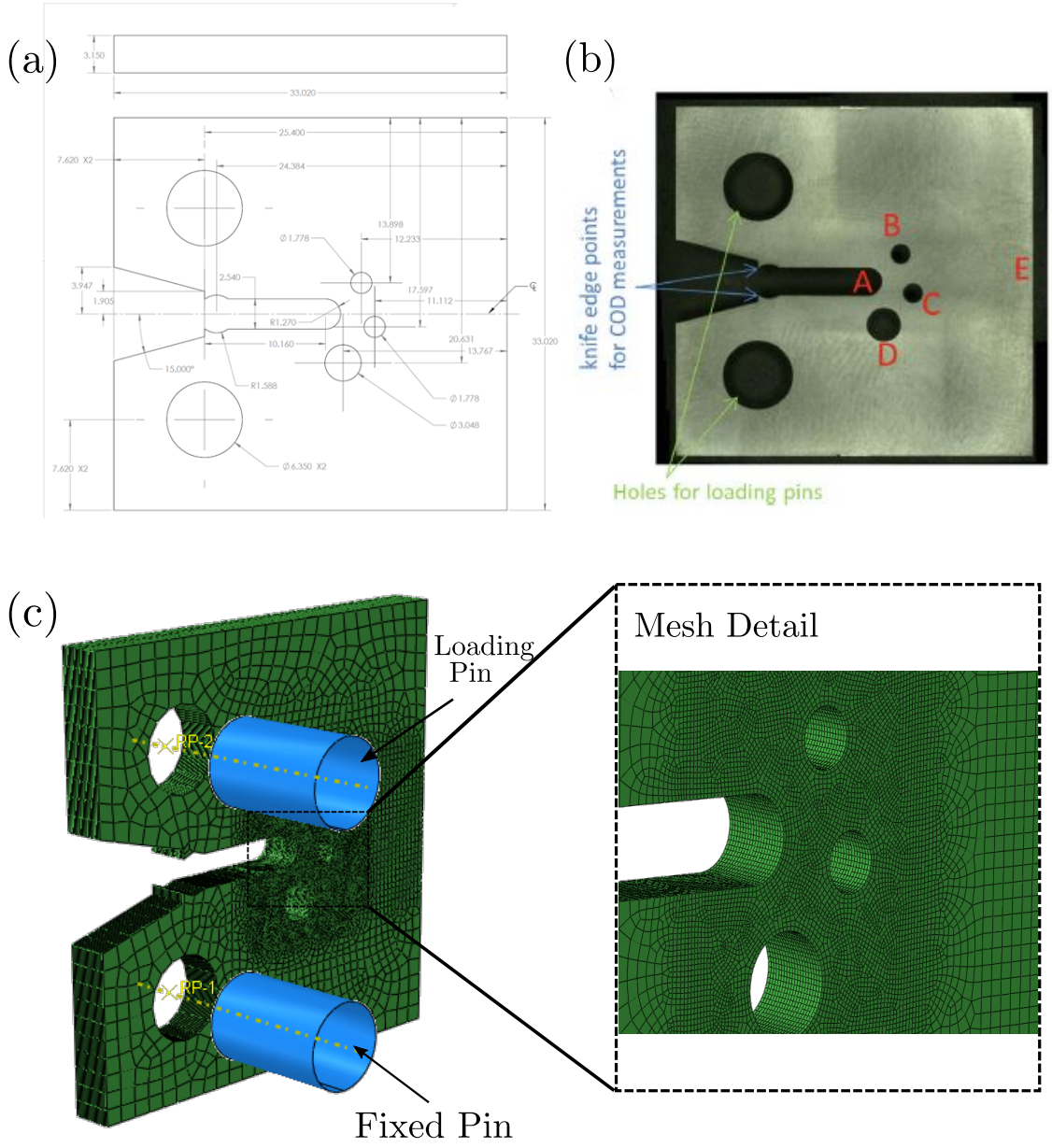

Figure 5.14 – (a) Mechanical drawing with dimensions (in mm) for the first SFC's fracture specimen, (b) Machined specimen used in real-world experiments with annotations for the holes and indication of the position of COD measurement points, and (c) Simulation setup for the first SFC specimen which includes the rigid loading and fixed pins (shown in blue) and the mesh used in the calculations.

mechanics community to accurately forecast ductile fracture of structural components. This is done through a blind, round-robin setup where mechanicians are tasked with predicting the deformation and failure of a specimen with non-conventional geometry, utilizing provided experimental calibration data. The philosophy of Sandia Fracture Challenges (SFCs) is the intention of replicating real-world engineering conditions (such as limited time, budget and information) under which the predictions have to be made as well as to asses the fidelity of the whole stream of methods involved (i.e., physical assumptions, numerical tools and calibration methods).

The first SFC (Boyce et al., 2014) was issued in May 2012 and a total of 13 international

teams from various universities participated and conducted blind ductile fracture predictions for the specimen presented in Fig. 5.14a,b. The scenario involved the prediction of crack initiation and propagation of this fracture specimen under quasi-static, room temperature test conditions. Annotations A-E were adopted for later reference to the crack path observed from both experiments and numerical simulations. Experimental data from four uniaxial tension tests (engineering stress-strain curves), three compact tension tests under mode I loading, and material information (such as chemical composition, heat treatment and limited microstructural information) were provided to all teams for model calibration purposes. All specimens (including the challenge's fracture specimen) were cut from the same heat treated sheet made of a 15-5 PH precipitation hardened martensitic stainless steel. The uniaxial tension tests from the four dog-bone specimens (which were cut in different orientations relative to the rolling and transverse-to-rolling directions of the sheet) led to similar engineering stress-strain curves, indicating that the material at hand could be considered as approximately isotropic. Metallographic analysis reported a grain size in the range of $5 - 20\mu m$.

A total of 13 fracture specimens such as the one shown in Fig. 5.14b were used in experiments at three different laboratories, ten at Sandia's Mechanics and Materials laboratories and three at University of Texas' at Austin Materials laboratory. Two different crack paths were observed, namely A-D-C-E and A-C-E. All specimens with dimensions *within the predefined machining tolerances failed following A-C-E*; failure along the A-D-C-E path was primarily attributed to geometrical imperfections related to the machining process (Boyce et al., 2014). A significant variety of numerical approaches was employed by the participants (e.g., von Mises/Hill plasticity, porous plasticity models, damage models, and non-local peridynamics among others). Although both crack paths were numerically predicted by the teams depending on material parameter selection and consideration of geometrical imperfections, non of the participants were able to accurately reproduce the total experimental force-COD (crack opening displacement) curves. Also, the largest deviations were observed on the reported COD values at which the numerical models predicted the initiation of the first and second macroscopic cracks.

5.8.1 Simulation of the first SFC's fracture specimen

In order to investigate the capability of the new model proposed in this work to predict ductile fracture in complex geometries and loading conditions, the non-local isotropic projection model is used to simulate the first SFC's fracture problem. Due to the problem involving both contact and crack propagation, ABAQUS/Explicit solver along with a VUMAT user-subroutine are used to obtain a solution. The finite element model used in the simulations is shown in Fig. 5.14c. Both pins of the experimental setup are model as rigid shell surfaces. The specimen has overall initial dimenensions $L_0 = W_0 = 33.02\,mm$, an initial measured thickness $t_0 = 3.124\,mm$, and a notch with initial radius $R_0^{notch} = 1.27\,mm$. Three holes were machined in the vicinity of the notch, two small ones with an initial diameter $D_0^{small} = 1.778\,mm$ and a larger one with initial diameter $D_0^{large} = 3.048\,mm$. The SCF specimen used in the numerical simulations is designed based on *nominal dimensions* and geometrical imperfections are not considered. All degrees of freedom of the bottom pin are constrained while the top pin is allowed to only move in the vertical direction. The solution is then driven by a constant vertical displacement $\hat{u}_y^{top}$ applied to the reference node of the top pin and frictionless contact is assumed between the pins and the specimen.

The mesh used consists of 175 062 eight-node hexahedral, coupled-temperature displacement elements with reduced integration and "hourglass control" (C3D8RT in ABAQUS/Explicit). A magnification of the mesh density used in the vicinity of the notch and the holes is shown on the right part of Fig. 5.14c. Elements with initial dimensions $0.15 \times 0.15 \times 0.15\, mm$ are used in that area and a total of 20 elements are used through the thickness.

Table 5.3 – Matrix material properties for the 15-5 martensitic stainless steel.

Property	Symbol	Value	Units
Young's modulus	E	195	GPa
Poisson's ratio	ν	0.3	-
Initial yield strength	σ_0	1080	MPa
Hardening exponent	m	0.55	-
Power Law Parameter	B	540	MPa
Initial mass density	ρ_0	7850×10^4	$\frac{kg}{m^3}$
Specific heat	c	2×10^{-12}	$\frac{m^3\, s}{kg\, K}$

Table 5.4 – Normalizing parameters used in the SFC simulations.

Normalizing Property	Symbol	Value	Units
Stress	Σ_{norm}	1080	MPa
Length	L_{norm}	1	m
Time	t_{norm}	1	s
Temperature	T_{norm}	1	K

The material parameters used in the numerical simulations are drawn from the work of Nahshon et al. (2014) and are shown in Table 5.3. In that work, the hardening law was determined utilizing an inverse fitting procedure based on the uniaxial tension test data reading

$$\sigma_y = \sigma_0 + B(\bar{\varepsilon}^p)^m \tag{5.70}$$

where B is a fitting parameter with dimensions of stress. In order to accelerate calculations, mass scaling is used where the initial density in the model is increased by a factor of 10^4; such an artificial increase in density was deemed to be acceptable since the kinetic energy in all cases was found to be less than 1% of the corresponding strain energy developed in the specimen, ensuring the quasi-static character of the solution. The corresponding normalizing parameters are shown in Table 5.4. An initial porosity $f_0 = 0.5\%$ is considered in all simulations, the material is assumed to fail locally when the non-local porosity f^{nl} reaches the critical value of $f_F = 0.15$, and the element deletion technique is employed to simulate crack propagation; when this value is reached at an integration point, the material in the element is assumed to lose its load-carrying capacity, all stress components are set to zero, and the element is removed from the mesh. The characteristic length of the non-local model is taken as $\ell \approx 3.36\bar{d}_{gr} = 42\,\mu m$ where $\bar{d}_{gr} = 12.5\,\mu m$ is the average grain size

reported from the metallurgical analysis of the microstructure. The same calculations were also realized for a higher ($\ell \approx 10.2\bar{d}_{gr} = 127\,\mu m$) and a lower value ($\ell \approx 1.7\bar{d}_{gr} = 21\,\mu m$) of the regularization length and no significant difference was found in the predictions for $\ell \leq 3.4\bar{d}_{gr}$.

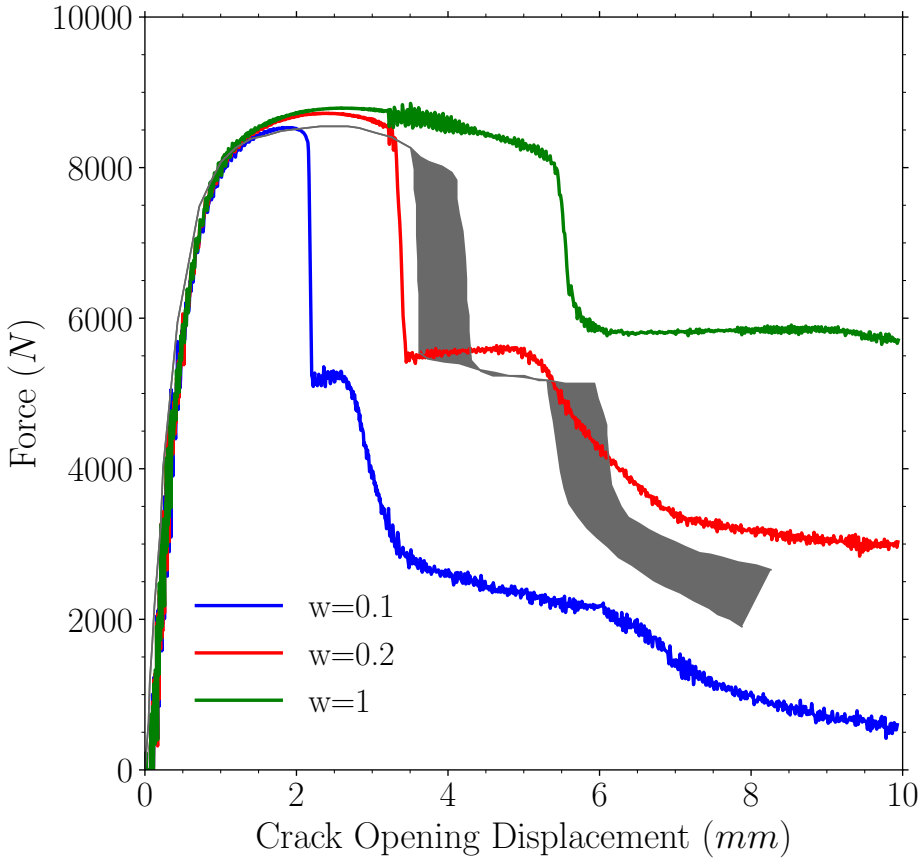

Figure 5.15 – Force-COD curves for the SFC as predicted by the implicit gradient model for various aspect ratio values. The shaded gray area denotes the range from the real-world experiments for specimens that failed in the A-C-E path as reported in the "master paper" of the challenge (Boyce et al. (2014)). A value of $\ell \approx 3.36\bar{d}_{gr} = 42\,\mu m$ is used in the calculations (where $\bar{d}_{gr} = 12.5\,\mu m$ is the average grain size reported).

Figure 5.15 shows the force-COD curves as predicted by the implicit non-local model for three different values of the aspect ratio parameter, $w = 0.1$, $w = 0.2$ and $w = 1$. The reported force corresponds to the vertical component of the reaction force developed at the reference node of the (top) loading pin while the reported COD to the vertical displacement of the node at the top knife-edge point indicated in Figure 5.14b. The area shaded in gray corresponds to the experimental range reported in Boyce et al. (2014) for the specimens that failed following the A-C-E path. Sudden load drops in both the experimental and numerically calculated curves are associated with crack propagation in the specimen. A summary of the numerically and experimentally predicted force-displacement values for each crack is given in Table 5.5. As it can be seen, the analysis with an aspect ratio $w = 0.2$ is the one that fits better the experimental results giving the closest predictions regarding the force and COD values of the first and second cracking events. The peak force is predicted relatively well in all cases while the COD values associated with crack initiation appear to be very sensitive to

the void shape parameter. Despite the strong non-linearity of the problem, the effect of the aspect ratio parameter is clearly depicted; lower values of the aspect ratio (corresponding to penny-shaped micro voids) lead to reduced fracture initiation COD while w values closer to unity (i.e., corresponding to almost spherical micro voids) lead to higher fracture COD values.

Table 5.5 – Force and correponding crack opening displacement values at the initiation of each crack in the specimen.

	First Crack (A-C)		Second Crack (C-E)	
	Force (kN)	COD (mm)	Force (kN)	COD (mm)
Model ($w = 0.1$)	8.527	2.137	5.216	2.60
Model ($w = 0.2$)	8.405	3.254	5.557	4.95
Model ($w = 1$)	7.957	5.458	5.844	9.27
Experiments	$7.832 - 8.066$	$3.542 - 4.115$	$5.132 - 5.173$	$5.217 - 5.933$

Figures 5.16 and 5.17 show the distribution of the equivalent plastic strain $\bar{\varepsilon}^p$ and stress triaxiality X_Σ in the vicinity of the notch area as the crack A-C-E propagates through the specimen. The contour plots correspond to the simulation with an aspect ratio value of $w = 0.2$. Initially, plastic deformation concentrates in the A-D and D-C ligaments but soon a shift takes place and deformation begins to localize in the A-C ligament where necking begins to take place as shown in Fig. 5.16a. Crack propagation starts at the middle of the necking region on the opposite side of the notch at a COD=3.23 mm, gradually propagating towards the notch and finally to the lateral surfaces of the specimen. This can be explained based on the stress triaxiality distribution shown in Fig. 5.17a; the highest triaxiality value is attained at the interior of the A-C ligament leading to local high porosity evolution in the region and the formation of an internal macroscopic crack. The A-C ligament is fully split apart at a COD=3.56 mm as shown in Fig. 5.16a. The abrupt drop in the force-COD curve associated with the A-C crack takes place at an intermediate value of COD= 3.35 mm. This behavior is in close qualitative agreement with the one observed during the actual experiment, where it was indicated that a subsurface crack has initially formed which later propagated to the surface bridging the ligament A-C as mentioned in Boyce et al. (2014).

With continued loading, plastic deformation starts to concentrate at the free surface of hole C where high stress triaxility conditions begin to develop promoting porosity growth, as shown in Figs. 5.16c and 5.17c respectively. The second crack starts to propagate at a COD=4.87 mm and a corresponding gradual drop in the force-COD curve can be observed. A more abrupt load drop related to the second crack was measured in the experiment. As the crack propagates towards the back of the specimen to point E, plastic deformation is distributed in a smooth manner while concentrated high stress triaxiality conditions develop at the macroscopic crack's front as shown in Figs. 5.16d and 5.17d respectively.

Driven by the analysis of this example problem, it worth emphasizing at this point the value of porous or damage plasticity models that combine a solid theoretical background able to account for key microstructural features with a reasonable amount of parameters allowing practical implementation and calibration. For instance, simulation of the same problem using variations of Gurson's model (Nahshon et al., 2014; Zhou et al., 2014b) or

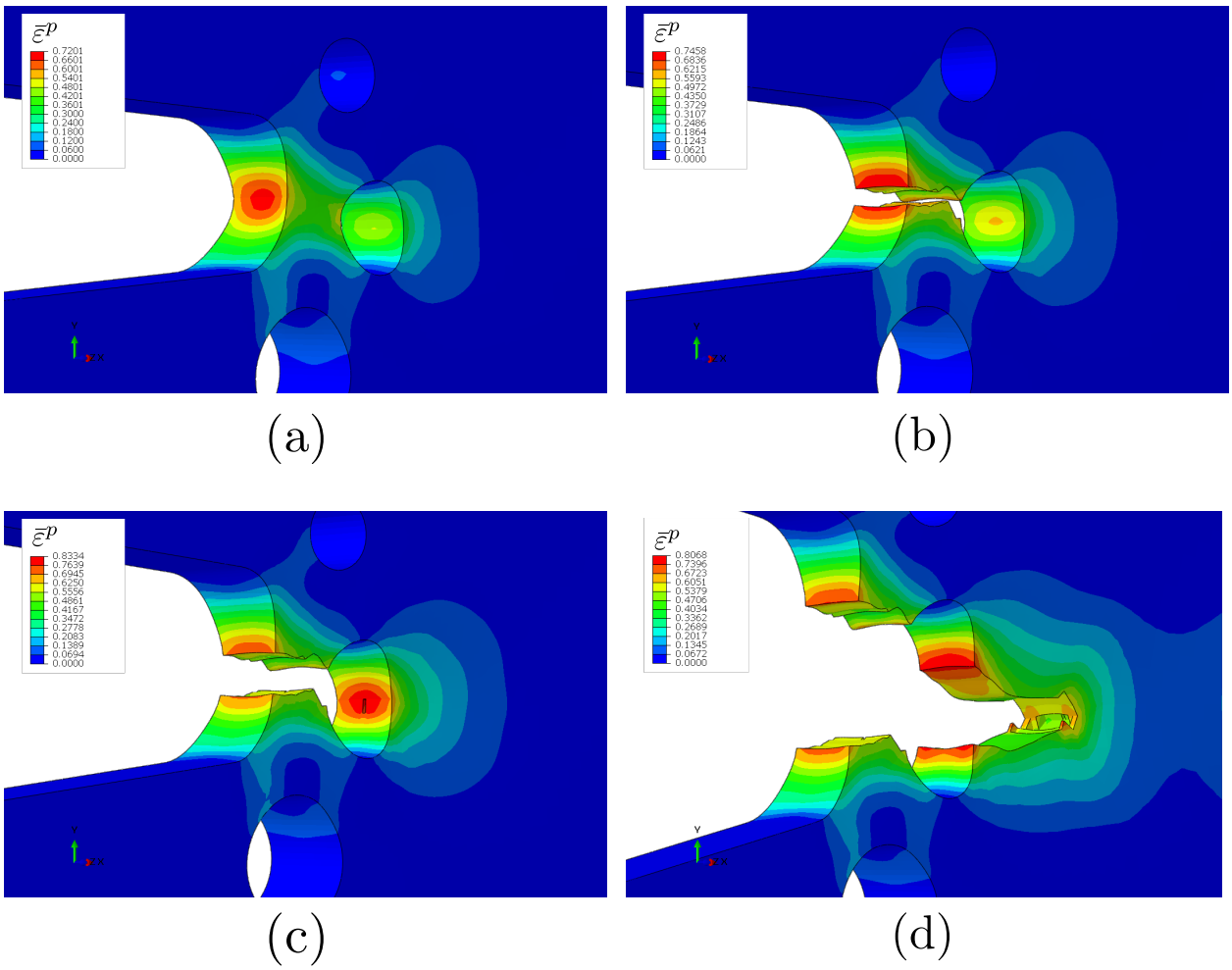

Figure 5.16 – Contours of the equivalent plastic strain $\bar{\varepsilon}^p$ as predicted by the implicit non-local model (a) just before the initiation of the first crack in the A-C ligament (COD=3.23 mm), (b) after A-C crack has fully bridged (COD=3.56 mm), (c) before the initiation of the second crack at point C (COD=4.87 mm), and (d) at the end of the analysis (COD=9.93 mm). The results shown correspond to the calculations with an aspect ratio $w = 0.2$.

damage plasticity models (Pack et al., 2014) by some of the original participants of the first SFC required the calibration of a large number of parameters yielding similar or in some cases worse predictions compared to the newly proposed porous plasticity model. On the other hand, the isotropic projection model used to simulate this problem contains (other than the initial porosity) only one, physically based, key parameter, the fixed aspect ratio w whose effect on porosity evolution is clearly established.

5.9 Concluding remarks

In this chapter, we have thoroughly discussed the numerical implementation of the implicit gradient isotropic projection model and used the models developed in this work for the solution of both quasi-static and dynamic BVPs. On the first part we presented the strong and weak forms of the governing equations and discretized the problem using the FE approximation. A simple algorithm for the numerical integration of the constitutive equations was also

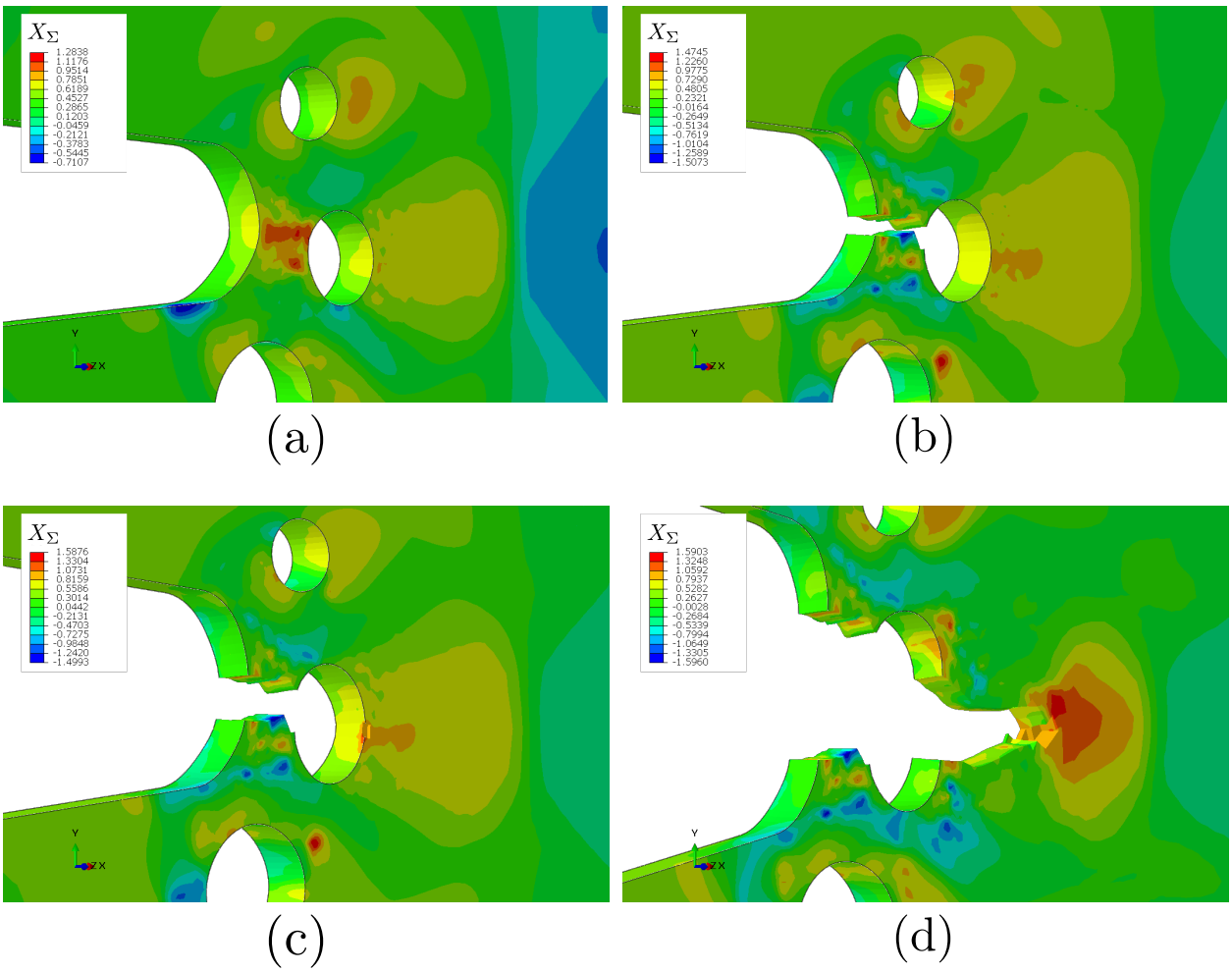

Figure 5.17 – Contours of stress triaxiality X_Σ at a cross-section $z = +1.562\,mm$ of the specimen as predicted by the implicit non-local model (a) just before the initiation of the first crack in the A-C ligament (COD=3.23 mm), (b) after A-C crack has fully bridged (COD=3.56 mm), (c) before the initiation of the second crack at point C (COD=4.87mm), and (d) at the end of the analysis (COD=9.93 mm). The results shown correspond to the calculations with an aspect ratio $w = 0.2$.

proposed. Then, attention is focused on describing an efficient implementation approach in ABAQUS commercial FE software. This is based on a thermomechanical analogy recently proposed by various authors (Azinpour et al., 2018; Seupel et al., 2018; Papadioti et al., 2019; Aravas and Papadioti, 2021). The industrially relevant problems of the hole expansion test, the Charpy V-notch test, the problem of cup-and-cone fracture of round bars and the ductile fracture of the first SFC's specimen were then analyzed using both ABAQUS/Standard and ABAQUS/Explicit solvers.

Numerical simulations have led to important conclusions regarding the effects of the model's parameters on the macroscopic structural response. First, in all cases, we find that porosity reaches much higher levels for materials comprising microstructures with low aspect ratio oblate voids when compared to those that consist of spherical voids. Numerical results were found to be in good qualitative agreement with a recent experimental realization of the hole expansion test regarding the prediction of macroscopic crack initiation position. Also, this problem highlights the necessity of using models that incorporate additional information other than just the equivalent plastic strain, for accurate prediction of ductile fracture ini-

tiation and propagation. Analysis of the cup-and-cone fracture phenomenon with both the local and non-local models shows that, in problems were strain localization is present, a regularized formulation is necessary in order to accurately describe the final failure mode of the structure. Another important observation is that macroscopic ductility of the material is an increasing function of the void aspect ratio w; the new model predicts that microstructures comprising penny-shaped voids exhibit reduced ductility, early macroscopic crack initiation, and can absorb less energy before fracture occurs as indicated by the simulation of the Charpy V-notch test. Finally, a good qualitative and quantitative agreement was found between numerical and experimental results in the ductile fracture simulation of the first SFC's specimen. These results are promising, indicating that the new porous elastic-plastic model can be used for structural calculations requiring only a small amount of parameters to be calibrated from either numerical or experimental data.

Conclusions and perspectives

Conclusions

In this work, we propose a new rate-independent, elastic-plastic model for porous metallic materials that consist of microstructures with randomly distributed and randomly oriented spheroidal voids for the investigation of the initial void shape on the effective response of the material. In the analytical model, we assume an infinite number of void families, which are all characterized by the same shape but different orientations. The equivalence between projection into the space of fourth-order isotropic tensors and orientation averaging is utilized, resulting in a constitutive model that depends only on the shape of the voids and not their orientations. To derive a sufficiently accurate model that is simple and computationally efficient for engineering applications, we take into account porosity and matrix equivalent plastic strain evolution and assume a negligible effect of the void shape evolution during plastic flow, so that the model remains isotropic. In this manner, we are able to take into account initial void shape effects with a single parameter (the void aspect ratio w) that enters the formulation seamlessly though homogenization and characterizes the shape of the randomly oriented voids in the matrix. The model is fully explicit, resembles closely the Gurson model, and is easily implemented in standard finite element codes.

The accuracy of the analytical model is then assessed by a comparison with results from numerical RVE homogenization simulations. Full-field finite element calculations are carried out, using three-dimensional unit cells containing random distributions of spheroidal voids of different volume fractions and shapes, under various combinations of average stress triaxiality and Lode angle. The convergence of the effective behavior with respect to the number of voids in the unit cell and different microstructural realizations is studied. We find that unit cells with as low as thirty randomly distributed and randomly oriented voids are enough to provide a behavior sufficiently close to isotropic and thus can be used as representative volume elements for the type of microstructures considered in this work. Sensitivity of the average RVE response with respect to the Lode angle (or equivalently to the third invariant J_3 of the deviatoric stress) is found to be relatively weak, especially at smaller values of the aspect ratio w, and thus such a dependence is not included in the analytical model. Also, examination of the local fields reveals that conditions of high stress triaxiality as well as higher plastic strains develop in microstructures comprising flat oblate voids compared to microstructures containing spherical voids. Good agreement between the average response of the RVEs and the analytical model is achieved with the introduction of only a few fitting parameters. It is also found that the average porosity evolution in unit cells containing flat-shaped voids with a low aspect ratio is greater compared to those containing spherical voids.

After calibration, the model is used to investigate the effects of void shape on the homogenized elastic-plastic response of the porous material. Material point (constitutive) calculations are carried out and evolution of microstructure as predicted by the analytical model is examined. Both high and moderate to low stress triaxiality stress states are considered as well as various microstructures consisting of voids with different aspect ratios. In particular, the model predicts rapid porosity evolution at low strain levels as the aspect ratio w takes smaller values (i.e., as the voids become more flat) resulting in significant softening. At lower stress triaxialities, a fast increase in porosity is observed for very flat penny-shaped voids ($w = 0.1$). This indicates that, even for stress states with a small hydrostatic component, the void shape effect can lead to overall softening. For low stress triaxialities, the equivalent plastic strain appears to be independent of the void shape. It is also shown that the present model can reproduce the response of the well-known Gurson–Tvergaard–Needleman (GTN) model by adjusting the void aspect ratio parameter for a given stress triaxiality. The effect of the initial porosity on the effective behavior is also found to be weaker compared to the effect of the initial shape of the voids.

Next, we examine in detail the computational issues related to the FE implementation of rate-independent constitutive models that can induce softening behavior as well as the regularization solutions available in the literature. We show analytically that, the use of a local porous plasticity model that does not include a characteristic length scale may lead to loss of ellipticity of the governing BVP resulting in a pathological mesh-dependence of the corresponding FE solutions. To regularize the problem, we propose an implicit non-local version of the new porous model based on the introduction of a non-local porosity variable. An implicit formulation is selected over an explicit one due to the associated implementation-wise advantages of the former. The non-local porosity at any point in the continuum can be interpreted as the volume average (surface average in 2D problems) of its local counterpart over a sphere (circle in 2D problems) the radius of which is directly related to the value of the characteristic length ℓ and is determined from the solution of an additional BVP. By examining the mathematical character of the non-local problem we find that the proposed isotropic implicit non-local model for porous metallic materials always preserves the elliptic properties of the corresponding governing equations. We then apply Rice's localization analysis in the problem of plane strain tension and show numerically that converged solutions in the post-bifurcation (i.e., softening) regime can be obtained by using the new non-local model, provided that a sufficiently fine spatial discretization is used. The value of the characteristic length is found to affect the slope of the post-bifurcation branch as well as the thickness of the highly strained region in the structure. We also find that the bifurcation point (i.e., the critical strain to localization) is an increasing function of the microvoids' aspect ratio parameter w; microstructures comprising very flat oblate exhibit lower critical localization strains compared to microstructures with spherical voids.

We also discuss the details concerning the numerical implementation of the non-local porous model using the finite element method. First, the strong and weak forms of the corresponding coupled BVP for the determination of the displacement field and the non-local porosity are stated. The problem is then discretized using the finite element approximation and the residuals of the problem are derived. Also, we propose a simple algorithm for the numerical integration of the non-local constitutive equations. The described formulation is general and can be implemented using either in-house or commercial FE softwares. Then, we present an efficient implementation of the proposed non-local model using ABAQUS. In particular, the non-local model is implemented using the UMAT and VUMAT user sub-

routines of ABAQUS/Standard and ABAQUS/Explicit respectively by taking advantage of a thermomechanical analogy between the modified Helmholtz BVP and the steady-state heat transfer BVP. This approach allows us to take advantage of the built-in capabilities of ABAQUS for the determination of the non-local porosity through appropriate variable identifications.

In the last part of this study, we utilize the models developed in this work for the solution of various BVPs using ABAQUS/Standard and ABAQUS/Explicit solvers under both quasi-static and dynamic conditions. In particular, the industrially relevant problems of the Hole Expansion (HET) and Charpy V-notch (CVN) test, the problem of cup-and-cone fracture of cylindrical specimens loaded in tension and the ductile fracture of a geometrically complex specimen used in the first Sandia Fracture Challenge (SFC) are numerically solved. The main purpose of these simulations is (a) to identify the role and effects of the various model parameters on the macroscopic structural response and (b) to investigate the capability of the proposed models to accurately predict experimental observations. In all cases it is found that porosity evolution is much higher for microstructures that consist of oblate voids with low aspect ratio compared to those comprising spherical or almost spherical voids. Consequently, the new model predicts that macroscopic ductility and the absorbed strain energy is an increasing function of the aspect ratio parameter w; materials whose microstructure comprises random distributions of penny-shaped microvoids (which in the limiting case can be considered as microcracks), exhibit early macroscopic crack initiation and reduced ductility. Also, the detailed analysis of the cup-and-cone fracture phenomenon with both the local and non-local models verifies that a regularized formulation is necessary to be considered in problems involving complex crack paths and strain localization in order to accurately predict the final failure pattern of the structure. Finally, the new porous model was able to closely reproduce the experimentally observed force-COD curves and the corresponding macroscopic failure path of the SFC's specimen by simply adjusting the value of the void aspect ratio w. This indicates that the proposed model can be used to make quantitative predictions with only a small number of parameters that can be calibrated from either numerically or experimentally available data.

Perspectives

Several research directions could be proposed for future work. An immediate generalization would be to consider a microstructure such as the one described in this work that comprises randomly oriented and distributed *ellipsoidal* voids (i.e., voids characterized by two aspect ratios $w_1 \neq w_2$) instead of spheroidal voids. As already mentioned, the difference in this case is that the calculation of the microstructural tensor $\boldsymbol{\mathcal{Q}}$ would require the numerical evaluation of elliptic integrals. Another direct extension consists in considering the limiting case of cracks, i.e., voids with aspect ratio $w \to 0$ together with porosity $f \to 0$. An analysis similar to that used by Willis (Willis, 1977, 1980c, 1981) could be used to derive estimates for porous materials with randomly oriented cracks. Also, the proposed isotropic projection approach could be used along with nonlinear estimates for porous microstructures derived by more advanced homogenization methods such as the "second order" method of Ponte Castañeda and co-workers (Ponte Castañeda, 1996, 2002a; Danas et al., 2008b). These estimates would allow to incorporate a dependence on the third invariant of the stress tensor J_3 in the model at the expense of a more involved numerical implementation in a finite element setting for the solution of structural problems.

The present model may also be extended in the context of rate-dependent viscoplasticity, either heuristically via the inclusion of strain-rate effects in the matrix flow stress (Papadioti et al., 2019; Aravas and Papadioti, 2021) or by considering the viscoplastic version of the LCC homogenization method (Idiart and Ponte Castañeda, 2007; Danas et al., 2008b). In the last case one should be careful on how to include the interpolation function α introduced in equation (2.59). In addition, given that the present porous model is very similar to Gurson's (and its variants), one could extent it in a straightforward manner to include terms related to void nucleation such as those presented in Benzerga et al. (2016) and Lode-dependent porosity evolution similar to that presented in Nahshon and Hutchinson (2008). Also, for problems where thermal effects could be of interest, temperature dependence can be easily incorporated in the model by assuming a temperature dependent matrix flow stress along with an additional thermal contribution to the total rate-of-deformation decomposition in equation (2.44) (e.g., see the works of Benzerga et al. (2002), Tvergaard and Needleman (2005), and Tanguy et al. (2005a)).

The model could also be used to make predictions in various loading scenarios. For instance, it would be of interest to use the proposed model (or its possible extensions) to predict the ductile fracture of structures for shear dominated stress states under quasi-static or dynamic conditions. The fracture of the Arcan specimen (e.g., see Galyon et al. (2009), Ghahremaninezhad and Ravi-Chandar (2013)) or the dynamic shear tests discussed in Peirs et al. (2012) and Jia et al. (2020) could be numerically simulated in this case and comparison with experiments be carried out. Another interesting class of problems would be ones involving cyclic loads. In these problems, the effects of elasticity and kinematic matrix hardening on porosity evolution become important and should be taken into account in order to capture the "porosity ratcheting" phenomenon (Cheng et al., 2017; Remmal and Leblond, 2024). It should be noted however that for cyclic loadings, the decoupled homogenization scheme used in this work could potentially introduce errors, especially for high inclusion (or void) volume fractions and low number of cycles and has to be used with caution in such cases (Idiart and Lahellec, 2016; Cheng et al., 2017).

Appendices

APPENDIX A

Appendix A. Explicit expressions for the components of $\mathcal{Q}$ as a function of void shape

In the general case of an isotropic matrix phase and ellipsoidal voids with semi-axes a_1, a_2, a_3 (with $a_1 \geq a_2 \geq a_3$), one may derive explicit expressions for the corresponding components of the microstructural tensor $\boldsymbol{\mathcal{Q}}$ with respect to a local system defined by the principal axes of the ellipsoids (i.e., defined by the unit vectors $\mathbf{n}^{(i)}$, $i = 1, 2, 3$). These expressions are semi-analytical, involve the numerical computation of elliptic integrals, and can be found in Mura (1987) . For the special case of *spheroidal* voids (where $a_1 = a_2 = a$ and $a_3 \neq a_1, a_2$), explicit analytical expressions were derived by Cao et al. (2015), but as functions of the semi-axes defining the voids shape. Since the voids' aspect ratio is the main parameter considered in this work, a simple reformulation of the expressions presented in the aforementioned works was carried out and the results are summarized below for both general ellipsoidal and spheroidal voids.

The expressions for the components $\mathcal{Q}_{ijkl}$ given in the following are with respect to the local coordinates system defined by the $\mathbf{n}^{(i)}$'s. The non-zero components of the microstructural tensor are given as

$$\mathcal{Q}_{1111}(\nu_\mathtt{m}, w) = \frac{1}{2\,\pi(1-\nu_\mathtt{m})}\left(4\,\pi - \frac{1}{2}I_1 - J_{11}\right), \tag{A.1}$$

$$\mathcal{Q}_{2222}(\nu_\mathtt{m}, w) = \frac{1}{2\,\pi(1-\nu_\mathtt{m})}\left(4\,\pi - \frac{1}{2}I_2 - J_{22}\right), \tag{A.2}$$

$$\mathcal{Q}_{3333}(\nu_\mathtt{m}, w) = \frac{1}{2\,\pi(1-\nu_\mathtt{m})}\left(4\,\pi - \frac{1}{2}I_3 - J_{33}\right), \tag{A.3}$$

$$\mathcal{Q}_{1112}(\nu_\mathtt{m}, w) = \frac{1}{8\,\pi(1-\nu_\mathtt{m})}\left[16\,\pi\,\nu_\mathtt{m} + (1-4\,\nu)(I_1+I_2) - J_{12}\right], \tag{A.4}$$

$$\mathcal{Q}_{1113}(\nu_\mathtt{m}, w) = \frac{1}{8\,\pi(1-\nu_\mathtt{m})}\left[16\,\pi\,\nu_\mathtt{m} + (1-4\,\nu)(I_1+I_3) - J_{13}\right], \tag{A.5}$$

$$\mathcal{Q}_{2233}(\nu_\mathtt{m}, w) = \frac{1}{8\,\pi(1-\nu_\mathtt{m})}\left[16\,\pi\,\nu_\mathtt{m} + (1-4\,\nu)(I_2+I_3) - J_{23}\right], \tag{A.6}$$

$$\mathcal{Q}_{1212}(\nu_\mathtt{m}, w) = 1 - \frac{1}{8\,\pi(1-\nu_\mathtt{m})}\left[(1-2\,\nu_\mathtt{m})(I_1+I_2) + J_{12}\right], \tag{A.7}$$

$$\mathcal{Q}_{1313}(\nu_\mathtt{m}, w) = 1 - \frac{1}{8\,\pi(1-\nu_\mathtt{m})}\left[(1-2\,\nu_\mathtt{m})(I_1+I_3) + J_{13}\right], \tag{A.8}$$

$$\mathcal{Q}_{2323}(\nu_{\mathtt{m}}, w) = 1 - \frac{1}{8\,\pi(1-\nu_{\mathtt{m}})}\left[(1-2\,\nu_{\mathtt{m}})(I_2+I_3) + J_{23}\right], \tag{A.9}$$

where $\nu_{\mathtt{m}}$ is the Poisson's ratio of the matrix material and is set to $\nu_{\mathtt{m}} = 1/2$ for the plasticity case. In the case of general ellipsoidal voids characterized by two aspect ratios (i.e., $w_1 = a_3/a_1$ and $w_2 = a_3/a_2$) the coefficients I_i and J_{ij} $(i,j = 1,2,3)$ are given as:

- general ellipsoids ($0 < w_1 < 1$ and $w_1 < w_2$):

$$I_1 = \frac{4\pi w_1^2 w_2}{(w_2^2 - w_1^2)\sqrt{1-w_1^2}}\left[F(\theta,k) - E(\theta,k)\right], \tag{A.10}$$

$$I_2 = 4\pi - I_1 - I_3, \tag{A.11}$$

$$I_3 = \frac{4\pi w_2}{(1-w_2^2)\sqrt{1-w_1^2}}\left[\frac{\sqrt{1-w_1^2}}{w_2} - E(\theta,k)\right], \tag{A.12}$$

$$J_{11} = 2\pi - \frac{1}{2}\left[\frac{w_2^2}{w_2^2-w_1^2}(I_2-I_1) + \frac{1}{1-w_1^2}(I_3-I_1)\right], \tag{A.13}$$

$$J_{22} = 2\pi - \frac{1}{2}\left[\frac{w_1^2}{w_2^2-w_1^2}(I_2-I_1) + \frac{1}{1-w_2^2}(I_2-I_3)\right], \tag{A.14}$$

$$J_{33} = 2\pi - \frac{1}{2}\left[\frac{w_1^2}{1-w_1^2}(I_3-I_1) + \frac{w_2^2}{1-w_2^2}(I_3-I_2)\right], \tag{A.15}$$

$$J_{12} = \frac{w_2^2+w_1^2}{w_2^2-w_1^2}(I_2-I_1), \qquad J_{13} = \frac{1+w_1^2}{1-w_1^2}(I_3-I_1), \qquad J_{23} = \frac{1+w_2^2}{1-w_2^2}(I_3-I_2) \tag{A.16}$$

with

$$F(\theta,k) = \int_0^\theta \frac{1}{\sqrt{1-k^2\sin^2\phi}}d\phi, \qquad E(\theta,k) = \int_0^\theta \sqrt{1-k^2\sin^2\phi}\,d\phi \tag{A.17}$$

$$\theta = \sin^{-1}\left(\sqrt{1-w_1^2}\right), \qquad k = \frac{\sqrt{w_2^2-w_1^2}}{w_2\sqrt{1-w_1^2}} \tag{A.18}$$

In the above expressions, $F(\theta,k), E(\theta,k)$ are elliptic integrals of the first and second kind that need to be evaluated numerically for the determination of the components of $\boldsymbol{\mathcal{Q}}$. Details on the numerical evaluation of these integrals can be found in Appendix A of Aravas and Ponte Castañeda (2004).

In the special case of spheroidal voids, the model proposed in this work admits one aspect ratio $w = a_3/a_1 = a_3/a_2 = a_3/a$ as the parameter that defines the void shape and the above coefficients can be determined analytically as follows

- oblate voids ($0 < w < 1$):

$$I_1 = I_2 = \frac{2\,\pi\,w}{(1-w^2)^{3/2}}\left[\cos^{-1}(w) - w(1-w^2)^{1/2}\right], \quad I_3 = 4\,\pi - 2\,I_2 \tag{A.19}$$

$$J_{11} = \frac{3}{2}\left(\pi - \frac{1}{4}\frac{I_3-I_1}{1-w^2}\right), \quad J_{22} = J_{11}, \quad J_{33} = 2\,\pi - \frac{w^2}{1-w^2}(I_3-I_1), \tag{A.20}$$

$$J_{12} = 2\,\pi - \frac{1}{2}\frac{I_3-I_1}{1-w^2}, \quad J_{13} = \frac{1+w^2}{1-w^2}(I_3-I_1), \quad J_{23} = J_{13} \tag{A.21}$$

- prolate voids ($w > 1$):

$$I_1 = I_2 = \frac{2\,\pi\,w}{(w^2-1)^{3/2}}\left[w(w^2-1)^{1/2} - \cosh^{-1}(w)\right], \quad I_3 = 4\,\pi - 2\,I_2 \tag{A.22}$$

$$J_{11} = \frac{3}{2}\left(\pi - \frac{1}{4}\frac{I_2 - I_3}{w^2-1}\right), \quad J_{22} = J_{11}, \quad J_{33} = 2\,\pi - \frac{w^2}{w^2-1}(I_2 - I_3), \tag{A.23}$$

$$J_{12} = 2\,\pi - \frac{1}{2}\frac{I_2 - I_3}{w^2-1}, \quad J_{13} = \frac{w^2+1}{w^2-1}(I_2 - I_3), \quad J_{23} = J_{13} \tag{A.24}$$

- spherical voids ($w = 1$):

$$I_1 = I_2 = I_3 = \frac{4\,\pi}{3}, \tag{A.25}$$

$$J_{11} = J_{22} = J_{33} = \frac{6\,\pi}{5}, \tag{A.26}$$

$$J_{12} = J_{13} = J_{23} = \frac{8\,\pi}{5}. \tag{A.27}$$

The remaining non-zero components are determined by using the minor and major symmetries of $\boldsymbol{\mathcal{Q}}$.

APPENDIX B

Appendix B. Exact Jacobians for the non-local problem

As mentioned in Section 5.3.1, if an implicit scheme is used for the solution of the discretized global problem, the equilibrium equations and the equation for the non-local porosity are written at the end of the increment resulting in sets of nonlinear equations for the global unknowns. An iterative solution method is used in this case (such as the Newton-Raphson) and the derivatives $\partial\boldsymbol{\sigma}/\partial\mathbf{E}$, $\partial\boldsymbol{\sigma}/\partial f^{\mathrm{nl}}$, $\partial f/\partial\mathbf{E}$, and $\partial f/\partial f^{\mathrm{nl}}$ at the end of the increment need to be provided for the calculation of the global Jacobian of the system. These quantities depend on the algorithm used for the numerical integration of the constitutive equations and in general will be different than the "tangent" expressions derived from the corresponding rate (continuum) form of the equations.

Depending on the numerical integration scheme employed and the complexity of the constitutive model, exact expressions for these quantities might be difficult to derive and implement numerically. In this case, the exact derivatives are replaced by the corresponding "tangent" ones which are usually easier to derive. It should be emphasized that approximation of these expressions affects only the quadratic convergence of the global problem and not the accuracy of the results (Simo and Hughes, 1998). However, such approximations can lead to convergence issues in highly nonlinear problems or if large time increments are used. For this reason, we outline in the following the derivation of exact expressions for the required derivatives based on the algorithm used for the numerical integration of the constitutive equations in Section 5.2.1. These can be used instead of the "tangent" derivatives (5.59)–(5.60) to achieve better rate of convergence in the iterative solution of the global problem.

Starting from expression (5.49) and accounting for the isotropy of the effective fourth-order elasticity tensor $\boldsymbol{\mathcal{L}}$ of the porous material, the variation of the stress tensor $\hat{\boldsymbol{\sigma}}$ is given as:

$$\partial\hat{\boldsymbol{\sigma}}_{n+1} = \boldsymbol{\mathcal{L}}_n : \partial\mathbf{E} - \kappa\,\partial\Delta\varepsilon_m\boldsymbol{\delta} - 2\mu\left(\partial\Delta\varepsilon_{eq} + \Delta\varepsilon_{eq}\partial\hat{\mathbf{n}}_{n+1}\right) \tag{B.1}$$

Using now equations (5.53) and (5.54) we have:

$$\begin{aligned}\partial\Delta\varepsilon_m\frac{\partial\Phi}{\partial\hat{\sigma}_e} - \Delta\varepsilon_m\left(\frac{\partial^2\Phi}{\partial\hat{\sigma}_e\partial\hat{p}}\partial\hat{p} + \frac{\partial^2\Phi}{\partial\hat{\sigma}_e^2}\partial\hat{\sigma}_e + \frac{\partial^2\Phi}{\partial\hat{\sigma}_e\partial\bar{\varepsilon}^p}\partial\bar{\varepsilon}^p + \frac{\partial^2\Phi}{\partial\hat{\sigma}_e\partial f^{\mathrm{nl}}}\partial f^{\mathrm{nl}}\right) - \\ - \partial\Delta\varepsilon_{eq}\frac{\partial\Phi}{\partial\hat{p}} - \Delta\varepsilon_{eq}\left(\frac{\partial^2\Phi}{\partial\hat{p}^2}\partial\hat{p} + \frac{\partial^2\Phi}{\partial\hat{p}\partial\hat{\sigma}_e}\partial\hat{\sigma}_e + \frac{\partial^2\Phi}{\partial\hat{p}\partial\bar{\varepsilon}^p}\partial\bar{\varepsilon}^p + \frac{\partial^2\Phi}{\partial\hat{p}\partial f^{\mathrm{nl}}}\partial f^{\mathrm{nl}}\right) = 0\end{aligned} \tag{B.2}$$

and

$$\frac{\partial \Phi}{\partial \hat{p}} \partial \hat{p} + \frac{\partial \Phi}{\partial \hat{\sigma}_e} \partial \hat{s}_e + \frac{\partial \Phi}{\partial \bar{\varepsilon}^p} \partial \bar{\varepsilon}^p + \frac{\partial \Phi}{\partial f^{\mathrm{nl}}} \partial f^{\mathrm{nl}} = 0 \tag{B.3}$$

The variations $\partial \hat{p}, \partial \hat{\sigma}_e$, and $\partial \bar{\varepsilon}^p$ can be calculated using equations $(5.50)_1$, $(5.50)_2$, and (5.51) as

$$\partial \hat{p} = \kappa\, \boldsymbol{\delta} : \partial \mathbf{E} - \kappa\, \partial \Delta \varepsilon_m \tag{B.4}$$

$$\partial \hat{\sigma}_e = 2\mu\, \hat{\mathbf{n}}_{n+1} : \partial \mathbf{E} - 3\mu\, \partial \Delta \varepsilon_{eq} \tag{B.5}$$

$$\partial \bar{\varepsilon}^p = \frac{\partial \bar{\varepsilon}^p}{\partial \Delta \varepsilon_m} \partial \Delta \varepsilon_m + \frac{\partial \bar{\varepsilon}^p}{\partial \Delta \varepsilon_{eq}} \Delta \varepsilon_{eq} + \frac{\partial \bar{\varepsilon}^p}{\partial f^{\mathrm{nl}}} \partial f^{\mathrm{nl}} \tag{B.6}$$

Substituting relations (B.4)–(B.6) into (B.2)–(B.3) and carrying out the algebra we arrive at the following system of equations for the variations $\partial \Delta \varepsilon_m, \partial \Delta \varepsilon_{eq}$

$$A_{11} \partial \Delta \varepsilon_m + A_{12} \partial \Delta \varepsilon_{eq} = (B_{11} \boldsymbol{\delta} + B_{12} \hat{\mathbf{n}}_{n+1}) : \mathbf{E} + C_1 \partial f^{\mathrm{nl}} \tag{B.7}$$

$$A_{21} \partial \Delta \varepsilon_m + A_{22} \partial \Delta \varepsilon_{eq} = (B_{21} \boldsymbol{\delta} + B_{22} \hat{\mathbf{n}}_{n+1}) : \mathbf{E} + C_2 \partial f^{\mathrm{nl}} \tag{B.8}$$

with the corresponding coefficients being given as

$$A_{11} = \frac{\partial \Phi}{\partial \hat{\sigma}_e} + \Delta \varepsilon_m \left(\frac{\partial^2 \Phi}{\partial \hat{\sigma}_e \partial \bar{\varepsilon}^p} \frac{\partial \bar{\varepsilon}^p}{\partial \Delta \varepsilon_m} - \kappa \frac{\partial^2 \Phi}{\partial \hat{\sigma}_e \partial \hat{p}} \right) + \Delta \varepsilon_{eq} \left(\kappa \frac{\partial^2 \Phi}{\partial \hat{p}^2} - \frac{\partial^2 \Phi}{\partial \hat{p} \partial \bar{\varepsilon}^p} \frac{\partial \bar{\varepsilon}^p}{\partial \Delta \varepsilon_m} \right), \tag{B.9}$$

$$A_{12} = -\frac{\partial \Phi}{\partial \hat{p}} + \Delta \varepsilon_m \left(\frac{\partial^2 \Phi}{\partial \hat{\sigma}_e \partial \bar{\varepsilon}^p} \frac{\partial \bar{\varepsilon}^p}{\partial \Delta \varepsilon_{eq}} - 3\mu \frac{\partial^2 \Phi}{\partial \hat{\sigma}_e^2} \right) + \Delta \varepsilon_{eq} \left(3\mu \frac{\partial^2 \Phi}{\partial \hat{p} \partial \hat{\sigma}_e} - \frac{\partial^2 \Phi}{\partial \hat{p} \partial \bar{\varepsilon}^p} \frac{\partial \bar{\varepsilon}^p}{\partial \Delta \varepsilon_{eq}} \right), \tag{B.10}$$

$$A_{21} = \kappa \frac{\partial \Phi}{\partial \hat{p}} + \frac{\partial \Phi}{\partial \bar{\varepsilon}^p} \frac{\partial \bar{\varepsilon}^p}{\partial \Delta \varepsilon_m}, \qquad A_{22} = -3\mu \frac{\partial \Phi}{\partial \hat{\sigma}_e} + \frac{\partial \Phi}{\partial \bar{\varepsilon}^p} \frac{\partial \bar{\varepsilon}^p}{\partial \Delta \varepsilon_{eq}}, \tag{B.11}$$

$$B_{11} = \kappa \left(\Delta \varepsilon_{eq} \frac{\partial^2 \Phi}{\partial \hat{p}^2} - \Delta \varepsilon_m \frac{\partial^2 \Phi}{\partial \hat{\sigma}_e \partial \hat{p}} \right), \qquad B_{12} = 2\mu \left(\Delta \varepsilon_{eq} \frac{\partial^2 \Phi}{\partial \hat{p} \partial \hat{\sigma}_e} - \Delta \varepsilon_m \frac{\partial^2 \Phi}{\partial \hat{\sigma}_e^2} \right), \tag{B.12}$$

$$B_{21} = -\kappa \frac{\partial \Phi}{\partial \hat{p}}, \qquad B_{22} = -2\mu \frac{\partial \Phi}{\partial \hat{\sigma}_e} \tag{B.13}$$

$$C_1 = \Delta \varepsilon_{eq} \left(\frac{\partial^2 \Phi}{\partial \hat{p} \partial f^{\mathrm{nl}}} + \frac{\partial^2 \Phi}{\partial \hat{p} \partial \bar{\varepsilon}^p} \frac{\partial \bar{\varepsilon}^p}{\partial f^{\mathrm{nl}}} \right) - \Delta \varepsilon_m \left(\frac{\partial^2 \Phi}{\partial \hat{\sigma}_e \partial f^{\mathrm{nl}}} + \frac{\partial^2 \Phi}{\partial \hat{\sigma}_e \partial \bar{\varepsilon}^p} \frac{\partial \bar{\varepsilon}^p}{\partial f^{\mathrm{nl}}} \right), \tag{B.14}$$

$$C_2 = -\left(\frac{\partial \Phi}{\partial \bar{\varepsilon}^p} \frac{\partial \bar{\varepsilon}^p}{\partial f^{\mathrm{nl}}} + \frac{\partial \Phi}{\partial f^{\mathrm{nl}}} \right) \tag{B.15}$$

The derivatives of the yield function appearing in the coefficients (B.9)–(B.15) can be calculated explicitly at the end of the increment by using equation (4.15). The system of equations (B.7)–(B.8) can be solved analytically yielding the following expressions for the variations $\partial \Delta \varepsilon_m, \partial \Delta \varepsilon_{eq}$ in terms of $\partial \mathbf{E}, \partial f^{\mathrm{nl}}$:

$$\partial \Delta \varepsilon_m = (a_{p\delta} \boldsymbol{\delta} + a_{pn} \hat{\mathbf{n}}_{n+1}) : \partial \mathbf{E} + a_{pf} \partial f^{\mathrm{nl}} \tag{B.16}$$

$$\partial \Delta \varepsilon_{eq} = (a_{q\delta} \boldsymbol{\delta} + a_{qn} \hat{\mathbf{n}}_{n+1}) : \partial \mathbf{E} + a_{qf} \partial f^{\mathrm{nl}} \tag{B.17}$$

where

$$a_{p\delta} = \frac{1}{\Delta}\left(A_{22}B_{11} - A_{12}B_{21}\right), \quad a_{pn} = \frac{1}{\Delta}\left(A_{22}B_{12} - A_{12}B_{22}\right), \quad a_{pf} = \frac{1}{\Delta}\left(A_{22}C_1 - A_{12}C_2\right), \tag{B.18}$$

$$a_{q\delta} = \frac{1}{\Delta}\left(A_{11}B_{21} - A_{21}B_{11}\right), \quad a_{qn} = \frac{1}{\Delta}\left(A_{11}B_{22} - A_{21}B_{12}\right), \quad a_{qf} = \frac{1}{\Delta}\left(A_{11}C_2 - A_{21}C_1\right), \tag{B.19}$$

$$\Delta = A_{11}A_{22} - A_{21}A_{12} \tag{B.20}$$

Also, using $(5.48)_3$, the variation $\partial\hat{\mathbf{n}}_{n+1}$ can be shown to be given as:

$$\partial\hat{\mathbf{n}}_{n+1} = \frac{3\mu}{\hat{\sigma}_e^e}\left(\boldsymbol{\mathcal{K}} - \frac{2}{3}\hat{\mathbf{n}}_{n+1}\hat{\mathbf{n}}_{n+1}\right) \tag{B.21}$$

Substitution of expressions (B.16), (B.17), and (B.21) into equation (B.1) leads to

$$\begin{aligned}\partial\hat{\boldsymbol{\sigma}}_{n+1} = \Bigg\{ & \boldsymbol{\mathcal{L}}_n - \kappa\,\boldsymbol{\delta}\left(a_{p\delta}\boldsymbol{\delta} + a_{pn}\hat{\mathbf{n}}_{n+1}\right) - \\ & - 2\mu\left[\hat{\mathbf{n}}_{n+1}\left(a_{q\delta}\boldsymbol{\delta} + a_{qn}\hat{\mathbf{n}}_{n+1}\right) + \left(1 - \frac{\hat{\sigma}_e}{\hat{\sigma}_e^e}\right)\left(\boldsymbol{\mathcal{K}} - \frac{2}{3}\hat{\mathbf{n}}_{n+1}\hat{\mathbf{n}}_{n+1}\right)\right]\Bigg\} : \partial\mathbf{E} - \\ & - \left(\kappa\, a_{pf}\boldsymbol{\delta} + 2\mu\, a_{qf}\hat{\mathbf{n}}_{n+1}\right)\partial f^{\mathrm{nl}}\end{aligned} \tag{B.22}$$

Last equation implies that

$$\begin{aligned}\frac{\partial\hat{\boldsymbol{\sigma}}_{n+1}}{\partial\mathbf{E}_{n+1}} = & \boldsymbol{\mathcal{L}}_n - \kappa\,\boldsymbol{\delta}\left(a_{p\delta}\boldsymbol{\delta} + a_{pn}\hat{\mathbf{n}}_{n+1}\right) - \\ & - 2\mu\left[\hat{\mathbf{n}}_{n+1}\left(a_{q\delta}\boldsymbol{\delta} + a_{qn}\hat{\mathbf{n}}_{n+1}\right) + \left(1 - \frac{\hat{\sigma}_e}{\hat{\sigma}_e^e}\right)\left(\boldsymbol{\mathcal{K}} - \frac{2}{3}\hat{\mathbf{n}}_{n+1}\hat{\mathbf{n}}_{n+1}\right)\right]\end{aligned} \tag{B.23}$$

$$\frac{\partial\hat{\boldsymbol{\sigma}}_{n+1}}{\partial f^{\mathrm{nl}}_{n+1}} = -\left(\kappa\, a_{pf}\boldsymbol{\delta} + 2\mu\, a_{qf}\hat{\mathbf{n}}_{n+1}\right) \tag{B.24}$$

Similarly, by taking the variation of the local porosity at the end of the increment given by equation (5.52) and using expressions (B.16) and (B.17), we arrive at the following expression

$$\partial f_{n+1} = \left[\left(1 - f^{\mathrm{nl}}\right)\left(a_{p\delta}\boldsymbol{\delta} + a_{pn}\hat{\mathbf{n}}_{n+1}\right)\right] : \partial\mathbf{E} + \left[\left(-\Delta\varepsilon_m + \left(1 - f^{\mathrm{nl}}\right)a_{pf}\right)\right]\partial f^{\mathrm{nl}} \tag{B.25}$$

which implies that

$$\frac{\partial f_{n+1}}{\partial\mathbf{E}_{n+1}} = \left(1 - f^{\mathrm{nl}}\right)\left(a_{p\delta}\boldsymbol{\delta} + a_{pn}\hat{\mathbf{n}}_{n+1}\right) \tag{B.26}$$

$$\frac{\partial f_{n+1}}{\partial f^{\mathrm{nl}}_{n+1}} = -\Delta\varepsilon_m + \left(1 - f^{\mathrm{nl}}\right)a_{pf} \tag{B.27}$$

Bibliography

Abaqus, 2021. CAE/2021. Simulia, RI, USA.

Abatour, M., Forest, S., 2023. Strain gradient plasticity based on saturating variables. European Journal of Mechanics - A/Solids, 105016.
URL https://www.sciencedirect.com/science/article/pii/S0997753823001080

Agoras, M., Ponte Castañeda, P., 2013. Iterated linear comparison bounds for viscoplastic porous materials with "ellipsoidal" microstructures. Journal of the Mechanics and Physics of Solids 61 (3), 701–725.
URL https://www.sciencedirect.com/science/article/pii/S0022509612002414

Agoras, M., Ponte Castañeda, P., 2014. Anisotropic finite-strain models for porous viscoplastic materials with microstructure evolution. International Journal of Solids and Structures 51 (5), 981–1002.
URL https://www.sciencedirect.com/science/article/pii/S002076831300468X

Aifantis, E., 1984. On the microstructural origin of certain inelastic models. Journal of Engineering Materials and Technology 106 (4), 326–330.
URL https://doi.org/10.1115/1.3225725

Aifantis, E., 1987. The physics of plastic deformation. International Journal of Plasticity 3 (3), 211–247.
URL https://www.sciencedirect.com/science/article/pii/0749641987900210

Aifantis, E., 1992. On the role of gradients in the localization of deformation and fracture. International Journal of Engineering Science 30 (10), 1279–1299.
URL https://www.sciencedirect.com/science/article/pii/0020722592901413

Aifantis, E., 1999. Strain gradient interpretation of size effects. International Journal of Fracture, 299–314.

Anderson, P. M., Fleck, N. A., Johnson, K. L., 1990. Localization of plastic deformation in shear due to microcracks. Journal of the Mechanics and Physics of Solids 38 (5), 681–699.
URL https://www.sciencedirect.com/science/article/pii/0022509690900283

Andrews, D., L., Thirunamachandran, T., 1977. On three-dimensional rotational averages. Journal of Chemical Physics 67, 5026–5033.
URL https://doi.org/10.1063/1.434725

Andrews, S. S., 2004. Using rotational averaging to calculate the bulk response of isotropic and anisotropic samples from molecular parameters. Journal of Chemical Education 81 (6), 877.
URL https://doi.org/10.1021/ed081p877

Anoukou, K., Brenner, R., Hong, F., Pellerin, M., Danas, K., 2018. Random distribution of polydisperse ellipsoidal inclusions and homogenization estimates for porous elastic materials. Computers & Structures 210, 87–101.
URL https://www.sciencedirect.com/science/article/pii/S0045794918304565

Aravas, N., 1987. On the numerical integration of a class of pressure-dependent plasticity models. International Journal for Numerical Methods in Engineering 24 (7), 1395–1416.
URL https://onlinelibrary.wiley.com/doi/abs/10.1002/nme.1620240713

Aravas, N., Papadioti, I., 2021. A non-local plasticity model for porous metals with deformation-induced anisotropy: Mathematical and computational issues. Journal of the Mechanics and Physics of Solids 146, 104190.
URL https://www.sciencedirect.com/science/article/pii/S0022509620304154

Aravas, N., Ponte Castañeda, P., 2004. Numerical methods for porous metals with deformation-induced anisotropy. Computer Methods in Applied Mechanics and Engineering 193 (36), 3767–3805.
URL https://www.sciencedirect.com/science/article/pii/S0045782504001422

Arts, R., Helbig, K., Rasolofosaon, P., 2005. General anisotropic elastic tensor in rocks: Approximation, invariants, and particular directions. pp. 1534–1537.
URL https://library.seg.org/doi/abs/10.1190/1.1888997

Azinpour, E., Ferreira, J., Parente, M., Cesar de Sa, J., 2018. A simple and unified implementation of phase field and gradient damage models. Advanced Modeling and Simulation in Engineering Sciences 5, 1–24.
URL https://amses-journal.springeropen.com/articles/10.1186/s40323-018-0106-7

Bai, Y., Wierzbicki, T., 2008. A new model of metal plasticity and fracture with pressure and Lode dependence. International Journal of Plasticity 24 (6), 1071–1096.
URL https://www.sciencedirect.com/science/article/pii/S0749641907001246

Bao, Y., Wierzbicki, T., 2004. On fracture locus in the equivalent strain and stress triaxiality space. International Journal of Mechanical Sciences 46 (1), 81–98.
URL https://www.sciencedirect.com/science/article/pii/S0020740304000360

Barlo, A., Sigvant, M., Pérez, L., Islam, M., Pilthammar, J., 2022. A study of the boundary conditions in the ISO-16630 Hole Expansion Test. IOP Conference Series: Materials Science and Engineering 1238, 012031.
URL https://dx.doi.org/10.1088/1757-899X/1238/1/012031

Barnwal, V., Lee, S.-Y., Yoon, S., Kim, J.-H., Barlat, F., 2020. Fracture characteristics of advanced high strength steels during hole expansion test. International Journal of Fracture 224, 217–233.
URL https://doi.org/10.1007/s10704-020-00458-y

Barrera, O., Tarleton, E., Tang, H., Cocks, A., 2016. Modelling the coupling between hydrogen diffusion and the mechanical behaviour of metals. Computational Materials Science 122, 219–228.
URL https://www.sciencedirect.com/science/article/pii/S0927025616302658

Barsoum, I., Faleskog, J., 2007. Rupture mechanisms in combined tension and shear—Micromechanics. International Journal of Solids and Structures 44 (17), 5481–5498.
URL https://www.sciencedirect.com/science/article/pii/S0020768307000182

Bažant, Z., Belytschko, T., Chang, T., 1984. Continuum theory for strain-softening. Journal of Engineering Mechanics 110, 1666–1692.
URL https://ascelibrary.org/doi/10.1061/%28ASCE%290733-9399%281984%29110%3A12%281666%29

Bažant, Z., Pijaudier-Cabot, G., 1988. Nonlocal continuum damage, localization instability and convergence. Journal of Applied Mechanics 55, 287–293.
URL https://asmedigitalcollection.asme.org/appliedmechanics/article-abstract/55/2/287/423310/

Bažant, Z., Pijaudier-Cabot, G., 1989. Measurement of characteristic length of nonlocal continuum. Journal of Engineering Mechanics 115, 755–767.
URL https://ascelibrary.org/doi/10.1061/%28ASCE%290733-9399%281989%29115%3A4%28755%29

Bele, E., A., G., Pickering, E., Borstnar, G., Katsamenis, O., Pierron, F., Danas, K., Deshpande, V., 2017. Deformation mechanisms of idealised cermets under multi-axial loading. Journal of the Mechanics and Physics of Solids 102, 80–100.
URL https://www.sciencedirect.com/science/article/pii/S0022509616308146

Bellégo, C., Dubé, J., Pijaudier-Cabot, G., Gérard, B., 2003. Calibration of nonlocal damage model from size effect tests. European Journal of Mechanics - A/Solids 22 (1), 33–46.
URL https://www.sciencedirect.com/science/article/pii/S099775380201255X

Benallal, A., Tvergaard, V., 1995. Nonlocal continuum effects on bifurcation in the plane strain tension-compression test. Journal of the Mechanics and Physics of Solids 43 (5), 741–770.
URL https://www.sciencedirect.com/science/article/pii/002250969500002Z

Benhizia, A., Kanit, T., Outtas, T., Madani, S., Imad, A., 2014. Computation of effective behavior of isotropic transverse composite in nonlinear problems. Mechanics Research Communications 59, 6–13.
URL https://www.sciencedirect.com/science/article/pii/S0093641314000305

Bensaada, R., Kanit, T., Imad, A., Almansba, M., Saouab, A., 2022. Void-growth computational analysis in elastic-plastic porous materials. International Journal of Mechanical Sciences 217, 107021.
URL https://www.sciencedirect.com/science/article/pii/S0020740321007086

Benzerga, A., Leblond, J.-B., 2010. Ductile fracture by void growth to coalescence. Advances in Applied Mechanics 44, 169–305.
URL https://www.sciencedirect.com/science/article/pii/S006521561044003X

Benzerga, A., Leblond, J.-B., Needleman, A., Tvergaard, V., 2016. Ductile failure modeling. International Journal of Fracture 201, 29–80.
URL https://doi.org/10.1007/s10704-016-0142-6

Benzerga, A., Tvergaard, V., Needleman, A., 2002. Size Effects in the Charpy V-Notch Test. International Journal of Fracture 116, 275–296.
URL https://doi.org/10.1023/A:1020112028641

Bergheau, J.-M., Leblond, J.-B., Perrin, G., 2014. A new numerical implementation of a second-gradient model for plastic porous solids, with an application to the simulation of ductile rupture tests. Computer Methods in Applied Mechanics and Engineering 268, 105–125.
URL https://www.sciencedirect.com/science/article/pii/S0045782513002338

Bigoni, D., Hueckel, T., 1991. Uniqueness and localization—I. associative and non-associative elastoplasticity. International Journal of Solids and Structures 28 (2), 197–213.
URL https://www.sciencedirect.com/science/article/pii/002076839190205T

Bilger, N., Auslender, F., Bornert, M., Moulinec, H., Zaoui, A., 2007. Bounds and estimates for the effective yield surface of porous media with a uniform or a nonuniform distribution of voids. European Journal of Mechanics - A/Solids 26 (5), 810–836.
URL https://www.sciencedirect.com/science/article/pii/S099775380700023X

Bouby, C., Morin, L., Bignonnet, F., Dormieux, L., Kondo, D., 2023. On the thermodynamics consistency of Gurson's model and its computational implications. International Journal of Solids and Structures 279, 112359.
URL https://www.sciencedirect.com/science/article/pii/S0020768323002561

Bouchet, C., Tanguy, B., Besson, J., Bugat, S., 2005. Prediction of the effects of neutron irradiation on the Charpy ductile to brittle transition curve of an A508 pressure vessel steel. Computational Materials Science 32 (3), 294–300, iWCMM.
URL https://www.sciencedirect.com/science/article/pii/S0927025604002071

Boyce, B., Kramer, S., Bosiljevac, T. R., Corona, E., Moore, J. A., Elkhodary, K., Simha, C. H. M., Williams, B., Cerrone, A., Nonn, A., Hochhalter, J., Bomarito, G., Warner, J., Carter, B. J., Warner, D. H., Ingraffea, A., Zhang, T., Fang, X., Lua, J., Liang, X., 2016. The Second Sandia Fracture Challenge: Predictions of Ductile Failure under Quasi-Static and Moderate-Rate Dynamic Loading. International Journal of Fracture 198, 5–100.
URL https://doi.org/10.1007/s10704-016-0089-7

Boyce, B., Kramer, S., Fang, H., Cordova, T., Neilsen, M., Dion, K., Kaczmarowski, A., Karasz, E., Xue, L., Gross, A., Ghahremaninezhad, A., Ravi-Chandar, K., Lin, S.-P., Chi, S.-W., Chen, J.-S., Yreux, E., Rüter, M., Qian, D., Zhou, Z., Wierzbicki, T., 2014. The Sandia Fracture Challenge: blind round robin predictions of ductile tearing. International Journal of Fracture 10, 5–68.
URL https://doi.org/10.1007/s10704-013-9904-6

Bush, A., 1992. Perturbation Methods for Engineers and Scientists. CRC-Press.
URL https://doi.org/10.1201/9780367804602

Cao, T., S., Mazière, M., Danas, K., Besson, J., 2015. A model for ductile damage prediction at low stress triaxialities incorporating void shape change and void rotation. International Journal of Solids and Structures 63, 240–263.
URL https://www.sciencedirect.com/science/article/pii/S0020768315001080

Charles, Y., Mougenot, J., Gaspérini, M., 2021. Effect of transient trapping on hydrogen transport near a blunting crack tip. International Journal of Hydrogen Energy 46 (18), 10995–11003.
URL https://www.sciencedirect.com/science/article/pii/S036031992034787X

Cheng, L., Danas, K., Constantinescu, A., Kondo, D., 2017. A homogenization model for porous ductile solids under cyclic loads comprising a matrix with isotropic and linear kinematic hardening. International Journal of Solids and Structures 121, 174–190.
URL https://www.sciencedirect.com/science/article/pii/S0020768317302354

Chu, C., Needleman, A., 1980. Void nucleation effects in biaxially stretched sheets. Journal of Engineering Materials and Technology 102, 249–256.
URL https://doi.org/10.1115/1.3224807

Coleman, B., Hodgdon, M., 1985. On shear bands in ductile materials. Archive for Rational Mechanics and Analysis, 219–247.
URL https://doi.org/10.1007/BF00251732

Dæhli, L. E., Morin, D., Børvik, T., Hopperstad, O. S., 2018. A Lode-dependent Gurson model motivated by unit cell analyses. Engineering Fracture Mechanics 190, 299–318.
URL https://www.sciencedirect.com/science/article/pii/S0013794417306872

Danas, K., 2008. Homogenization-based constitutive models for viscoplastic porous media with evolving microstructure. Ph.D. thesis, University of Pennsylvania.

Danas, K., Aravas, N., 2012. Numerical modeling of elasto-plastic porous materials with void shape effects at finite deformations. Composites Part B: Engineering 43, 2544–2559.
URL https://www.sciencedirect.com/science/article/pii/S1359836812000029

Danas, K., Idiart, M., Ponte Castañeda, P., 2008a. A homogenization-based constitutive model for two-dimensional viscoplastic porous media. Comptes Rendus Mécanique 336 (1), 79–90.
URL https://www.sciencedirect.com/science/article/pii/S1631072107001994

Danas, K., Idiart, M., Ponte Castañeda, P., 2008b. A homogenization-based constitutive model for isotropic viscoplastic porous media. International Journal of Solids and Structures 45 (11), 3392–3409.
URL https://www.sciencedirect.com/science/article/pii/S0020768308000656

Danas, K., Ponte Castañeda, P., 2009a. A finite-strain model for anisotropic viscoplastic porous media: I – Theory. European Journal of Mechanics - A/Solids 28 (3), 387–401.
URL https://www.sciencedirect.com/science/article/pii/S0997753808001150

Danas, K., Ponte Castañeda, P., 2009b. A finite-strain model for anisotropic viscoplastic porous media: II – Applications. European Journal of Mechanics - A/Solids 28 (3), 402–416.
URL https://www.sciencedirect.com/science/article/pii/S0997753808001149

Danas, K., Ponte Castañeda, P., 2012. Influence of the Lode parameter and the stress triaxiality on the failure of elasto-plastic porous materials. International Journal of Solids and Structures 49 (11), 1325–1342.
URL https://www.sciencedirect.com/science/article/pii/S0020768312000467

de Borst, R., Pamin, J., Sluys, L., 1995. Computational issues in gradient plasticity. Wiley, United States, pp. 159–200.

DeSandre, D., Benzerga, A., Tvergaard, V., Needleman, A., 2004. Material inertia and size effects in the Charpy V-notch test. European Journal of Mechanics - A/Solids 23 (3), 373–386.
URL https://www.sciencedirect.com/science/article/pii/S0997753804000221

Dunand, M., Mohr, D., 2011. Optimized butterfly specimen for the fracture testing of sheet materials under combined normal and shear loading. Engineering Fracture Mechanics 78 (17), 2919–2934.
URL https://www.sciencedirect.com/science/article/pii/S0013794411003067

Dunand, M., Mohr, D., 2014. Effect of Lode parameter on plastic flow localization after proportional loading at low stress triaxialities. Journal of the Mechanics and Physics of Solids 66, 133–153.
URL https://www.sciencedirect.com/science/article/pii/S0022509614000180

El Moumen, A., Imad, A., Kanit, T., Hilali, E., El Minor, H., 2014. A multiscale approach and microstructure design of the elastic composite behavior reinforced with natural particles. Composites Part B: Engineering 66, 247–254.
URL https://www.sciencedirect.com/science/article/pii/S1359836814002066

El Moumen, A., Kanit, T., Imad, A., El Minor, H., 2015a. Computational thermal conductivity in porous materials using homogenization techniques: Numerical and statistical approaches. Computational Materials Science 97, 148–158.
URL https://www.sciencedirect.com/science/article/pii/S0927025614006685

El Moumen, A., Kanit, T., Imad, A., El Minor, H., 2015b. Effect of reinforcement shape on physical properties and representative volume element of particles-reinforced composites: Statistical and numerical approaches. Mechanics of Materials 83, 1–16.
URL https://www.sciencedirect.com/science/article/pii/S016766361400221X

Enakoutsa, K., 2014. An improved nonlocal Gurson model for plastic porous solids, with an application to the simulation of ductile rupture tests. Applied Mathematical Modelling 38 (11), 2791–2799.
URL https://www.sciencedirect.com/science/article/pii/S0307904X13007427

Enakoutsa, K., Leblond, J.-B., Perrin, G., 2007. Numerical implementation and assessment of a phenomenological nonlocal model of ductile rupture. Computer Methods in Applied Mechanics and Engineering 196 (13), 1946–1957.
URL https://www.sciencedirect.com/science/article/pii/S004578250600329X

Engelen, R., Geers, M., Baaijens, F., 2003. Nonlocal implicit gradient-enhanced elastoplasticity for the modelling of softening behaviour. International Journal of Plasticity 19,

403–433.
URL https://www.sciencedirect.com/science/article/pii/S0749641901000420

Eringen, A., Suhubl, E., 1964a. Nonlinear theory of simple micro-elastic solids - I. International Journal of Engineering Science 2 (2), 189–203.
URL https://www.sciencedirect.com/science/article/pii/0020722564900047

Eringen, A., Suhubl, E., 1964b. Nonlinear theory of micro-elastic solids - II. International Journal of Engineering Science 2 (4), 389–404.
URL https://www.sciencedirect.com/science/article/pii/0020722564900175

Eshelby, J. D., 1957. The determination of the elastic field of an ellipsoidal inclusion, and related problems. Proceedings of the Royal Society of London. Series A, Mathematical and Physical Sciences 241 (1226), 376–396.
URL http://www.jstor.org/stable/100095

Fleck, N., Hutchinson, J., 1993. A phenomenological theory for strain gradient effects in plasticity. Journal of the Mechanics and Physics of Solids 41 (12), 1825–1857.
URL https://www.sciencedirect.com/science/article/pii/002250969390072N

Fleck, N., Hutchinson, J., 1997. Strain gradient plasticity. Advamces in Applied Mechanics 33, 295–361.

Fleck, N., Hutchinson, J., 2001. A reformulation of strain gradient plasticity. Journal of the Mechanics and Physics of Solids 49 (10), 2245–2271.
URL https://www.sciencedirect.com/science/article/pii/S0022509601000497

Fleck, N., Muller, G., Ashby, M., Hutchinson, J., 1994. Strain gradient plasticity: Theory and experiment. Acta Metallurgica et Materialia 42 (2), 475–487.
URL https://www.sciencedirect.com/science/article/pii/0956715194905029

Forest, S., 2009. Micromorphic approach for gradient elasticity, viscoplasticity, and damage. Journal of Engineering Mechanics 135 (3), 117–131.
URL https://ascelibrary.org/doi/abs/10.1061/%28ASCE%290733-9399%282009%29135%3A3%28117%29

Fraeijs de Veubeke, B., 1979. A Course in Elasticity. Applied Mathematical Sciences. Springer New York.
URL https://link.springer.com/book/10.1007/978-1-4612-6226-8

Galyon, S., Arunachalam, S., Greer, J., Hammond, M., Fawaz, S., 2009. Three Diminsional Crack Growth Prediction. pp. 1035–1068.
URL https://doi.org/10.1007/978-90-481-2746-7_57

Gatt, J., M., Monerie, Y., Laux, D., Baron, D., 2005. Elastic behavior of porous ceramics: application to nuclear fuel materials. Journal of Nuclear Materials 336 (2), 145–155.
URL https://www.sciencedirect.com/science/article/pii/S0022311504006920

Gazis, D., Tadjbakhsh, I., Toupin, R., 1963. The elastic tensor of given symmetry nearest to an anisotropic elastic tensor. Acta Crystallographica 16 (9), 917–922.
URL https://onlinelibrary.wiley.com/doi/abs/10.1107/S0365110X63002449

Geers, M., Engelen, R., Ubachs, R., 2001. On the numerical modelling of ductile damage with an implicit gradient-enhanced formulation. Revue Européenne des Éléments Finis 10 (2-4), 173–191.
URL https://doi.org/10.1080/12506559.2001.11869246

Ghahremaninezhad, A., Ravi-Chandar, K., 2013. Crack nucleation from a notch in a ductile material under shear dominant loading. International Journal of Fracture 184, 253–266.
URL https://doi.org/10.1007/s10704-013-9883-7

Gologanu, M., Leblond, J.-B., Devaux, J., 1993. Approximate models for ductile metals containing non-spherical voids-case of axisymmetric prolate ellipsoidal cavities. Journal of the Mechanics and Physics of Solids 41 (11), 1723–1754.
URL https://www.sciencedirect.com/science/article/pii/002250969390029F

Gologanu, M., Leblond, J.-B., Devaux, J., 1994. Approximate models for ductile metals containing non-spherical voids-case of axisymmetric oblate ellipsoidal cavities. Journal of Engineering Materials and Technology 116 (3), 290–297.
URL https://doi.org/10.1115/1.2904290

Gologanu, M., Leblond, J.-B., Perrin, G., Devaux, J., 1997. Recent extensions of Gurson's model for porous ductile metals. Springer Vienna, Vienna, pp. 61–130.
URL https://doi.org/10.1007/978-3-7091-2662-2_2

Gurson, A., L., 1977. Continuum theory of ductile rupture by void nucleation and growth: Part I—yield criteria and flow rules for porous ductile media. Journal of Engineering Materials and Technology 99 (1), 2–15.
URL https://doi.org/10.1115/1.3443401

Gurtin, M., 2003. On a framework for small-deformation viscoplasticity: free energy, microforces, strain gradients. International Journal of Plasticity 19 (1), 47–90.
URL https://www.sciencedirect.com/science/article/pii/S0749641901000183

Gurtin, M., Anand, L., 2005. A theory of strain-gradient plasticity for isotropic, plastically irrotational materials. part I: Small deformations. Journal of the Mechanics and Physics of Solids 53 (7), 1624–1649.
URL https://www.sciencedirect.com/science/article/pii/S0022509605000220

Gurtin, M. E., Fried, E., Anand, L., 2010. The Mechanics and Thermodynamics of Continua. Cambridge University Press.
URL https://doi.org/10.1017/CBO9780511762956

Hashimoto, K., Kuwabara, T., Iizuka, E., Yoon, J.-W., 2010. Hole expansion simulation of high strength steel sheet. International Journal of Material Forming 3, 259–262.
URL https://doi.org/10.1007/s12289-010-0756-6

Hashin, Z., Shtrikman, S., 1962b. On some variational principles in anisotropic and nonhomogeneous elasticity. Journal of the Mechanics and Physics of Solids 10 (4), 335–342.
URL https://www.sciencedirect.com/science/article/pii/0022509662900042

Hashin, Z., Shtrikman, S., 1963. A variational approach to the theory of the elastic behaviour of multiphase materials. Journal of the Mechanics and Physics of Solids 11 (2), 127–140.
URL https://www.sciencedirect.com/science/article/pii/0022509663900607

He, Z., Zhu, H., Hu, Y., 2021. An improved shear modified GTN model for ductile fracture of aluminium alloys under different stress states and its parameters identification. International Journal of Mechanical Sciences 192, 106081.
URL https://www.sciencedirect.com/science/article/pii/S0020740320323055

Helbig, K., 1996. Representation and approximation of elastic tensors. In: Seismic Anisotropy. Society of Exploration Geophysicists.
URL https://doi.org/10.1190/1.9781560802693.ch3

Hill, R., 1958. A general theory of uniqueness and stability in elastic-plastic solids. Journal of the Mechanics and Physics of Solids 6 (3), 236–249.
URL https://www.sciencedirect.com/science/article/pii/0022509658900292

Hill, R., 1963. Elastic properties of reinforced solids: Some theoretical principles. Journal of the Mechanics and Physics of Solids 11 (5), 357–372.

Holte, I., Nielsen, K., Martínez-Pañeda, E., Niordson, C., 2023. A micro-mechanics based extension of the GTN continuum model accounting for random void distributions. European Journal of Mechanics - A/Solids, 105123.
URL https://www.sciencedirect.com/science/article/pii/S0997753823002152

Hooshmand-Ahoor, Z., Tarantino, M., Danas, K., 2022. Mechanically-grown morphogenesis of Voronoi-type materials: Computer design, 3D-printing and experiments. Mechanics of Materials 173, 104432.
URL https://www.sciencedirect.com/science/article/pii/S0167663622002010

Huerta, A., Pijaudier-Cabot, G., 1994. Discretization influence on regularization by two localization limiters. Journal of Engineering Mechanics 120 (6), 1198–1218.
URL https://ascelibrary.org/doi/10.1061/%28ASCE%290733-9399%281994%29120%3A6%281198%29

Hughes, T. J. R., Winget, J., 1980. Finite rotation effects in numerical integration of rate constitutive equations arising in large-deformation analysis. International Journal for Numerical Methods in Engineering 15 (12), 1862–1867.
URL https://onlinelibrary.wiley.com/doi/abs/10.1002/nme.1620151210

Iacono, C., Sluys, L., van Mier, J., 2006. Estimation of model parameters in nonlocal damage theories by inverse analysis techniques. Computer Methods in Applied Mechanics and Engineering 195 (52), 7211–7222.
URL https://www.sciencedirect.com/science/article/pii/S0045782505004081

Idiart, M., Lahellec, N., 2016. Estimates for the overall linear properties of pointwise heterogeneous solids with application to elasto-viscoplasticity. Journal of the Mechanics and Physics of Solids 97, 317–332.
URL https://www.sciencedirect.com/science/article/pii/S0022509615303744

Idiart, M., Ponte Castañeda, P., 2007. Variational linear comparison bounds for nonlinear composites with anisotropic phases. I. General results. Proceedings: Mathematical, Physical and Engineering Sciences 463 (2080), 907–924.
URL http://www.jstor.org/stable/20209159

ISO 148-1:2016, 2016. Metallic materials - Charpy pendulum impact test - Part 3: Preparation and characterization of Charpy V-notch test pieces for indirect verification of pendulum impact machines, ISO 148-1:2016 Edition. International Organization for Standardization.
URL https://www.iso.org/obp/ui/en/#iso:std:iso:148:-1:ed-3:v1:en

ISO 16630:2017, 2017. Metallic materials - Sheet and strip - Hole expanding test, ISO 16630:2017 Edition. International Organization for Standardization.
URL https://www.iso.org/standard/69771.html

Jia, B., Rusinek, A., Pesci, R., Bernier, R., Bahi, S., Wood, P., 2020. A novel technique for dynamic shear testing of bulk metals with application to 304 austenitic stainless steel. International Journal of Solids and Structures 204-205, 153–171.
URL https://www.sciencedirect.com/science/article/pii/S0020768320303243

Jiràsek, M., 2000. Comparative study on finite elements with embedded discontinuities. Computer Methods in Applied Mechanics and Engineering 188 (1), 307–330.
URL https://www.sciencedirect.com/science/article/pii/S0045782599001541

Jiràsek, M., Bažant, Z., 2002. Inelastic Analysis of Structures. Wiley.

Jiràsek, M., Rolshoven, S., Grassl, P., 2004. Size effect on fracture energy induced by non-locality. International Journal for Numerical and Analytical Methods in Geomechanics 28, 653 – 670.
URL http://dx.doi.org/10.1002/nag.364

Joseph, D., Saut, J.-C., 1990. Short-wave instabilities and ill-posed initial-value problems. Theoretical and Computational Fluid Dynamics 1, 191–227.
URL https://link.springer.com/article/10.1007/BF00418002

Kailasam, M., Ponte Castañeda, P., Willis J., R., 1997. The effect of particle size, shape, distribution and their evolution on the constitutive response of nonlinearly viscous composites. Philosophical Transactions of the Royal Society. B 355, 1835–1852.
URL https://royalsocietypublishing.org/doi/abs/10.1098/rsta.1997.0092

Kailasam, M., Ponte Castañeda, P., 1998. A general constitutive theory for linear and nonlinear particulate media with microstructure evolution. Journal of the Mechanics and Physics of Solids 46 (3), 427–465.
URL https://www.sciencedirect.com/science/article/pii/S0022509697000951

Kanit, T., Forest, S., Galliet, I., Mounoury, V., Jeulin, D., 2003. Determination of the size of the representative volume element for random composites: statistical and numerical approach. International Journal of Solids and Structures 40 (13), 3647–3679.
URL https://www.sciencedirect.com/science/article/pii/S0020768303001434

Khan, I., Benzerga, A., Needleman, A., 2023. A shear modified enhanced Gurson constitutive relation and implications for localization. Journal of the Mechanics and Physics of Solids 171, 105153.
URL https://www.sciencedirect.com/science/article/pii/S0022509622003295

Kim, J., Pham, Q., Kim, Y., 2021. Thinning prediction of hole-expansion test for DP980 sheet based on a non-associated flow rule. International Journal of Mechanical Sciences 191, 106067.
URL https://www.sciencedirect.com/science/article/pii/S0020740320307049

Kramer, S., Jones, A., Mostafa, A., Ravaji, B., Tancogne-Dejean, T., Roth, C., Gorji, M., Pack, K., Foster, J., Behzadinasab, M., Sobotka, J., McFarland, M., Stein, J., Spear, A., Newell, P., Czabaj, W., Williams, B., Simha, H., Gesing, M., Boyce, B., 2019. The third Sandia Fracture Challenge: predictions of ductile fracture in additively manufactured metal. International Journal of Fracture, 5–61.
URL https://doi.org/10.1007/s10704-019-00361-1

Kuwabara, T., Hashimoto, K., Iizuka, E., Yoon, J.-W., 2011. Effect of anisotropic yield functions on the accuracy of hole expansion simulations. Journal of Materials Processing Technology 211 (3), 475–481.
URL https://www.sciencedirect.com/science/article/pii/S0924013610003407

Leblond, J.-B., Perrin, G., Devaux, J., 1994a. Bifurcation effects in ductile metals with nonlocal damage. Journal of Applied Mechanics 61 (2), 236–242.
URL https://doi.org/10.1115/1.2901435

Leblond, J.-B., Perrin, G., Suquet, P., 1994b. Exact results and approximate models for porous viscoplastic solids. International Journal of Plasticity 10 (3), 213–235.
URL https://www.sciencedirect.com/science/article/pii/0749641994900019

Leclerc, J., Nguyen, V.-D., Pardoen, T., Noels, L., 2020. A micromechanics-based non-local damage to crack transition framework for porous elastoplastic solids. International Journal of Plasticity 127, 102631.
URL https://www.sciencedirect.com/science/article/pii/S0749641919303821

Lee, J.-Y., Lee, K.-Y., Lee, M.-G., Kuwabara, T., Barlat, F., 2019. Numerical modeling for accurate prediction of strain localization in hole expansion of a steel sheet. International Journal of Solids and Structures 156-157, 107–118.
URL https://www.sciencedirect.com/science/article/pii/S002076831830324X

Limodin, N., Dahdah, N., Wang, L., El Bartali, A., Witz, J.-F., Buffiere, J.-Y., Charkaluk, E., 2023. Characterisation of 3D strain heterogeneity at the microstructure scale during low cycle fatigue of an AlSi7Cu3Mg alloy at 250 °C. International Journal of Fatigue 172, 107476.
URL https://www.sciencedirect.com/science/article/pii/S0142112322007265

Lopez-Pamies, O., Goudarzi, T., Danas, K., 2013. The nonlinear elastic response of suspensions of rigid inclusions in rubber: II—A simple explicit approximation for finite-concentration suspensions. Journal of the Mechanics and Physics of Solids 61 (1), 19 – 37.
URL https://doi.org/10.1016/j.jmps.2012.08.013

Luo, H., Hooshmand-Ahoor, Z., Danas, K., Diani, J., 2023. Numerical estimation via remeshing and analytical modeling of nonlinear elastic composites comprising a large volume fraction of randomly distributed spherical particles or voids. European Journal of Mechanics - A/Solids, 105076.
URL https://www.sciencedirect.com/science/article/pii/S0997753823001687

Madou, K., Leblond, J.-B., 2012a. A Gurson-type criterion for porous ductile solids containing arbitrary ellipsoidal voids—I: Limit-analysis of some representative cell. Journal of the Mechanics and Physics of Solids 60 (5), 1020–1036.
URL https://www.sciencedirect.com/science/article/pii/S0022509611002201

Madou, K., Leblond, J.-B., 2012b. A Gurson-type criterion for porous ductile solids containing arbitrary ellipsoidal voids—II: Determination of yield criterion parameters. Journal of the Mechanics and Physics of Solids 60 (5), 1037–1058.
URL https://www.sciencedirect.com/science/article/pii/S002250961200018X

Madou, K., Leblond, J.-B., Morin, L., 2013. Numerical studies of porous ductile materials containing arbitrary ellipsoidal voids – II: Evolution of the length and orientation of the void axes. European Journal of Mechanics - A/Solids 42, 490–507.
URL https://www.sciencedirect.com/science/article/pii/S0997753813000703

Mandel, J., 1966. Contribution théorique à l'étude de l' écrouissage et des lois de l' écoulement plastique.

Mbiakop, A., Constantinescu, A., Danas, K., 2015a. A model for porous single crystals with cylindrical voids of elliptical cross-section. International Journal of Solids and Structures 64-65, 100–119.
URL https://www.sciencedirect.com/science/article/pii/S0020768315001328

Mbiakop, A., Constantinescu, A., Danas, K., 2015b. An analytical model for porous single crystals with ellipsoidal voids. Journal of the Mechanics and Physics of Solids Volume 84, 436–467.
URL https://doi.org/10.1016/j.jmps.2015.07.011

Meyer, C., 2000. Matrix Analysis and Applied Linear Algebra. Society for Industrial and Applied Mathematics.
URL https://books.google.gr/books?id=m7W2748ynMcC

Meynard, J., Ibrahim, M., Monnier, A., Bornert, M., Castelier, E., Duguay, C., Gărăjeu, M., Masson, R., 2022. Effective properties of an isotropic solid weakened by micro-cracks located at inter-granular boundaries. Journal of the Mechanics and Physics of Solids 158, 104647.
URL https://www.sciencedirect.com/science/article/pii/S0022509621002866

Michel, J., C., Suquet, P., 1992. The constitutive law of nonlinear viscous and porous materials. Journal of the Mechanics and Physics of Solids 40 (4), 783–812.
URL https://www.sciencedirect.com/science/article/pii/002250969290004L

Michel, J., Moulinec, H., Suquet, P., 1999. Effective properties of composite materials with periodic microstructure: a computational approach. Computer Methods in Applied Mechanics and Engineering 172 (1), 109–143.
URL https://www.sciencedirect.com/science/article/pii/S0045782598002278

Mindlin, R., 1964. Micro-structure in linear elasticity. Archive for Rational Mechanics and Analysis 16, 51–78.
URL https://link.springer.com/article/10.1007/BF00248490

Mindlin, R., Eshel, N., 1968. On first strain-gradient theories in linear elasticity. International Journal of Solids and Structures 4 (1), 109–124.
URL https://www.sciencedirect.com/science/article/pii/002076836890036X

Moakher, M., Norris, A., 2006. The closest elastic tensor of arbitrary symmetry to an elasticity tensor of lower symmetry. Journal of Elasticity 85, 215–263.
URL https://doi.org/10.1007/s10659-006-9082-0

Moriconi, C., Hénaff, G., Halm, D., 2014. Cohesive zone modeling of fatigue crack propagation assisted by gaseous hydrogen in metals. International Journal of Fatigue 68, 56–66.
URL https://www.sciencedirect.com/science/article/pii/S0142112314001704

Morin, L., Leblond, J.-B., Mohr, D., Kondo, D., 2017. Prediction of shear-dominated ductile fracture in a butterfly specimen using a model of plastic porous solids including void shape effects. European Journal of Mechanics - A/Solids 61, 433–442.
URL https://www.sciencedirect.com/science/article/pii/S0997753816301176

Morin, L., Leblond, J.-B., Tvergaard, V., 2016. Application of a model of plastic porous materials including void shape effects to the prediction of ductile failure under shear-dominated loadings. Journal of the Mechanics and Physics of Solids 94, 148–166.
URL https://www.sciencedirect.com/science/article/pii/S0022509616302393

Mühlhaus, H.-B., Alfantis, E., 1991. A variational principle for gradient plasticity. International Journal of Solids and Structures 28 (7), 845–857.
URL https://www.sciencedirect.com/science/article/pii/002076839190004Y

Mura, T., 1987. Micromechanics of Defects in Solids. Kluwer, Dordrecht. Second, revised edition.
URL https://link.springer.com/book/10.1007/978-94-009-3489-4

Nagtegaal, J., Veldpaus, F., 1984. On the implementation of finite strain plasticity equations in a numerical model. In: Numerical methods in industrial forming processes : [papers presented at the international conference, held at Swansea, UK, 12-16 July 1982] / Ed. J.F.T. Pittman. Wiley series in numerical methods in engineering. Wiley-Interscience, pp. 351–371.
URL https://pure.tue.nl/ws/files/4426882/604366.pdf

Nahshon, K., Hutchinson, J. W., 2008. Modification of the Gurson model for shear failure. European Journal of Mechanics - A/Solids 27 (1), 1–17.
URL https://www.sciencedirect.com/science/article/pii/S0997753807000721

Nahshon, K., Miraglia, M., Cruce, J., DeFrese, R., Moyer, E., 2014. Prediction of the Sandia Fracture Challenge using a shear modified porous plasticity model. International Journal of Fracture 186, 93–105.
URL https://doi.org/10.1007/s10704-013-9909-1

Navidtehrani, Y., Betegón, C., Martínez-Pañeda, E., 2021. A simple and robust Abaqus implementation of the phase field fracture method. Applications in Engineering Science 6, 100050.
URL https://www.sciencedirect.com/science/article/pii/S2666496821000169

Needleman, A., Tvergaard, V., 1998. Dynamic crack growth in a nonlocal progressively cavitating solid. European Journal of Mechanics - A/Solids 17 (3), 421–438.
URL https://www.sciencedirect.com/science/article/pii/S0997753898800533

Nielsen, K., Dahl, J., Tvergaard, V., 2012. Collapse and coalescence of spherical voids subject to intense shearing: Studied in full 3D. International Journal of Fracture 177, 97–108.
URL https://doi.org/10.1007/s10704-012-9757-4

Nielsen, K. L., Tvergaard, V., 2011. Failure by void coalescence in metallic materials containing primary and secondary voids subject to intense shearing. International Journal of Solids and Structures 48 (9), 1255–1267.
URL https://www.sciencedirect.com/science/article/pii/S0020768311000175

Nikolakopoulos, K., Crété, J.-P., Longére, P., 2021. Progressive failure of ductile metals: Description via a three-dimensional coupled CZM–XFEM based approach. Engineering Fracture Mechanics 243, 107498.
URL https://www.sciencedirect.com/science/article/pii/S0013794420310584

Noell, P., Carroll, J., Boyce, B., 2018. The mechanisms of ductile rupture. Acta Materialia 161, 83–98.
URL https://www.sciencedirect.com/science/article/pii/S1359645418307006

Noell, P., Sabisch, J., Medlin, D., Boyce, B., 2020. Nanoscale conditions for ductile void nucleation in copper: Vacancy condensation and the growth-limited microstructural state. Acta Materialia 184, 211–224.
URL https://www.sciencedirect.com/science/article/pii/S1359645419307530

Norris, D., 1979. Computer simulation of the Charpy V-Notch toughness test. Engineering Fracture Mechanics 11 (2), 261–274.
URL https://www.sciencedirect.com/science/article/pii/0013794479900031

Oh, C.-S., Kim, Y.-J., Yoon, K.-B., 2010. Coupled analysis of hydrogen transport using ABAQUS. Journal of Solid Mechanics and Materials Engineering 4, 908–917.
URL https://www.jstage.jst.go.jp/article/jmmp/4/7/4_7_908/_article

Pack, K., Luo, M., Wierzbicki, T., 2014. Sandia Fracture Challenge: blind prediction and full calibration to enhance fracture predictability. International Journal of Fracture 186, 155–175.
URL https://doi.org/10.1007/s10704-013-9923-3

Papadioti, I., Aravas, N., Lian, J., Münstermann, S., 2019. A strain-gradient isotropic elasto-plastic damage model with J3 dependence. International Journal of Solids and Structures 174-175, 98–127.
URL https://www.sciencedirect.com/science/article/pii/S0020768319302689

Papadioti, I., Danas, K., Aravas, N., 2016. A methodology for the estimation of the effective yield function of isotropic composites. International Journal of Solids and Structures 87, 120–138.
URL https://www.sciencedirect.com/science/article/pii/S0020768316000846

Pardoen, T., Hutchinson, J., 2000. An extended model for void growth and coalescence. Journal of the Mechanics and Physics of Solids 48 (12), 2467–2512.
URL https://www.sciencedirect.com/science/article/pii/S0022509600000193

Paul, S., Mukherjee, M., Kundu, K., Chandra, S., 2014. Prediction of hole expansion ratio for automotive grade steels. Computational Materials Science 89, 189–197.
URL https://www.sciencedirect.com/science/article/pii/S0927025614002018

Peerlings, R., 2007. On the role of moving elastic–plastic boundaries in strain gradient plasticity. Modelling and Simulation in Materials Science and Engineering 15, S109–S120.
URL https://iopscience.iop.org/article/10.1088/0965-0393/15/1/S10

Peerlings, R., de Borst, R., Brekelmans, W., de Vree , J., 1995. Computational modelling of gradient-enhanced damage for fracture and fatigue problems. In: Owen, D., Oñate, E. (Eds.), Computational plasticity: fundamentals and applications : proceedings of the 4th international conference held in Barcelona, Spain, 3-6 April 1995. Pineridge Press, pp. 975–986.

Peerlings, R., de Borst, R., Brekelmans, W., de Vree, J., Spee, I., 1996. Some observations on localisation in non-local and gradient damage models. European Journal of Mechanics - A/Solids 15, 937–953.
URL https://repository.tudelft.nl/islandora/object/uuid%3A734d4d63-dc5b-424d-a47e-0fabfc312c48

Peerlings, R., de Borst, R., Brekelmans, W., Geers, M., 2002. Localisation issues in local and nonlocal continuum approaches to fracture. European Journal of Mechanics - A/Solids 21 (2), 175–189.
URL https://www.sciencedirect.com/science/article/pii/S0997753802012111

Peerlings, R., Geers, M., de Borst, R., Brekelmans, W., 2001. A critical comparison of nonlocal and gradient-enhanced softening continua. International Journal of Solids and Structures 38 (44), 7723–7746.
URL https://www.sciencedirect.com/science/article/pii/S0020768301000877

Peirs, J., Verleysen, P., Degrieck, J., 2012. Novel technique for static and dynamic shear testing of Ti6Al4V sheet. Experimental Mechanics 52 (7), 729–741.
URL http://doi.org/10.1007/s11340-011-9541-9

Pijaudier-Cabot, G., Bažant, Z., 1987. Nonlocal damage theory. Journal of Engineering Mechanics-ASCE 113 (10), 1512–1533.
URL http://dx.doi.org/10.1061/(ASCE)0733-9399(1987)113:10(1512)

Ponte Castañeda, P., 1991. The effective mechanical properties of nonlinear isotropic composites. Journal of the Mechanics and Physics of Solids 39 (1), 45–71.
URL https://www.sciencedirect.com/science/article/pii/002250969190030R

Ponte Castañeda, P., 1996. Exact second-order estimates for the effective mechanical properties of nonlinear composite materials. Journal of the Mechanics and Physics of Solids 44 (6), 827–862.
URL https://www.sciencedirect.com/science/article/pii/0022509696000154

Ponte Castañeda, P., 2002a. Second-order homogenization estimates for nonlinear composites incorporating field fluctuations: I—theory. Journal of the Mechanics and Physics of Solids 50 (4), 737–757.
URL https://www.sciencedirect.com/science/article/pii/S0022509601000990

Ponte Castañeda, P., 2012. Bounds for nonlinear composites via iterated homogenization. Journal of the Mechanics and Physics of Solids 60 (9), 1583–1604.
URL https://www.sciencedirect.com/science/article/pii/S0022509612001093

Ponte Castañeda, P., Willis, J., 1988. On the overall properties of nonlinearly viscous composites. Proceedings of the Royal Society of London. Series A, Mathematical and Physical Sciences 416 (1850), 217–244.
URL http://www.jstor.org/stable/2398256

Ponte Castañeda, P., Willis, J., 1995. The effect of spatial distribution on the effective behavior of composite materials and cracked media. Journal of the Mechanics and Physics of Solids 43 (12), 1919–1951.
URL https://www.sciencedirect.com/science/article/pii/002250969500058Q

Ramaswamy, S., Aravas, N., 1998a. Finite element implementation of gradient plasticity models Part I: Gradient-dependent yield functions. Computer Methods in Applied Mechanics and Engineering 163 (1), 11–32.
URL https://www.sciencedirect.com/science/article/pii/S0045782598000280

Ramaswamy, S., Aravas, N., 1998b. Finite element implementation of gradient plasticity models Part II: Gradient-dependent evolution equations. Computer Methods in Applied Mechanics and Engineering 163 (1), 33–53.
URL https://www.sciencedirect.com/science/article/pii/S0045782598000279

Remmal, A., Leblond, J.-B., 2024. Ductile rupture under cyclic loadings at high triaxiality: The influence of strain hardening and elasticity. Mechanics of Materials 192, 104982.
URL https://www.sciencedirect.com/science/article/pii/S0167663624000747

Renardy, M., Rogers, R., 2004. An Introduction to Partial Differential Equations. Texts in Applied Mathematics. Springer New York.
URL https://books.google.gr/books?id=0RmDjrFO3CUC

Rice, J., 1976. Localization of plastic deformation. In: In Koiter, W. (Ed.), Proceedings of the 14th International Congress of Theoretical and Applied Mechanics. North-Holland Publishing Corporation, Los Angeles, CA, pp. 207–220.
URL https://www.osti.gov/biblio/7343664

Rolshoven, S., 2003. Nonlocal plasticity models for localized failure. Ph.D. thesis, École Polytechnique Fédéral de Laussane (EPFL).
URL http://infoscience.epfl.ch/record/33362

Rousselier, G., 2022. Lode-dependent second porosity in porous plasticity for shear-dominated loadings. International Journal of Plasticity 159, 103446.
URL https://www.sciencedirect.com/science/article/pii/S0749641922002248

Rudnicki, J., Rice, J., 1975. Conditions for the localization of deformation in pressure-sensitive dilatant materials. Journal of the Mechanics and Physics of Solids 23 (6), 371–394.
URL https://www.sciencedirect.com/science/article/pii/0022509675900010

Santisi d'Avila, M., Triantafyllidis, N., Wen, G., 2016. Localization of deformation and loss of macroscopic ellipticity in microstructured solids. Journal of the Mechanics and Physics of Solids 97, 275–298.
URL https://www.sciencedirect.com/science/article/pii/S0022509616304677

Scheider, I., Brocks, W., 2003. Simulation of cup–cone fracture using the cohesive model. Engineering Fracture Mechanics 70 (14), 1943–1961.
URL https://www.sciencedirect.com/science/article/pii/S0013794403001334

Seupel, A., Hütter, G., Kuna, M., 2018. An efficient FE-implementation of implicit gradient-enhanced damage models to simulate ductile failure. Engineering Fracture Mechanics 199, 41–60.
URL https://www.sciencedirect.com/science/article/pii/S0013794417311669

Shen, W., Lin, J., Zhu, Q., Monchiet, V., Kondo, D., 2011. Macroscopic yield criterion for ductile materials containing randomly oriented spheroidal cavities. International Journal of Damage Mechanics 20, 1198–1216.
URL https://doi.org/10.1177/1056789510395552

Simo, J., Hughes, T., 1998. Computational Inelasticity. Interdisciplinary Applied Mathematics. Springer New York.
URL https://books.google.fr/books?id=ftL2AJL8OPYC

Skallerud, B., Zhang, Z., 1997. A 3D numerical study of ductile tearing and fatigue crack growth under nominal cyclic plasticity. International Journal of Solids and Structures 34 (24), 3141–3161.
URL https://www.sciencedirect.com/science/article/pii/S0020768396001370

Song, D., Ponte Castañeda, P., 2018. A multi-scale homogenization model for fine-grained porous viscoplastic polycrystals: I – finite-strain theory. Journal of the Mechanics and Physics of Solids 115, 102–122.
URL https://www.sciencedirect.com/science/article/pii/S0022509618300322

Srivastava, A., Ponson, L., Osovski, S., Bouchaud, E., Tvergaard, V., Needleman, A., 2014. Effect of inclusion density on ductile fracture toughness and roughness. Journal of the Mechanics and Physics of Solids 63, 62–79.
URL https://www.sciencedirect.com/science/article/pii/S0022509613002111

Stören, S., Rice, J., 1975. Localized necking in thin sheets. Journal of the Mechanics and Physics of Solids 23 (6), 421–441.
URL https://www.sciencedirect.com/science/article/pii/0022509675900046

Suquet, P., M., 1987. Elements of homogenization for inelastic solid mechanics. In: Sanchez-Palencia, E., Zaoui, A. (Eds.), Homogenization Techniques for Composite Media. Springer Berlin Heidelberg, Berlin, Heidelberg, pp. 193–198.
URL https://doi.org/10.1007/3-540-17616-0_15

Talbot, D., Willis, J., 1985. Variational principles for inhomogeneous non-linear media. IMA Journal of Applied Mathematics 35 (1), 39–54.
URL https://doi.org/10.1093/imamat/35.1.39

Tanguy, B., Besson, J., Piques, R., Pineau, A., 2005a. Ductile to brittle transition of an A508 steel characterized by Charpy impact test: Part I: experimental results. Engineering Fracture Mechanics 72 (1), 49–72.
URL https://www.sciencedirect.com/science/article/pii/S0013794404000840

Tanguy, B., Besson, J., Piques, R., Pineau, A., 2005b. Ductile to brittle transition of an A508 steel characterized by Charpy impact test: Part II: modeling of the charpy transition curve. Engineering Fracture Mechanics 72 (3), 413–434.
URL https://www.sciencedirect.com/science/article/pii/S0013794404000852

Tarantino, M., Zerhouni, O., Danas, K., 2019. Random 3D-printed isotropic composites with high volume fraction of pore-like polydisperse inclusions and near-optimal elastic stiffness. Acta Materialia 175, 331–340.
URL https://doi.org/10.1016/j.actamat.2019.06.020

Tekoğlu, C., Hutchinson, J., Pardoen, T., 2015. On localization and void coalescence as a precursor to ductile fracture. Phil. Trans. R. Soc. A 373, 20140121.
URL https://royalsocietypublishing.org/doi/10.1098/rsta.2014.0121

Tuhami, A. E. O., Feld-Payet, S., Quilici, S., Osipov, N., Besson, J., 2022. A two characteristic length nonlocal GTN model: Application to cup–cone and slant fracture. Mechanics of Materials 171, 104350.
URL https://www.sciencedirect.com/science/article/pii/S0167663622001272

Tvergaard, V., 1981. Influence of voids on shear band instabilities under plane strain conditions. International Journal of Fracture 17, 389–407.
URL https://api.semanticscholar.org/CorpusID:136549697

Tvergaard, V., 2009. Behaviour of voids in a shear field. International Journal of Fracture 158, 41–49.
URL https://doi.org/10.1007/s10704-009-9364-1

Tvergaard, V., Needleman, A., 1984. Analysis of the cup-cone fracture in a round tensile bar. Acta Metallurgica 32 (1), 157–169.
URL https://www.sciencedirect.com/science/article/pii/000161608490213X

Tvergaard, V., Needleman, A., 2005. Weld investigations by 3D analyses of Charpy V-notch specimens. Latin American Journal of Solids and Structures 2, 103–112.
URL https://www.lajss.org/index.php/LAJSS/article/view/72

Van Dyke, M., 1975. Perturbation Methods in Fluid Mechanics.

Vincent, M., 2006. Contributions à la modélisation micromécanique de l'endommagement et de la fatigue des métaux ductiles. Ph.D. thesis, University of Lille I.
URL http://www.theses.fr/2006LIL10129

Vincent, P.-G., Monerie, Y., 2008. Yield criterion for a rigid-ideally plastic material with randomly oriented cracks. Comptes Rendus Mecanique 336, 297–303.
URL https://doi.org/10.1016/j.crme.2007.11.020

Wang, L., Limodin, N., El Bartali, A., Charkaluk, E., 2021. Coupling of X-ray computed tomography and surface in situ analysis combined with digital image correlation method to study low cycle fatigue damage micromechanisms in lost foam casting A319 alloy. Fatigue & Fracture of Engineering Materials & Structures 44 (4), 916–932.
URL https://onlinelibrary.wiley.com/doi/abs/10.1111/ffe.13402

Weyl, H., 1946. The classical groups: their invariants and representations. No. 1. Princeton University Press.
URL https://www.jstor.org/stable/j.ctv3hh48t

Willis, J., R., 1977. Bounds and self-consistent estimates for the overall properties of anisotropic composites. Journal of the Mechanics and Physics of Solids 25 (3), 185–202.
URL https://www.sciencedirect.com/science/article/pii/0022509677900229

Willis, J., R., 1980c. A polarization approach to the scattering of elastic waves – II. Multiple scattering from inclusions. Journal of the Mechanics and Physics of Solids 28 (5), 307–327.
URL https://www.sciencedirect.com/science/article/pii/0022509680900228

Willis, J., R., 1981. Variational and related methods for the overall properties of composites. Advances in Applied Mechanics 21, 1–78.
URL https://www.sciencedirect.com/science/article/pii/S0065215608703302

Willis, J., R., 1982. Elasticity theory of composites. In: Hopkins, H., Sewell, M. (Eds.), Mechanics of Solids. Pergamon, Oxford, pp. 653–686.
URL https://www.sciencedirect.com/science/article/pii/B9780080254432500252

Willis, J., R., 1991. On methods for bounding the overall properties of nonlinear composites. Journal of the Mechanics and Physics of Solids 39 (1), 73–86.
URL https://www.sciencedirect.com/science/article/pii/002250969190031I

Wu, J.-Y., Huang, Y., 2020. Comprehensive implementations of phase-field damage models in Abaqus. Theoretical and Applied Fracture Mechanics 106, 102440.
URL https://www.sciencedirect.com/science/article/pii/S0167844219306871

Xenos, D., Grégoire, D., Stéphane, M., Grassl, P., 2015. Calibration of nonlocal models for tensile fracture in quasi-brittle heterogeneous materials. Journal of the Mechanics and Physics of Solids 82, 48–60.
URL https://www.sciencedirect.com/science/article/pii/S0022509615001301

Zauderer, E., 2006. Partial Differential Equations of Applied Mathematics. Pure and Applied Mathematics: A Wiley Series of Texts, Monographs and Tracts. Wiley.
URL https://onlinelibrary.wiley.com/doi/book/10.1002/9781118033302

Zerhouni, O., Brisard, S., Danas, K., 2021. Quantifying the effect of two-point correlations on the effective elasticity of specific classes of random porous materials with and without connectivity. International Journal of Engineering Science 166, 103520.
URL https://www.sciencedirect.com/science/article/pii/S0020722521000677

Zerhouni, O., Tarantino, M., Danas, K., 2019. Numerically-aided 3D printed random isotropic porous materials approaching the Hashin-Shtrikman bounds. Composites Part B: Engineering 156, 344 – 354.
URL https://www.sciencedirect.com/science/article/pii/S1359836818310710

Zhou, J., Gao, X., Sobotka, J. C., Webler, B. A., Cockeram, B. V., 2014a. On the extension of the Gurson-type porous plasticity models for prediction of ductile fracture under shear-dominated conditions. International Journal of Solids and Structures 51 (18), 3273–3291.
URL https://www.sciencedirect.com/science/article/pii/S0020768314002224

Zhou, Z., Bhamare, S., Qian, D., 2014b. Ductile fracture in thin sheet metals: A FEM study of the Sandia Fracture Challenge problem based on the Gurson–Tvergaard–Needleman fracture model. International Journal of Fracture 186, 185–200.
URL https://doi.org/10.1007/s10704-014-9930-z

ECOLE DOCTORALE

Titre : Modélisation théorique et numérique des matériaux poreux

Mots clés : Métaux poreux, Homogénéisation, Théories non-locales, Simulations de formage, Simulations de rupture ductile

Résumé : Ce travail porte sur le développement, la calibration et l'implémentation numérique d'un nouveau modèle élastoplastique entièrement explicite, isotrope et indépendant du taux de déformation pour les matériaux métalliques poreux. La microstructure est supposée être constituée d'une distribution aléatoire de vides sphéroïdaux de même forme, orientés de manière aléatoire et avec une probabilité uniforme. Le modèle proposé est basé sur des estimations d'homogénéisation antérieures qui utilisent une théorie de comparaison composite linéaire (LCC). Pour évaluer l'exactitude du modèle analytique, nous réalisons des simulations éléments finis tridimensionnelles à grandes déformations d'éléments de volume représentatifs (RVE) avec les microstructures correspondantes. Une calibration appropriée des paramètres du modèle conduit à un accord assez précis des prédictions analytiques avec les contraintes moyennes éléments finis et l'évolution de la porosité. Nous montrons, à la fois analytiquement et numériquement, que le rapport d'aspect initial des vides a un effet significatif sur la réponse effective homogénéisée du matériau poreux, entraînant des réponses extrêmement souples pour les vides très oblates, surtout à des triaxialités de contraintes élevées. Ensuite, nous examinons les problèmes computationnels liés à l'implémentation numérique de modèles constitutifs indépendants du taux de déformation qui conduisent à un comportement d'adoucissement. Il est démontré analytiquement que les modèles élastoplastiques basés sur des formulations continues "locales" peuvent entraîner une perte d'ellipticité des équations aux dérivées partielles (EDP) et des solutions numériques dépendantes du maillage. Pour remédier les problèmes numériques associés, nous proposons une version implicite non locale du nouveau modèle poreux, basée sur l'introduction d'une variable de porosité non locale déterminée à partir de la solution d'une EDP supplémentaire. Nous montrons à la fois analytiquement et numériquement que la version régularisée du modèle permet de préserver les propriétés elliptiques des équations du problème, produisant des solutions convergentes indépendantes du maillage dans le régime post-bifurcation. Le point de bifurcation s'avère être fortement dépendant de la forme des micro-vides, avec des vides très plats (par exemple, un rapport d'aspect inférieur à 0,3) entraînant des déformations à la localisation plus faibles. Il est constaté que la longueur matérielle introduite par la formulation non locale a un effet minimal sur le point de bifurcation prédit, affectant uniquement le gradient post-bifurcation de la courbe contrainte-déformation macroscopique et la taille de la zone fortement déformée dans la structure. Dans la dernière partie de cette étude, les versions locale et non locale du modèle sont efficacement implémentées dans un code commercial d'éléments finis (ABAQUS) et utilisés pour la solution numérique de problèmes de valeurs limites liés aux processus de formage et de rupture ductile. En particulier, les problèmes de test d'expansion de trou (TET) et de test d'impact Charpy (essai Charpy), le phénomène de rupture "cup-and-cone" ainsi que la rupture ductile d'un spécimen à géométrie complexe et la comparaison avec les résultats expérimentaux correspondants sont analysés en détail. Les prédictions numériques indiquent que la ductilité est une fonction croissante du paramètre de forme des vides, et les matériaux composés de vides oblates de faible rapport d'aspect présentent une initiation et une propagation macroscopiques de fissures prématurées par rapport aux matériaux avec des vides sphériques ou presque sphériques. Enfin, la capacité du modèle à reproduire les résultats expérimentaux avec une précision suffisante suggère qu'il peut être utilisé pour fournir des prédictions avec seulement un petit nombre de paramètres qui peuvent être calibrés à partir de calculs micromécaniques ou de données expérimentales.

Title : Porous materials: constitutive modeling and computational issues

Keywords : Porous metals, Homogenization, Non-local theories, Forming simulations, Ductile fracture simulations

Abstract : This work is concerned with the development, calibration, and numerical implementation of a novel fully explicit isotropic, rate-independent, elasto-plastic model for porous metallic materials. The microstructure is assumed to consist of a random, with uniform probability, distribution of randomly oriented spheroidal voids of the same shape. The proposed model is based on earlier homogenization estimates that use a Linear Comparison Composite (LCC) theory. The resulting expressions exhibit the simplicity of the well known Gurson model and, thus, their numerical implementation in a finite element code is straightforward. To assess the accuracy of the analytical model, we carry out detailed finite-strain, three-dimensional finite element (FE) simulations of representative volume elements (RVEs) with the corresponding microstructures. Proper parameter calibration of the model leads to fairly accurate agreement of the analytical predictions with the corresponding FE average stresses and porosity evolution. We show, both analytically and numerically, that the initial aspect ratio of the voids has a significant effect on the homogenized effective response of the porous material leading to extremely soft responses for flat oblate voids (e.g., aspect ratio less than 0.5) especially at high stress triaxialities. Next, we examine the computational issues related to the numerical implementation of rate- independent constitutive models that lead to softening behavior. It is shown analytically that elastic-plastic models based on "local" continuum formulations that do not incorporate a characteristic length scale may lead to loss of ellipticity of the governing partial differential equations (PDEs) and mesh-dependent numerical solutions. To remedy the associated numerical problems, we propose an implicit non-local version of the porous model developed in this work which is based on the introduction of a non-local porosity variable determined from the solution of an additional PDE. We show both analytically and numerically that the regularized version of the model allows for preservation of the elliptic properties of the governing equations yielding mesh-independent, converged solutions in the post-bifurcation regime. The bifurcation point (i.e., strain-to-localization) is found to be highly dependent on the micro-void's shape, with very flat voids (e.g., aspect ratio less than 0.3) leading to lower localization strains. The material length introduced by the non-local formulation is found to have minimal effect on the predicted bifurcation point, only affecting the post-bifurcation gradient of the macroscopic stress-strain curve and the size of the highly strained zone in the structure. In the last part of this study, both the local and the non-local versions of the model are efficiently implemented in a commercial finite element code (ABAQUS). The models are used for the numerical solution of boundary value problems (BVPs) related to forming and ductile fracture processes under both quasi-static and dynamic conditions. In particular, the industrially relevant problems of Hole expansion (HET) and Charpy impact (CVN) test, the cup-and-cone fracture phenomenon as well as ductile fracture of a specimen with complex geometry and comparison with corresponding experimental results are analyzed in detail. Numerical predictions in all cases indicate that ductility is an increasing function of the void shape parameter and materials comprising flat oblate voids of low aspect ratio exhibit early macroscopic crack initiation and propagation compared to materials with spherical/almost spherical voids. Finally, the model's capability to reproduce experimental results with sufficient accuracy suggests that it can be utilized to provide predictions with only a small amount of parameters that may be calibrated from either micromechanics calculations or experimental data.

Institut Polytechnique de Paris
91120 Palaiseau, France